Novel injection and targetry in laser wakefield acceleration

Savio Vinod Rozario



September 2019

Supervised by Zulfikar Najmudin

Submitted in partial fulfilment of the requirements for the degree of
Doctor of Philosophy of Imperial College London

Department of Physics
Imperial College London
Prince Consort Road
London SW7 2BZ

Declaration

All the work outlined in this thesis is the authors work unless otherwise acknowledged within the text.

Savio Rozario
September 2019

Copyright

The copyright of this thesis rests with the author and is made available under a Creative Commons Attribution Non-Commercial No Derivatives licence. Researchers are free to copy, distribute or transmit the thesis on the condition that they attribute it, that they do not use it for commercial purposes and that they do not alter, transform or build upon it. For any reuse or redistribution, researchers must make clear to others the licence terms of this work.

Abstract

This thesis presents experimental research into laser wakefield accelerators. It is divided into two main themes; the first was the examination of a novel injection mechanism for wakefield acceleration using a clustered medium and the second was the use of density-length scans to study the optimum conditions for different injection mechanisms.

First, we address an experiment that examined cluster injection, where methane was used for the clustering medium. A clustered target, with cluster radii of $\approx 5 - 10\,\mathrm{nm}$, were observed to generate electron beams with $60.0 \pm 2.5\,\mathrm{pC}$, which was an increase in the charge of the electron beam by a factor of 24 when compared to molecular methane in a gas cell, when driven with a 10 TW laser pulse. The clustered target generates 20% more charge, than the highest charge beams from self-injection in the gas cell. This demonstrates that the injection mechanism was distinct from ionisation injection.

Next, a clustered target was examined at a higher power laser facility, where a 100 TW laser pulse was used to drive a wakefield accelerator. In the same gas jet, helium (SI), helium + 1% nitrogen (II) and methane (CI) were used. The total charge of the electron beam generated for all three targets was $\approx 100\,\mathrm{pC}$. For cluster injection at higher densities, the electron beam was observed to develop transverse oscillations which were attributed to the onset of the hosing instability. This oscillation also coincides with a large increase in x-ray flux. The highest flux betatron beam from CI was 38% higher than II and 8 times greater than SI.

The latter two chapters of this thesis discuss a multi-parameter scan, where density and length were varied sequentially. For self-injection, the highest beam energy observed was $210 \pm 19\,\mathrm{MeV}$ and the highest beam charge measured was $50.0 \pm 2.3\,\mathrm{pC}$ and the lowest beam divergence measured was $1.5 \pm 0.1\,\mathrm{mrad}$.

The final chapter examined a density-length parameter scan using ionisation injection. The maximum energy observed was $159 \pm 22\,\mathrm{MeV}$, the highest charge measured was $35.7 \pm 3.4\,\mathrm{pC}$ and the lowest divergence measured was $1.6 \pm 0.1\,\mathrm{mrad}$. The lowest eccentricity for II was measured to be 23% lower for II than SI. We conclude that for the highest charge beam, SI in a gas cell or CI is the ideal target. Electron beams from SI reach the highest energies and the lowest divergence. Electron beams from II have the lowest eccentricity, pointing deviation and transverse momentum.

Role of the Author

The results shown in this thesis are collated from two experiments performed in 2016 on the Astra-Gemini TA2 and TA3 laser facility. The author acknowledges the support from the Central laser facility in conducting these experiment.

- **TA2 2016 February-March**
  The data from this experiment is presented in Chapter 4, 6 and 7. J. Cole was the Target Area Operator for this experiment. E. Gerstmayr was responsible for the probe beam line, N. Lopes designed the gas targets and commissioned the gas delivery system for this experiment, D. Rusby, L. Wilson, E. Zemaityte set up the electron spectrometer and assisted with the day-to-day alignment. The author worked on the forward transmitted beamline, the electron spectrometer and also assisted with the day-to-day aliment of the experiment. This experiment was funded by DSTL and the author acknowledges their support.
  With the exception of the interferometry analysis for the TA2 experiment (which was analysed by J. Cole), the author analysed all the data from the electron spectrometer, beam profile monitor and focal spot camera for this experiment.

- **TA3 2016 July**
  The data from this experiment is presented in Chapter 5. For this experiment, J. Cole and J. Wood were the Target Area Operators. J. Cole commissioned the probe line, J. Wood commissioned the x-ray diagnostic, N. Lopes worked on the targetry and gas delivery and the author aligned the electron spectrometer and was involved in the day-to-day alignment of the setup.
  For the TA3 experiment, the author analysed all diagnostics on this experiment, which included the electron spectrometer, interferometer, x-ray camera and focal spot diagnostic.

All the simulations shown in this thesis have been performed by the author on the HPC clusters available at Imperial College [1], cx1 and cx2 using the SMILEI [2] and FBPIC [3] particle in cell codes. The author acknowledges the John Adams Institute (grant code: P63914) for its funding towards the experiments performed in the thesis. The author

also acknowledges the assistance of MURI (grant code: PSB235) in funding the work presented in this thesis.

Output of thesis

The work performed in this thesis has informed decisions towards target choice which has resulted in two publications [4, 5]. The first chapter is currently being written up for submission as the first experimental comparison demonstrating how clusters modify the underlying dynamics of wakefield acceleration. The second chapter is yet to be written up, but will highlight how a clustered target can increase the flux of betatron x-rays generated by a laser wakefield accelerator.
The third chapter will be written up for publications exploring the multi-dimensional parameter scan and the range of attainable beam parameters in a single configuration. The final chapter will also be written up highlighting the evolution length concept, how it varies depending on the injection mechanism and its application towards improving the predictability of the scaling laws for mismatched conditions.

Acknowledgements

While coming to the end of my PhD after 4 years of fascinating, (some times frustrating) but mostly interesting research, have I come to realise what an extraordinary opportunity it has been. Much like many of the experiments I have been fortunate enough to be involved in, my PhD has involved the support, wisdom and kindness of the many people. It takes a village to raise a PhD student in this field. I would like to thank Stuart, with whom I stumbled upon this avenue of research for my masters project. His encouragement and feedback have helped me solve problems which I would have previously been stuck on. Next, I am enormously grateful to Zulfikar, for the countless hours spent reading and listening to various research problems I have stumbled upon his office door with. He also has to take the credit for my much improved ability to draw beautiful graphics. Without his emphasis, this thesis would have far less exciting figures. I would like to thank Nelson, Jason, Jon and Kristjan who, during my early years as a PhD student rather patiently spend many hours teaching me how to work in the lab, all the while juggling their own responsibilities and sleep derivation from long campaigns. I certainly would not have progressed, as much as I have, without them taking the time to show me the various eccentricities of experimental physics. Next I would like to thank my cohort companions, Elias and Emma who have been a source of much needed sanity during the write-up phase. Thesis writing is far less isolating with people who are also going through it with you. The coffee and crossword crew, Ollie, George, Rory, Brendon and Spencer who offered a welcome distraction from physics when it was sorely needed. I would also like to thank Matt, Rob, Nic and Michael for their fine humour, interesting chats and evening excursions to the pub during experiments, when, I probably needed a break the most. The staff at the CLF who work tirelessly to ensure that when we turn up there is a facility with which to do experiments. Next, I would like to thank my parents, who have been enormously supportive in this pursuit, from my application to study physics as an undergraduate to where I am now, believing all the while I could do this, when often I struggled to see how. Finally, I would like to thank my partner Kate, who has had to bear the brunt of my PhD woes. Without her support and encouragement, I would not be where I am.

Contents

1 Introduction **22**
1.1 Particle accelerators . . . 22
1.1.1 Applications for conventional accelerators . . . 26
1.2 Plasma accelerators . . . 27
1.2.1 From beat wave to laser wakefield acceleration . . . 28
1.2.2 Applications for plasma accelerators . . . 29
1.3 Thesis summary . . . 30

2 Theory **33**
2.1 Gaussian laser pulses . . . 33
2.2 Plasma properties . . . 35
2.3 Ionisation mechanisms . . . 37
2.4 Laser-particle interaction . . . 39
2.4.1 Laser strength parameter . . . 39
2.4.2 Single particle motion . . . 39
2.4.3 Ponderomotive force . . . 41
2.5 Laser-cluster interaction . . . 42
2.5.1 Cluster generation mechanism . . . 43
2.5.2 Ionisation mechanisms . . . 44
2.5.3 Heating mechanisms . . . 45
2.5.4 Expansion mechanisms . . . 46
2.5.5 Self-focussing in a clustered medium . . . 49
2.6 Laser-plasma interaction . . . 50
2.6.1 Self-focussing in plasma . . . 50
2.6.2 Pulse compression in a plasma . . . 51
2.6.3 Large amplitude plasma waves . . . 52
2.6.4 Wave breaking . . . 53
2.7 Laser wakefield acceleration . . . 55
2.7.1 Focussing and accelerating fields . . . 55
2.7.2 Particle trapping . . . 56
2.7.3 Injection mechanisms . . . 58
2.7.4 Wake phase velocity . . . 61

2.7.5 Energy gain in a wakefield accelerator . . . 61
2.7.6 Scaling laws . . . 65
2.7.7 Beam loading . . . 65
2.7.8 Betatron radiation . . . 66

3 Methods 69
3.1 High power lasers . . . 69
3.1.1 Chirped pulse amplification . . . 70
3.1.2 Astra Gemini . . . 71
3.2 Targetry . . . 71
3.3 Diagnostics . . . 74
3.3.1 Laser diagnostics . . . 74
3.3.2 Electron beam diagnostics . . . 76
3.3.3 Plasma diagnostics . . . 80
3.3.4 X-ray diagnostics . . . 84
3.4 Numerical tools . . . 91
3.4.1 Particle-in-cell simulations . . . 91
3.4.2 Kernel density estimation . . . 92
3.4.3 Data binning procedure . . . 94

4 Laser wakefield acceleration in a clustered medium 97
4.1 Introduction . . . 97
4.2 Experimental setup . . . 100
4.3 Results . . . 108
4.4 Simulations: Clustered medium vs un-clustered medium . . . 112
4.5 Discussion . . . 117
4.6 Conclusion . . . 123

5 Comparison between cluster injection, self-injection and ionisation injection at 200 TW 125
5.1 Introduction . . . 125
5.2 Experimental setup . . . 126
5.3 Results . . . 130
5.4 Discussion . . . 137
5.5 Conclusion . . . 141

6 Investigation of the density-length parameter space in a mismatched, self-guided, self-injecting laser wakefield accelerator at 10 TW 143
6.1 Introduction . . . 143

6.2 Experimental setup . . . 147
6.3 Results . . . 148
6.4 Simulations: 6mm density scan of self injection at TA2 . . . 157
6.5 Discussion . . . 168
6.6 Conclusion . . . 175

7 Examining the density-length parameters space for ionisation injection in a self-guided wakefield accelerator at 10TW 179
7.1 Introduction . . . 179
7.2 Experimental setup . . . 182
7.3 Results . . . 183
7.4 Simulations: 8mm density scan of ionisation injection at TA2 . . . 191
7.5 Discussion . . . 202
7.6 Conclusion . . . 212

8 Conclusion 217
8.1 Summary of results . . . 217
8.2 Future outlook . . . 220

9 Appendix 224
9.1 Symbols and fundamental constants . . . 224
9.2 Maxwell's equations . . . 224

List of Tables

2.1 Scaling laws for laser wakefield accelerators 65

3.1 Baseline parameters for the laser facilities where experiments were formed for this thesis. 71

4.1 Prior work in the field of electron acceleration from a clustered medium. . 97
4.2 Laser parameters used in Chapter 4 100
4.3 Target parameters used in Chapter 4 102
4.4 Electron spectrometer setup in Chapter 4. 104
4.5 Input simulation parameters for Chapter 4 115
4.6 Table recapping the main results from Chapter 4 124

5.1 Laser parameters for Chapter 5 127
5.2 Target parameters for Chapter 5 127
5.3 Electron spectrometer setup in Chapter 5. 129

6.1 Target parameters for Chapter 6. 147
6.2 Laser parameters for Chapter 6. 147
6.3 Input simulation parameters for self-injection simulation in Chapter 6. . . . 158
6.4 Summary table of key results from Chapter 6. 175

7.1 Target parameters for Chapter 7. 183
7.2 Laser parameters for Chapter 7. 183
7.3 Ionisation energies for helium, carbon, oxygen 192
7.4 Input parameters for simulations in Chapter 7. 192
7.5 Summary table of key results from Chapter 7. 213

9.1 Symbols and fundamental constants 224

List of Figures

1.1 Image of cockcroft and walton generator in the National Museum of Scotland. 22
1.2 Superconducting RF cavity used in the LHC 23
1.3 Image of a dipole magnet at KEK 23
1.4 Livingston plot for conventional and laser plasma accelerators 24
1.5 Aerial view of the LHC 25
1.6 Aerial view of SLAC 25
1.7 Protein structure of RNA 26
1.8 The evolution of laser driven plasma based electron accelerators. 28
1.9 Laser bay from the Astra Gemini laser facility 29

2.1 Illustration of various scales of laser-matter interaction 33
2.2 Focussing of a gaussian laser pulse 34
2.3 Plasma slab oscillation diagram 35
2.4 Illustration of various ionisation regimes. 38
2.5 Single particle motion in an electromagnetic plane wave 40
2.6 Illustration showing the various stages of laser-cluster interaction 43
2.7 Illustration of various levels of cluster ionisation 44
2.8 Real component of the time-evolving polarisability of a cluster 49
2.9 Pulse compression diagram 51
2.10 Numerical solution to the 1D non-linear wave equation for laser driven plasma waves 54
2.11 Solution to the 3D linear wakefield equation 56
2.12 Seperatrix plot using the 1D non-linear wakefield equation 57
2.13 Ionisation fraction for carbon using ADK rates. 59
2.14 Dephasing of electron beams in laser wakefield accelerators 62
2.15 Betatron motion illustration 67

3.1 Illustration of Chirped Pulse Amplification 70
3.2 Gas target schematics 72
3.3 Idealised target profile for LWFA 73
3.4 Shadowgraphy and interferometry of the gas cell. 73

3.5 Energy deposition of LANEX for a range of different energies reproduced from [6]. 77
3.6 Illustration of the beam profile diagnostic 78
3.7 Particle tracking trajectories for magnets used in this thesis 79
3.8 Illustration of the principles of scheimpflug for the correction of a tilted focal plane. 80
3.9 Shadowgraphy and interferometry from a 10 mm exit diameter gas jet with helium 80
3.10 Illustration of a common path interferometer 81
3.11 Interferometry anaysis steps 82
3.12 Pressure vs density from interferometry 83
3.13 Illustration of the setup for characterising betatron radiation 85
3.14 Schematic of the filter pack used in this thesis 86
3.15 Raw image showing the x-ray transmission through various elements of the filter pack. Z is the atomic number of the filter element and t is its thickness. 87
3.16 Filter transmission estimate using kernel density estimate 88
3.17 Critical energy determination 89
3.18 The steps taken in a general PIC code. 91
3.19 Comparison between a histogram and kernel density estimate for the sum of two offset Gaussian distributions. 93
3.20 Confidence interval of a kernel density estimation using bootsrapping . . . 94
3.21 Data binning procedure for non-uniformly sampled data 95

4.1 Labelled schematic for gas jets and gas cells used in Chapter 4 100
4.2 Sequoia measurement with carbon energy levels for TA2 101
4.3 Matrix showing the various injection mechanisms for targets in Chapter 4 . 102
4.4 Experiment layout for Chapter 3 103
4.5 Layout of the electron spectrometer in Chapter 4 104
4.6 Energy resolution of the electron spectrometer in Chapter 4 106
4.7 Analysis steps for the beam profile monitor in Chapter 4 107
4.8 Sample data from the beam profile diagnostic for Chapter 4 108
4.9 Sample data from the electron spectrometer diagnostic for Chapter 4 . . . 108
4.10 Charge as a function of density for Chapter 4 109
4.11 Max energy as a function of density for Chapter 4 110
4.12 Beam divergence as a function of density for Chapter 4 111
4.13 Random position of cluster centers 114
4.14 Simulation overview figure for Chapter 4 showing the momentum evolution, density map and wake evolution in a clustered media. 116

5.1 Experiment layout for Chapter 5 . . . 126
5.2 Sample images from the interferometer used in Chapter 5. . . . 128
5.3 Electron spectrometer setup for Chapter 4 . . . 129
5.4 Analysis steps for the electron spectrometer used in Chapter 5 . . . 131
5.5 Overview of raw data from electron spectrometer and x-ray diagnostic used in Chapter 5 . . . 132
5.6 Charge as a function of density for the various targets used in Chapter 5. . 133
5.7 Maximum and mean energy as a function of density for the various targets examined in Chapter 5. . . . 134
5.8 Critical energy as a function of density for the various targets used in Chapter 5. . . . 135
5.9 Photon flux as a function of density for the various targets used in Chapter 5. . . . 136

6.1 Initial parameter space estimate for self-injection in Chapter 6 . . . 146
6.2 Front and side view of the gas cell used in Chapter 6. . . . 147
6.3 a_0 stability for Chapter 6. . . . 148
6.4 Overview data for the electron spectrometer for Chapter 6. . . . 149
6.5 Overview data for the beam profile monitor for Chapter 6. . . . 149
6.6 Charge as a function of density and length for self injection in Chapter 6. . 150
6.7 Charge observed on the low energy electron spectrometer ($10\,\mathrm{MeV} < E < 45\,\mathrm{MeV}$), as a function of density and length for self injection in Chapter 6. 151
6.8 Max energy as a function of density and length for self injection in Chapter 6. . . . 152
6.9 Beam divergence as a function of density and length for self injection in Chapter 6. . . . 153
6.10 Eccentricity as a function of density and length for self injection in Chapter 6. . . . 154
6.11 Transverse momentum as a function of density and length for self injection in Chapter 6. . . . 155
6.12 Simulation overview figure for Chapter 6. . . . 159
6.13 Pulse evolution properties in simulation for Chapter 6. . . . 160
6.14 Evolution of beam charge in simulation for Chapter 6. . . . 162
6.15 Comparison between experiment and simulation for beam charge in Chapter 6. . . . 162
6.16 Evolution of max energy in Chapter 6. . . . 163
6.17 Comparison between experiment and simulation for max energy in Chapter 6. . . . 164
6.18 Example use of cumulative charge for determination of injection point. . . 165

6.19 Evolution length for self-injection from simulations in Chapter 6. 166
6.20 Peak a_0 evolution from simulations in Chapter 6. 167
6.21 Optimum charge as a function of cell length for self-injection in Chapter 6. 169
6.22 Maximum energy as a function of cell length for self-injection in Chapter 6. 171
6.23 Scaling for beam divergence as a function of cell length for self-injection in Chapter 6. 173
6.24 Density-length parameter space with notable results overlaid in Chapter 6. 176

7.1 Ionisation probabilities for different a_0 for Chapter 7 181
7.2 Stability of the a_0 of the laser pulse for Chapter 7. 182
7.3 Sample data from the electron spectrometer for Chapter 7. 184
7.4 Sample data from the beam profile monitor in Chapter 7. 184
7.5 Charge as a function of density and length for ionisation injection in Chapter 7. 185
7.6 Max energy as a function of density and length for ionisation injection in Chapter 7. 186
7.7 Beam divergence as a function of density and length for ionisation injection in Chapter 7. 187
7.8 Pointing deviation as a function of density and length for ionisation injection in Chapter 7. 188
7.9 Beam eccentricity as a function of density and length for ionisation injection in Chapter 7. 189
7.10 Transverse momentum as a function of density and length for ionisation injection in Chapter 7. 190
7.11 Simulation overview figure from Chapter 7. 193
7.12 Evolution of pulse parameters from simulations in Chapter 7. 194
7.13 Evolution of charge from simulations in Chapter 7. 195
7.14 Comparison between experiments and simulation for charge in Chapter 7. . 196
7.15 Evolution of max energy from simulations in Chapter 7. 197
7.16 Comparison between experiments and simulation for max energy in Chapter 7. 198
7.17 Evolution length extracted from simulations for ionisation injection in Chapter 7. 199
7.18 Peak a_0 from simulations for a range of densities in Chapter 7. 200
7.19 Peak a_0 from simulations for a range of densities in Chapter 7. 201
7.20 Optimum charge as a function of cell length in Chapter 7. 203
7.21 Effective a_0 from data using the energy gain equation, density and maximum energy in Chapter 7. 205
7.22 Pointing offset schematic in Chapter 7. 208

7.23 Comparison between eccentricity of self-injected beams and ionisation injected beams in Chapter 7. 210
7.24 Density-length parameter space with notable results for both self-injection and ionisation injection overlaid in Chapter 7. 214

1 Introduction

The field of particle accelerators was born out of a need to understand the fundamental building blocks of the universe. By colliding high energy particles, we can test our models of the fundamental constituents of matter. Sources of high energy particles are available naturally in the form of radioactive sources such as alpha particles, beta particles, gamma radiation and cosmic rays.

The scattering of these particles through gold foil by Rutherford [7] allowed Bohr to formulate a theory of atomic structure. However, this was only the beginning, Rutherford realised that he would need particles with significantly more energy than those available from radioactive sources in order to probe the inner workings of the nuclei. This lead Cockcroft and Walton to construct a device, which in 1932, would split the lithium nucleus with 400 keV protons [8], in what would be the birth of the world's first particle accelerator [9, 10]. A replica of this accelerator is hosted in the National Museum of Scotland as can be seen in Figure 1.1.



Figure 1.1: Replica of the first particle accelerator built by Cockcroft and Walton [11].

1.1 Particle accelerators

The first particle acceleration devices fall into the family of electrostatic accelerators, where the acceleration is provided by static electric fields of a large amplitude. They could provide a tunable source of radiation which, at the time, allowed them to gener-

ate particles with more energy than available with natural sources. The Cockcroft and Walton accelerator became superseded by another design which is still used in teaching laboratories across the world; this is the Van de Graaff generator [12].

These machines were still far off from the requirements of high energy physics experiments and alternatives were being sought. The use of time varying fields was first proposed by Ising, using a radio frequency (RF) cavity. In 1928, Wideroe constructed the first ever accelerator based upon the principles of time-varying fields [10]. Most modern linear accelerators are rooted in this basic idea, where the particle beams gain energy by being at the appropriate phase of the time varying electric fields. Many innovative ways of achieving higher energies were pursued in the decades after such as the cyclotron [13], synchrotron [14, 15] and the betatron [16].

In order to go to higher energies, accelerator physicists had to worry about more than just acceleration fields. The idea of strong focusing, which ensures the beams stay on their intended acceleration path [17], allowed an unprecedented leap in particle beam energies as the beams could now be accelerated over significantly greater acceleration lengths. Advances in superconductivity allowed strong magnetic fields to be employed in the bending magnets [18] and radio-frequency cavities to be operated at a higher frequency [19]. Both of these effects allowed the particle energies to be increased further [9]. While there have been advancements in conventional accelerator technologies since, the main contribution to the increase in particle beam energy is achieved by building machines of ever increasing size.

One of the fundamental reasons, why the acceleration gradients in particle accelerators cannot be increased indefinitely, is because of a phenomena called electrical breakdown, also known as electron field emission [22, 23]. The large electric fields present in these accelerating structures can cause arcs which damage the cavity and reduce its perfor-

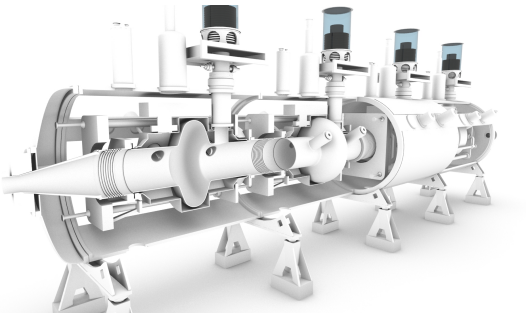


Figure 1.2: Superconducting RF cavity used in the LHC [20]



Figure 1.3: Dipole magnet used to steer the particle beams [21]

mance. Conventional particle accelerators are limited in their accelerating gradients in the $10-100\,\mathrm{MV\,m^{-1}}$ range, which is below the breakdown threshold. However, these high field accelerators also have a higher failure rate when operated close the the breakdown threshold. As such, they are operated at field strengths lower than the peak fields they are capable of generating [24], in the interest of safety.

In the field of accelerator physics, the rapid increase in the centre of mass energy of the particle accelerators is represented by a plot called the Livingston plot shown in Figure 1.4. However, the trend to higher energies has been sustained in recent times by building ever larger colliders. The sheer magnitude of these machines has motivated the search for higher gradient accelerating schemes. Laser-plasma accelerators are one such alternative and the equivalent rate of advance for this field is also shown in Figure 1.4.
The rate of energy doubling is similar for plasma accelerators compared to conventional accelerators at 3.4 years between the doubling of the beam energies. The size of the machines generating particle beams from laser plasma sources are however significantly smaller than their conventional counterparts.

It should also be noted that conventional particles accelerators have not seen an increase in the centre of mass energies since the completion of the Large Hadron Collider at CERN [25]. The Livingston plot in Figure 1.4 shows signs that the rate of increase in the energy of the accelerated particles is slowing down for conventional accelerators. While the field of plasma accelerators is still relatively new, the growth of the field is comparable to the early years of conventional accelerators.

The primary goal of building the LHC was to test the Standard Model [26], currently

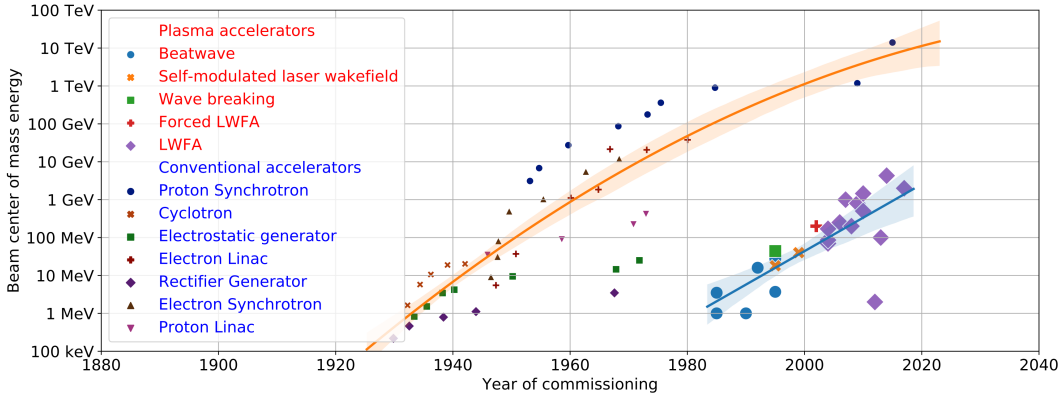


Figure 1.4: Livingston plot for conventional and laser plasma accelerators. Data for the conventional accelerators is extracted from [10] and for plasma accelerators is compiled from notable results from literature.



Figure 1.5: Aerial view of the Large Hadron collider (LHC). This machine can accelerate protons to a centre of mass energy of 14 TeV [30].

the most comprehensive theory of the fundamental forces of nature. Experimental validation of the electroweak theory [27] and the discovery of the quarks [28] helped provide firm evidence that these theories described the fundamental forces of nature. The Large Hadron Collider [25], as seen in Figure 1.5 is a circular proton-anti proton particle accelerator. The LHC recently provided experimental evidence of the Higgs boson [29], which was one of the key predictions of the Standard model. While the Standard Model itself is mathematically complete, it is not a fully unified theory of physics, sometimes referred to as a Grand Unified Theory or GUT [32].

Gravity, the last of the fundamental forces to be unified, is not included within this framework. The Standard Model also predicts that neutrinos should be massless; exper-

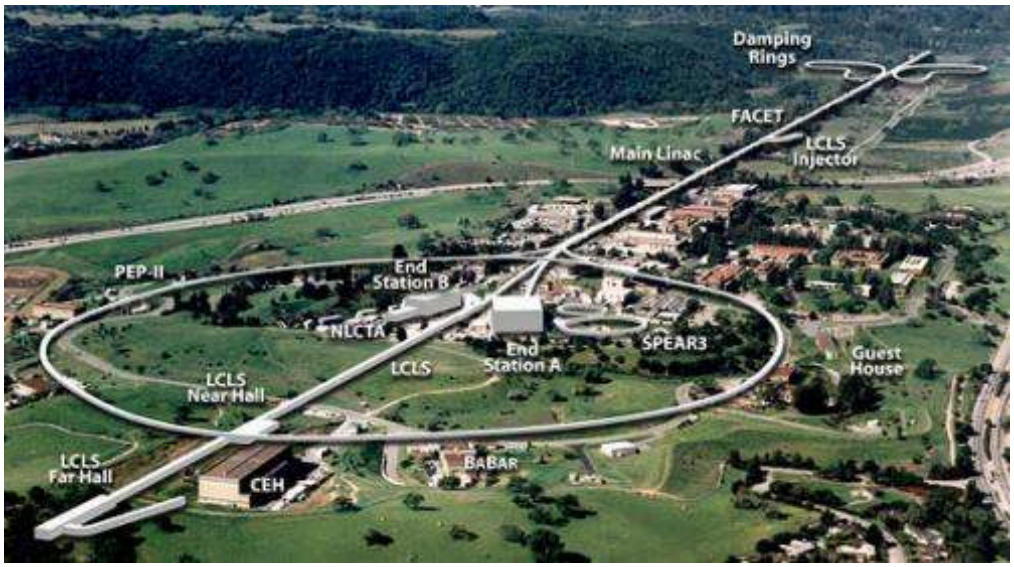


Figure 1.6: Aerial view of the Stanford linear collider (SLAC). The worlds highest energy linear electron accelerator achieving beam energies of 50 GeV [31]

iments have proven this to be incorrect [33] and the origin for the mass of neutrinos is currently an open question in particle physics.

There are many free parameters for the standard model [34], all of which are not believed to be fundamental. These parameters which include the coupling constants between the various forces have to be measured experimentally [35]. This body of research is the next frontier which experimental particle physics will focus its attention towards, collectively referred to as Beyond-Standard model (BSM) physics [36].

1.1.1 Applications for conventional accelerators

The advent of particle accelerators has also opened up new ways to examine matter. In electron synchrotron machines, the radiation generated by bending the path of the electron beam, known as synchrotron radiation, can be so intense that it is capable of melting the walls of the accelerator [37]. This emission of radiation reduces the overall energy of the accelerated particles.

Engineers and physicists work extremely hard to replenish the energy of electron beams in ring based accelerators as their synchrotron losses can be significant. Some realised that this radiation could be a very interesting source of x-ray radiation and soon dedicated synchrotron facilities were built for the purpose of using this radiation.

The first dedicated machine built for the application of this radiation was the Synchrotron Radiation Source (SRS) at the Daresbury Laboratory in the UK [39]. As applications of these intense sources of radiation were being discovered (x-ray spectroscopy,



Figure 1.7: Protein structure of RNA polymerase II was determined using LCLS [38]. Kornberg was awarded the Nobel prize for this discovery.

diffractive imaging, x-ray microscopy [40]), another even brighter source of radiation called the Free Electron Laser (FEL) was conceived.

Unlike a conventional laser which generates radiation by amplification in a cavity, a FEL uses the electron beam to generate radiation by oscillating a charge bunch in a magnetic field. The emitted radiation feeds back on the electron beam causing it to bunch up and radiate such that the generated radiation is in phase and results in the generation of a bright, coherent source of radiation. FELs can generate radiation over a wide range of wavelengths. FELs operated in the x-ray regime are called XFELs [41]. They provide the highest quality beams, in terms of brightness and temporal bandwidth, for this wavelength regime.

XFELs also represent a phenomenal feat of engineering. The cost of these machines is also extremely high. The accelerating portion of the Stanford Linear Accelerator (SLAC) was converted into the Linac Coherent Light Source (LCLS), which can be seen in Figure 1.6. The machine was upgraded to LCLS-II, which was estimated to cost approximately $400M [42]. This is justified by the superior imaging capability that it offers for probing nanometre scale objects on the femtosecond scale at high repetition (MHz) rate. Such impressive probing capabilities allowed applications such as unravelling the structure of complex protein molecules in Figure 1.7 to become feasible.

1.2 Plasma accelerators

While electrical breakdown might be a limitation for conventional particle accelerators, it is the genesis of plasma accelerators. One definition for a plasma is a “collection of quasi-neutral charged particles which exhibits collective behaviour” [43]. The idea of using a plasma for particle acceleration was first proposed by Veksler in 1956 [44] and then followed up by Fainberg [45]. Plasmas can support electric fields far greater than any conventional accelerators. These electric fields can be created by charge separation and even result in a travelling wave structure.

While Fainberg conceived these waves could be driven by particle beams, which lead to the field of plasma wakefield acceleration, the method of using a high intensity laser pulse to drive a plasma wave was first outlined by Tajima and Dawson in a seminal paper in 1979 [46]. It sparked phenomenal interest in the field known as laser wakefield acceleration as it promised acceleration gradients many orders of magnitude greater than were possible in conventional accelerators.

1.2.1 From beat wave to laser wakefield acceleration

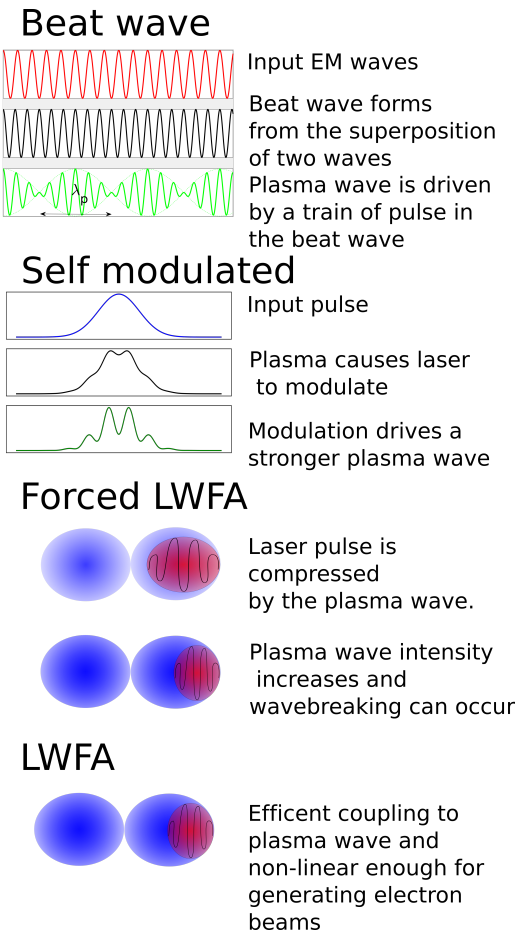


Figure 1.8: The evolution of laser driven plasma based electron accelerators.

In 1979, laser pulse intensities and pulse durations were orders of magnitude away from realising the LWFA idea in its original form. The state-of-the-art laser pulses had pulse durations on the picosecond timescale with peak powers approaching a gigawatt [47]. Generating a plasma wave from a laser pulse was challenging given the technology at the time. The beat-wave scheme was realised to overcome these limitations [48]. Two laser pulses with different frequencies are propagated through a plasma. If the plasma is at the appropriate density, the ponderomotive force of the beat, resonantly drives the generation of a large amplitude plasma wave. This idea seemed promising for low intensities but as the amplitude grows, the phase matching conditions vary and the process falls out of resonance [49]. This is schematically shown in Figure 1.8.

Around the same time that beatwave experiments were occurring, the field of high power lasers was about to experience a breakthrough in laser technology called chirped pulse amplification [50]. This technique allowed laser powers to be increased dramatically and suddenly the dream of driving a plasma wave using a single laser pulse was much more feasible. The self-modulated laser wakefield accelerator (SM-LWFA) was the next idea to be explored [51–53]. This relies on an instability, called the self-modulation instability. The laser pulse causes density perturbations in the medium, which in turn caused the laser pulse to break up into beam-lets separated by the plasma wavelength. Since wavebreaking is not actively controlled in SM-LWFA, electron beams with exponential spectra are generated.

With steady improvements in laser technology, laser pulses became short enough to fit inside a plasma wave. This form of acceleration allows the injected particles to accelerate electron beams with narrow energy spreads. In 2004, the first observation of narrow

energy spread electron beams, with 3% energy spread from a plasma was reported [54–56]. The field has since been growing rapidly, exploring various ways of improving the energy gain and improving the beam quality from these accelerators by tailoring the injection process [57–60], the guiding [56, 61] etc. The highest reported energy at the time of writing is 7.8 GeV [62] but improvements in laser technology and targetry will see these accomplishments being rapidly overtaken in the near future.

1.2.2 Applications for plasma accelerators

In a laser wakefield accelerator, there are not only accelerating forces on the particle beam, but also focussing forces in the transverse direction to the propagation of the beam. This causes the electron beam to oscillate about the axis and generate collimated radiation in the propagation direction, for a typical GeV class LWFA system this is in the 10s of keV range [63]. The laser area for the 200 TW the Astra-Gemini laser facility is shown in Figure 1.9. This facility is routinely used to generated 10s keV betatron radiation for various experiments [63–65].

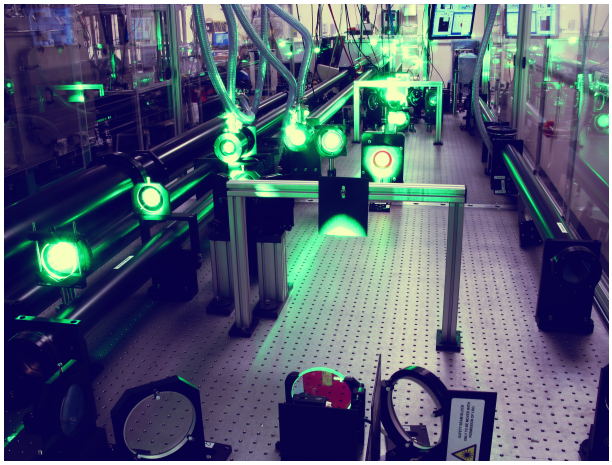


Figure 1.9: Laser bay from the Astra Gemini laser facility [66]

The electron beam from a LWFA has been used to generate radiation via inverse compton scattering [67], bremsstrahlung [68], terahertz [69] and in an undulator [70]. The versatility of a compact accelerator opens up a host of various research opportunities as well as industrial applications. We do note that while the compactness of LWFA's is often touted, the lesser appreciated fact is that it takes a significantly large high power laser system to drive this accelerator. Developments in high power laser technology, have dramatically reduced the footprint of TW systems, which are now capable of truly table-top performance.

They find a host of applications in x-ray imaging [63, 65, 71, 72], nuclear transmutation [73] and probing the quantum radiation reaction models [74, 75] to name a few. While the feasibility of building a collider from laser-plasma accelerators might still be decades away, the field of plasma-wakefield accelerators has recently achieved an impressive milestone. The proton beam from the Super Proton Synchrotron (SPS) was used to drive a self-modulated plasma wave and accelerate electrons to 2 GeV in 10 m.

The advantage of using the proton beam as the driver for the wakefield is two-fold. The phase velocity of the wake is equivalent to the velocity of the driver. As proton beams can be accelerated to 14 TeV at CERN, in principle, linear electron acceleration to the TeV level is also possible [76]. The alternative to accelerate electron beams to the TeV level would require 30 km of accelerator infrastructure to be built [77].

1.3 Thesis summary

This thesis reports on experiments detailing the exploration of novel targets towards electron acceleration, a comparison of their relative stability and radiation generation. The outlook of these experiments will aide in the future development of targets for LWFA experiments. Each chapter presents the exploration of a particular idea, presentation of experimental data towards the topic explored, supported by simulations and/or theoretical understanding of the phenomena.

Ch. 2: Theory

The theoretical frameworks for the various experimental topics are discussed such as laser-matter interaction, laser-cluster interaction, plasma wave formation, electron acceleration, associated scaling laws and betatron radiation.

Ch. 3: Methods

Information about the laser systems used in performing these experiments is outlined. The range of targets operated on these experiments and their associated properties are discussed. The diagnostics employed in laser-wakefield experiments are examined. The various numerical tools used are described.

Ch. 4: Laser wakefield acceleration in a clustered medium

The laser wakefield mechanism in the presence of a clustered medium was explored. It is hypothesized that clustering will improve the performance of the accelerator. Experimental data is presented to support this claim and simulations are presented to show how this interaction generates beams of electrons. The performance of a clustered medium was examined at a 10 TW laser facility.

Ch. 5: Comparison between cluster injection, self-injection and ionisation injection at 200 TW

The cluster injection mechanism was examined using a 200 TW laser facility and compared to self-injection and ionisation injection. The generated electron beam and betatron radiation from the interaction are compared across a range of densities.

Ch. 6: Investigation of the density-length parameter space in a mismatched, self-guided, self-injecting laser wakefield accelerator at 10 TW

A multi-parameter scan involving density and length was performed using helium in a gas cells using a 10 TW laser facility. The energy, charge and divergence of self-injected electron beams are studied across this parameter space. Modification to scaling laws were proposed and a comparison to predicted beam properties from PIC simulations are presented.

Ch. 7: Examining the density-length parameters space for ionisation injection in a self-guided wakefield accelerator at 10 TW

The density and length parameter space was investigated using helium +5% carbon dioxide in a gas cells using a 10 TW laser facility. The experimental conditions, apart from the injection mechanism were identical to those in Chapter 6. The energy, charge and divergence of the ionisation-injected electron beams were studied across this parameter space. A modification to the matched evolution scaling laws were proposed and compared to beam parameters from the experiments and PIC simulations. Additionally, ionisation injected electron beams were compared to self-injected electron beams with respect to their energies and divergence.

2 Theory

We begin by exploring the mathematical description of ideal laser pulses and the various parameters which define plasma dynamics. These plasma parameters are important in distinguishing various regimes of laser-plasma interactions. We then examine the interaction of laser pulses with single particles as they form the basis for all laser-matter interactions. The inclusion of neighbouring particles leads to a regime where we see collective effects starting to have an impact on the system. This represents the field of laser-cluster interaction, where we explore some important aspects of such a medium such as Coulomb expansion and cluster self-focussing. Finally, we build up in scale to laser-plasma interactions and highlight wave generation, wave-breaking, pulse modification before addressing the physics of laser-plasma accelerators. As is illustrated in Figure 2.1, these topic represent a variety of different spatial scales. As we increase in spatial scale, we transition from describing the interaction as a wave-particle interaction to a wave-wave model.

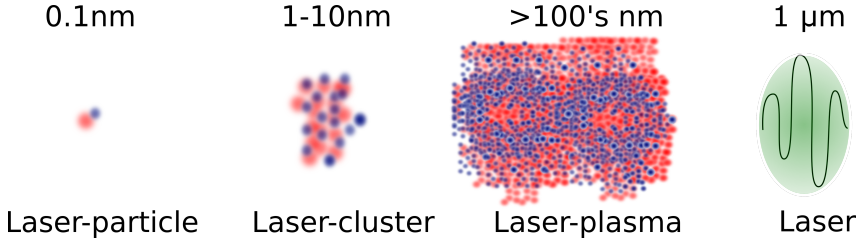


Figure 2.1: Illustration of various scales of laser-matter interaction. Laser fields interact with atoms on the 0.1 nm scale, on the left hand side of this figure. On the other side, the laser wavelength is of the order of 1 μm and plasma waves can be larger still at 10s of μm.

2.1 Gaussian laser pulses

Laser pulses are generated by amplification in resonant optical cavities. Only a specific set of pulses can satisfy the boundary conditions of a resonant cavity, these are called the Hermite-gaussian modes. They are solutions to the wave-equation under the paraxial approximation, which assumes rays only deviate by a small angle from the optical axis,

$$\left[\frac{1}{r}\frac{\partial}{\partial r}\left(r\frac{\partial}{\partial r}\right)+2ik\frac{\partial}{\partial z}\right]\mathbf{E}(r,z)=0. \tag{2.1}$$

The lowest order mode, for this family of solutions is called the Gaussian mode. The equations describing such a mode can be expressed as

$$\begin{aligned} E(r,z) &= E_0 \frac{w_0}{w(z)} \exp\left(-\frac{r^2}{w(z)^2}\right) \exp\left(-i\left[kz - \tan^{-1}\left(\frac{z}{z_r}\right) + \frac{kr^2}{2R(z)}\right]\right), \\ w(z) &= w_0\sqrt{1+\frac{z}{z_r}}, \\ z_r &= \frac{\pi w_0^2}{\lambda}, \\ R(z) &= z\left[1+\left(\frac{z_r}{z}\right)^2\right], \end{aligned} \tag{2.2}$$

where, w_0 is the $1/e^2$ waist of the intensity of the laser pulse, $w(z)$ is the spot size at a distance z away from the focal plane and z_R is the Rayleigh range. This represents the distance over which the intensity drops by a factor of 2. These parameters of a focussing Gaussian laser pulse are shown in Figure 2.2. E_0 is the peak amplitude of the electric field and R is the radius of curvature. The Gaussian description of a laser pulse is useful

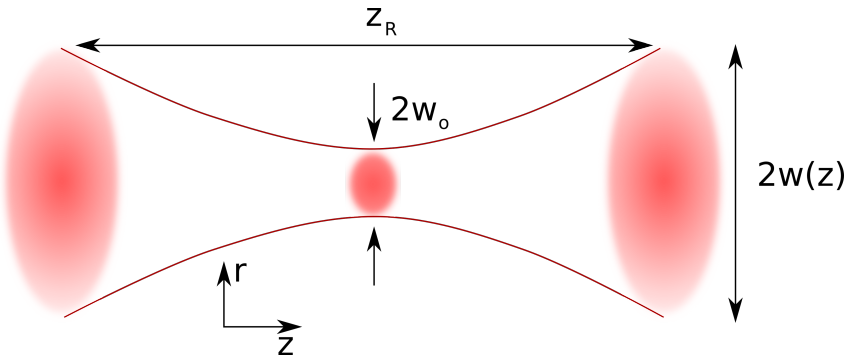


Figure 2.2: Focussing of a gaussian laser pulse with some key parameters overlayed. The laser pulse is focussing in the z direction. When focus the radius of the beam is w_0 and the distance over which the beam radius is less than twice its minimum value is its Rayleigh range z_R.

for experimental design as it allows one to predict the evolution of the pulse for a wide range of parameters. Real world large-aperture beams however often have a more top-hat or super-Gaussian profile. The top-hat profile results in an Airy pattern when focussed down. For laser-plasma experiments, the laser pulse typically needs to be focused to a spot on the order of 10s μm. This means that the useful interaction length - z_r is extremely short. The mitigation of this issue is addressed later on in this chapter.

This description of laser pulses is not valid for extremely tight focusing geometries, where the paraxial approximation breaks down. However, for the experiments performed in this thesis, the paraxial approximation holds as $w_0 \gg \lambda$ [78].

Beam propagation factor

Real laser pulses can vary from the ideal gaussian or top-hat descriptions of beams for a variety of reasons such as misalignment, optimal extraction from amplification cavities etc. One way to describe how these beams propagate is to introduce a quality factor called beam propagation factor, also known as M^2 [79]. The M^2 of a beam is typically calculated by measuring the beam radius as a function of distance from the focal plane. Using a modified version of the expression of the Rayleigh range,

$$z_R = \frac{\pi w_0^2}{M^2 \lambda}, \tag{2.3}$$

we can calculate the M^2 of the beam. For a diffraction limited beam, we obtain $M^2 \equiv 1$.

2.2 Plasma properties

Plasma frequency

Plasmas are defined as quasi-neutral collections of charged particles which exhibit collective behaviour [80]. Consider, in the simplest case a uniform block of electrons and ions as depicted in Figure 2.3. When they are forced apart, an electric field is built up due

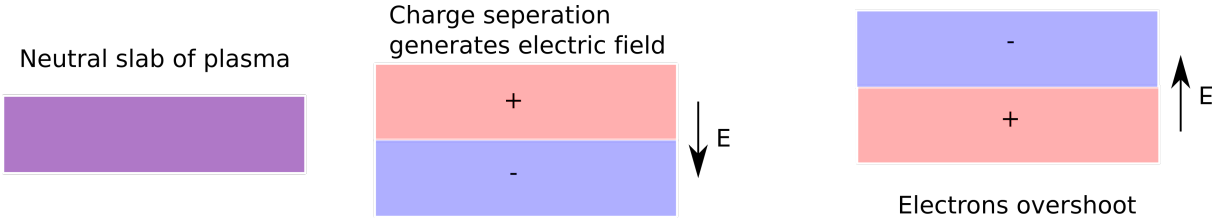


Figure 2.3: Simple harmonic oscillation set up the charge separation and release of a uniform block of plasma.

to charge separation. This force will act on the electrons, which will move on a faster time-scale, as they are much lighter than the ions,

$$\begin{aligned} \nabla \cdot \vec{E} &= \frac{e n_e}{\epsilon_0}, \\ E_x &= \frac{e n_e x}{\epsilon_0}, \end{aligned} \tag{2.4}$$

Where, E_x is the electric field, n_e is the electron density, e is the charge of the electron and ϵ_0 is the dielectric constant. Now, consider the equation of motion of this elemental

volume of electron plasma,

$$\begin{aligned} m_e\ddot{x} &= eE_x, \\ \ddot{x} - \frac{e^2 n_e}{m_e \epsilon_0} x &= 0, \end{aligned} \tag{2.5}$$

where m_e is the mass of the electron. This is the standard form of a harmonic oscillator where the characteristic frequency of oscillation, called the plasma frequency ω_p, is given by,

$$\omega_p = \sqrt{\frac{n_e e^2}{\epsilon_0 m_e}}. \tag{2.6}$$

Electromagnetic (EM) waves can propagate through plasma if its density is below a critical value. The dispersion relation for such waves in plasmas is given as [81],

$$(ck)^2 = \omega_p^2 - \omega^2, \tag{2.7}$$

where c is the speed of light and k is the wave vector of the EM wave. From this equation, we can see that when the frequency of the EM wave (ω) approaches ω_p, the wave can no longer propagate. The number density at which this occurs at is called the critical density, and is defined as follows,

$$n_c = \frac{\epsilon_0 m_e \omega_L^2}{e^2}, \tag{2.8}$$

where ω_L is the frequency of the EM wave. Physically, this can be understood as the density at which the time-scale of the plasma oscillations is short enough to allow it to react and oppose the incident field.

Skin depth

When an electromagnetic wave is incident into a medium which is of a density greater than the critical density n_c, it is reflected by the medium. An evanescent wave propagates into the medium and the length scale associated with this wave is called the skin depth, which is defined as,

$$l_s = \frac{c}{\omega_p}. \tag{2.9}$$

An under-dense medium is defined as one where an oscillatory electromagnetic wave can propagate inside. Conversely, in an over-dense medium only an evanescent wave can propagate up to a skin-depth l_s into the medium.

Debye length

Plasma will act collectively to screen any bare charge. Consider a charge Ze, at rest, in a plasma of uniform electron density of n_e with immobile ions. Poisson's equation for this system, where $E = -\nabla\phi$ is as follows,

$$\nabla^2\phi = -\frac{\rho}{\epsilon_0} = \frac{e}{\epsilon_0}(Zn_i - n_e), \tag{2.10}$$

where, ϕ is the electric potential. Assuming an isothermal equation of states, where $p_e = n_e k_b T_e$, k_b is the Boltzmann constant and T_e is the temperature of the plasma. We can use the Boltzmann distribution to relate the perturbed electron density n_e to the initial electron density, $n_0 = Zn_i$ in thermal equilibrium as,

$$n_e = n_0 \exp\left(-\frac{E}{k_b T_e}\right) = n_0 \exp\left(-\frac{e\phi}{k_b T_e}\right), \tag{2.11}$$

where T_e it the electron temperature. Substituting Eq. 2.11 into Eq. 2.10, we obtain,

$$\nabla^2\phi = \frac{n_0 e}{\epsilon_0}\left[\exp\left(-\frac{e\phi}{k_b T}\right) - 1\right]. \tag{2.12}$$

Next, we assume that $\frac{e\phi}{k_b T} \ll 1$ which physically means that the kinetic energy of the plasma is greater than the potential energy. We Taylor expand the exponential to obtain

$$\nabla^2\phi = -\frac{n_0 e^2}{\epsilon_0 k_b T_e}\phi. \tag{2.13}$$

This equation can be solved using the following ansatz,

$$\begin{aligned} \phi(r) &= \frac{Ze}{4\pi\epsilon_0}\frac{\exp\left(-\frac{r}{\lambda_D}\right)}{r}, \\ \lambda_D &= \sqrt{\frac{\epsilon_0 k_b T_e}{n_e e^2}}. \end{aligned} \tag{2.14}$$

where λ_D, is called the Debye length and represents the length scale over which plasma will act to shield any bare charge within it. This phenomena is also referred to as screening. The debye length will be important during the discussion of clusters in plasmas.

2.3 Ionisation mechanisms

The generation of a plasma medium requires that some fraction of the electrons bound inside atoms to be liberated from their bound orbital state to a free continuum state. A

crucial part of the definition of plasma, is that the medium is at least partially ionised. One way to achieve this is by using the electric fields present in a high power laser pulse. The ionisation mechanism of the medium will depend on whether the ionisation mechanism is collisional or collisionless.

Field ionisation mechanisms

There are three main regime for ionisation for low density media, tunnel ionisation [82], barrier suppression [81] and multi-photon ionisation [83]. In order to determine which regime we are in, we consider the Keldysh parameter,

$$\begin{aligned} \gamma_K &\approx \sqrt{\frac{U_{ion}}{\phi_{pond}}}, \\ \phi_{pond} &= \frac{e^2 E_L^2}{4 m_e \omega_L}, \end{aligned} \tag{2.15}$$

where, γ_K is the Keldysh parameter, U_{ion} is the binding energy of the ion, I_L is the intensity of the laser pulse, ϕ_{pond} is the ponderomotive potential and E_L is the peak electric field of the laser. This compares the magnitude of the ionisation potential of the ion to the ponderomotive potential of the laser. If $\gamma > 1$, we are in the multi-photon regime, if $\gamma < 1$ we are in the tunnel and barrier suppression ionisation regime.
Typical laser wakefield experiments involve atomic species where $U_{ion} \approx 10 - 500\,\mathrm{eV}$, $E_L = 3 \times 10^{13}\,\mathrm{V\,m^{-1}}$, $\lambda_L = 0.8\,\mu\mathrm{m}$ gives $\gamma_K = 0.07 - 0.47$ and we are mostly in the tunnel ionisation regimes.

A model developed, initially by Ammosov [84], has been experimentally verified over

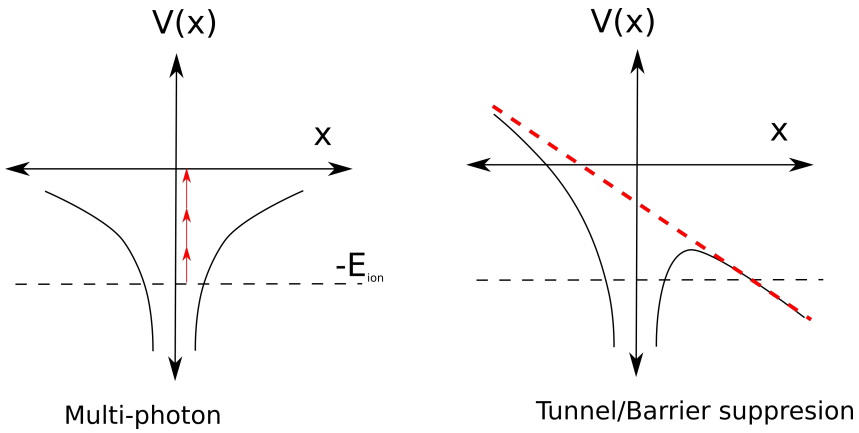


Figure 2.4: Illustration of various ionisation regimes. On the left hand figure the red arrows represent the energy provided by individual photons which can add up to provide enough energy to escape the potential well. On the right hand side, the electric field of the laser can lower the binding potential of the atom and lower the ionisation threshold.

several orders of magnitude, to describe tunnel ionisation for many atom systems [85]. Referred to as the Ammosov-Delone-Krainov (ADK) model, it can be used to determine the ionisation probabilities for various atomic species [86],

$$\begin{aligned} R &\approx 1.52 \frac{4^n U_{ion}}{n\Gamma(2n)} \left(20.5 \frac{U_{ion}^{3/2}}{E_L}\right)^{2n-1} \exp\left[-6.83\left(\frac{U_{ion}^{3/2}}{E_L}\right)\right], \\ n &= 2.69 \frac{Z}{\sqrt{U_{ion}}}, \end{aligned} \tag{2.16}$$

where, R is the rate of ionisation in fs, U_{ion}[eV] is the ionisation potential of the electron, E_L is the laser electric field and n is the effective quantum number of the electron.

2.4 Laser-particle interaction

2.4.1 Laser strength parameter

A key parameter in laser-plasma interactions is the peak normalised vector potential a_0. This is defined as

$$a_0 = \frac{eE_0}{m_e \omega c}, \tag{2.17}$$

where ω is the frequency of the laser. The importance of this parameter can be illustrated by considering the 1D Lorentz equation for a single particle oscillating in a laser field in the non-relativistic case,

$$\begin{aligned} \frac{dp}{dt} &= eE_0 \sin(\omega t), \\ p &= eE_0 \cos(\omega t), \\ \frac{p}{m_e c} &= \frac{eE_0 \cos(\omega t)}{m_e \omega c} = a_0 \cos(\omega t), \end{aligned} \tag{2.18}$$

where p is the momentum of the particle. The normalised transverse momentum that the particle attains is related to the normalised vector potential. This parameter also defines the onset of relativistic effects when $a_0 > 1$. A useful formula for a_0 is,

$$a_0 = 0.855 \sqrt{I_{18} \lambda_{\mu m}}. \tag{2.19}$$

where $I_{18} = I[10^{18} \mathrm{W\,cm^{-2}}]$ and $\lambda_{\mu m}$ is the wavelength of the laser pulse in micrometres.

2.4.2 Single particle motion

The starting point for understanding how a laser interacts with matter is by considering how a single electron behaves in the presence of a plane electromagnetic wave of varying

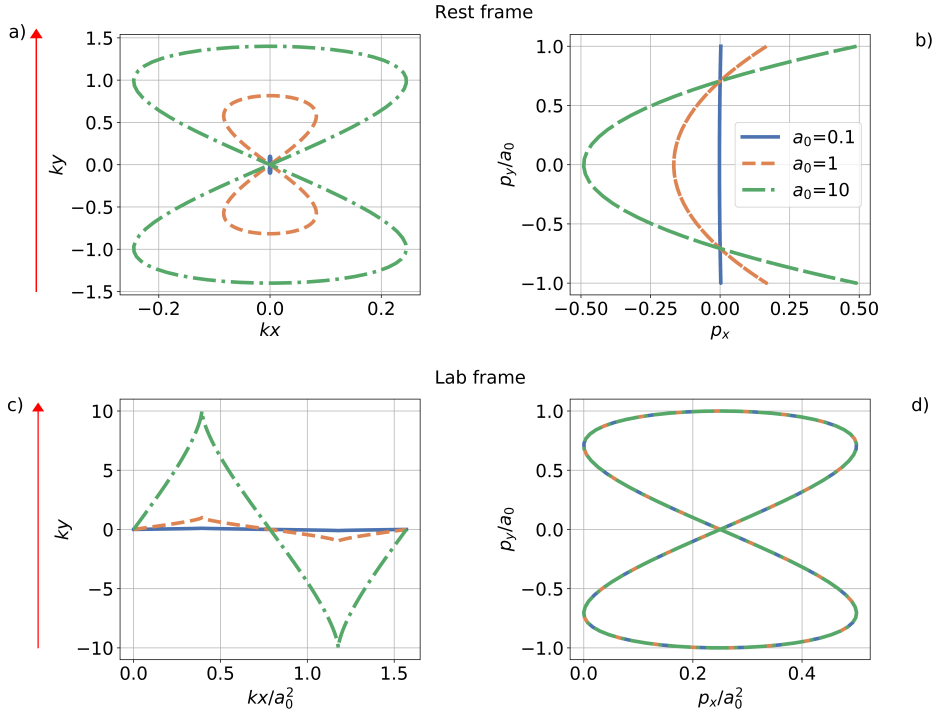


Figure 2.5: Single particle motion for a linearly polarised EM plane wave in the rest frame of the oscillating particle and the lab frame. The red arrows denote the polarisation direction. In panel a) we see the figure-of-eight motion, in the rest-frame of an electron, oscillating in a sinusoidal EM field. In panel c) the kx-ky position of the electron in the lab frame is shown. In panel b) and d) the momentum space for the electron is shown.

amplitudes. Consider the full Lorentz force and energy conservation equation for this system,

$$\begin{aligned} \frac{d\boldsymbol{p}}{dt} &= -e(\boldsymbol{E} + \frac{1}{c}\boldsymbol{v} \times \boldsymbol{B}), \\ \frac{d}{dt}(\gamma mc^2) &= -e(\boldsymbol{v} \cdot \boldsymbol{E}), \\ \boldsymbol{A}(\omega, k) &= \begin{pmatrix} 0 \\ \delta a_0 \cos(\phi), \\ (1-\delta^2)^{1/2} a_0 \sin(\phi), \end{pmatrix} \end{aligned} \tag{2.20}$$

where ϕ is the phase of the laser pulse, $\boldsymbol{A}$ is the vector potential of the plane wave, $\boldsymbol{B}$ is the magnetic field of the plane wave, γ is the Lorentz factor of the particle, $\boldsymbol{p}$ is the momentum of the electron and $\boldsymbol{v}$ is the momentum of the electron. Solving this equation for the position of the electron, $\boldsymbol{r}$, we arrive at the following result for the motion of the

electron in the average rest frame.

$$\begin{aligned} \boldsymbol{r} = \begin{pmatrix} x \\ y \\ z \end{pmatrix} &= \begin{pmatrix} \left(\delta^2 - \frac{1}{2}\right) q^2 \sin(2\phi), \\ 2\delta q \sin(\phi), \\ -2(1-\delta^2)^{1/2} q \cos(\phi), \end{pmatrix} \\ \gamma_0 &= \sqrt{1 + \frac{a_0^2}{2}}, \\ q &= \frac{a_0}{\gamma_0} \end{aligned} \tag{2.21}$$

where δ controls the degree of polarisation of the laser pulse, x, y, z are the scalar positions of electron. The results are summarised in Figure 2.5, where we see the well known figure-of-eight motion of the electron under the influence of an intense planar laser field can be seen in the lab frame $k_x - k_y$ figure.

In Figure 2.5, we can see that in the lab frame the particle drifts forwards with a drift velocity $\propto a_0^2$

2.4.3 Ponderomotive force

A laser pulse consists of electric and magnetic fields which are oscillatory in nature in the absences of collisions. These fields will return particles to their original position and the particles will not have gained significant net momentum over a laser cycle. In fact, it is a higher-order effect called the ponderomotive force which is responsible for the transfer of energy from the laser pulse to a plasma for the generation of a charge separation in the medium.

It pushes particles away from regions of high vector potential of the laser pulse. As the electrons are significantly lighter than ions, charge separation can be established in the medium and a plasma wave is subsequently formed. In order to derive the ponderomotive force [87], we begin with the electron fluid momentum equation and the Lorentz force in normalised units,

$$\begin{aligned} \left(\frac{\partial}{\partial t} + \boldsymbol{v} \cdot \nabla\right)(\gamma \boldsymbol{v}) &= -(\boldsymbol{E} + \boldsymbol{v} \times \boldsymbol{B}), \\ &= \frac{\partial \boldsymbol{A}}{\partial t} - \boldsymbol{v} \times (\nabla \times A). \end{aligned} \tag{2.22}$$

Using the vector identity

$$(\boldsymbol{v} \cdot \boldsymbol{\nabla})\gamma \boldsymbol{v} = \nabla\gamma - \boldsymbol{v} \times [\nabla \times (\gamma \boldsymbol{v})], \tag{2.23}$$

we obtain,

$$\frac{\partial}{\partial t}(\gamma \boldsymbol{v} - \boldsymbol{A}) = \boldsymbol{v} \times [\nabla \times (\gamma \boldsymbol{v} - \boldsymbol{A})] - \nabla\gamma. \tag{2.24}$$

Consider the curl of this equation, sometimes known as the relativistic vorticity equation,

$$\frac{\partial}{\partial t}[\nabla \times (\gamma \boldsymbol{v} - \boldsymbol{A})] = \nabla \times (\boldsymbol{v} \times (\nabla \times (\gamma \boldsymbol{v} - \boldsymbol{A}))), \tag{2.25}$$

For a plasma at rest, before the laser pulse is incident, we can see that,

$$\nabla \times (\gamma \boldsymbol{v} - \boldsymbol{A}) = 0. \tag{2.26}$$

As this quantity is 0 initially, we can see that Eq. 2.25 ensures that this quantity must be remain 0 for all time. Hence, we can rewrite Eq. 2.24 as,

$$\begin{aligned} \frac{\partial(\boldsymbol{u} - \boldsymbol{A})}{\partial t} &= -\nabla\gamma, \\ \boldsymbol{u} &= \gamma \boldsymbol{v}, \\ \gamma &= (1 + u^2)^{1/2}. \end{aligned} \tag{2.27}$$

Where v is the fluid velocity and γ is the Lorentz factor associated with the fluid element. The term on the RHS of the equation is the ponderomotive force. Gradients in the local Lorentz factor of the fluid element results in a force which acts to push particles away from high intensity regions. The oscillations in the Lorentz force of the fluid elements are related to the a_0 of the laser pulse, as such, the ponderomotive force will act to push electrons away along the gradients of a_0.

2.5 Laser-cluster interaction

A cluster is a collection of atoms ranging from 100s to $> 10^6$ of atoms/molecules large. In a clustered gas, these solid density, typically $100n_c$ electron density, collections of atoms are interspersed across an under dense medium. These clusters typically have dimensions which are significantly smaller than the wavelength of laser pulses they are interacting with. As such, they do not interact with laser pulses, in the same way as uniform plasmas. This topic represents a highly active body of research in its own right. Only the mechanism relevant to the electron acceleration experiments, performed in the later chapters of the thesis, are examined.

The various stages of laser-cluster expansion are shown in Figure 2.6. Inner ionisation is the liberation of bound charge from atoms in a cluster. This leads to the cluster gaining thermal energy. Additionally, the cluster also begins to lose electrons to the continuum as

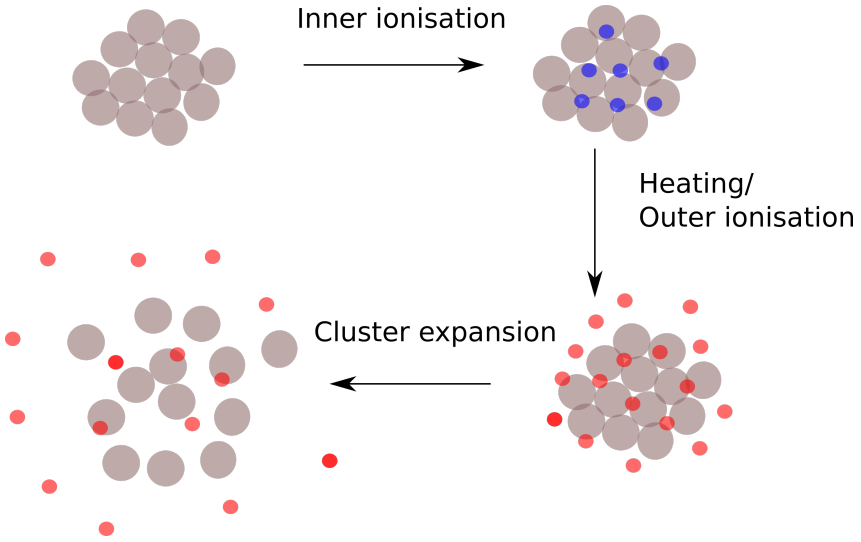


Figure 2.6: Illustration showing the various stages of laser-cluster interaction. The electrons must first be ionised from the bound atomic ionisation states, termed inner ionisation. Once a small fraction of these atoms are ionised, they can go on to ionise other bound states and increase the overall temperature of the cluster. This build up of space charge forces and thermal pressure leads to the expansion of the cluster core.

can be seen in Figure 2.7, in what is known as outer ionisation. This causes the cluster to become charged and results in an expansion of the ion core of the cluster called a Coulomb expansion.

2.5.1 Cluster generation mechanism

Clusters can be generated in a gas jet, where the gas undergoes rapid cooling due to adiabatic expansion and undergoes a phase transition. This results in the formation of microscopic aggregations of molecules in the flow which are of solid density. A simple semi-empirical scaling law to predict the global properties of a clustered target were introduced by Hagena [88],

$$\begin{aligned} \Gamma^* &= k_h \left(\frac{0.74d}{\tan(\alpha)^{0.85}} \right) P_0 T_0^{-2.29}, \\ \langle N \rangle &= 33 \left(\frac{\Gamma^*}{1000} \right)^{2.35}, \end{aligned} \tag{2.28}$$

where, Γ^* is termed the Hagena parameter, k_h is a parameter related to the condensation properties of the gas, α is the half angle of the nozzle, d is the critical diameter in micrometers, P_0 is the backing pressure in millibar, T_0 is the initial temperature of the gas in kelvin and $\langle N \rangle$ is the average number of atoms in a cluster. The Hagena parameter accounts for geometrical factors concerning the condensation process. However, there

are other cluster parameters which have to be assumed based on measurements from literature, as they cannot be parametrised in terms of the geometry of the nozzle, namely the cluster mass fraction and the cluster concentration [89]. For the discussion in later chapters, the mass fraction is assumed to be 25% as this is what is reported from literature for the Hagena parameter [90, 91]. The Hagena parameter also presents only the mean size of clusters in a gas target. Experiments examining the distribution of the cluster sizes have measured log-normal distributions, where the width of the distribution is approximately the Hagena parameter [92].

2.5.2 Ionisation mechanisms

When a short pulse, high intensity laser interacts with an cluster, the system will quickly transition into a non-local thermal equilibrium state [81]. Equations typically used to calculate the ionisation state, such as the Saha-Boltzmann equation, are not valid in this regime. In a cluster, there are additional definitions for ionisation [93]. While an electron can be free from its parent atom, it can still be bound to its cluster. This is referred to as inner ionised. When the electron is free from its parent cluster it is termed outer ionised and becomes part of the ambient plasma.

Currently there exists no analytic model to describe the ionisation rates (inner and outer) of electrons from a cluster in the relativistic regime. This is partly due to the interplay between multiple ionisation states and the evolution of the cluster ions, since as their temperature and/or average charge state increases, the radius of the cluster also increases. This leads to the potential of the cluster to be reduced, modifying the electron density of the plasma formed near the cluster. The ion density of a laser heated cluster is also rapidly decreasing and the system becomes highly dynamical, evolving on the time-scale of the outer ionisation of the clusters.

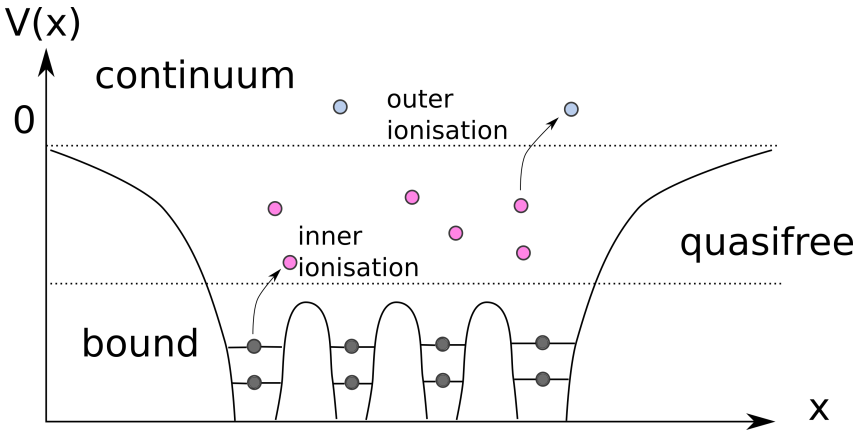


Figure 2.7: Illustration of various levels of cluster ionisation

Inner ionisation mechanisms

In addition to field ionisation, clusters can experience a range of different inner ionisation mechanisms. Ionisation ignition [94] occurs when the total electric field of a charged cluster can enhance field ionisation when the respective field components add up. This occurs once a few electrons have been inner ionised and the cluster can have an appreciable polarisation field. This has the effect of lowering the ionisation potential for the bound electrons in the cluster. Collisional ionisation, or electron impact ionisation (EII), can also occur once a small fraction of the atoms have been liberated by optical field ionisation. Inner ionised electrons trapped inside the cluster can collide inelastically with cluster ions/neutral atoms to release additional bound electrons. EII rates are modelled using empirical cross sections [95]. The relative contribution of each of these ionisation mechanisms is still a disputed topic with some authors claiming collisional ionisation plays a small part [96] whereas others have suggested that collisional ionisation is dominant for large clusters [97].

2.5.3 Heating mechanisms

Several mechanisms are reported in literature for the heating of clusters. Due to their finite size, the heat absorbed by clusters cannot be transported away efficiently, resulting in cluster temperatures reaching the keV regime.

Inverse bremsstrahlung is one of the primary heating mechanisms for a cluster. As the laser pulse causes an inner ionised electron to oscillate, it inelastically collides with an ion causing it to heat up. The collisional heating rate for a uniform dielectric sphere is given as [93],

$$\frac{\partial \mathcal{E}}{\partial t} = \frac{9\epsilon_0 \omega_L^2 \omega_p^2 \nu_{ei} |E|^2}{2[9\omega_L^2(\omega_L^2 + \nu_{ei}^2) + \omega_p^2(\omega_p^2 - 6\omega_L^2)]}. \tag{2.29}$$

Where the electron-ion collision rate is given by Silin's equation [98] as,

$$\nu_{ei} = \begin{cases} \frac{4}{9}\left(\frac{2\pi}{3}\right)^{1/2} Z^2 e^4 n_i m_e^{1/2} (k_b T_e)^{-3/2} \ln\Lambda & v_{osc} \leq v_{kT}, \\ 16 Z^2 e n_i m_e \omega^3 E_0^{-3} (\ln(\nu_{osc}/2v_{k_bT} + 1)) \ln\Lambda & v_{osc} \geq v_{kT}. \end{cases} \tag{2.30}$$

Here E_0 is the amplitude of the electric field, ω_p is the plasma frequency, ω_L is the frequency of the laser, T_e is the electron temperature, $\ln\Lambda$ is the Coulomb logarithm where for our particular case, $\ln\Lambda = ln(\lambda_D/r_{min})$ where r_{min} is the either the minimum distance of approach or the de Broglie wavelength, which ever of the two is the lower quantity.

From this equation, we can see that IB heating increases with density and decreases with temperature. The rate is particularly enhanced at the cluster resonance where $n_e = 3n_c$.

The concept of resonance has been experimentally observed where the absorption of laser energy has an optimum value when the the laser energy was fixed but the pulse duration was varied. The maximum absorption occurs when the point at which the density $n_e = 3n_c$ coincides with the point at which the intensity of the laser pulse is at its maxima.

Another mechanism by which clusters heat up is collective resonant absorption. This is when the electron cloud surrounding the cluster core oscillates due to the laser field. Depending on its relative phase compared to the oscillation of the electric field of the laser, it can gain energy from the laser pulse. This oscillation can collisionally transfer energy to the ions and this transfer of energy increase the temperature of the cluster ions. We follow the derivation from [99]. Consider the equation of motion of an electron cloud driven by a planar field,

$$\begin{aligned} \ddot{x_e} + 2\Gamma\dot{x_e} + \omega_{cl}x_e &= \frac{-eE_0\sin(\omega t)}{m_e}, \\ \omega_{cl} &= \sqrt{\frac{e}{4\pi\epsilon_0 m_e}\frac{Q}{R^3}}, \end{aligned} \tag{2.31}$$

where Q is the total charge of the cluster, R is the cluster radius and ω_{cl} is the eigenfrequency of the oscillation of the cluster, x_e is the position of the centroid of the electron cloud and Γ is the damping rate.

At early times in the evolution of the cluster, when ω_{cl} is less than that laser frequency, IB heating is the dominant heating mechanism of a cluster. However, as the cluster is expanding, ω_{cl} increases and when this is greater than the laser frequency, collective resonance absorption dominates over IB. In strong fields, the picture is complicated by the appearance of non-linear resonant absorption [100] as this will also impact the heating rate of a cluster.

The last heating mechanism present in clusters is called Brunel (or vacuum) heating [43]. This is particularly important when the electron density is significantly greater than the critical density and does not experience any enhancements at the resonant density. Electrons are driven out of the plasma by the laser field and then sent back into the plasma and gain energy from the laser pulse. When the transit time for electrons across the cluster matches the laser period, they can be in the accelerating phase of the electric field of the laser and strong absorption of laser energy can occur.

2.5.4 Expansion mechanisms

Whilst a cluster is gaining thermal energy from its interaction with the laser pulse, it is also losing electrons and subsequently becoming charged. The thermal pressure of the

electron cloud pushes against the electrostatic force of the ions and drags them radially, this is referred to as the hydrodynamic expansion regime of clusters. If the electrons within a cluster can be outer ionised fast enough, the cluster will expand due to the coulombic force of nearby ions and this regime is called Coulomb expansion.

In general both forms of expansion will be present and the nature of expansion will depend on the laser field, the Z of the atomic species making up a cluster and the radius of a cluster. For high Z cluster, if the cluster potential is stronger than the laser, it will hold onto its electron cloud and hydrodynamic forces will play a greater role. Conversely, for the case of low Z clusters, if the cluster potential is weaker than that of the laser pulse, the expansion will be coulombic.

Consider a cluster as a uniform sphere where the density is decreasing with time. The following equation can be derived for the time-dependant cluster radius assuming the expansion is driven by both forces and by considering energy conservation in the system,

$$\begin{aligned} \frac{\partial \mathcal{E}_k}{\partial t} &= (P_e + P_c) 4\pi R^2 \frac{\partial R}{\partial t}, \\ \mathcal{E}_k &= \frac{1}{2}\left(\frac{4\pi R^3}{3}\right) n_i m_i \left(\frac{\partial R}{\partial t}\right)^2, \\ \frac{\partial^2 R}{\partial t^2} &= \frac{3(P_e + P_c)}{n_i m_i R}, \end{aligned} \tag{2.32}$$

where P_e is the thermal pressure and P_c is the pressure due to the coulomb force.

Hydrodynamic expansion

For the hydrodynamic case, we can relate the thermal pressure, P_e to the temperature of the medium.

$$P_e = n_e k_b T_e. \tag{2.33}$$

Hence, the time dependent temperature of the electrons will drive the expansion of the cluster. Hydrodynamic expansion occurs at the characteristic ion acoustic velocity,

$$v_s = \sqrt{\frac{Z^* k_b T_e}{m_i}}. \tag{2.34}$$

We can calculate the time $t_{d,HE}$ it takes the cluster radius to double under a purely hydrodynamic expansion case,

$$t_{d,HE} = R_0 \sqrt{\frac{m_i}{Z^* k_b T_e}}. \tag{2.35}$$

Coulombic expansion

Consider two ions with charge Z^*e and mass m_i, the time needed to increase their distance to $R(t)$ is [99],

$$\begin{aligned} t_e &= \int_{R_0}^{R} \sqrt{\frac{m_i}{2\mathcal{E}_k(R)}} dr, \\ \mathcal{E}_k(R) &= \frac{Z^{*2}e^2}{4\pi\epsilon_0}\left(\frac{1}{R_0} - \frac{1}{R}\right). \end{aligned} \tag{2.36}$$

This integration yields the following result,

$$\begin{aligned} f(R_0/R) &= \frac{\sqrt{1 - R_0/R}}{R_0/R} + \frac{1}{2}\ln\left(\frac{1+\sqrt{1+R_0/R}}{1-\sqrt{1-R_0/R}}\right), \\ t_E(R) &= \sqrt{\frac{2\pi\epsilon_0 m_i R_0^3}{Z^*e}} f(R_0/R). \end{aligned} \tag{2.37}$$

We consider the doubling distance by setting $R_0/R = 0.5$ which given $f(0.5) = 2.3$. To extend to the case of many charges, we replace one of the charges by Z^*e and the other charge, by that of of the uniform sphere $4\pi R_0^3 n_i Z^* e/3$. This give cluster doubling time from columbic expansions as,

$$t_{d,CE} \approx 0.8\sqrt{\frac{4\pi\epsilon_0 m_i}{n_i Z^{*2}} e^2}. \tag{2.38}$$

An interesting observation from this calculation is that the time that it takes for a cluster to double its radius is independent of initial cluster radius R_0.

One of the first models to be proposed to explain laser-cluster interactions is called the nanoplasma model [101]. In this model, the cluster is modelled as a homogeneous sphere where a plasma on the nanometre scaled is formed. Its simplicity, and ability to predict some experimental features, has encouraged its use for a range of laser-cluster parameters. However, it assumes that the interaction is radially symmetric and the energy spectrum of the electrons is maxwellian.

This has been extended by Milchberg et al. [102] by allowing the radial profile to vary. However, this is still a hydrodynamic model and not valid for the relativistic interaction regime that laser-wakefield experiments are performed in. We examine clusters, and all associated ionisation and heating mechanisms, using Particle-in-Cell (PIC) codes for the parameter ranges explored in experiments. These codes are valid for relativistic intensities and can capture the wide range of different ionisation/heating mechanisms present in these systems [96, 100, 103].

2.5.5 Self-focussing in a clustered medium

Experiments in the field of laser-cluster interactions have observered additional mechanisms for guiding the pulse over interaction lengths significantly longer than the Rayleigh range. One way that this can occur is known as the transient beam lensing effect [104]. Consider the polarisation dipole moment of a spherical plasma γ,

$$\begin{aligned} \mathbf{p} &= \gamma \mathbf{E} \\ \gamma_r &= -\frac{n_e}{3n_c - n_e + \delta} R(t)^3, \end{aligned} \tag{2.39}$$

where γ_r is the real part of the complex polarisability of a cluster and R is the radius of the cluster and δ is a factor to account for damping in this resonant system.

For early times when $t < t_{peak}$, the polarisability of a cluster, $\gamma_r > 0$, is positive. As it expands, on approaching the resonant density of $n_e = 3n_c$, the real component of the polarisability γ_r reaches a maximum. Below the resonant density, γ_r decreases and becomes negative.

On the axis of the laser pulse, the cluster will expand faster than on the edges. As such,

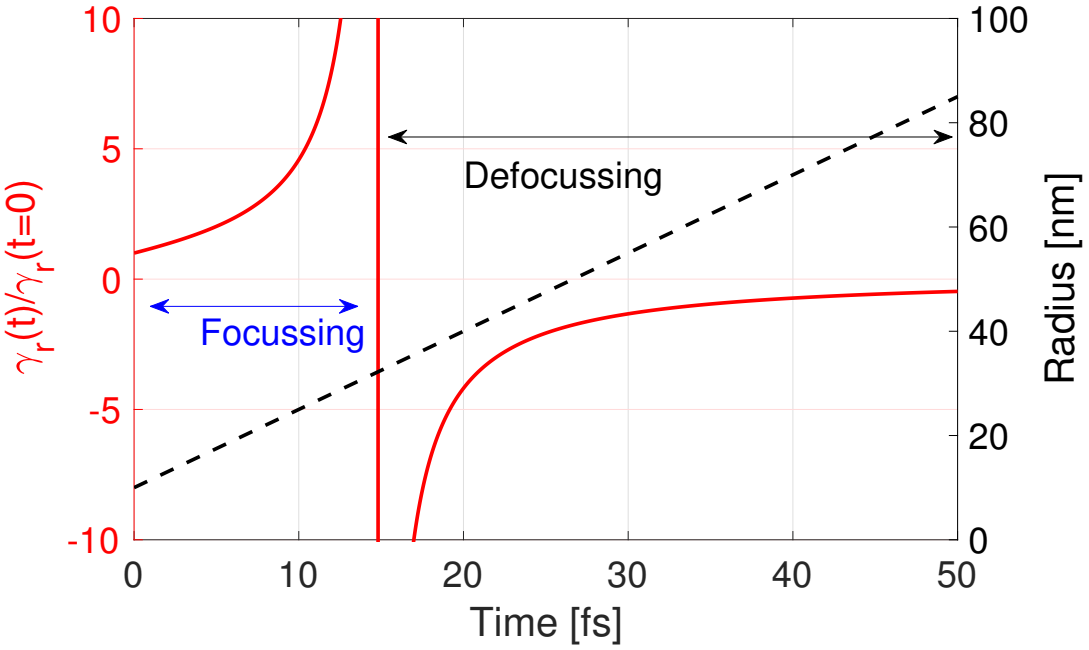


Figure 2.8: On the left axis, $\gamma_r(t)/\gamma_r(t)$ is the real component of the refractive index normalised to its initial value at $t = 0$. On the right axis, the radius of the cluster for a constant expansion velocity is shown. We can see that the refractive index changes sign at $\approx 15\,\text{fs}$ and in the early part of its evolution, the plasma behaves as a focussing lens.

for the clustered medium will appear like a positive lens to the pulse. This is showing in Figure 2.8, where we have assumed a constant cluster expansion velocity of $\beta = 0.005$, initial cluster density of $100n_c$ and initial radius of 10 nm.

The critical power for the onset of self-focusing in a clustered medium [105, 106] is given as

$$P_{sf,cl} = 112\left(\frac{R_0}{R(t)}\right)^7\left(\frac{n_e a_0}{\omega}\right), \tag{2.40}$$

where R_0 is the initial radius and $R(t)$ is the evolving cluster radius. In Symes et al. [105], it is noted that cluster self-focusing is only present, when the time for the cluster to reach its resonance density, is less than the time for the peak of the pulse to pass through the cluster.

Clustered media can also be exploited for their enhanced laser absorption properties, where upto 95% of the energy of the laser pulse can be absorbed by the clustered medium [107]. This has been used to generate a plasma waveguide with modest laser pulse energies of 25 mJ for a 10 mm plasma waveguide [108]. This an order of magnitude less energy than a plasma waveguide generated in a non-clustered medium [109]. This can be estimated using the radius doubling timescale $t_{d,CE}$ or $t_{d,HE}$ but is typically on the order of 1-10 ps.

2.6 Laser-plasma interaction

2.6.1 Self-focussing in plasma

A laser pulse will self-focus if the refractive index of the medium has a maxima on-axis. We can describe the refractive index of the medium as

$$\begin{aligned}\eta(r) &= \frac{ck}{\omega} \\ &= \left[1 - \frac{\omega_p^2}{\omega^2[1 + a(r)^2/2]^{1/2}}\right]^{1/2}, \\ &\approx 1 - \frac{\omega_p^2}{\omega^2}\left(1 + \frac{n}{n_0} - \frac{a_0^2}{4}\right).\end{aligned} \tag{2.41}$$

The second term $\frac{n}{n_0}$ represents the effect of density modulations in the plasma. The third term represents the effective mass of the electrons increasing as they undergo relativistic oscillations which changes the refractive index.

By considering the non-linear properties of the medium we can ask what the threshold to see self-focusing effects are. Interestingly, the threshold depends on power and not the

intensity of the pulse and is aptly named the critical power,

$$P_c \approxeq 17.5\left(\frac{\omega}{\omega_p}\right)^2 [\text{GW}]. \tag{2.42}$$

When the laser power exceeds the critical power at a particular density, self-focussing will occur in the medium.

2.6.2 Pulse compression in a plasma

Along with transverse gradients experienced by the laser pulse, in a wakefield, longitudinal gradients in density can result in the compression of the laser pulse. This occurs because the front of the pulse experiences lower group velocity, compared to the rear which causes the duration of the pulse to decrease. We can see in Figure 2.9 that this leads to pulse compression. This gradient in refractive index also leads to photon acceleration/deceleration [110]. Photon deceleration occurs in the leading edge of the laser pulse as it loses energy to the wakefield, resulting in redshifted photons. The opposite phenomena will occur in the the rear of the bubble where the wavelength of the laser pulse will decrease, this is called photon acceleration.

Schreiber et al. [111], gives the variation in pulse duration as a function of density as,

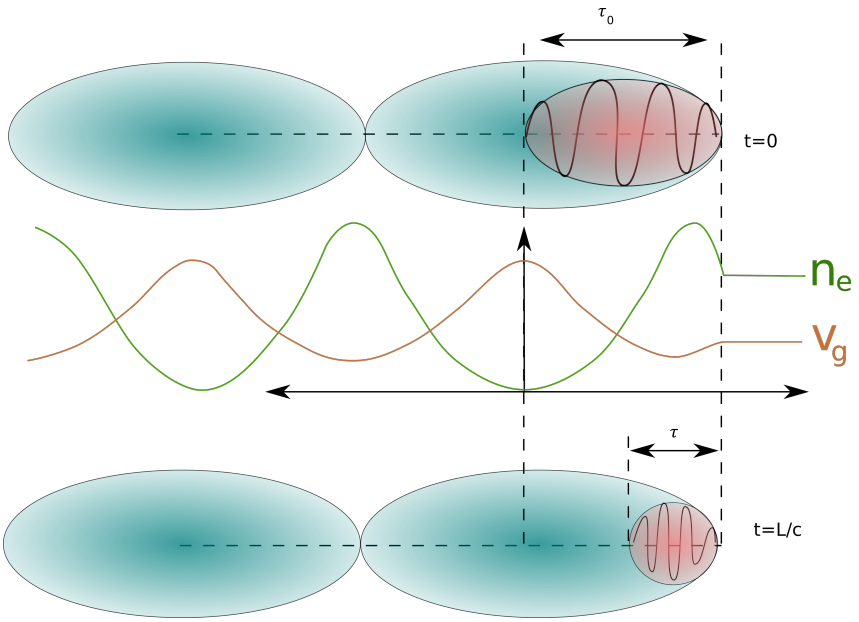


Figure 2.9: n_e is the electron density of the medium and v_ϕ is the local phase velocity. τ_0 is the initial pulse duration and τ is the pulse duration reached by Equation 2.43 at a time $t = \frac{L}{c}$, where L is the length of plasma that the pulse has travelled in.

$$\tau = \tau_0 - \frac{n_{e0} l}{2 c n_c}, \tag{2.43}$$

where τ_0 is the initial pulse duration and n_{e0} is the initial electron density. Pulse compression has been observed to amplify the peak power of the laser pulse even though the pulse is losing energy in the medium [112]. Once the power in the leading edge of the pulse drops below the critical power for self-focussing, the pulse diffracts away. Streeter et al. [112], states that the maximum power amplification occurs at a length, L_{evo},

$$L_{evo} = \tau_0 c \left(\frac{2n_c}{3n_e}\right) \sqrt{\frac{1}{2} \ln\left(\frac{P_0}{P_c}\right)}, \tag{2.44}$$

where τ_0 is the pulse duration, P_0 is the initial power, P_c is the critical power. This evolution length corresponds to when the pulse energy is reduced by 50%.

2.6.3 Large amplitude plasma waves

A plasma wave is the accelerating structure for laser wakefield accelerators (LWFA). The separation of the ions and the electrons in a plasma results in the generation of an electric field. This forces electrons to return to their original position in order to neutralise the plasma, but they end up overshooting and performing an oscillation which manifests as a longitudinal wave.

Linear plasma wave

The equations governing the evolution of a plasma wave driven by a laser pulse in the linear regime are given as,

$$\begin{aligned} \left(\frac{\partial^2}{\partial t^2} + \omega_p^2\right) \frac{n_e}{n_0} &= \frac{c^2}{2} \nabla^2 a^2, \\ \left(\frac{\partial^2}{\partial t^2} + \omega_p^2\right) \phi &= \omega_p^2 \frac{a^2}{2}, \end{aligned} \tag{2.45}$$

where a is the vector potential of the laser pulse driving the wave. sThis is a driven oscillator equation which can be solved by using Green's function methods, as is derived in [81]. We can see that these equations describe a wave with oscillation frequency at the plasma frequency,

$$\begin{aligned} \phi &= \frac{\omega_p}{2} \int_0^t dt' \sin(\omega_p (t - t')) a^2, \\ \frac{n}{n_0} &= \frac{c^2}{2\omega_p} \int_0^t dt' \sin(\omega_p (t - t')) \nabla^2 a^2. \end{aligned} \tag{2.46}$$

1D non-linear plasma wave

In the solution of the linear plasma wave equation, we can see how a laser pulse leads to the formation of a wakefield with sinusoidal fields. LWFA is however often performed in the non-linear regime. As such, the effects of non-linearity in 1D will be explored. Using the continuity equation and Maxwell's equation and under the approximation that the laser pulse does not vary over the timescale of the evolution of the plasma wave, the quasi-static approximation, we can derive the 1D non-linear plasma wave equation. The equations are given as

$$\begin{aligned} \frac{\partial^2 \phi}{\partial \zeta} &= k_p^2 \gamma_g^2 \left[\frac{\beta_g}{\Phi} - 1 \right], \\ n &= \gamma_g^2 \beta_g (\Phi^{-1} - \beta_g), \\ u &= (\beta_g - \Phi)(1 - \beta_g \Phi)^{-1}, \\ \Phi &= \left(1 - \frac{1 + a^2}{\gamma_g^2 (1 + \phi)^2} \right)^{1/2}, \end{aligned} \tag{2.47}$$

where β_g is the group velocity beta, k_p is the plasma wavelength, ζ is the wake frame coordinate, n is the density perturbation defined as $n = \frac{n_e}{n_0}$, Φ is a pseudo-potential term containing the driver term for these equations. We can solve this equation numerically to obtain Figure 2.10, where we can see that for linear waves $a_0 < 1$, the density and electric field are sinusoidal in form. However, as we pass the relativistic threshold, non-linearities cause the density to spike, the plasma wavelength to increase and the electric field to take a linear form inside the wakefield. In 1D, full cavitation, where all the electrons are expelled from the trough of the wave, does not occur. In 3D, this is possible as will be seen in PIC simulations.

2.6.4 Wave breaking

While plasmas can support electric fields of an enormous magnitude, there is an inherent limit to the amplitude of a plasma wave. If the amplitude of the wave exceeds a certain threshold, the trajectories of particles forming the wave crosses over, the wave loses coherence and breaks down; this is called wave-breaking. The cold relativistic wave breaking field of a plasma wave E_{WB}, was first analysed by Dawson et al. [113] as,

$$\begin{aligned} E_{WB} &= \sqrt{2(\gamma_p - 1)} E_0 \\ E_0 &= \frac{m_e c \omega_p}{e}. \end{aligned} \tag{2.48}$$

This model was extended [114], to include the effects of temperature,

$$E_{WB,thermal} = E_0 \beta^{-1/4} (\ln 2\gamma_{ph}^{1/2} \beta^{1/4})^{1/2}, \tag{2.49}$$

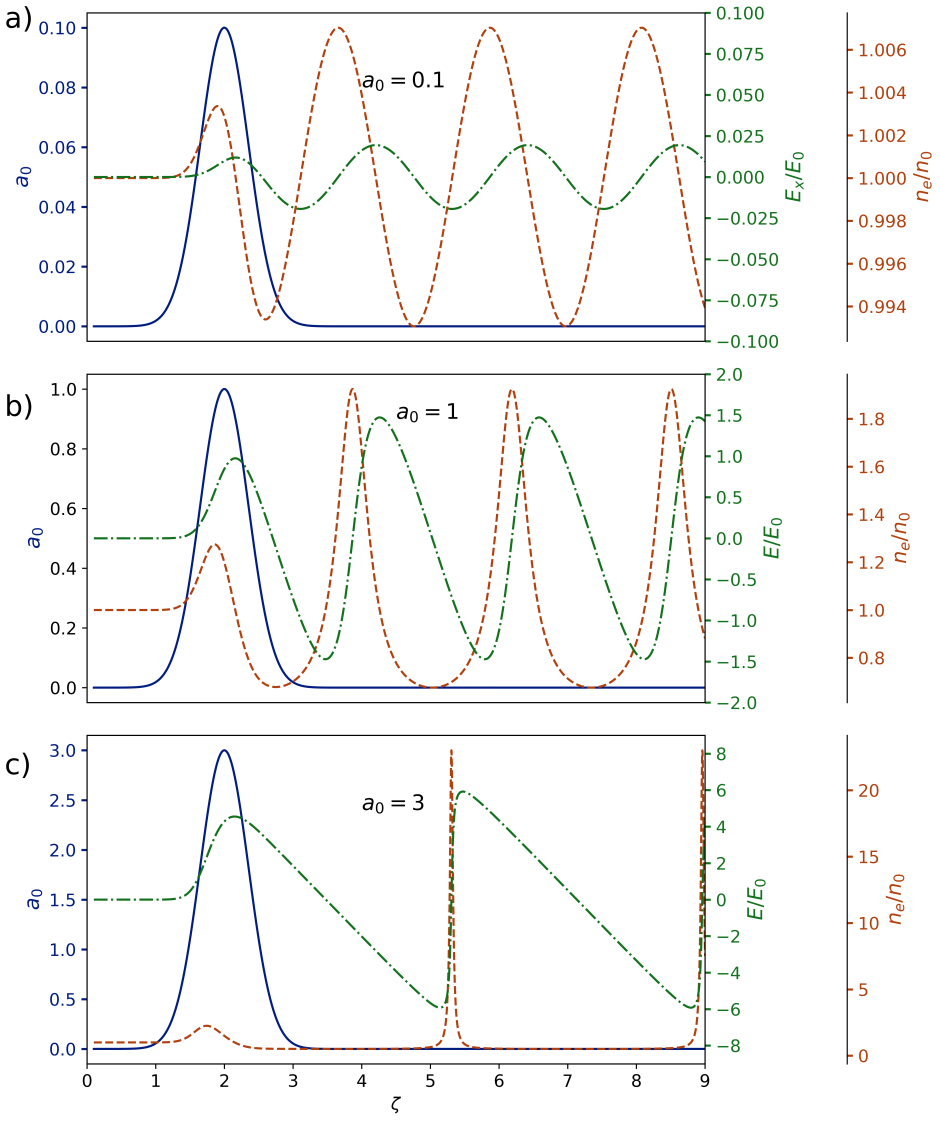


Figure 2.10: Numerical solution to the 1D non-linear wave equation. The blue line denotes the laser pulse and the amplitude of this wave is shown on the left hand axis. The density modulation generated by this laser pulse is shown in red and the corresponding electric field of this wake is shown in green. In panel a), b) and c) the amplitude of the driving laser pulse is 0.1, 1 and 10 respectively. As the a_0 of the driving laser becomes greater than unity, the plasma wavelength increases and the longitudinal electric field inside the plasma cavity becomes linear.

where $\beta = 3T/mc^2$. The temperature of the plasma will act to lower the wave-breaking amplitude. The temperature of laser-generated plasmas for wakefield acceleration is mostly determined by tunnel-ionisation. Hence, the medium is born with lower thermal energy compared to its wake phase velocity.

2.7 Laser wakefield acceleration

A laser wakefield accelerator uses a plasma wave as its accelerating structure. The accelerator can have linear or sinusoidal fields depending on the amplitude of the plasma wave. We also need to consider how to place electrons at the appropriate phase in order to accelerate them. This is called the injection mechanism and will be explored in this section. We discuss the limitations to the energy gain of these accelerators and ways to mitigate them.

We then summarising the scaling laws for the key parameters pertaining to LWFA for various a_0 regimes. This can be useful for predicting the energy gain by these accelerators under a set of experimental conditions. This section concludes with the radiation generated by these accelerators and models predicting their properties are highlighted.

2.7.1 Focussing and accelerating fields

Laser wakefield accelerators have a useful property whereby the injected particle is not only accelerated by the wave, but it is also focused. In the linear regime, the fields take a sinusoidal form, whereas in the non-linear regime the accelerating field is linear with the co-moving coordinate ζ. The focussing and accelerating fields for the linear case where $a_0 = 0.1$ are shown in Figure 2.11 obtained from solving Eq. 2.45.

We can see that the electron density modulation and the focussing fields are out of phase with the accelerating fields. The ideal region for acceleration is hence where there is a focussing and accelerating field for electrons, which occurs for $\frac{1}{2}$ of the total wave period.

The peak accelerating and focussing fields for a gaussian laser pulse in the various wakefield regimes are given as,

$$\frac{E_{accel}}{E_0} = \begin{cases} \sqrt{\frac{\pi}{2e}} a_0^2 & a_0 \ll 1 \\ \frac{a_0^2/2}{\sqrt{1+a_0^2/2}} & a_0 \approx 1 \\ \sqrt{a_0} & a_0 \geq 2 \end{cases} \qquad F_{focus} \propto \begin{cases} \frac{r \cdot a_0^2}{w_0^2} & a_0 \ll 1 \\ r & a_0 \geq 2 \end{cases} \tag{2.50}$$

where $E_0 = mc\omega_p/e$, the cold wave-breaking electric field amplitude. LWFA experiments are typically performed in the $a_0 \approxeq 1 - 3$ regime. For the non-linear regime, there is also an azimuthal B-field along with the axial electric field which provides additional focussing force for electron beams. For the focussing field in the linear regime, we assumed that the driver is a gaussian laser pulse. The optimal acceleration regime is where the focussing fields are linear with the co-moving coordinate [115].

2.7.2 Particle trapping

For particles to gain energy from a wave, they have to be placed at the appropriate phase of the wave. As the wave is also moving, particles additionally need a minimum velocity to be trapped by the wave. We follow the analysis for particle trapping using hamiltonian dynamics in the 1D non-linear case as first evaluated by Essarey et al. [116]. The following hamiltonian describe the motion of a test electron with velocity, γ, in a plasma wave with

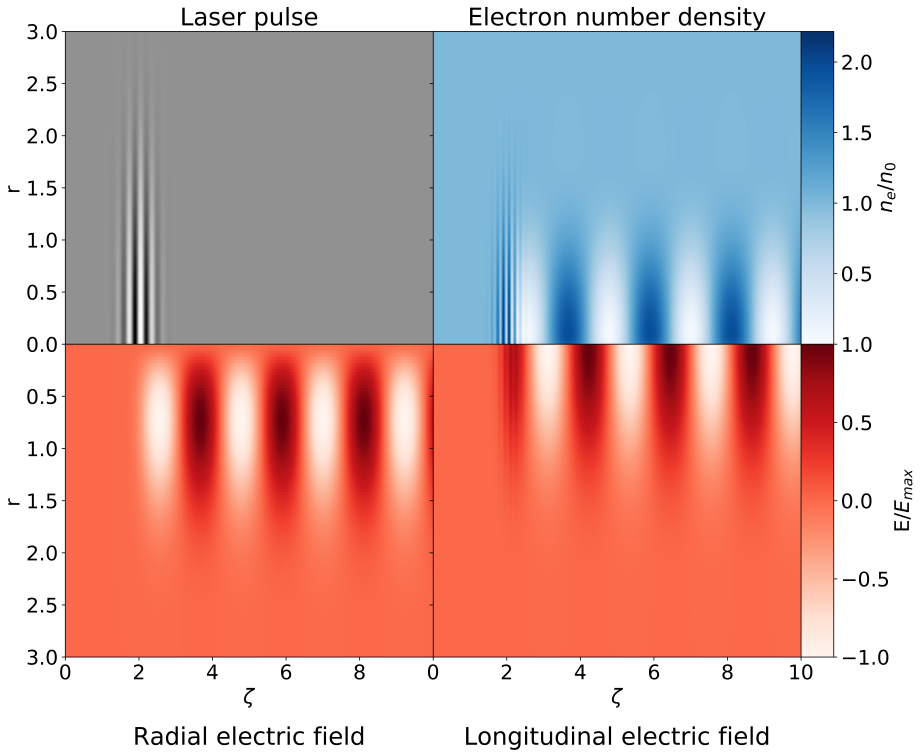


Figure 2.11: The linear wakefield solution for an $a_0 = 0.1$ laser pulse with its corresponding focussing and accelerating fields obtained by solving Eq.2.46.

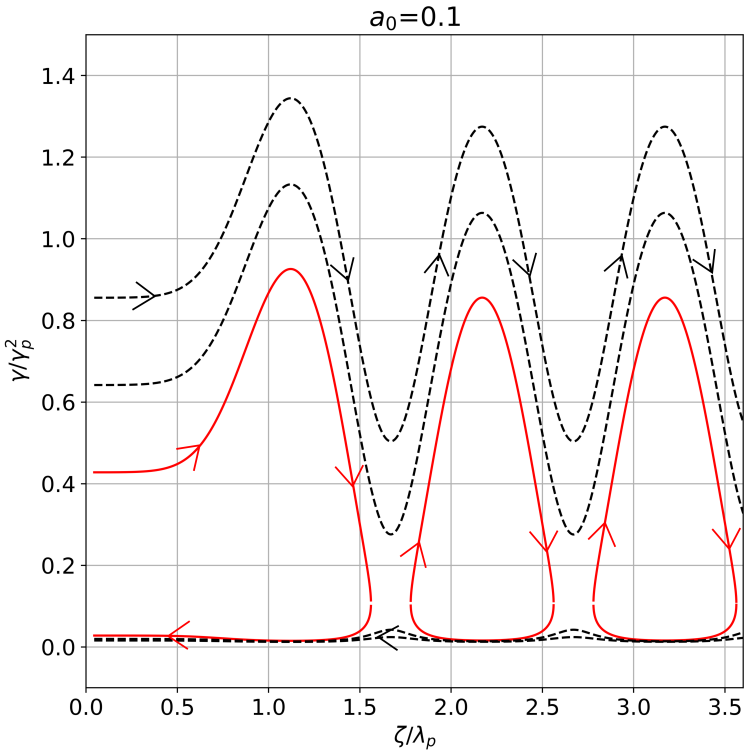


Figure 2.12: Seperatrix plot using the 1D non-linear wakefield equation for a_0=0.1. The red line is the separatrix which defines the boundary between the trajectories of the particles which get trapped in the potential. The black dashed lines are the untrapped particle trajectories.

phase velocity γ_p, under a potential ϕ,

$$\mathcal{H}(\gamma, \zeta) = \gamma(1 - \beta\beta_p) - \phi(\zeta) \tag{2.51}$$

As the hamiltonian is only a function of ζ and γ, this system is conservative. This means that the total value of the hamiltonian does not change over the evolution of the system. As such, if a particle has some initial gamma factor, we can describe its evolution by solving the following equation

$$\begin{aligned} \gamma_0 - \beta_p\sqrt{\gamma_0^2 - 1} &= \gamma - \beta_p\sqrt{\gamma^2 - 1} - \phi(\zeta) \\ \gamma &= \alpha\gamma_p^2 \pm \gamma_p\sqrt{\alpha^2\gamma_p^2 - (\alpha^2 + \beta_p^2)} \\ \alpha &= \gamma_0 - \beta_p\sqrt{\gamma_0^2 - 1} + \phi(\zeta) \end{aligned} \tag{2.52}$$

The solution to this hamiltonian for a linear plasma wave is shown in Figure 2.12. The separatrix is the line which defines the boundary between trapped and free orbits, which

in Figure 2.12 is given by the red line. Particles can be trapped by the plasma wave if they are in the phase space region corresponding to these trapped orbits. The height of the separatrix defines the maximum energy that particles can gain form the potential of the wakefield. The width of the separatrix is related to the useful distance over which particles can gain energy.

2.7.3 Injection mechanisms

The trapped orbits are where we would like to inject particles into the plasma accelerator. The way in which particles are injected into the plasma wave will dramatically influence the properties of the electron beam. We will address the three most commonly examined injection techniques described in the literature; self-injection, ionisation injection and density transition injection.

Self-injection

The easiest way to inject particles into a plasma wave is by relying on the plasma wave breaking. Electrons which form part of the wave are injected into the plasma wave. This mechanism is known as self-injection (SI). As wave-breaking is an inherently non-linear process, estimating the threshold for this process has been the subject of much theoretical work. Wave-breaking can occur transversely as-well as longitudinally. These types of SI have different origins and result in different properties in terms of the produced electron beams [117].

Longitudinal SI is when the wave breaks from the back of the bubble with significantly less transverse momentum. The expansion of the plasma bubble can also cause this form of injection, where a build up of electron density at the back of the bubble can lower the injection threshold for self-injection [118]. Longitudinal SI is purported by Corde et al., to inject less charge than transverse SI, but is much more stable and can have much narrower energy spread in the generated electron beams [117].

A static bubble model for SI using elliptical trajectories was examined in [119] where the trapping threshold is given by,

$$R_b \geq \frac{2}{k_p}\sqrt{\ln\left(2\gamma_p^2\right)}. \tag{2.53}$$

A semi-empirical model [120], building on this threshold by including the effects of pulse compression and self-focussing gives the following estimate for the threshold for injection provided knowledge of the nominal laser parameters such as the laser energy, pulse duration, target electron number density and focal spot quality α. Here α is defined as the

fraction of energy contained within the full-width half-maximum of the laser focal spot,

$$\frac{\alpha P}{P_c} > \frac{1}{16}\left[\ln\left(\frac{2n_c}{3n_e}\right) - 1\right]^3. \tag{2.54}$$

Ionisation injection

While SI is easy to achieve if one is at the intensities needed to drive a plasma wave, it's non-linear nature, makes it difficult to control and as such the electrons from SI can vary dramatically in their nature. Poorly constructed targetry or asymmetries in the quality of the focus can result in injection occurring at random locations along the accelerators length [121]. The need for a more stable injection method led to the development of ionisation injection [122, 123].

Ionisation injection works by using a medium doped with atoms where the binding potential for the inner shell electrons is high enough, such that they are born later than the ones forming the plasma wave. By delaying the generation of electrons, these electrons feel less of a ponderomotive push from the laser pulse and can be trapped by the wake. The trapping and injection process was examined by Chen et al. [124], using the familiar hamiltonian analysis of particles in a potential. The crucial difference in this case is that the hamiltonian of the electron ionised by the laser pulse is given by,

$$\mathcal{H}_i = \gamma_\perp(\Psi_i) - \phi(\Psi_i) = 1 - \phi(\Psi_i), \tag{2.55}$$

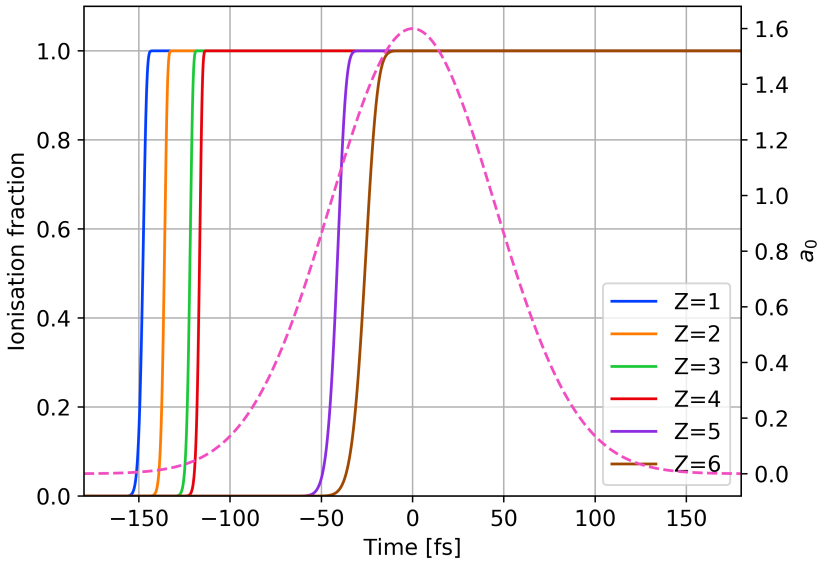


Figure 2.13: Ionisation fractions for electrons from carbon with $a_0 = 1.6$ and $\tau = 45\,\text{fs}$, where τ is defined as the full width half maximum of the intensity of the laser. The magenta dashed line shows the a_0 profile of the laser pulse.

where Ψ_i is the injection phase of the electron and $\gamma_\perp$ is the energy associated with the transverse direction to propagation. The seperatix orbit is given by,

$$\mathcal{H}_s = \frac{\gamma_\perp(\Psi_{min})}{\gamma_p} - \phi_{min}. \tag{2.56}$$

This gives the following condition on initial phase of the ionisation for trapping,

$$\begin{aligned} 1 + \phi_{min} - \phi(\Psi_{min}) &\leq \frac{(1+a_\perp^2)^{1/2}}{\gamma_p}, \\ \gamma_\perp &= 1 + a_\perp^2. \end{aligned} \tag{2.57}$$

In Chen et al. [124], the author assumes a Gaussian pulse where $k_p L_{rms} = 1$, where k_p is the plasma wave vector and L_{rms} is the rms intensity length for a intensity profile of $a = a_0 \exp\left[\frac{\Psi^2}{4(k_p L_{rms})^2}\right]$. Assuming a $\gamma_p = 33$, the minimum a_0 for trapping was shown to be ≈ 1.6 by Chen et al. [124]. This gives us an estimate for the amplitude of the driver pulse in order to inject particles into the wake by ionisation injection. In Figure 2.13, we plot the ionisation probabilities as a function of a_0 for the various energy levels of carbon using the ADK ionisation rate [84, 86]. We can see that the outer shell electrons are ionised early on in the interaction and these form the background but the inner shell electrons are ionised near the peak. As they are dephased from the motion of the electrons forming the plasma wave they can be trapped by the wake.

Density transition injection

Another way to control the injection of particles in the wakefield is by using sharp gradients in density. By varying the phase velocity of the plasma wave, it is possible to inject particles into the acceleration phase of a wake. Following the discussion in [125, p.32], we consider the effective wave number and angular frequency,

$$\begin{aligned} \Psi &= k_p(z) \cdot (z - ct) \quad \text{to 1st order}, \\ \omega_{p,eff} &= -\frac{\partial \Psi}{\partial t}, \\ k_{p,eff} &= -\frac{\partial \Psi}{\partial z}, \\ v_p &= \frac{\omega_{p,eff}}{k_{p,eff}}, \end{aligned} \tag{2.58}$$

where Ψ is the position of the peak of the plasma wave, $\omega_{p,eff}$ is the local plasma frequency, $k_{p,eff}$ is the local plasma wavevector and v_p is the local phase velocity. Substituting $\omega_{p,eff} = \sqrt{(ck_{p,eff})^2 + \omega^2}$ in the equation for the local phase velocity and taylor expanding

the result we arrive at,

$$\begin{aligned} \beta_p - 1 &\approx -\frac{\zeta}{k_p}\frac{dk_p}{dz}, \\ \beta_p &\propto \frac{\zeta}{n}\frac{dn}{dz}, \end{aligned} \tag{2.59}$$

where $\zeta = z - ct$. We can see here that negative gradients in density lead to a reduction in the phase velocity of the wake and subsequent trapping for electrons at the accelerating phase of the plasma wave. Experimentally, this is achieved by creating a orthogonal parabolic density channels [126] or using a wire in the gas flow to tailor the longitudinal density profile [127, 128].

2.7.4 Wake phase velocity

The phase velocity of a plasma wave in the non-linear regime was first analysed by Decker et al. [129],

$$\gamma_p = \left(1 - \left(1 - \frac{3n_e}{2n_c}\right)^2\right)^{-\frac{1}{2}} \approxeq \sqrt{\frac{n_c}{3n_e}}. \tag{2.60}$$

The group velocity of the laser pulse in the linear regime is given as $\gamma_p = \sqrt{\frac{n_c}{n_e}}$, in the non-linear regime, the front of the laser pulse loses energy due to driving a wakefield. The pulse etches back at a constant rate of $\beta_{etch} = \frac{n_e}{n_c}$ which results in a reduction to the group velocity of the laser pulse for non-linear plasma waves.

2.7.5 Energy gain in a wakefield accelerator

The electric field of a wake depends on the density of the medium and the amplitude of the driver. Consider the energy gain by a single particle in the presence of a linear electric field,

$$\varepsilon = \int_0^L eE_{max}\left(1 - \frac{z}{L_{dp}}\right)\mathrm{d}x, \tag{2.61}$$

where L_{dp} is the dephasing length. This term arises because the wave has a phase velocity which is less than the speed of light. As the particle gains energy from the wake, it catches up with the wake and outruns it. If we assume we are in the $a_0 > 1$ regime, the electric field is approximately linear and we can use the relativistic wave breaking amplitude, $E_{max} = \dfrac{\sqrt{a_0} m_e c \omega_p}{e}$ to obtain,

$$\varepsilon = \sqrt{a_0}\omega_p m_e c \int_0^L \left(1 - \frac{z}{L_{dp}}\right)\mathrm{d}x. \tag{2.62}$$

The highest energy gain is achieved when we have accelerated the particle for a full dephasing length as is shown in Figure 2.14. Hence, we obtain

$$\begin{aligned} \varepsilon_{max} &= \sqrt{a_0}\omega_p m_e c\left[z - \frac{z^2}{2L_{dp}}\right]_0^{L_{dp}}, \\ \frac{\varepsilon_{max}}{m_e c^2} &= \frac{\sqrt{a_0}k_p L_{dp}}{2}. \end{aligned} \tag{2.63}$$

The dephasing time for a wakefield accelerator can be expressed as the time it takes for the electron beam to travel $\frac{1}{2}\lambda_p$.

$$t_d = \frac{\frac{1}{4}\lambda_p}{c(1-\beta_p)}, \tag{2.64}$$

where $\beta_p = \sqrt{1-\frac{n_e}{n_c}} \approx 1 - \frac{1}{2}\frac{n_c}{n_e}$. The plasma wavelength and the phase velocity can be different for the linear and non-linear regime, this leads to a different dephasing limit for the linear/non-linear case [130],

$$L_{dp} = \frac{1}{k_p}\frac{n_c}{n_e}\begin{cases} 1 & a_0 \ll 1 \\ 4a_0^2 & a_0 \gtrsim 1 \\ \frac{4}{3}\sqrt{a_0} & a_0 \gtrsim 2 \end{cases} \tag{2.65}$$

The dependence of the dephasing length on the a_0 of the laser pulse is a consequence on the increase in the plasma wavelength due to relativistic effects $\lambda_{p,NL} = \lambda_p\sqrt{a_0}$. Using the dephasing length for the 3D non-linear case $L_{dp} = \frac{4\sqrt{a_0}}{3k_p}\frac{n_c}{n_e}$ with Eq. 2.63, we obtain

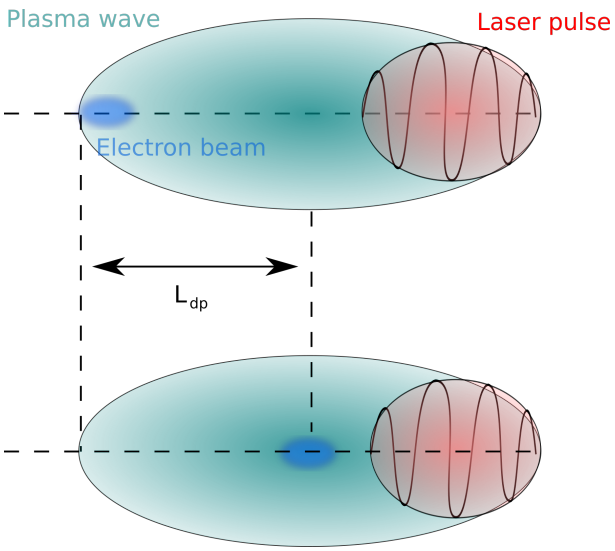


Figure 2.14: Schematic showing the dephasing of the electron beam as it gains energy and outruns the wakefield.

the maximum energy gain for the 3D non-linear case as

$$\frac{\varepsilon_{max}}{m_e c^2} = \frac{2a_0}{3c}\frac{n_c}{n_e}. \tag{2.66}$$

While dephasing is the ideal limit to the energy gain of a wakefield accelerator, there are also other factors which can limit the energy gain of the accelerator.

Guiding limited energy gain

Another limitation of the energy gain in laser wakefield accelerators is the ability to maintain a stable accelerating medium. The Rayleigh range of a laser pulse is often taken as an estimate of the useful length over which an unguided laser pulse can drive a plasma wave. The natural diffraction of a laser pulse can be balanced by using non-linearities in the medium to extend the interaction length. The operation of a laser wakefield accelerator when the self-focusing from the medium balances the natural diffraction inside the medium is termed the self-guided regime. The equation for the evolution of the spot size of a laser pulse [131] is given as,

$$\frac{d^2R}{dz^2} = \frac{1}{z_r^2 R^3}\left(1 - \frac{P}{P_c}\right). \tag{2.67}$$

Where $R = \dfrac{r}{w_0}$, w_0 is the vacuum spot size and z_r is the Rayleigh range. r is defined as the $1/e$ width of the electric field, P is the peak power of laser pulse and P_c is the critical power for self-focussing.

The choice of focussing geometry also heavily influences the guiding of the laser pulse. For short focal length geometries $w_0 < \lambda_p$, it was shown by Thomas et al. [132] that the beam breaks up into multiple modes and prevents the self-guiding of the laser pulse. Instead, by increasing the focal lengths $w_0 > \lambda_p$ and relying on relativistic self-focussing, a single mode driving the wakefield develops. This contains much more energy within its full-width half-max and guides for much longer lengths. An envelope equation for the laser pulse for this situation is given as

$$\begin{aligned} \frac{\partial^2 \bar{w}}{\partial^2 t} &= V_0\left(\frac{1}{\bar{w}^3} - \frac{16P\sqrt{2}}{P_{cr}}\right) \\ \bar{w} &= \frac{w}{w_0 a_0} \\ V_0 &= \left(\frac{c\lambda_0}{\pi w_0^2 a_0^2}\right)^2. \end{aligned} \tag{2.68}$$

The slower evolution of the amplitude of the plasma wave allows the density modulation of the wake to trap more energy into the central spot. This becomes the guided filament which drives the wakefield, as it contains more energy, the laser pulse depletes over much

longer lengths.

An alternative method to guide the laser pulse in the medium is to use a parabolic density channel, also known as channel guiding. This has challenges of its own as the generation of a density channel increases the complexity of the experimental setup. The channel depth Δn, needed to guide a laser pulse with a spot size w_0 is given by Geddes et al. [133].

$$\Delta n = \frac{1}{\pi r_e w_0^2}, \tag{2.69}$$

where $r_e = \dfrac{e^2}{mc^2}$, the classical electron radius. All of the results presented in this thesis will be in the self-guided regime.

Depletion limited energy gain

The front of the pulse experiences defocussing due to the density modulations of the wake. On top of that, energy is being lost to drive the wakefield. This loss of energy causes the leading edge of the laser pulse to move back relative to the peak of the pulse and is called pulse front etching. It is responsible for the depletion of the laser pulse in the bubble regime. Estimates for the pump depletion length made by considering the energy transfer to the wakefield, are examined in [134],

$$L_{dep} = \lambda_p \frac{n_c}{n_e} \begin{cases} 2.8/a_0^2 & a_0 \ll 1, \\ 1.4 & a_0 \gg 1. \end{cases} \tag{2.70}$$

A local pump depletion model for the bubble regime $a_0 > 3$, was analysed by [129]. The etching of the front of the pulse occurs at a constant velocity, moving behind the peak of the pulse,

$$\begin{aligned} \frac{v_{etch}}{c} &= \left(\frac{n_c}{n_e}\right), \\ \frac{v_g}{c} &= 1 - \frac{3n_c}{2n_e}, \\ L_{dep} &\approx \frac{n_c}{n_e} c\tau_{FWHM}. \end{aligned} \tag{2.71}$$

Although, it should be noted, that pulse lengths far from the wavelength of the plasma wave, will result in inefficient coupling of energy to the plasma wave as, so this expression is only valid for $c\tau \leq \lambda_p$.

2.7.6 Scaling laws

In Table 2.1, we present all the important scaling laws for wakefield accelerators from Lu et al. [135]. The various a_0 regimes have different associated scaling laws. $k_p w_0$ is often called the matched spot size condition and is a constraint requiring a balance between the space charge force and the ponderomotive force. L_{dp} is the dephasing length, the length over which the injected particles outrun the wake. L_{pd} is the pump depletion length, the length over which the pulse loses energy and is unable to sustain the wakefield. γ_p is the Lorentz factor of the wake and $\Delta W/mc^2$ is the maximum energy electrons can gain from the wakefield accelerator.

	a_0	$k_p w_0$	L_{dp}	L_{pd}	γ_p	$\Delta W/mc^2$
3D Linear	$\ll 1$	2π	$\frac{1}{k_p}\frac{n_c}{n_e}$	$\frac{\omega_p \tau}{k_p a_0^2}\frac{n_c}{n_e}$	$\sqrt{\frac{n_c}{n_e}}$	$a_0^2\frac{n_c}{n_e}$
1D Non-linear	> 1	2π	$\frac{4a_0^2}{k_p}\frac{n_c}{n_e}$	$\frac{\omega_p \tau}{3k_p}\frac{n_c}{n_e}$	$\sqrt{a_0\frac{n_c}{n_e}}$	$4a_0^2\frac{n_c}{n_e}$
3D Non-linear	> 2	$2\sqrt{a_0}$	$\frac{4\sqrt{a_0}}{3k_p}\frac{n_c}{n_e}$	$\frac{\omega_p \tau}{k_p}\frac{n_c}{n_e}$	$\sqrt{\frac{n_c}{3n_e}}$	$\frac{2a_0}{3}\frac{n_c}{n_e}$

Table 2.1: Scaling laws for the different regimes of LWFA [135].

2.7.7 Beam loading

When the charge of the injected beam is large enough to cancel the electric field of the cavity providing the accelerating forces, the accelerator is said to be beam loaded. This represents the maximum charge that can be accelerated in such a system. This has been analysed in the linear regime [136],

$$\begin{aligned} N_0 &= 5 \times 10^5 \left(\frac{\delta n}{n_0}\right)\sqrt{n_0}A, \\ N_0 &\approx \frac{1.5 \times 10^{17}}{\sqrt{n_0[cm^{-3}]}}\left(\frac{\delta n}{n_0}\right), \end{aligned} \tag{2.72}$$

where N_0 is the number of particles, δn is the density perturbation of the wake, n_0 is the plasma density and A is the cross sectional area of the wake. For the non-linear regime of wakefield accelerations, within a 3D framework, the beam loading charge is given as [137],

$$\begin{aligned} N_0 &= \frac{\pi R_b^4}{E_t} n_0 k_p^{-3}, \\ N_0 &\approx \frac{R_b^4 3 \times 10^{16}}{E_t\sqrt{n_e[cm^{-3}]}}, \\ R_b &= 2\sqrt{a_0}, \end{aligned} \tag{2.73}$$

where E_t is the normalised electric field in front of the beam-loading charge and R_b is the maximum radius of the blow-out. It has been shown that in the non-linear regime, significantly more charge can be accelerated by the wakefield. As such, for optimised performance of a wakefield accelerator, we aim to operate in this regime.

2.7.8 Betatron radiation

The focusing forces of a plasma wave cause the injected electron beam to perform oscillations perpendicular to their direction of acceleration. This causes radiation to be emitted from the bunch, which is known as betatron radiation. In Figure 2.15, we can see an illustration of this radiation generation process. Our starting point for the analysis of this radiation is the Larmour equation [138]. This describes the emission of radiation from a relativistic particle with an arbitrary trajectory.

$$\frac{d^2I}{d\omega d\Omega} = \frac{e^2}{16\pi^3\epsilon_0 c}\left|\int_{-\infty}^{+\infty} e^{i\omega[t-\vec{n}\cdot\vec{r}(t)/c]}\frac{\vec{n}\times[(\vec{n}-\vec{\beta})\times\dot{\vec{\beta}}]}{(1-\vec{\beta}\cdot\vec{n})}\,\mathrm{d}t\right|. \tag{2.74}$$

In this equation, $\vec{n}$ is the vector from where the radiation is being observed, I is the intensity of the radiation, Ω is the solid angle, ω is the frequency of the radiation emitted and $\beta = \frac{v}{c}$. We follow the discussion from Corde et al. [139], to understand the properties of betatron radiation. Consider the denominator $(1-\vec{\beta}\cdot\vec{n})$, this will be maximized when $\beta \approx 1$ and $\vec{\beta} \parallel \vec{n}$. The emission will maximised when the particle velocity is aligned to the observation direction and it will have a divergence angle of $\theta = \dfrac{1}{\gamma}$ [138].

We can also consider the phase term,

$$e^{i\omega[t-\vec{n}\cdot\vec{r}(t)/c]} \approx e^{i\omega(1-\beta)t}. \tag{2.75}$$

When this term is integrated over time, it will given a non-zero results only when the integrand, excluding the exponential, varies at the same frequency as the phase term.

$$\begin{aligned} \omega_e &= \omega_\beta(1-\beta) \\ \omega_\beta &= \frac{\omega_e}{(1-\beta)} \\ \omega_\beta &\approxeq 2\gamma^2\omega_e \end{aligned} \tag{2.76}$$

The frequency of the radiation is upshifted by a factor of γ^2 compared to the oscillation frequency of the particles. This relativistic upshift is what puts betatron radiation in the x-ray regime for typical LWFA experiments. There are two regimes for radiation generated by the oscillation of charged particles; wiggler and undulator radiation, and

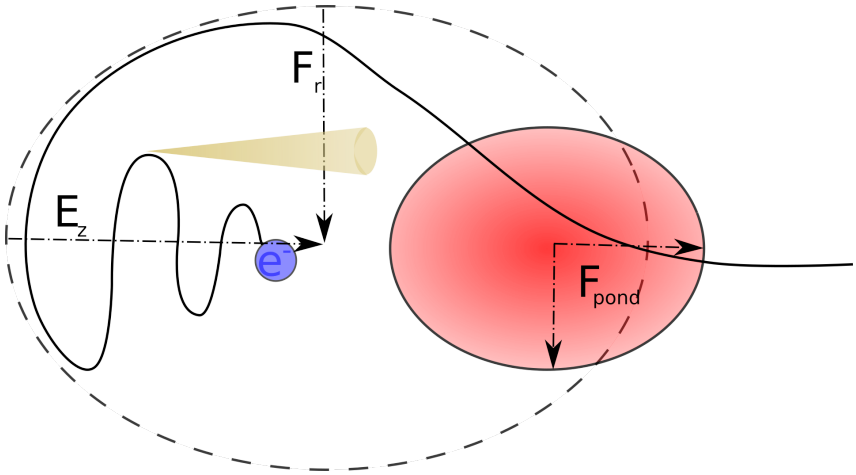


Figure 2.15: Illustration showing the trajectory of particles performing betatron radiation. F_{pond} is the ponderomotive force of the laser pulse, F_r is the radial force of the plasma wave, E_z is the electric field responsible for the acceleration of the electron beam. The dashed black line is the extent of the plasma cavity.

they are parametrized by the wiggler parameter, which is defined as,

$$\begin{aligned} k_\beta &= \frac{\omega_p}{\sqrt{2\gamma}} \\ K &= \gamma r_\beta k_\beta. \end{aligned} \tag{2.77}$$

Here r_β is the oscillation amplitude, γ is the relativistic factor of the accelerating particle and k_β is the wave vector of the betatron oscillation. For $K < 1$, the oscillation amplitude is small enough that radiation emitted from each period can constructively interfered to generated a narrow bandwidth spectrum consisting of peaks of odd integer harmonics. For $K > 1$, the oscillation amplitude and the spectral width of the emitted radiation are large. The spectral shape of betatron radiation can be approximated by a synchrotron profile. The synchrotron spectrum is typically defined by the critical frequency which scales as,

$$\omega_c \approx \frac{\gamma^3 c}{\rho}, \tag{2.78}$$

where ρ is the radius of curvature of the orbit. For the specific case of betatron radiation, the expression for the critical frequency is given as [117],

$$\begin{aligned} \hbar\omega_c &= 5.25 \times 10^{-11} \gamma^{1.5} \sqrt{n_e[\mathrm{cm}^{-3}]} \qquad \text{for } K \ll 1 \\ \hbar\omega_c &= 5.24 \times 10^{-21} \gamma^2 n_e[\mathrm{cm}^{-3}] r_\beta[\mu\mathrm{m}] \quad \text{for } K \gg 1. \end{aligned} \tag{2.79}$$

3 Methods

In this chapter, we provide a brief overview of the high power lasers which are used to perform these experiments, the Astra Gemini-TA2 and TA3 laser facilities. Laser-plasma experiments employ a host of different techniques in their design and implementation. A variety of targets are examined and their relevant parameters are highlighted. The typical diagnostics used in these experiments and their associated working principles are outlined. Numerical tools are used extensively in the field to understand how they will perform in experiments. Particle-in-cell simulations [2] were performed in order to understand the underlying interaction. As experimental time at a facility is often in short supply, by designing targets of appropriate densities to examine the physical systems of interest, we can improve the performance of these plasma accelerators.

3.1 High power lasers

The first successful operation of an optical laser is credited to T. Maiman in 1960 [140]. The acronym, LASER, aptly summarises its own working principles, "Light Amplified by Stimulated Emission of Radiation". By pumping a medium, where the electrons can be excited to a higher energy state, energy can be stored in the medium, known as population inversion. This energy can then, be released by another pulse which stimulates optical transitions as it passes by. When such a medium is built inside a optical cavity, a feedback loop occurs where the energy inside the pulse becomes amplified.

The development of high power lasers begins with the advent of pulsed lasers. The first technique used to achieve this is known as Q-switching [141]. Lasers are resonant cavities and as such have a quality factor, which is related to the loss inside the cavity. By tailoring the loss, it becomes possible to abruptly switch the lasing process on or off. This generates a short burst of photons which achieve pulse durations on the order of nanoseconds.

The next major advance in high powered lasers allowed the transition from nanosecond lasers to picosecond and femtosecond pulse durations and is referred to as mode-locking [142, 143]. A pulse train is formed inside the lasing cavity, where individual modes are separated in frequency $\Delta\omega = \pi c/L$, where L is the length of the cavity. Only frequencies

which fall within the spectrum of the gain window can be amplified. Consider a popular gain medium used in research laboratories, titanium:sapphire, which has a gain bandwidth of $\Delta\omega_{cav} = 90\text{THz}$ which results in $\approx 10^5$ modes. The width of each individual pulse in the pulse train is $2L/N$. So the more modes which can be combined from the spectral plane, the narrower each individual pulse will be in time.

The coherent combination of these modes only occurs if they have a fixed phase relation between them. Once a few modes have started coherently combining, these modes will gain more energy than the incoherent combination of modes, generating the required spectral shape to generate an ultra short laser pulse. This technique can generate pulses which are fs in duration [144] and have peak powers of 10s of kW. Above these peak powers, the laser pulse will begin to damage the gain medium which is ultimately what limited the peak power that these systems could attain. These pulses needed to be amplified to the TW level to be used for the application of laser wakefield accelerators.

3.1.1 Chirped pulse amplification

The extremely large power of mode-locked pulse poses a problem for their subsequent amplification. One way in which this limitation can be overcome is by stretching the pulse in time, there-by reducing its peak power, amplifying this stretched pulse and then re-compressing it, using reflective optics. This technique allowed the peak power of laser pulses to the reach the TW level and above. An illustration of this technique is shown in Figure 3.1. This technique was pioneered by Donna Strickland and Gerard Mourou, for which they were awarded the Nobel prize in 2018 and is called Chirped Pulse Amplification (CPA)[50].

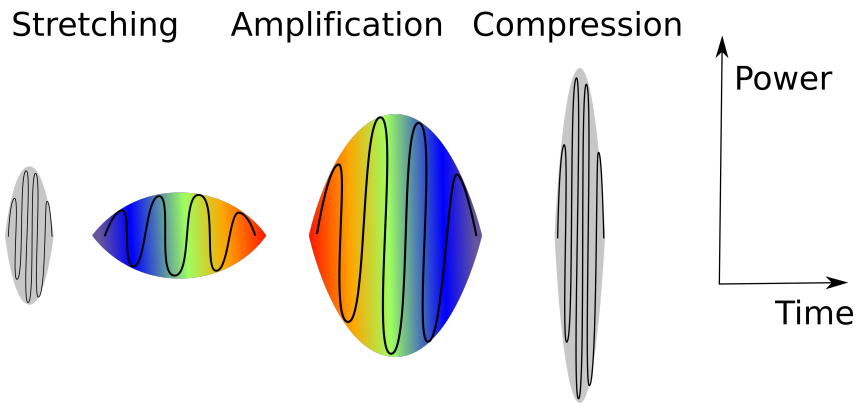


Figure 3.1: Illustration of Chirped Pulse Amplification. A low power, short pulse can be amplified without destroying its gain medium to yield a higher power pulse.

3.1.2 Astra Gemini

The Astra Gemini system, is a chirped pulse laser, located at the Central Laser Facility at Rutherford Appleton Laboratory in the UK. It consists of two experimental areas, named Target Area 2 (TA2) and Target Area 3 (TA3). Experiments performed in the thesis are from both of these target areas. The baseline parameters of these target areas are shown in Table 3.1. Both these target areas share the same master oscillator where the pulse begins at a duration of 12 fs. The TA2 facility provides compressed energies of $\approx$ 500mJ. The pulse goes through additional amplification stages before arriving in TA3 where it is amplified to the 15J level.

TA3 is also a dual-beam facility, both beams are amplified independently and a controllable delay allows many dual-beam configurations of experiments in this area. For the experiments presented in the later chapters, the second beam was used for optical probing. For the TA3 experiment, laser parameters such as the energy of the beam and its pulse duration are provided by the facility via an online data acquisition system called eCat [145].

	TA2	TA3
Energy on target [J]	0.5	$10-15$
Pulse duration [fs]	$30-45$	$40-45$
Focussing geometry	$f/18$	$f/40$
Beam diameter [mm]	55	150
Repetition rate [Hz]	5	0.3

Table 3.1: Nominal laser parameters for the experiments performed in this thesis [146].

3.2 Targetry

Much of the research in laser wakefield acceleration is dominated by target development as it plays a crucial role in determining the properties of the accelerating medium and generated radiation. Supersonic gas jets [147] have been used extensively throughout the field for the generation of a uniform medium for acceleration. These nozzles are pulsed, using solenoid values, with various gases and timed so that the laser pulse coincides with the stable phase of the gas flow. These gas jets can be made to have a cylindrical or rectangular outlet [148]. However, the former is more widely adopted as it is easier to construct and the cylindrical symmetry allows for a smoother gas profile. The following

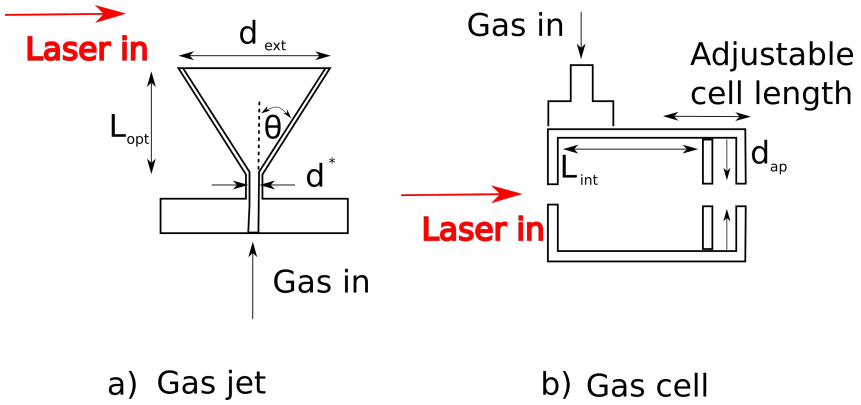


Figure 3.2: Schematic of the various gas targets used in the experiments presented in this thesis, a) gas jet and b) gas cell

expression, is used to estimate the density at the exit of the nozzle [149]

$$
\begin{aligned}
n_{ext} &= \frac{P_0}{k_b T_0}\left[1+\left(\frac{\gamma-1}{2}M^2\right)\right]^{\frac{1}{1-\gamma}} \\
aM^b &= c+\left(\frac{b}{2}\right)M^2 \\
a &= \left(\frac{d_{ext}}{d^*}\right)^{2b} \\
b &= 2\frac{\gamma-1}{\gamma+1} \\
c &= \frac{2}{\gamma+1}
\end{aligned}
\tag{3.1}
$$

Here d_{ext} is the exit diameter, d^* is the critical diameter of the nozzle, M is the Mach number of the flow, P_0 is the reservoir backing pressure, T_0 is the temperature of the reservoir and γ is the ratio of specific heats for a particular gas. In Figure 3.2, we can see the exit diameter and the throat diameter labelled for a cross-section view of a gas jet.

The uniformity of the longitudinal density profile of the gas jet, is sensitive, to the manufacturing defects around the throat of the nozzle. This can degrade the performance of a plasma accelerator. Some gas jets would result in stable profiles, whereas others would have ripples in their gas flow [150], where an idealised target profile is shown in Figure 3.3.

This variability in performance, lead to the development of a gas cell [151], which is a reservoir of gas with entrance and exit hole. Filled much more slowly than the gas jet, gas cells have been observed to have significantly smoother density profiles and result in much more stable electron beams. Gas cells can also be designed to have a continuously variable interaction length [152]. This additional advantage allows one to study the evo-

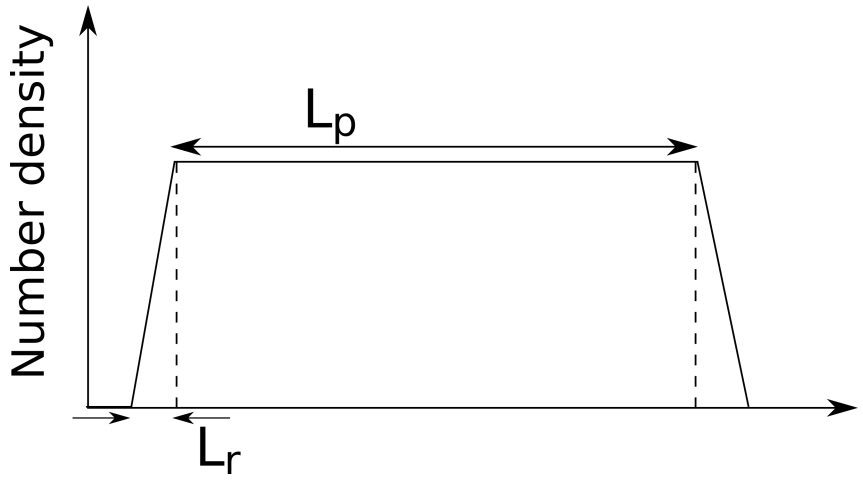
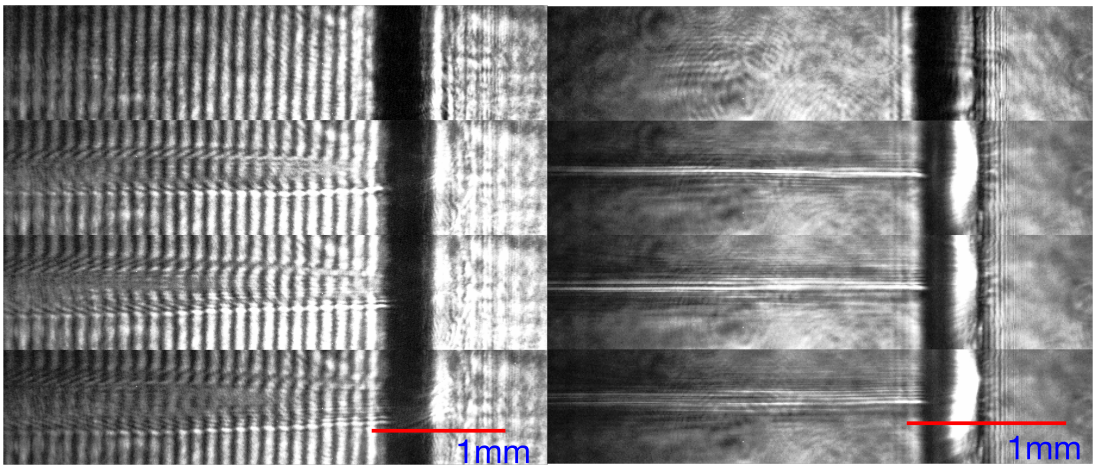


Figure 3.3: Idealised target profile for LWFA. L_r is the scale length of the ramp, L_p is the length of the uniform section of plasma.

lution of the acceleration mechanism inside the target and fine tune the performance of the accelerator to extract electrons at their dephasing lengths for a particular density.

Experiments performed in this thesis employed both gas jets and gas cells. The gas cell used is shown in Figure 3.2b. All gas targets used in these experiments were also diagnosed in-situ using interferometry as can be seen from Figure 3.4. The detailed discussion of these diagnostics is presented in the relevant experimental chapter.



a) Interferometry b) Shadowgraphy

Figure 3.4: Interferometry a) and shadowgraphy b) of the gas cell used in experiments. The laser pulse is incident from the left hand side. The gas cell's design aperture was 100 µm, however, the laser pulse very quickly increased the aperture to approximately 300 µm. The first row is performed with no gas inside the cell and the pressure is sequentially increased in the gas cell for each row below.

3.3 Diagnostics

The key to performing a successful experiment, is to understand the parameters of the interaction being studied. Diagnostics play a crucial role in the measurement of many challenging observables from experimental campaigns. We begin by reviewing the key laser diagnostics frequently employed on these experiments. Some of these, like the energy of the laser pulse and its temporal duration are provided by the laser facility, others, such as the focal spot quality and wavefront, are measured on a day-to-day basis.

This is followed by the particle diagnostics that look at the spatial and spectral structure of the particle beam. We then examine some optical plasma diagnostics which are used to diagnose the properties of the channel formed by the laser pulse as it exits the plasma. This is used to assess the performance of the targetry. We then examine techniques to measure the betatron radiation generated in such an interaction. The transmitted light can be used to infer properties such as the guiding of the laser pulse or the amplitude of the wakefield in the interaction.

3.3.1 Laser diagnostics

Wavefront sensor

Real laser pulses will have some aberrations in their wavefront, arising from imperfections in the surface quality of optics and non-linearities in amplification of these pulses and even misalignments onto the primary focussing optic in the target chamber. These imperfections will result in the profile of the focussed beam to depart from its optimal shape. A common way of characterising these aberrations in the wave-front is by using Zernike polynomials. These represent a decomposition over an orthogonal basis functions on the unit circle.

Various Zernike orders can represent a range of different aberrations. Aberrations in the wave-front can have an impact on the interaction as they reduce the peak intensity of the laser pulse. Additional, higher order aberrations can influence the evolution of the system. Adding coma to the wavefront of the pulse has been shown to increase the divergence of the electron beam while keeping the energy relatively unchanged [153]. A flat wave-front results in a symmetric transverse wakefield and a symmetric electron beam profile for self-injection [154].

The wavefront of the laser pulse was measured using a microlens array [155] and a camera. This diagnostic is referred to as a Shack-Hartmann wavefront sensor [156]. A

commercial wavefront sensor [157], called the HASO4, was used on the experiments in TA3 along with a deformable mirror, the ILAO [158], to correct the wavefront and attain a high quality focal spot. The deformable mirror consists of 52 actuators which were moved independently to correct aberrations in the wavefront. This feedback loop containing a deformable mirror and a wavefront sensor is called an Adaptive Optic (AO) system. This optimisation of the wavefront was performed on a daily basis by the user group in the target area.

Focal spot diagnostic

Measuring the focal spot requires the use of a microscope with extremely high magnification. This is because the focussed spot is typically of order 10's of µm, roughly the size of a single pixel on a camera chip. A microscope objective [159] is used in conjunction with a CCD camera. This is an infinity corrected, long working distance objective with $20\times$ magnification.

In order to calibrate this diagnostic, we need to know what a pixel corresponds to. This can be achieved by using a transmission grating, with a periodicity of 7 mm, placed in the collimated beam. When the beam is focussed with this pattern in its near-field, the far-field will consist of multiple spots. The separation of the spots is related to the periodicity of the grating by the following equation

$$n\lambda = d\sin(\theta) \tag{3.2}$$

where n is the order of the diffraction spot, d is the grating separation and θ is the angular separation of the diffraction spots.

The focal spot diagnostic is not only used to characterise the quality of the focus, it can also be used to position targets relative to the focal plane of the laser. This is achieved by placing a fiducial target, typically a wire mounted off-centre from the target, a known distance away from where the focus is intended to be. This fiducial is then imaged using the microscope objective. The target can subsequently be moved to a position relative to where the laser pulse focuses. The focal spot is measured and optimised daily and this data is incorporated in the estimate for the a_0 of the interaction.

Near field energy estimate

The energy of the laser pulse in these experiments is measured by reflecting the laser through an optic where a small fraction of the intensity is transmitted through, often called the leakage beam. This is typically performed when the pulse is stretched, before

it enters the compressor chamber. The near-field of the leakage beam is then measured using a CCD camera while the transmitted beam is measured using an energy meter. This provides a calibration where by the intensity of the transmitted beam can be inferred. The efficiency of the compressor, which is typically the energy of the laser pulse before and after the compressor chamber is used to estimate the final energy on target. This diagnostic is provided by the facility in the TA3 experiment but constructed by the experimental team on the TA2 experiment.

Pulse length measurements

The measurement of the duration of an ultra-short pulse poses an interesting challenge. Normally, in order to measure ultra-fast phenomena, one requires a detector with a response time smaller than the system being measured. However, femtosecond scales are far too short for electronic detectors. A standard way of performing this measurement, pioneered in the early days of ultra-short laser pulses is called frequency resolved optical grating (FROG) [160]. The pulse is split and recombined in a non-linear crystal to generate an autocorrelated pulse. This is then spectrally dispersed to generate the FROG image. A pulse retrieval algorithm is then used to generate the phase and temporal profile of the pulse. There are many variants of the FROG technique and the one used in these experiments is the second harmonic generation FROG (SHG-FROG).

3.3.2 Electron beam diagnostics

Scintillating screens

The most common method of detecting particle beams is to pass them through a material which scintillates, typically in the visible part of the spectrum. When a charged particle goes through a material, it can ionise some electrons in its path. The ionised electrons then go on to excite other bound electrons to a higher energy level. The resulting emission of light, as the excited electrons decay back to their ground state, is referred to as scintillation. This is routinely used in the diagnosis of high energy particles [161]. An extensive review of various scintillation sources for laser-plasma accelerators was performed by Buck et al. [162, 163], where it was observed that terbium doped Gadox scintillator, referred to in the field by its trademark name LANEX, shows a good linearity in its scintillation response (photons/charge) for a broad range of energies as can be seen in Figure 3.5.

LANEX works by the principle of fluorescence, this is where the energy stored in the upper state is released immediately. These scintillators also have a limit where the linearity between the intensity of scintillation light and the charge of the incident beam breaks down, this occurs at 10-100 $\mathrm{pC\,mm^{-2}}$ [162]. The spectrum of scintillation light

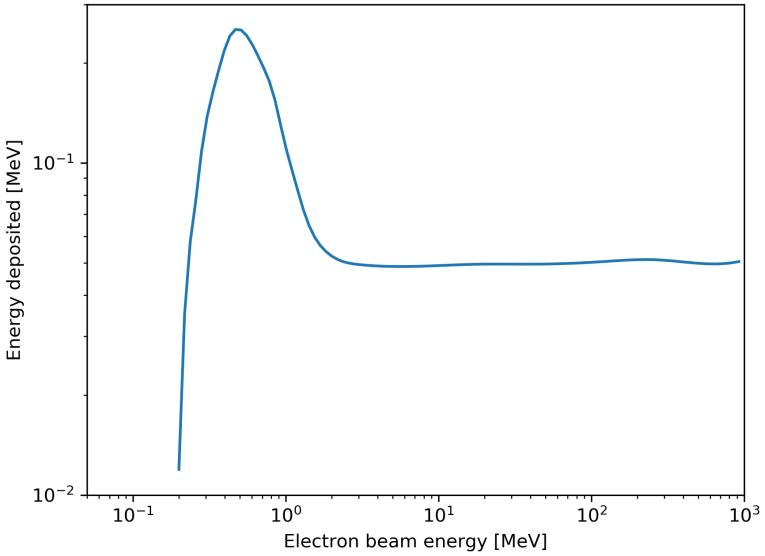


Figure 3.5: Energy deposition of LANEX for a range of different energies reproduced from [6].

from LANEX peaks at 546 nm and a transmission filter is used to exclude the reflections of laser light inside the target area [164]. In order to calibrate the efficiency of the imaging system, another scintillator called image plate (IP) is used. The output fluorescence of IP has been previously calibrated to give absolute charge directly [165, 166]. Ionising radiation, can cause electrons in the IP to enter a metastable state. This typically has a much larger upper state lifetime than fluorescence. When these particles are stimulated with a photon of the appropriate frequency, they decay to the ground state and emit a photon by a process called photo-stimulated luminescence (PSL).

The information about the incident radiation is then stored in the PSL levels and are then taken to a device (FLA-5000 fluorescence image analyser [167]) which exposes the IP to a laser which stimulates the decay of these electrons to their ground state. This outputs a quantity called the quantum level (QL) which must first be converted into photo-stimulated levels (PSL). PSL levels represents the stored energy from the metastable state in the image plate.

$$PSL = \left(\frac{R}{100}\right)^2 \left(\frac{4000}{S}\right) 10^{L(\frac{QL}{G} - 0.5)} \tag{3.3}$$

Where R is the resolution of the scanner in µm, S is the sensitivity (S=500), G is the bit depth of the scan (G=16), L stands for latitude which is a setting which allows the dynamic range of the measurement to be varied (L=5). The next step is to determine how many electrons correspond to a PSL level. This has been found experimentally, for the scanner used in these experiments to be $PSL/\text{MeV} = 7.9$ [168, p. 205] and this value

will be used in the determination of charge for the work presented in this thesis.

Using this technique we can calibrate the intensity of the light observed on the particle diagnostics to the charge observed on the IP. This procedure needs to be done once per configuration of an experimental setup and is subsequently valid (as long as the set-up is fixed) for the remainder of the experiment. The BAS-TR image plate [169] was used for all experiments presented in this thesis.

Electron beam profile monitor

The electron beam profile monitor consists of a sheet of LANEX, with aluminium on its glossy side, facing the target. This diagnostic is in the direct path of the high power laser pulse and the aluminium acts to protect the scintillator from damage. The scintillation light is imaged onto a camera, with a filter to select only the fluorescence frequency of LANEX. The beam profile diagnostic was only used on the experiments perform during the TA2 campaign. An illustration of this diagnostic is shown in Figure 3.6.

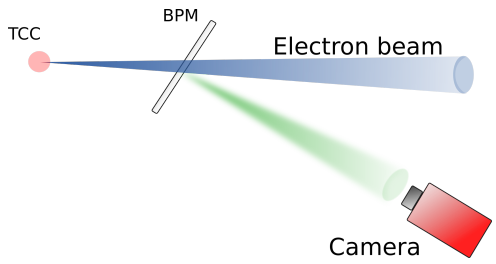


Figure 3.6: Illustration of the beam profile diagnostic. The electron beam propagates from TCC outwards. It intersects the beam profile monitor and causes it to scintillate. The light emitted from the rear surface of the LANEX is imaged using a CCD

Electron spectrometer

The electron spectrometer consists a dipole magnet which is used to disperse electrons, and a scintillating screen which allows the particle beam to be seen. The position at which the particle intersects with the LANEX screen will depend on its momentum and this can be used to unfold its energy spectrum. In order to determine the energy of the particles, which intersect at a particular length along the screen, we need to know the spatial profile of the magnetic field in the dipole magnet, its position relative to the source of the particle beam and the position of the scintillation screen.

The magnetic field profiles of these dipoles were analysed using a Hall probe [170] mounted on translation stages which samples the field at various locations, built by K. Poder [115]. This builds up a 2D profile of the magnetic field in the plane of dispersion.

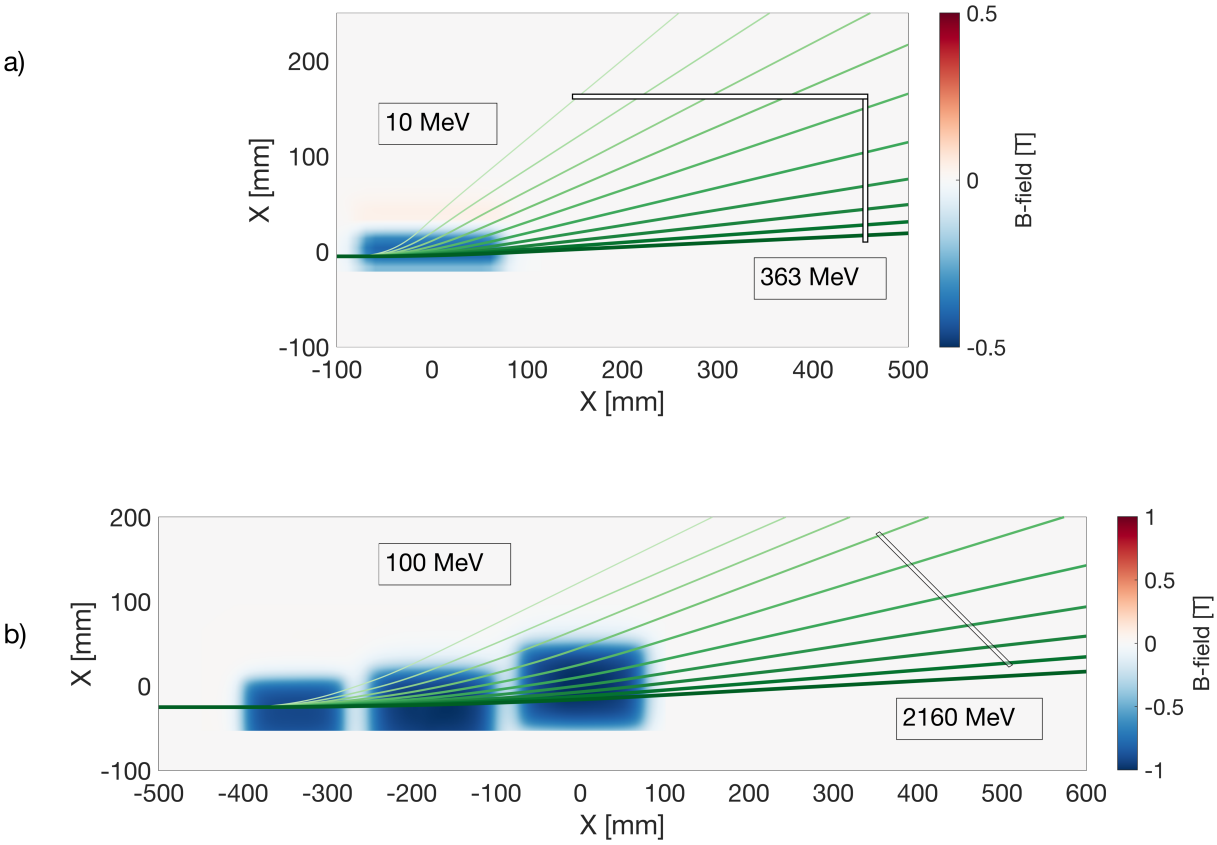


Figure 3.7: Particle tracking information from the a) TA2 experiment and the b) TA3 experiment. The peak B-field of the TA2 magnet is 0.4 T and the peak B-field for the TA3 magnet is 1.2 T. The lines represent the trajectories of 10 particles with logarithmically spaced energies.

Particles with a range of energies are tracked through, solving the equation of motion for a charged particle, for the magnetic field profile obtained. The position at which they intersect with the LANEX screen is subsequently determined. This was performed using a Matlab code developed by the JAI group at Imperial College London. The results for particle tracking, for both experiments are shown in Figure 3.7.

If the plane of the image and the object are not parallel, in this case the object is the electron spectrometer screens, for sufficiently large objects it will not be possible to have the whole image in focus. This effect can be compensated by tilting the lens and is known as the scheimpflug technique [115, 171, 172]. The lens, object plane and the image plane must intersect along a common point as is shown in Figure 3.8. Image warping can also be corrected using projective transformations [173].

3.3.3 Plasma diagnostics

Numerous techniques have been utilised in the diagnosis of plasma conditions for a wake-field accelerator. Interferometry is frequently used for the retrieval of electron density of the plasma immediately after it is generated. Shadowgraphy is mostly used to determine the presence of shocks in the medium arising from imperfections in the geometry of the nozzle [174] and the alignment of the laser pulse.

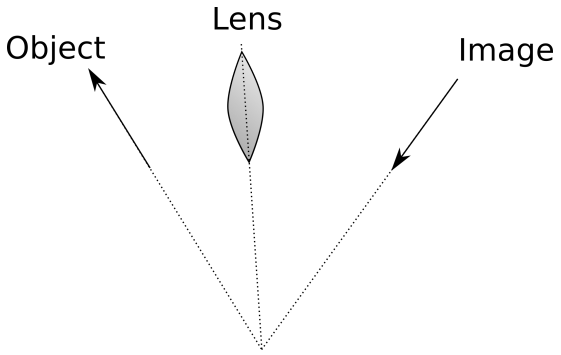


Figure 3.8: Illustration of the principles of scheimpflug for the correction of a tilted focal plane.

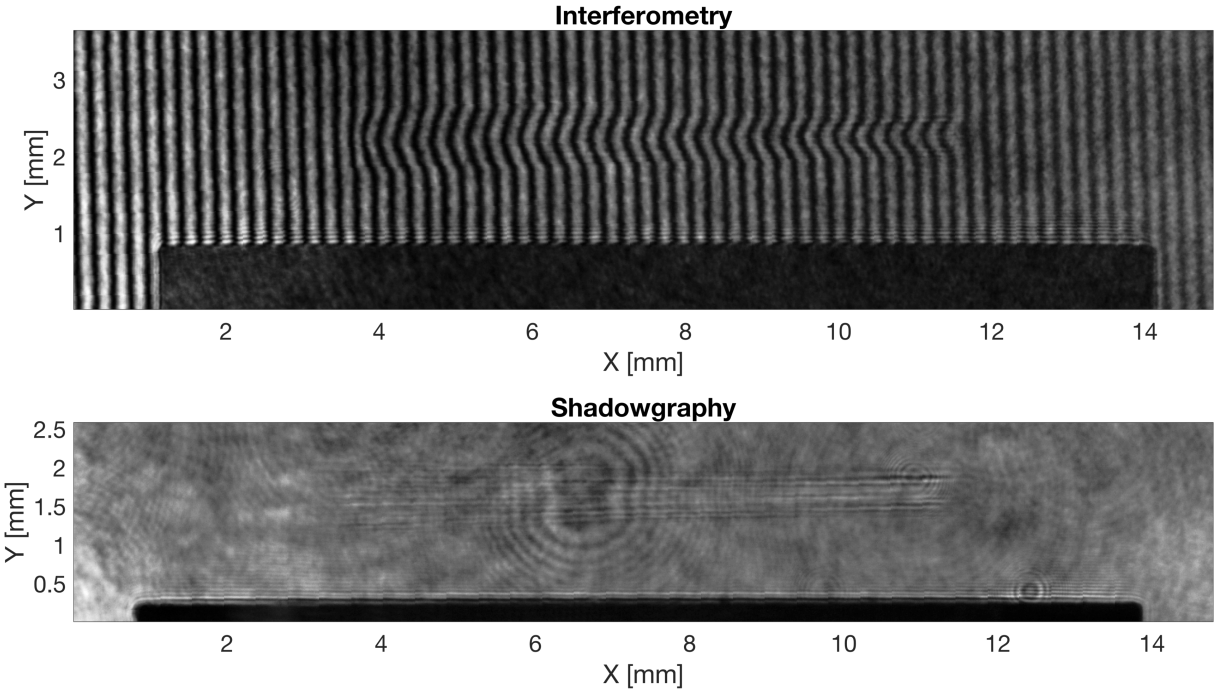


Figure 3.9: Shadowgraphy and interferometry from a 10 mm exit diameter gas jet with helium. The probe is timed such that the the laser pulse is exiting the plasma. The shadow of the gas jet nozzle can be seen at the bottom of both images. Note the length of plasma is not equivalent to the exit diameter of the jet. The circular feature on the lower image is diffraction from dust in the probe beam line.

Shadowgraphy

Shadowgraphy relies on the deviation of optical rays due to refraction. As such, it is sensitive to large transitions in density which can occur at shock boundaries. The fractional intensity variation is given as [175],

$$\frac{\Delta I_d}{I} = L\left[\nabla^2 \int \eta(x,y)\ \mathrm{dl}\right], \tag{3.4}$$

where I is the intensity of the light, ΔI_d is the difference in the intensity of the light, η is the refractive index and L is the distance between the image and detector plane. Shadowgraphy is sensitive to the second derivative of the refractive index and does not require a reference beam.

However, if the cumulative phase shift is large, the rays will cross and the determination of phase shift becomes ambiguous. Shadowgraphy also provides useful information about the alignment of the laser pulse as the expanding plasma column will be travelling along the optical axis. In Figure 3.9 we can see an example of the shadowgraphy and interferometry during a shot.

Interferometry

An interferometer measures the relative shift in phase between two beams. The common path interferometry, arranged in a Mach-Zender format, as is shown in the illustration in Figure 3.10, was employed in both experiments. The relative phase shift $\Delta\phi$ of region B in Figure 3.10 to the probe beam depends on the density of the medium, its wavelength

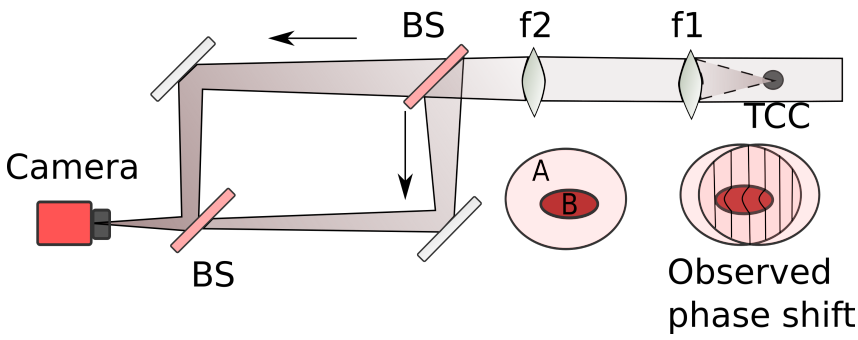


Figure 3.10: Illustration of an interferometer, where A denotes the reference portion of the beam and B denotes the region which has travelled through plasma.

and the length of plasma that the probe beam has traversed [173].

$$\begin{aligned}\Delta\phi &= \frac{2\pi}{\lambda}\int(1-\eta(x))dx \\ \eta &= \sqrt{1-\left(\frac{\omega_p}{\omega}\right)^2} \\ &\approx \frac{\lambda e^2}{4\pi m_e c^2 \epsilon_0}\int n_e(x,y,z)dy\end{aligned} \tag{3.5}$$

As such it is possible to relate the integrated phase shift to the density of the medium. However, the plasma will be cylindrically symmetric and the integrated phase shift on the

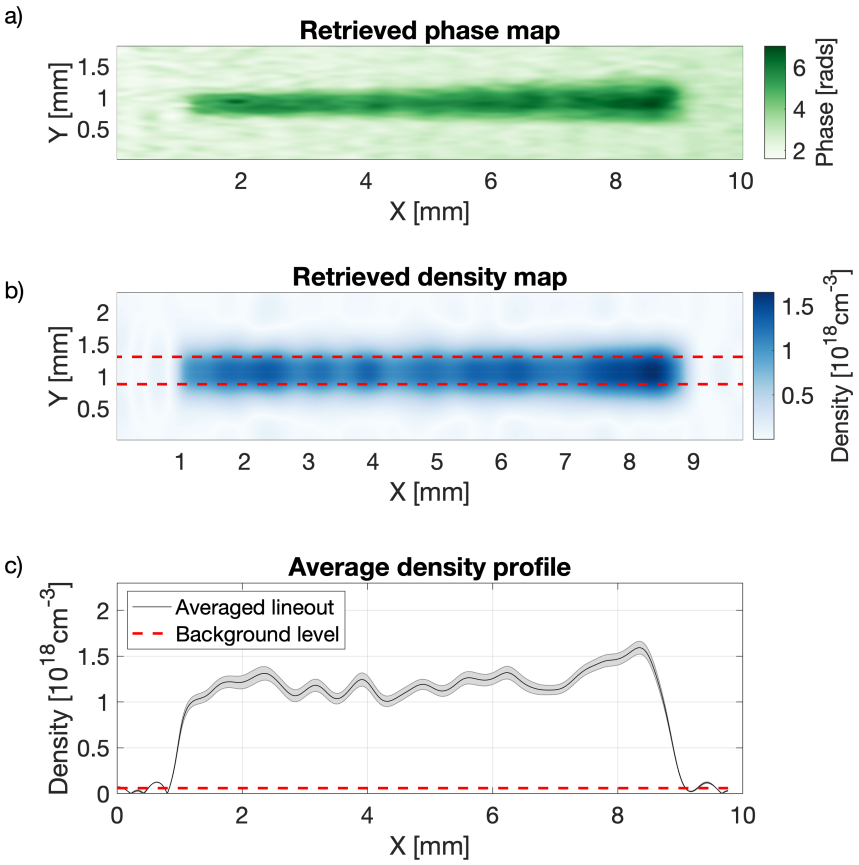


Figure 3.11: Analysis steps in retrieving the electron number density for a particular shot. In a) we can see the phase map that we extract from the interferometry image. In b) we show the extracted density profile that we obtain after the Abel inversion step. The region of interest is defined for a particular run and then the density profile is averaged between the dashed red bounds in b). In c) we can see the average density profile longitudinally. The shaded region represents the uncertainty on the mean density obtained from averaging. The oscillations in the density are attributed to variations in the energy deposited in the medium and as we measure the density after the laser pulse has exited the plasma.

optical axis will be greater than at the edges. This does not mean that the density was also greater on axis as the density we observe is the line-integrated density. Consider a radially symmetric function $f_r(r)$, the quantity f_{proj} which we observe is the projection of this on a plane

$$f_{proj} = 2\int_y^R \frac{r f_r(r)}{\sqrt{r^2 - y^2}}, \tag{3.6}$$

where R is the maximum radial extent, y is in the orthogonal direction to the propagation of the laser pulse. This function is called the Abel transformation. Extracting $f(r)$ given a particular f_{proj}, is known as the Abel inversion. This modifies the relationship between the measured electron density to the accumulated phase shift as follows

$$n_e(x,r) = \frac{\lambda e^2}{4\pi^2 m_e c^2 \epsilon_0}\int_r^\infty \frac{\mathrm{d}}{\mathrm{d}y}(\Delta\phi(x,y))\frac{1}{\sqrt{y^2 - r^2}}\,\mathrm{d}y \tag{3.7}$$

The phase information can be extracted from an interferogram in a variety of ways such as the Fourier transform [176], Hilbert transform [177] or the continuous wavelet transform [173]. Phase information can only be retrieved in $-\pi < \phi < \pi$. Realistic phase shifts routinely exceed this and the problem of extracting real phase shifts from the ones which

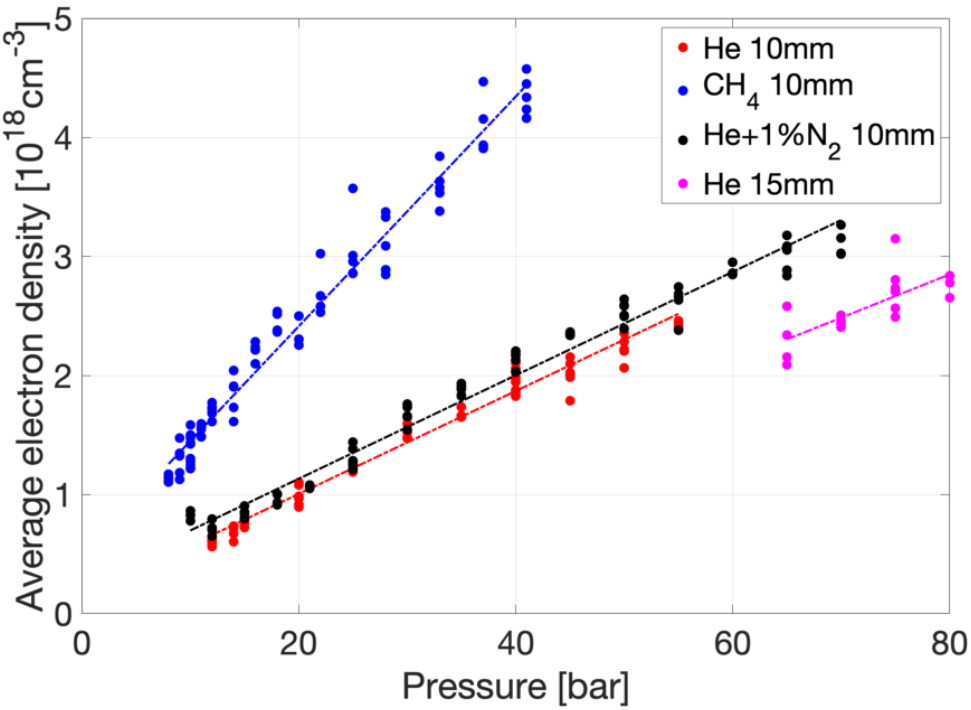


Figure 3.12: The relationship between density and backing pressure is used to calibrate the targetry as the pressure is immediately available during a shot. Two different types of gas jets with nozzle diameters of 10 mm and 15 mm are shown.

are *wrapped* between the $[-\pi, \pi]$ interval is known as phase unwrapping. Several phase unwrapping algorithms have been used in literature for this particular problem [178–180]. The Volkov method [180] is used for all the analysis as it was observed to be robust to the presence of experimental noise.

The analysis of interferometry data presented in this work is done using a MATLAB program called Interpret [181], written by J. Cole. This process, for a particular shot, is shown in Figure 3.11. In Figure 3.11a the phase image from the interferogram is retrieved. This is then processed in Figure 3.11b where the phase is unwrapped and the Abel inversion is performed to extract a map of the inferred electron number density. Finally in Figure 3.11c, we average over the region highlighted by the dashed red line in the density map to extract an averaged density profile of the target. By averaging over the approximately flat top region for this profile we obtain a value for the mean electron density of the medium.

Target density will often show a linear behaviour with backing pressure, when this was observed, the backing pressure can be calibrated against the data from interferometry and this can be used to determine the average electron number density of that shot. The pressure is measured using a pressure strain gauge located near the inlet for the gas target. Physically it measures voltage, which for a particular gas, is calibrated to pressure. This calibration of density against backing pressure is shown in Figure 3.12.

3.3.4 X-ray diagnostics

There are various ways of determining the properties of the betatron radiation generated from laser wakefield accelerators. The x-ray diagnostic was only used on the TA3 experiment and employed the indirect detection method [168, p .93]. This involves placing a scintillator, caesium iodide, in the path of the x-rays which convert the radiation into the visible frequency with some quantum efficiency. This light can then be observed using a CCD camera (iKon-L936 [182]). An illustration of the typical betatron radiation setup is shown in Figure 3.13.

X-ray filter pack

The x-ray filter pack can be used to determine the critical energy of the incident x-ray beam. This method consists of a series of filters of varying elemental composition and thickness, placed in the beam path. This results in a variation in intensity due to the loss in transmission going through a filter. By accounting for the loss in intensity through each filter and the non-uniformity of the x-ray beam profile, it is possible to extract the

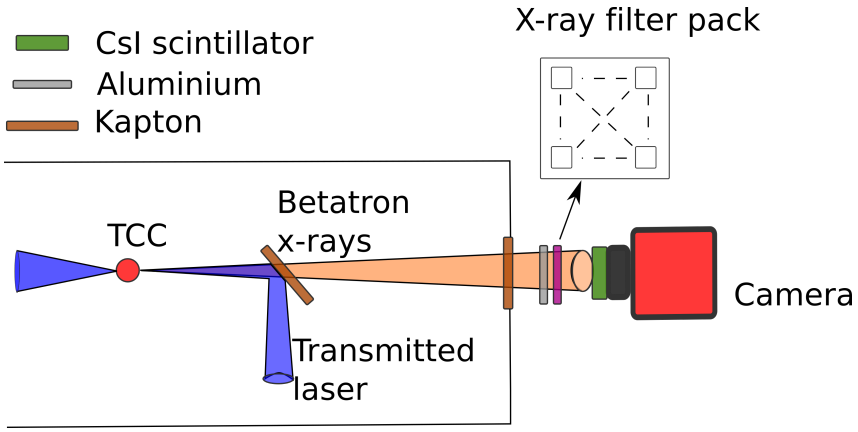


Figure 3.13: Illustration of the setup for characterising betatron radiation. The laser is dumped inside the vacuum chamber using a tape drive which reflects the IR radiation but allows x-rays to transmit through. A Kapton vacuum window is used to extract the x-ray beam from the vacuum chamber. The x-ray radiation is transmitted through a series of filters and then incident upon a scintillator. The light from the scintillator is then measured by a CCD camera outside the vacuum chamber.

critical energy of the x-rays in a single shot. This method for the determination of the spectrum is particularly suited to the broadband nature of betatron radiation. It also allows for the extraction of the spatial profile and divergence of the x-ray beam.

The filter pack used on this experiment was designed by M. S. Bloom [183] and its elemental composition and thickness is shown in Figure 3.14. In order to simultaneously measure the x-rays and forward transmitted light, a wedge with a hole was employed on the experiment. Only the highlighted filters are used in the analysis of the x-ray spectrum.

Critical energy determination

The betatron spectrum is assumed to have a synchrotron spectrum characterised by E_{crit}. We follow the steps outlined in [168] for determining the critical energies in betatron radiation with some modification. Consider the normalised synchrotron spectrum for a source with critical energy of E_c,

$$S(E, E_{crit}) = \frac{\left(\frac{E}{E_c}\right) K_{2/3}\left[\left(\frac{E}{2E_c}\right)^2\right]}{\int \left(\frac{E}{E_c}\right) K_{2/3}\left[\left(\frac{E}{2E_c}\right)^2\right] \mathrm{d}E}. \tag{3.8}$$

In this equation, $K_{2/3}$ is the modified Bessel equation of the second kind and E is the photon energy [138]. The expected transmission through a material of thickness t_i ,

attenuation coefficient μ_i and density ρ_i is,

$$T_i = \exp\left(-1.0\frac{\mu_i(E)t_i}{\rho_i}\right). \tag{3.9}$$

We can combine the transmission of x-rays through the various materials in the path of the x-ray beam, to calculate the expected transmission through each filter,

$$Y_i = \int S(E, E_c)\, Q(E) \prod T_i(E_c)\, \mathrm{d}E, \tag{3.10}$$

where $Q(E)$ is the quantum efficiency of the camera for a range of x-ray energies, i is the index of individual filter element, N is the total number of filters, T_i is the transmission of each filter element, $Q(E)$ is the quantum efficiency of the camera and Y_i is the experiment transmission through the filter. We have a free parameter in this fit, namely the critical energy E_c. So we define a residual Δ_{res},

$$\Delta_{res} = |Y_i - Y_{m,i}|, \tag{3.11}$$

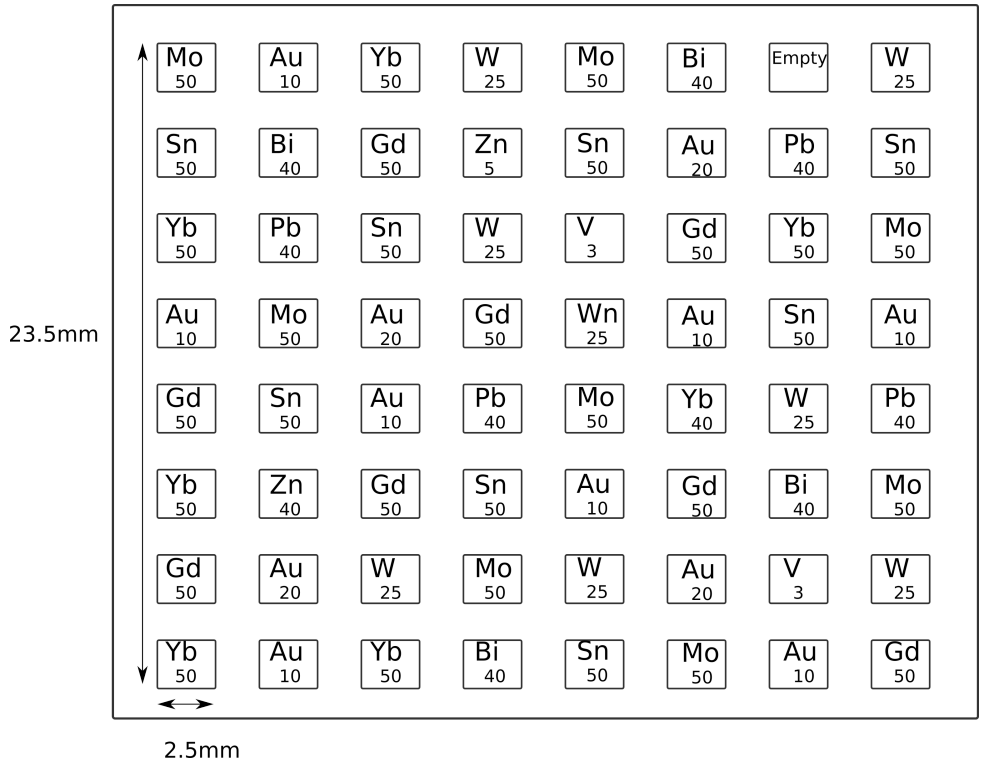


Figure 3.14: The filter pack on the experiment. The filter thickness are in µm and located below the chemical symbol for each filter element. The filter pack also consists of 2 layers of 6 µm Mylar with a flash coating of aluminium on the back surface.

where $Y_{m,i}$ is the measured transmission through the filter normalised to the unfiltered x-ray intensity. The transmission value was chosen by examining the histogram of pixel values and selecting a modal value as can be seen in Figure 3.16. By finding the value that minimises the residual, Δ_{res}, we obtain the effective E_c of the spectrum.

In Figure 3.15, we see a sample image that is formed using the betatron beam incident on a filter pack. Only a subset of filters which the x-ray beam falls on, are chosen for the determination of E_c. The circular clip in the beam is due to the hole in the wedge used for collecting the forward transmitted light from the interaction.

While the most obvious way would be to simply average all the pixels that the filter contains, the author choose to look at the distribution of counts and extract the modal value due to its robustness to the presence of hard-hits at low signal levels. We would expect the distribution of the photons to either be gaussian or poisson. For both these distributions the mean and the modal value are the same. However, in Figure 3.16 we can see that as the filter pack gets progressively higher in Z, the distribution becomes asymmetric and accumulates a high energy tail which does not decrease exponentially, as is expected of either distribution.

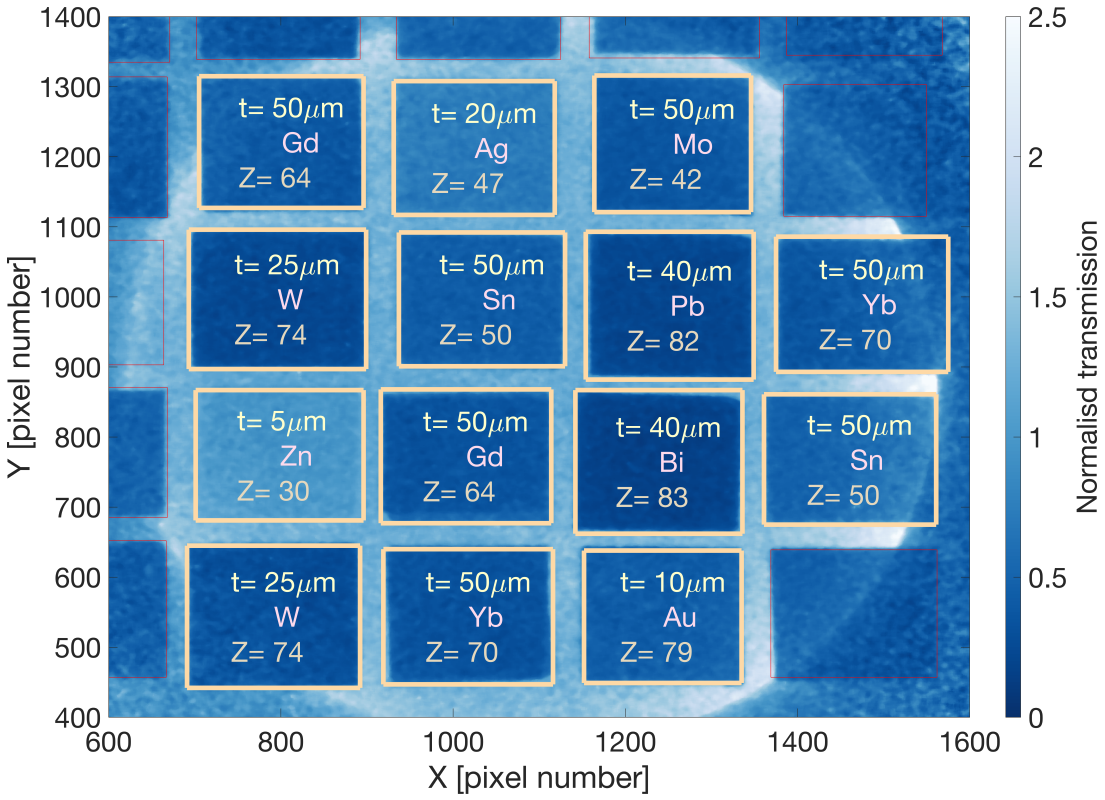


Figure 3.15: Raw image showing the x-ray transmission through various elements of the filter pack. Z is the atomic number of the filter element and t is its thickness.

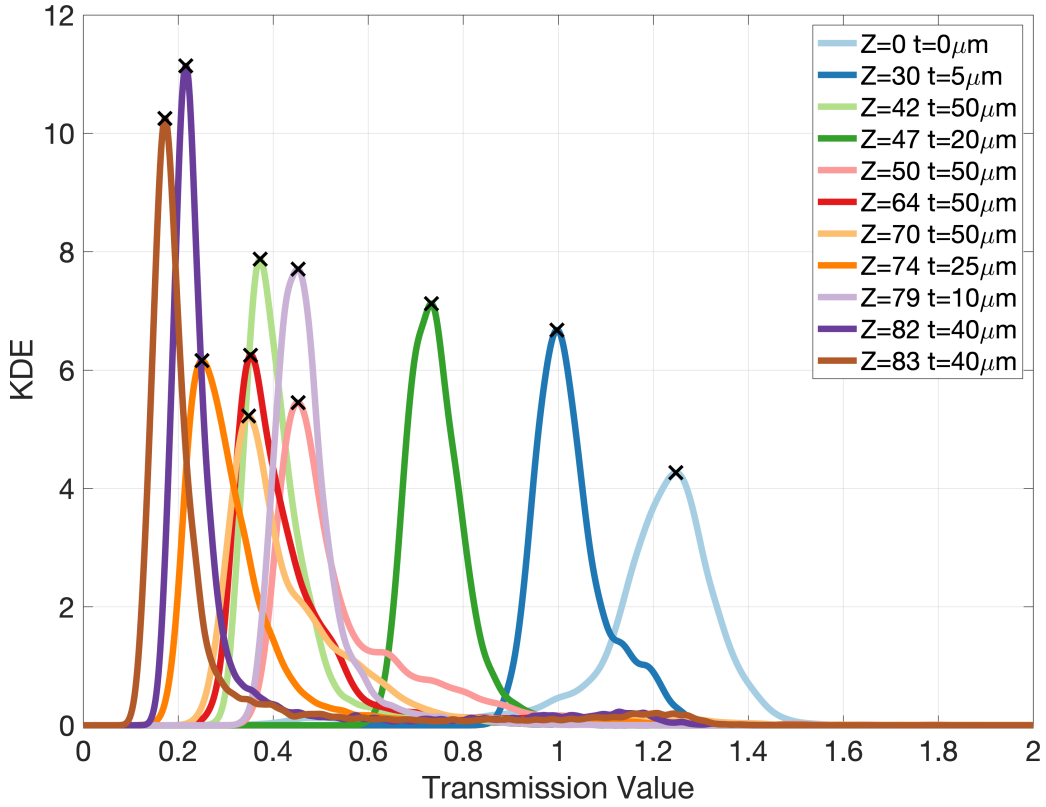


Figure 3.16: Kernel density estimation (KDE) of the normalised pixel values through each filter. Z is the atomic number of the filter element and t is its thickness.

This is attributed to the bremsstrahlung noise which could not be removed from background subtraction. A simple calculation of the mean will predict a higher value for the transmission of the x-rays than the mode suggests. Hence, the mode is a more reliable measurement of the betatron component of the x-rays. The KDE stands for the kernel density estimate and this is described in greater detail in the numerical tools section, towards the end of this chapter.

The error of the critical energy is estimated by propagating the maximum and minimum transmission for each filter to determine two bounds of E_c. The maximum and minimum of the transmissions for each filter element is obtained by taking the width (full-width half-max) of the peak in the KDE as the spread in the various values of $Y_{m,i}$. We then try and find the values of E_c for these extreme values of transmission. The minima for each of these residuals then provides the error in the calculated critical energy as can be seen in Figure 3.17.

In order to calculate the flux of the x-ray beam, we need to unfold the effect of the transmission filters. Due to the wedge for the forward transmitted light, the x-ray beam

is clipped and we cannot determine an absolute edge to the beam. We can none-the-less estimate a lower bound on the flux of photons and the peak brightness of the x-ray beam. Consider the relationship between the counts observed on the camera to the photons in

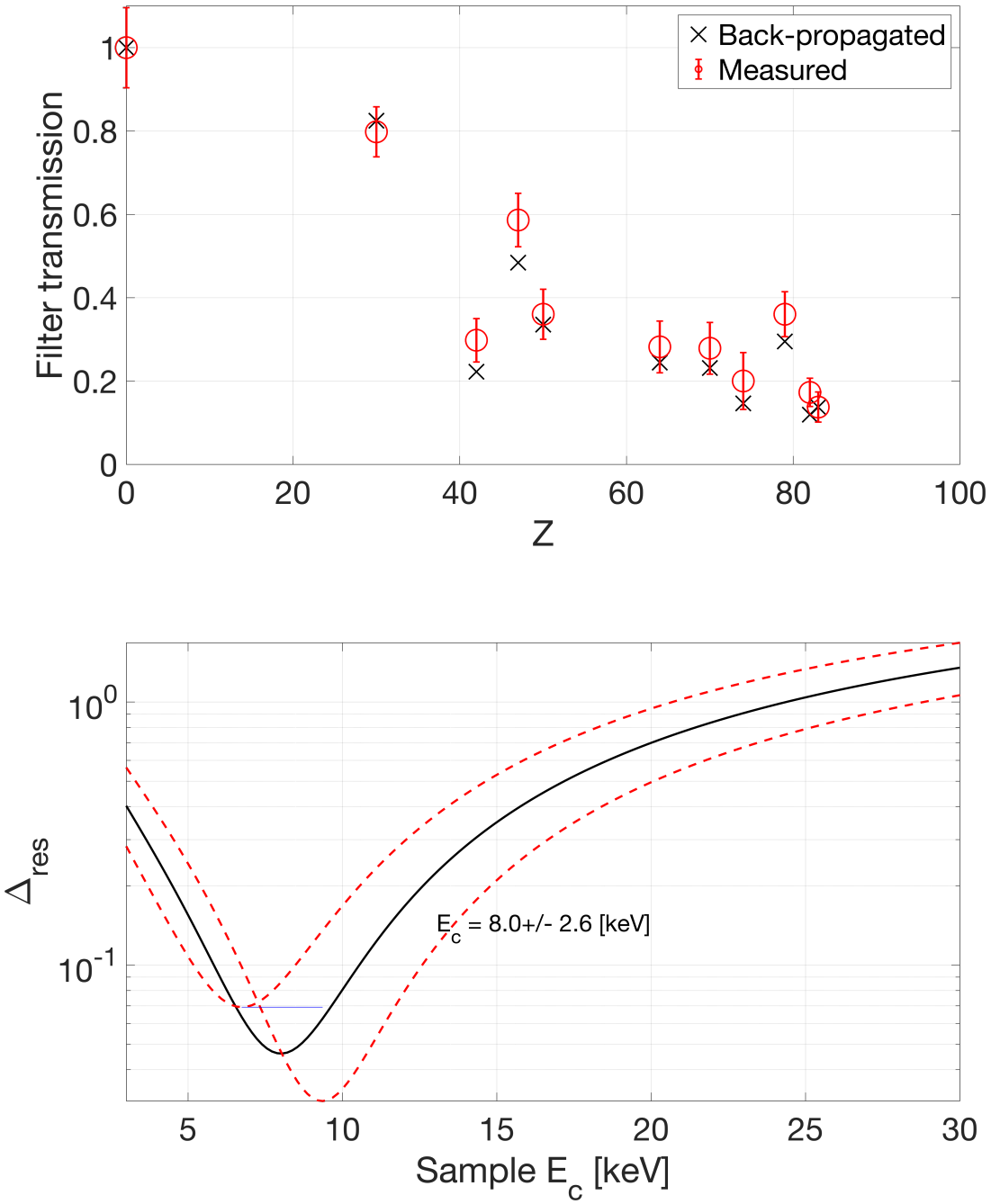


Figure 3.17: The determination of critical energy and its associated error for the image shown in Figure 3.15. The back-propagated transmissions are the estimated transmission through each filter for the optimal E_c. The red dashed lines represent the variation in the estimation of E_c due to the variances in transmitted intensity.

the x-ray beam, from Wood et al. [168, p.102],

$$N_{ph} = \frac{C}{\alpha \int ES(E, E_c)T(E)Q(E)\,\mathrm{d}E}, \tag{3.12}$$

where C is the counts observed on the camera and α is the number of x-rays per keV deposited in the scintillator.

3.4 Numerical tools

3.4.1 Particle-in-cell simulations

Numerical analysis was critical towards motivating research groups around the world to investigate plasma based sources of high-energy electron beams experimentally. Laser wakefield systems often rely on wave-breaking, which makes the use of fluid codes unsuitable as these phenomena can only be described by kinetic descriptions. On the other hand approaching this problem from a kinetic perspective is computationally expensive as capturing the dynamics of self-focussing and pulse evolution requires at-least 2-3 spatial dimensions.

Particle-in-cell (PIC) codes are a type of kinetic code, particularly well suited to this problem, as they offer a means to efficiently sample the phase space and permit the modelling of these systems with current computing architectures. They solve Maxwell's equations for the electromagnetic fields and self-consistently model the evolution of particles for a set of initial conditions.

Rather than simulating every particle, a quantity called the macroparticle is tracked. Each macroparticle represents many real particles and every species of macroparticles are

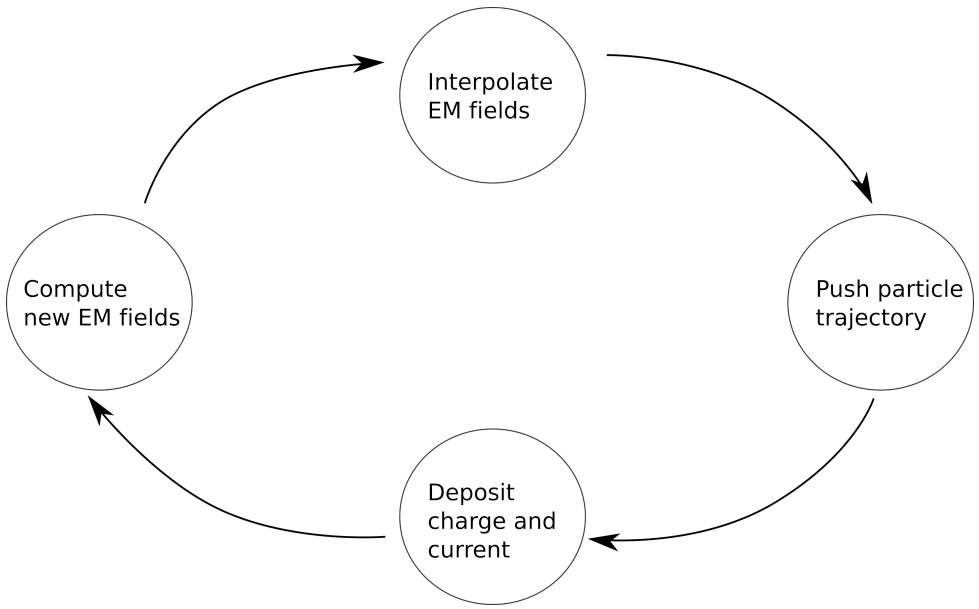


Figure 3.18: The steps taken in a general PIC code.

advanced by solving the relativistic equation of motion. [2],

$$\begin{aligned} \frac{d\vec{x_p}}{dt} &= \frac{\vec{u_p}}{\gamma_p}, \\ \frac{d\vec{u_p}}{dt} &= \frac{q_s}{m_s}\left(\vec{E_p} + \frac{\vec{u_p}}{\gamma_p} \times \vec{B_p}\right), \end{aligned} \tag{3.13}$$

where q_s is the charge of the species, m_s is the mass of the species, $\vec{u_p}$ is the velocity and γ_p is the Lorentz factor of the quasi-particle. Maxwell's equations are solved using a finite difference scheme on a staggered grid called the Yee method. The basic set of steps are summarised in Figure 3.18.

We begin by interpolating the fields at the particles position. Then the position of the particle and its velocity must be updated in the presence of the fields. This results in the redistribution of charge and generation of current which in turn will influence the new EM field available.

Modern PIC codes for laser-plasma interactions have many capabilities such as moving-window to reduce the number of particles being pushed, ionisation, collisions, Lorentz boosted frame, cylindrical geometries and envelope solvers [184–186].

In this work, SMILEI [2] and FBPIC [3] are the PIC codes of choice for the simulations present in the later chapters. Simulations are performed on the high performance computing facilities at Imperial College using the CX1 and CX2 supercomputers [1]. Depending on the nature of the simulations, the requirements vary from a few 100 core-hours to many 10s of thousands of core-hours.

3.4.2 Kernel density estimation

Non-parametric estimations of the density of a data set can be used to infer the functional form of the the underlying distribution, which can be a simple Gaussian distribution or something more complicated. The most commonly used density-estimation technique is the histogram. A histogram breaks up a dataset into discrete bins and we then count how many values are present in each bin. Histograms are discontinuous and the distribution can depend on the width of the bin and the end points of the bin.

Kernel density estimation (KDE) is a generalisation upon the idea of a histogram. A fixed rectangular bin is replaced with a smooth function. In Figure 3.19, we can see how the KDE can give a closer approximation to estimating the underlying distribution

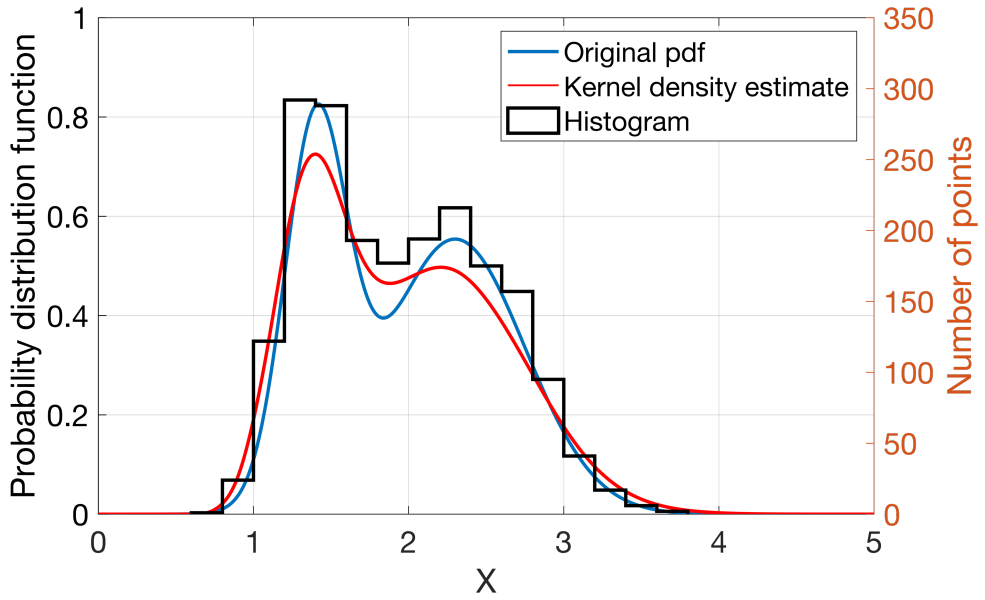


Figure 3.19: Comparison between a histogram and kernel density estimate for the sum of two offset Gaussian distributions.

function. For the univariate case, the optimal bandwidth selection, h^* is

$$\begin{aligned} \hat{f} &= \frac{1}{nh}\sum_i K\left(\frac{x_i - x_0}{h}\right), \\ h_* &= \left(\frac{\int K^2(x)dx}{n\sigma_K^2 \int f''(x)^2 dx}\right)^{1/5}, \end{aligned} \tag{3.14}$$

where K is the kernel used, f is the functional form of the true distribution, $\hat{f}$ is the estimate of the underlying distribution. The kernel density estimation method also has a lower optimal mean square error $O(n^{-2/3})$ when compared to that of a histogram $O(n^{-4/5})$ [187, 188].

These advantages are the primary reasons why kernel density estimation is used to estimate the stability of various experimental parameters throughout this work. Where appropriate, the author will also provide the corresponding histogram for the distribution. In order to calculate the error of the kernel density estimation, the author used bootstrapping. Consider a random variable,

$$X \in [X_0, X_1, ..., X_n]. \tag{3.15}$$

We assume that all variables are drawn from a distribution. If we randomly sample this variable to generate a smaller data set, it should also have the same underlying distribution,

$$X^* \in [X_0^*, X_1^*, ..., X_m^*], \tag{3.16}$$

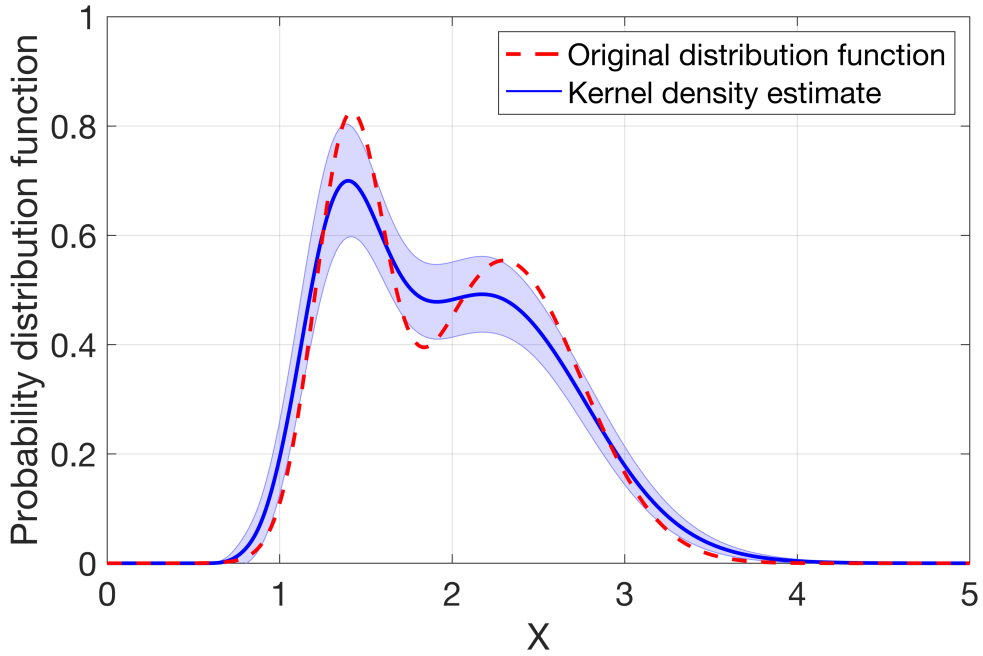


Figure 3.20: The mean KDE (solid blue line), its associated confidence interval estimated using bootstrapping (blue shaded error bar) and the original distribution (dashed red line).

where $n > m$. We can now apply the kernel density estimation on this new data-set. Once we have obtained a density estimation for this reduced subset of data we randomly sample the full distribution X again to obtain a new subset X^*. We repeat this process to generate a set of kernel density estimates.

The mean value of all these density estimates is taken to be the average kernel density estimate and the standard deviation is taken to be the uncertainty in the statistical estimate. This is the basic form of boot-strapping used in the analysis of kernel density estimation as is shown in Figure 3.20 [189]. This procedure informs us of the significance of inferences made using this statistical technique.

3.4.3 Data binning procedure

Experimental data is often acquired where the independent variable, typically pressure or density, is sampled with non-uniform intervals. In order to interpret the results from different datasets, a binning procedure is employed throughout this thesis. The results of this procedure are shown for some synthetic data in Figure 3.21. The steps of this binning procedure are as follows:

- Split independent variable into equal intervals
  The dataset is sorted such that values are classified into bins where the bin widths are chosen to be equally distributed over the range of the independent variable

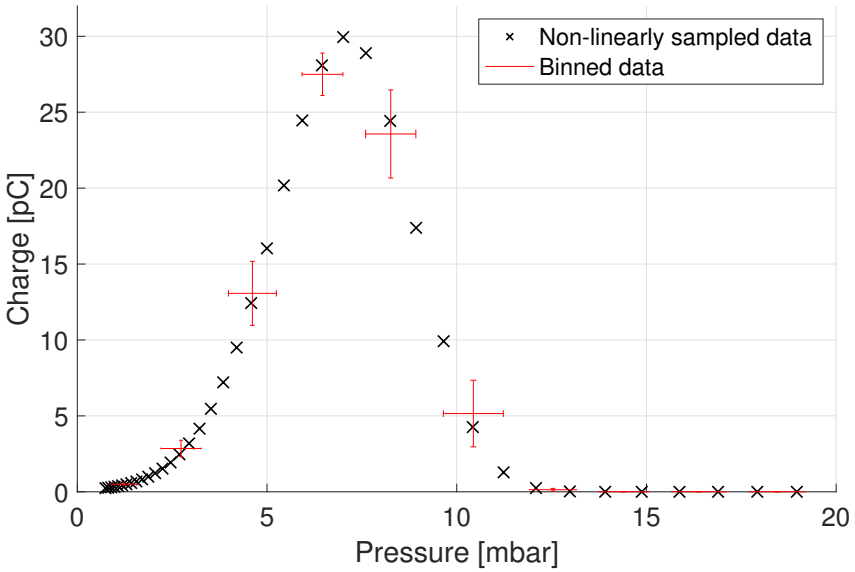


Figure 3.21: The black marker is synthetic experimental data generated for non-uniformly sampled pressures. The red marker shows the result of the binning procedure along with associated error-bars from the error on the mean of the data.

- Average over a bin

  All the shots which fall into a bin are averaged to obtain a mean value for the dependent and independent variable. This is shown in Figure 3.21 as the red markers. The error bars are propagated to include the errors in the data set and the standard deviation of the dependent data in each bin. These errors are combined in quadrature.

4 Laser wakefield acceleration in a clustered medium

4.1 Introduction

A clustered medium consists of solid density collections of atoms, interspersed across a uniform, underdense medium. The use of a clustered medium for the purposes of electron acceleration has been studied by various authors. First, it was explored by Fukuda et al. [190] at a 18 TW laser facility at average atomic densities around $9 \times 10^{19}\,\mathrm{cm}^{-3}$ in a medium consisting of argon clusters with an average cluster radius of $240 - 1000\,\mathrm{nm}$. In Table 4.1, other relevant experimental parameters are outlined. They observed a two temperature distribution of electron energies (2.8 and 18.8 MeV).

Using simulations, the author suggest that the higher energy electrons are directly accelerated by the laser pulse and the lower energy electrons are injected by wake-breaking. The size of the clusters in this experiment also approach the size of the wavelength of the laser pulse at which point the interaction is better described as a laser-droplet rather than a laser-cluster [191]. Mirzaie et al. [192] investigated laser wakefield acceleration using a clustered medium consisting of argon with 5.5×10^3 atoms in each cluster. It was noted

	Fukuda et al. 2007	Mirzaie et al. 2016	Wood et al. 2016
Power [TW]	18	17-50	10
Pulse duration [fs]	23	30	37.5
w_0 [µm]	10	28	15
Peak intensity [$10^{18}\mathrm{W\,cm}^{-2}$]	5.7	0.6-2	1.4
P [bar]	60	1.5-5	1-10
N_A	6.6×10^9	500-3000	2.0×10^4
n_e [cm^3]	9×10^{19}	5×10^{18}-1.2×10^{19}	8×10^{18}-2×10^{19}
Q [pC]	2100	3000	40-50
E_{max} [MeV]	58	160	250

Table 4.1: Parameters for other experimental work on laser wakefield acceleration in a clustered medium. These experiments were all performed using titanium:sapphire laser systems and had a central wavelength $\approx 800\,\mathrm{nm}$

that electron beams with an elliptical beam profile are generated by this interaction. Monoenergetic beams with a relative energy spread of 15% at 80 MeV were observed in such a medium when operating at electron densities of $5 \times 10^{18}\,\mathrm{cm}^{-3}$. The author states that the injection mechanism is truncated due to an evolving plasma wave structure. However, Mirzaie et al. [192] suggests that electron beams with 3 nC and 150 MeV can be generated with a 20 TW, 30 fs laser system, suggesting efficiencies of 45%, orders of magnitude higher than laser wakefield based electron acceleration from similar laser facilities [193] or even by the scaling laws for non-linear plasma waves [135]. As the author does not provide a model for how this occurs or simulations of the interaction between a plasma wake and the clusters, it is difficult to ascertain whether this acceleration is due to the clustered nature of the target or the ionisation of atomic species from a high Z target, i.e. ionisation injection.

Around the same time, an experiment was performed at the Astra-Gemini TA2 laser facility by Wood et al. [168, p.112-136]. This is a 10 TW, 45 fs and 450 mJ laser facility and the experiment was performed using an $f/18$ focussing geometry. Here the clustered medium was methane, with average cluster sizes of 2.0×10^4 atoms per cluster, inferred using scaling laws for the target. In this experiment, electron beams were similarly observed to have high degrees of eccentricity in the laser polarisation direction. Electron beams with energies up to 250 MeV and beam charge up to 50 pC were observed. A comparison was made with electron acceleration in a helium gas jet. Again, a clustered media was a preferable target for the acceleration of electrons as it generated as a clustered medium generates higher energy electron beams 249 ± 8 MeV compared to self-injection which attained 210 ± 7 MeV. The author does not describe the injection process of clusters into a wakefield but does discuss the increased transverse momentum from a clustered media.

It was hypothesised that the increase in the transverse momentum of the electron beam is due to the clustered medium guiding the laser pulse better than the unclustered medium, allowing for stronger electron beam-laser interactions. The stability of the electron beams generated in this medium are also higher when compared to helium, which did not cluster for their target configuration. However, it is also possible that this improved performance is due to ionisation injection rather than the clustered nature of the target. We can summarise the prior experimental work, pertaining to laser wakefield acceleration in a clustered media, in Table 4.5.

The use of nano-particles for the controlled injection of electrons into a wakefield has also been examined numerically by Cho et. al. [194]. PIC simulations of this system

suggest that a 0.5 PW laser pulse propagating through a 27 cm capillary can generate a 5.1 GeV with 0.8% energy spread. However, the author notes the interaction between a clustered media and the nano-particle injection are different as only a single nanoparticle is used in this scheme. The realisation of such a target poses many challenges and requires the design of aerodynamic lenses [195]. Some variants of nano-particle injection scheme using the ablation of 20 nm aluminium nano-particles has been shown to inject and acceleration electron beams in a wakefield accelerator [196].

Injection and trapping are not the only benefits a clustered medium can have towards the development of an efficient laser wakefield accelerator. Self-focussing in a clustered medium has been observed to extend the interaction length of the laser pulse [104]. The pre-pulse of the laser can be used to vary the self-focussing effects of the generated medium by generating a plasma waveguide structure [197, 198] or by using the transient beam lensing effect [104]. Guiding over 40 Rayleigh ranges with coupling efficiencies up-to 50% have been reported in this medium [198]. Control over the group velocity of the laser pulse has also been demonstrated in a clustered target [199], where the author suggests the possibility of limiting the issue of dephasing in laser wakefield accelerators.

This work follows on from the experimental work performed by Wood et al. [168] to examine laser wakefield acceleration in two types of targets, gas jets and gas cells. The aim of this work was to determine the role of clusters in the injection and acceleration of electron beams in the wakefield. As covered in the methods section in Chapter 3 on p.43, in gas jets, clustering can occur due to the adiabatic expansion causing the gas to cool and condense. In a gas cell, the flow occurs much more slowly. Clustering does not occur in such a medium as there is no corresponding cooling of the gas. Methane is again examined in both these types of targets and the properties of the electron beam are studied as a function of density. This provides a good control, to understand the differences in particle injection, that a clustered medium offers relative to an un-clustered medium. The experiment is performed at the same 10 TW, 500 mJ and 45 fs laser facility, Astra-Gemini TA2 and used the same $f/18$ focussing geometry as Wood et al. [168]

Clusters can act as large sources of charge, allowing greater control over the injection process than ionisation injection. In this section, we present data which shows how a clustered medium compares to a non-clustered target. Providing a direct comparison between the clustered nature of the target to understand how a clustered medium impacts the electron beam generated in a laser wakefield accelerator.

4.2 Experimental setup

This experiment is performed at the 10 TW laser facility Astra-Gemini TA2 [146, 200], at the Central laser facility (CLF) in Oxford, United Kingdom. This is a titanium:sapphire, CPA laser facility which delivered 532 ± 66 mJ in 45 fs. The pulse duration was measured by the facility using a SPIDER [201] and found to be 45 ± 2 fs.

Laser parameters	
Laser energy	532 $\pm$66 mJ
Pulse duration (τ)	45 $\pm$2 fs
Spot size (w_0)	$17 \pm 2 \times 23 \pm 5$ µm
Peak intensity	$3.0 \pm 0.2 \times 10^{18}$W cm^{-2}
Focussing geometry	$f/18$

Table 4.2: The laser parameters for this experiment.

The quality of the focal spot was measured on a day-to-day basis using a microscope objective and a camera. An $f/18$ off-axis parabola (OAP) is used to achieve a spot size of $(17 \pm 2 \times 23 \pm 5)$µm and fractional energy in the full width half maximum of the spot was measured to be 0.37 ± 0.02. The laser energy before the compressor was measured using a Gentec energy meter [202]. This was used to establish a correlation with the near field intensity obtained through a leakage mirror looking at the spatial profile of the laser pulse.

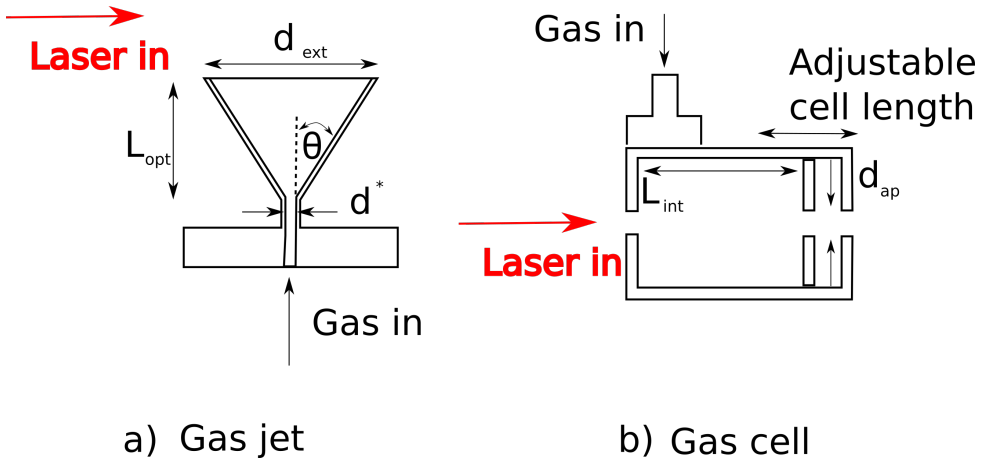


Figure 4.1: Labelled schematics showing the relevant parameters of the gas jet and gas cell used on this experiment. d^* is the exit diameter of the gas jet, d_{ext} is the diameter of the exit cone, L_{opt} is the length of the nozzle from its throat to its exit diameter and θ is the half angle of the gas jet. For the gas cell, d_{ap} is the aperture of the pinhole of the gas cell, L_{int} is the length of the gas cell longitudinally.

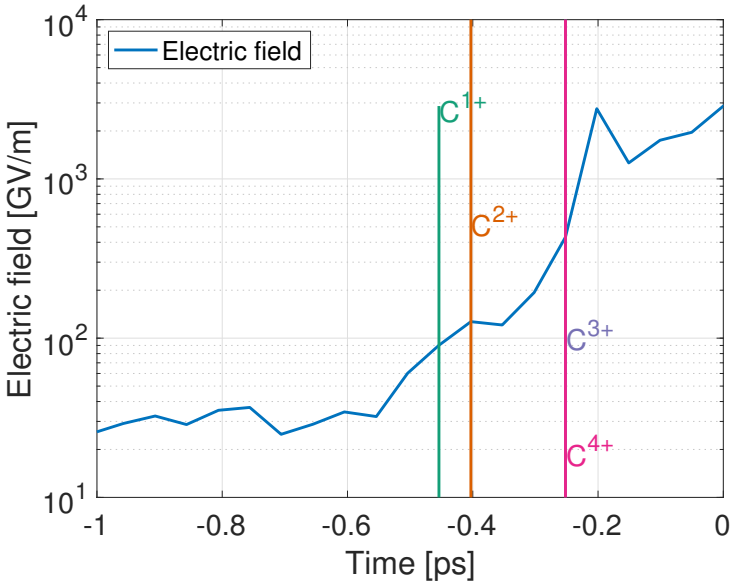


Figure 4.2: The Sequoia measurement of the prepulse intensity with the tunnel ionisation states using the ADK model [86] for carbon ions. The peak of the laser pulse occurs at time $t = 0$

The efficiency of the compressor was also measured to be 62.5% and this provides an estimate for the laser energy delivered to the target. Combining the near-field estimate for the energy of the laser pulse, the lower power focal spot information and the pulse duration, we obtain an a_0= 0.57±0.06 for the results presented in this chapter. The laser parameters for the experimental data-set shown in this chapter are highlighted in Table 4.2.

A gas cell and gas jet were used with methane and helium as their backing gas and their respective target parameters are shown in Table 4.3 and the schematic of both targets are shown in Figure 4.1.

Methane in a gas jet clusters at room temperature for this gas jet geometry. Helium is used as the control medium to show the equivalent performance of the targets. Self-injection is expected to be the main injection mechanism when helium is used as the backing medium. Helium has a very low condensation parameter of $k_{He} = 3.85$ [203], compared to methane $k_{CH_4} = 2360$ [204] and so we expect the formation of clusters, from helium at room temperature, to be negligible in comparison.

The contrast of the laser system is measured using a commercial third order auto-correlator called Sequoia [205]. In Figure 4.2, the outer level of carbon ionises 0.5 ps before the main pulse arrives. As we expect clusters to expand on the 5-10 ps time scale,

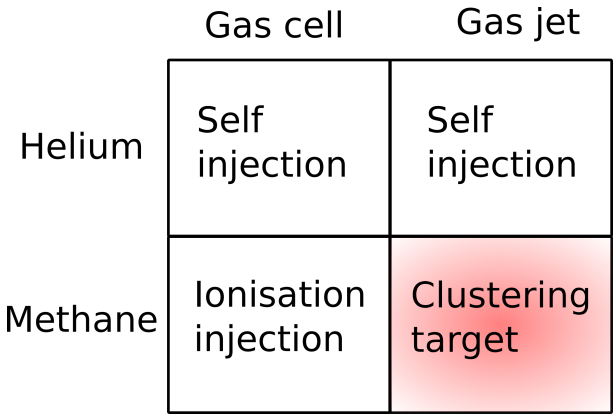


Figure 4.3: Matrix showing the different types of target examined in this chapter and their expected injection mechanism. The coloured target is the clustered target which we are comparing the other targets to.

Target parameters	Jet-CH_4	Cell-CH_4	Jet-He	Cell-He
Backing pressure [bar]	7-22	0.03-0.35	5-27	0.09-0.55
Electron number density [10^{18}cm^{-3}]	6-50	10-50	6-32	4-29
Length [mm]	5	4.4	3	2.8
Reduced Hagena parameter -Γ^*	4.4×10^4-1.2×10^5	N/A	N/A	N/A
Mean cluster size [No. of atoms]	1.8×10^5- 2.7×10^6	N/A	N/A	N/A

Table 4.3: Target parameters during TA2 experiment.

it is reasonable to assume that the clusters are still present when the main pulse arrives. In Figure 4.3, we outline the various combinations of targets used in this chapter.

The diagnostics used on this experiment can be broken into three distinct categories; optical diagnostics, forward transmitted diagnostics and particle diagnostics as is highlighted in the schematic diagram for this experiment in Figure 4.4.

Optical diagnostics

The optical diagnostics consisted of an interferometer and a shadowgraphy diagnostic. The interferometer is used for the measurement of averaged electron densities. The backing pressure of the target is also recorded using a pressure gauge. The backing pressure of the target can be correlated to the density measured using the interferometer to generate a density calibration for the target.

For data-sets missing interferometry data, the backing pressure is used to infer the elec-

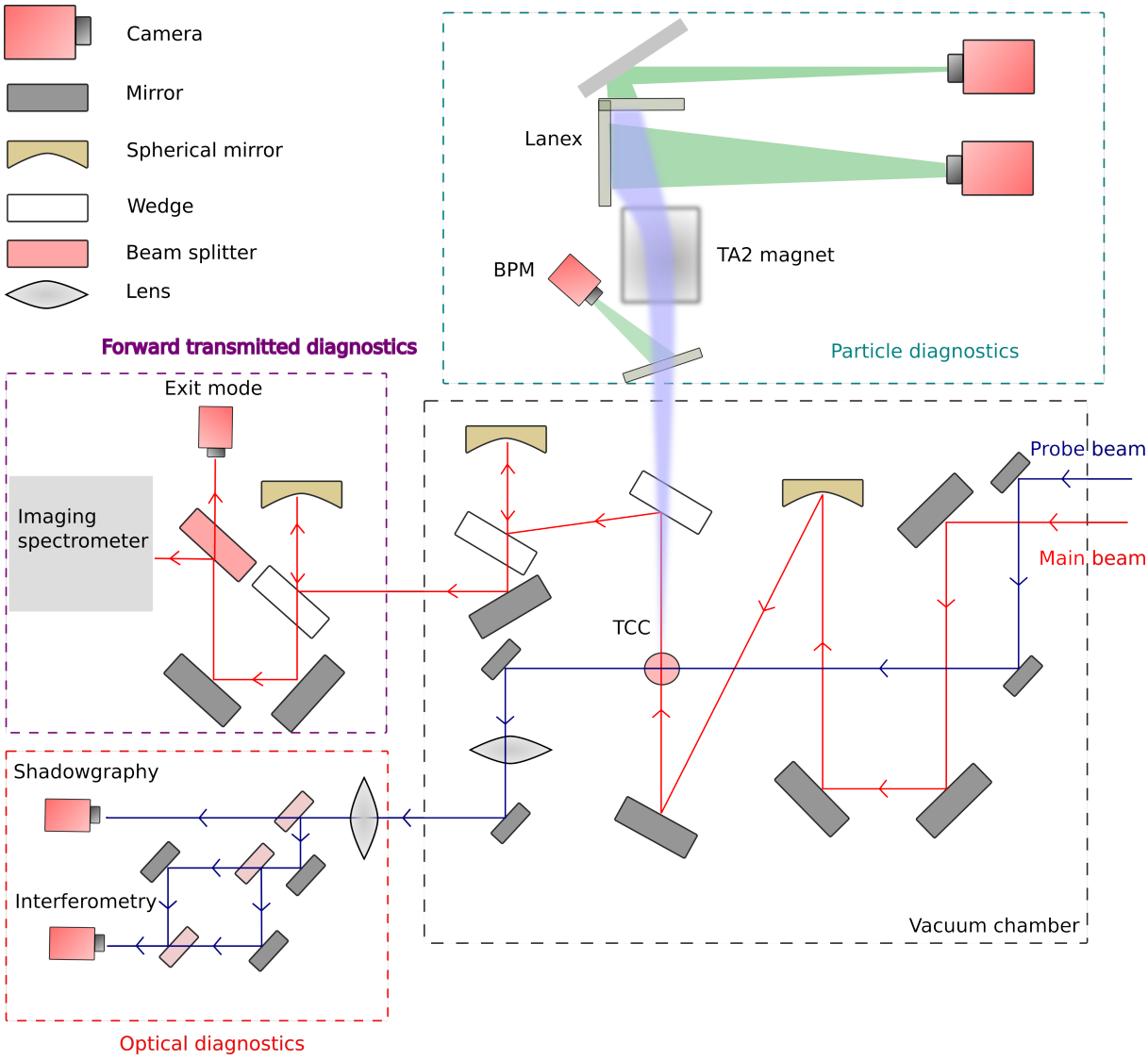


Figure 4.4: Schematic layout of the experiment performed in the TA2 chamber. TCC stands for target chamber centre, this is where the interaction occurs. The electron beam travels through a wedge with a hole in the centre and is analysed using the particle diagnostics.

tron density of the target. The forward transmitted diagnostics consisted of an exit mode diagnostic. A wedge was placed after TCC, with a hole which allows the electron beam to pass unperturbed, while collecting the majority of the forward transmitted light. The forward transmitted light is then imaged at the entrance slit of the imaging spectrometer to look at the spectrum of the forward transmitted beam.

Particle diagnostics

The particle diagnostics consist of three detectors; the electron beam profile monitor, low energy electron spectrometer ($10-45\,\mathrm{MeV}$) and high energy spectrometer ($45-300\,\mathrm{MeV}$).

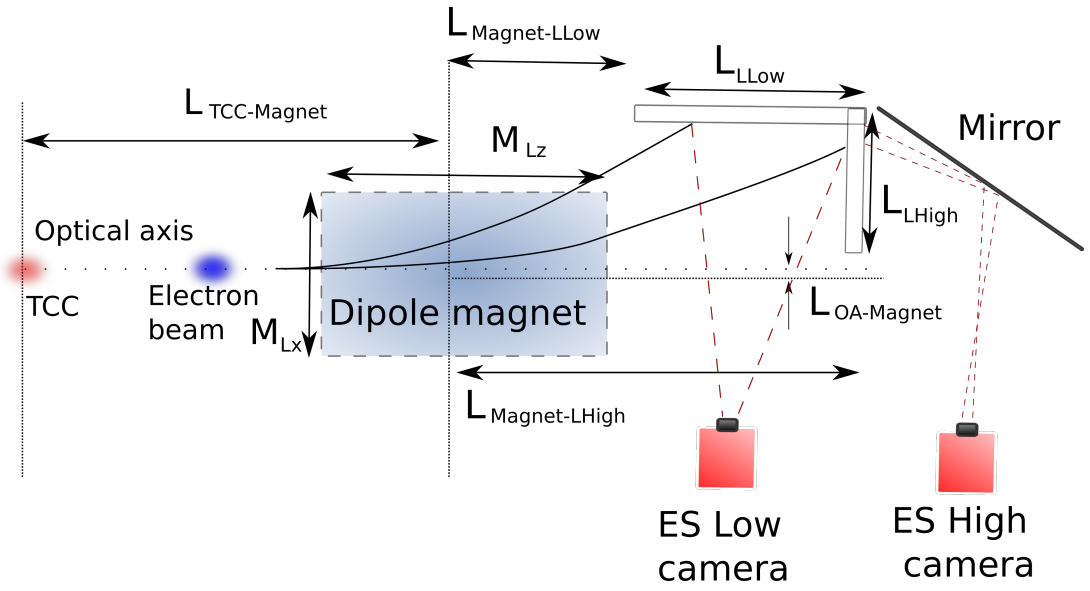


Figure 4.5: Illustration of the electron spectrometer diagnostic as viewed in the dispersion plane.

The magnet, used as part of this spectrometer, is a 0.4 T dipole magnet which dispersed the electron beam in the plane perpendicular to the polarisation plane of the main laser pulse. The spectrometer and beam profile diagnostics were contained in a lead enclosure to safely contain the electron beam and other sources of radiation.

In Figure 4.5 the layout of the electron spectrometer is outlined and the corresponding

Dimension	Value/mm	Description
M_{Lz}, M_{Lx}	150, 100	Length and width of the magnet
$L_{TCC-Magnet}$	852	Distance from TCC to magnet
$L_{OA-Magnet}$	5	Distance from the optical axis to the magnet center line
$L_{LLow,LHigh}$	300, 160	Length of the LANEX in the dispersion direction for the low and high energy spectrometer
$\theta_{OA-LLow,LHigh}$	0, 90	Angle between the optical axis and the respective LANEX screens
$L_{OA-LLow,LHigh}$	165, 165	Largest distance between the optical axis and the edge of the respective LANEX screens
$L_{Magnet-LLow,LHigh}$	153, 458	Distance from the midpoint of the magnet to the low energy edge of each respective LANEX screens
Peak B-field	0.4 T	Peak magnetic field of the magnet

Table 4.4: Revelant labelled dimensions of the electron spectrometer setup. All distances are in mm, with a measurement error of ±1 mm and angles in degrees. All distances from the magnet are relative to the midpoint of the magnet.

values for labelled dimensions is shown in Table 4.4. All distances are given in mm and all angles in degrees. The distance to the magnet is defined relative to the midpoint of the mapped field.

The beam profile diagnostic was combined with the electron spectrometer to correct the energy spectrum of the electron beam on every shot by correcting for the centroid pointing of the electron beam. While this mitigated any systematic errors due to pointing variations in the electron beam, the divergence of the beam combined with its distance from the source becomes the largest source of error in the energy axis at higher energies.

The relative error is defined as the uncertainty in the energy of the off-axis trajectories relative to the energy of trajectories on-axis. In Figure 4.6, the shaded error bar shows the uncertainty in the energy axis for a divergence of 10 mrad. We define the energy, at which the fractional uncertainty in energy $\sigma_{ES}(E)$, approaches 50%, as the energy that the electron spectrometer can resolve.

$$\begin{aligned} \sigma_{ES}(E) &= \frac{\sigma_E}{E} \\ E_{max,TA2} &= \sigma_{ES}^{-1}(0.5). \end{aligned} \tag{4.1}$$

From this, we obtain a threshold for the maximum energies that the spectrometer can resolve of 290 MeV. The analysis of the electron spectrometer diagnostic can be broken down into the following steps

1. **Image processing and background subtraction**
   Projective transformations [206] are used to correct the warping of the image. Rotations are applied to the image to align the image to the dispersion axis. Median filtering is used to remove hot pixel noise which arises from the camera being struck by stray high energy radiation inside the chamber. Background subtraction is performed, as the presence of high-energy electrons will cause the generation of secondary radiation which activates the LANEX.

2. **Feature extraction**
   From the resulting spectrum, we determine various parameters such as the maximum energy which corresponds to the energy at which the charge is 3σ from the background level. The peak energy/full-width half maximum is extracted using a local peak finding algorithm in MATLAB [207]. Charge is obtained by performing calibration shots using IP and LANEX simultaneously. The integrated charge from the image plate then provides a calibration value for the counts observed on the LANEX screen which can be converted into charge.

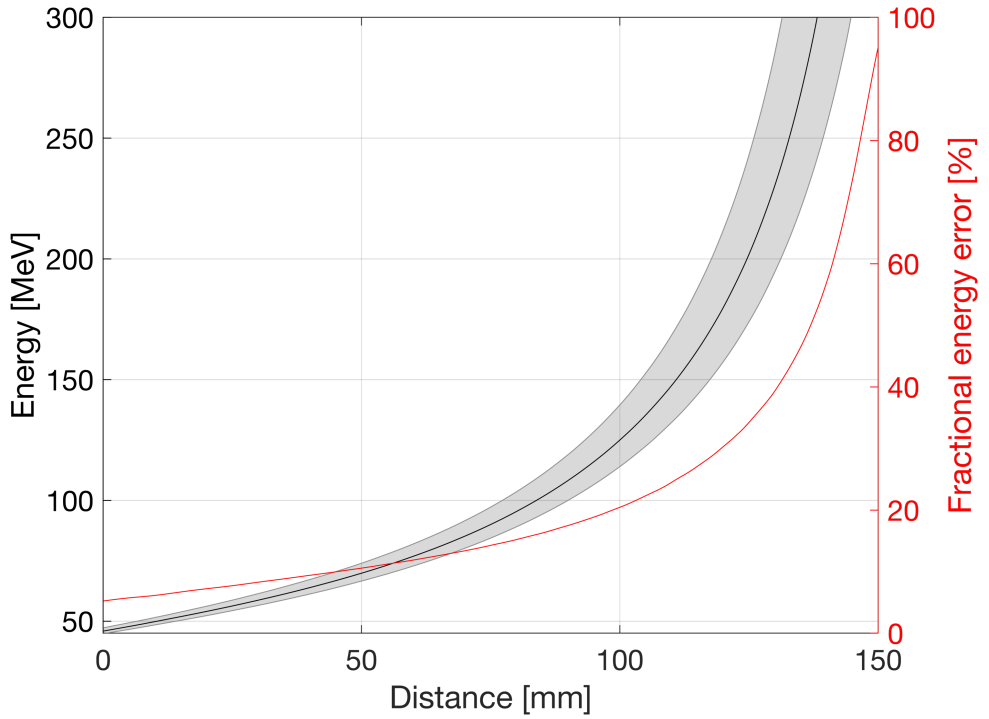


Figure 4.6: The left hand axis shows the energy of the electron beam as a function of distance from the edge of the scintillator. The right hand axis shows the fractional error in energy, arising from a 10 mrad uncertainty in the pointing of the electron beam.

The beam profile diagnostic consists of a sheet of LANEX in the path of the electron beam. This scintillator is imaged off-axis to avoid the electron beam colliding with the camera. The camera was also angled so as to avoid the focal plane varying along the plane of the scintillator.

The resolution of the imaging system was estimated using a resolution grid to be 12 µm. However, the resolution of the scintillator is typically ≈ 100 µm [168, p.202] by the grain size of the scintillator and this is the dominant error in the estimate of the spatial properties of the electron beam. The analysis is summarised into the following steps:

1. **Image processing and background subtraction**
   Projective transformations are used to correct the warping of the image due to camera alignment. Median filtering is used to remove hot pixel noise from the stray radiation. Background subtraction is also performed using the portion of LANEX not struck by the electron beam.

2. **Feature extraction**
   The features of interest for this diagnostic are primarily the beam divergence, beam centeroid and the charge. An ellipsoidal fit was used to extract the beam waist from the 50 % full width half maximum contour of each shot. The ellipse allows one to

determine the rotation angle to see if the beam is preferentially more divergent in one axis.

These steps are shown in Figure 4.7 for one particular electron beam shot. Figure 4.7a depicts the raw image seen on the CCD, Figure 4.7b has undergone projective transformations and been cropped. In Figure 4.7c, we can see the position of the laser axis using the low energy mode of the laser facility.

The laser pulse is visible through the LANEX screen and in Figure 4.7d, we plot the lineout of the beam profile at the centeroid of the beam. For this particular beam we can see that its divergence, in the axis parallel to the laser polarisation direction (Y), is higher that the divergence in the axis perpendicular to the laser polarisation axis (X). This particular image also has an offset between the electron beam and the laser pulse of $(3.4, 1.9) \pm 0.1$mm in the (X,Y) directions respectively.

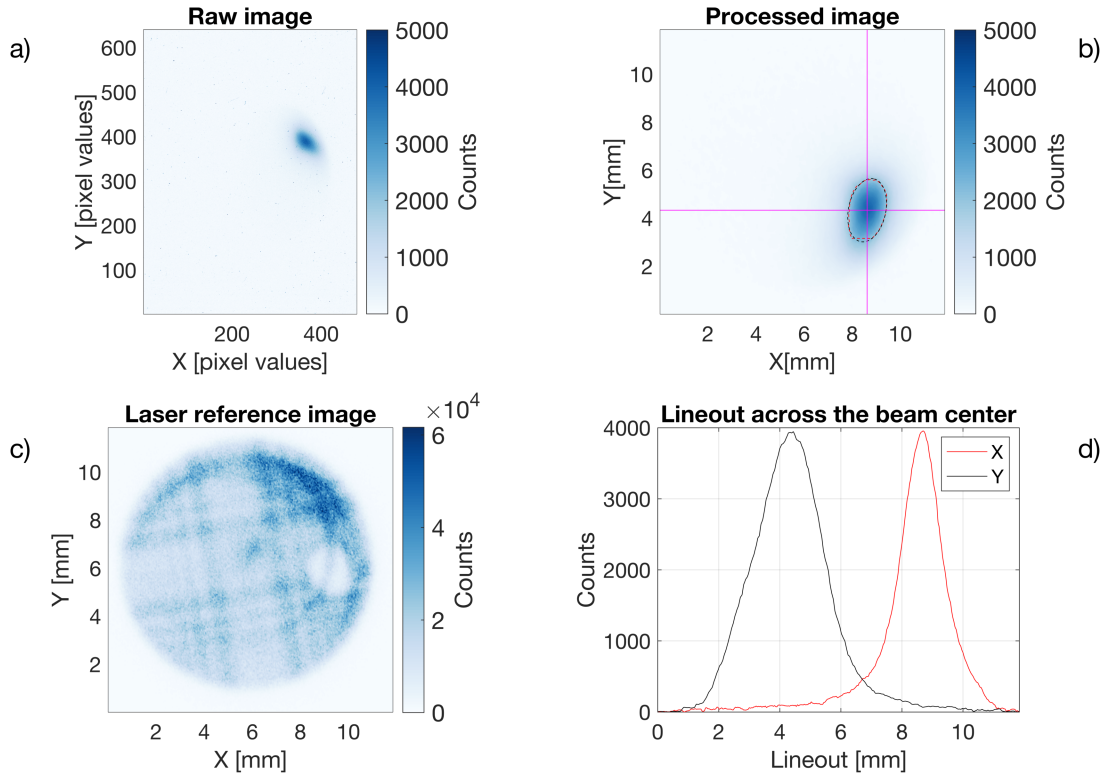
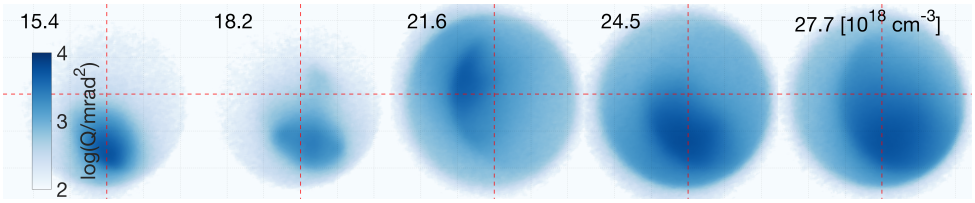


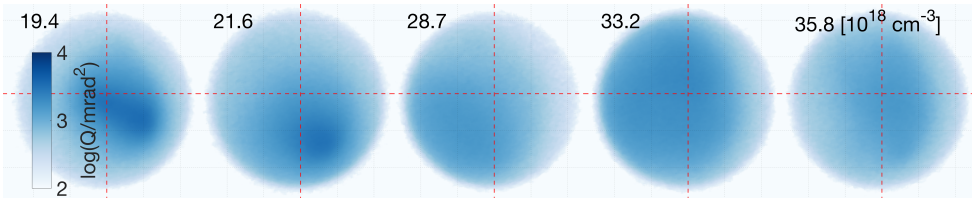
Figure 4.7: The steps taken in the analysis of the beam profile diagnostic. In panel a) the raw data from the electron beam profile diagnostic is shown. In panel b) the image is warped to account for angled viewing. In panel c) the laser is incident upon the LANEX screen. The diffraction cross is from an alignment crosshair in the main beam. The hole in the beam arises from a pickoff in the compressor chamber to measure the pulse duration of the main laser pulse. Panel d) shows lineouts through the center of the beam along the x and y axes.

4.3 Results

The backing pressure was varied for each target (referred to as a density scan) and the charge and spectrum of the electron beam recorded. In Figure 4.8, we show the raw data from the beam profile diagnostic over a range of electron number densities. We see that electron beams have higher charge in the clustered than the non-clustered case. For the lower density cluster case ($n_e = 1.5 \times 10^{19}\,\mathrm{cm}^{-3}$), the beams are more collimated than

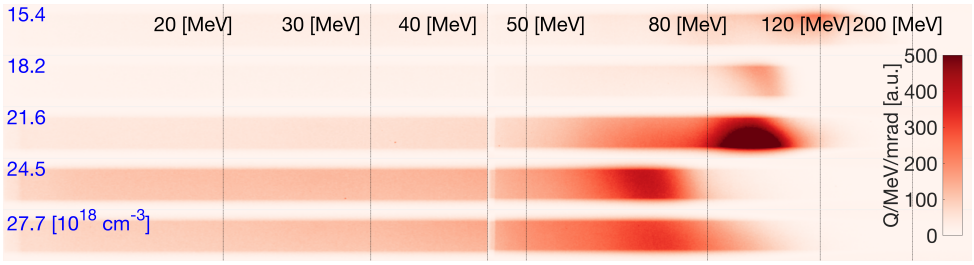


(a) Methane gas jet: Cluster injection

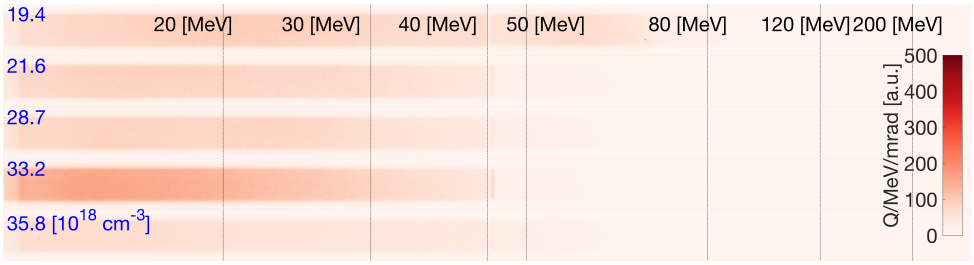


(b) Methane gas cell: Ionisation-injection

Figure 4.8: Raw data from the beam profile diagnostic. Five shots are chosen such that they are evenly spaced in electron number density. Panel a) is the data from methane in a gas jet and panel b) is from methane in a gas cell. The red line represents the position of the laser pulse in vacuum.



(a) Methane gas jet: Cluster injection



(b) Methane gas cell: Ionisation-injection

Figure 4.9: Raw data from both electron spectrometers for various densities. Panel a) is the data from methane in a gas jet and panel b) is from methane in a gas cell.

higher density ($n_e = 2.9 \times 10^{19}\,\mathrm{cm}^{-3}$). The beam profile monitor does not linearly map to charge as lower energy electron beams will cause LANEX to scintillate more than higher energy electrons. Not all the forward going radiation will be from the accelerated electron beam, this makes it difficult to determine absolute charge using this diagnostic, instead the high energy electron spectrometer is used for the measurement of beam charge. The pointing variation of the electron beam coupled with the narrow acceptance of the electron spectrometer will result in the charge between individual shots to vary. This variation is mitigated by splitting the data-set into bins of equal density and averaging measurements for each bin. We can see the effect of the narrow acceptance angle in Figure 4.9a for an electron density of $2.16 \times 10^{19}\,\mathrm{cm}^{-3}$

In Figure 4.9, raw data from both electron spectrometers are stacked side by side to show the charge and spectrum from 10 MeV-200 MeV. We can see that the electron beams in the clustered case go to higher energies than the non-clustered case. The presence of clusters not only influences the charge, but also the shape of the energy spectrum.

Charge

We begin by examining the beam charge, as observed on the high energy electron spectrometer $Q > 45\,\mathrm{MeV}$, in Figure 4.10. The dataset is split into bins of equal separation. Shots which fall into a particular density bin are averaged and the mean value is plotted in Figure 4.10. The error-bars represent the error on the mean for each density bin. Two combinations of targets (gas jet and gas cells), were examined with two different gases (helium and methane), where it was noted that methane in a gas jet will form clusters under these gas jet parameters.

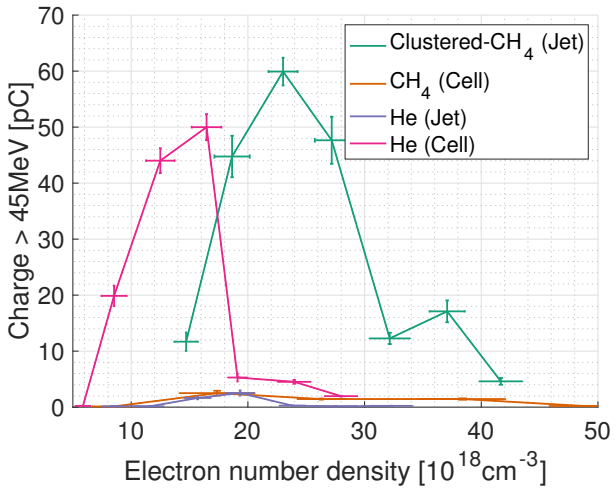


Figure 4.10: The charge observed on the electron spectrometer for a range of densities for helium and methane in a gas jet and gas cell.

The electron beam with the highest value of charge, across the various targets, was observed for the clustered target, where beam charge of $60.0 \pm 2.5\,\mathrm{pC}$ was measured at an electron density of $2.30 \pm 0.12 \times 10^{19}\mathrm{cm}^{-3}$. Methane in a gas cell was measured to have much less beam charge, with a maximum of $2.5 \pm 0.4\,\mathrm{pC}$ at an electron density of $1.93 \pm 0.12 \times 10^{19}\mathrm{cm}^{-3}$. For helium, the expected modality of injection was by self-injection (SI), where in the gas cell we observed a maximum beam charge, across the range of densities sampled of $50.0 \pm 2.3\,\mathrm{pC}$. For helium in a gas jet, we observed maximum beam charges of $2.5 \pm 0.5\,\mathrm{pC}$ at a density of $1.93 \pm 0.12 \times 10^{19}\mathrm{cm}^{-3}$. The electron density required for injection for the clustered case was greater than SI across a large range of densities, with its optimum density for charge occurring at a higher value. We now move onto addressing the maximum energy of the electron beams generated for these different targets.

Maximum energy

The maximum energy was extracted by looking at the point at which the cumulative charge as a function of energy, approaches 3σ of its maximum value. Data is sorted into equal intervals of density, where all data points which fall into a particular density bin are averaged. The error on the mean was used as the uncertainty gathered from the variation in these points. The mean value was plotted in Figure 4.11 as a function of density for various target configurations. We have excluded shots where the charge of the electron

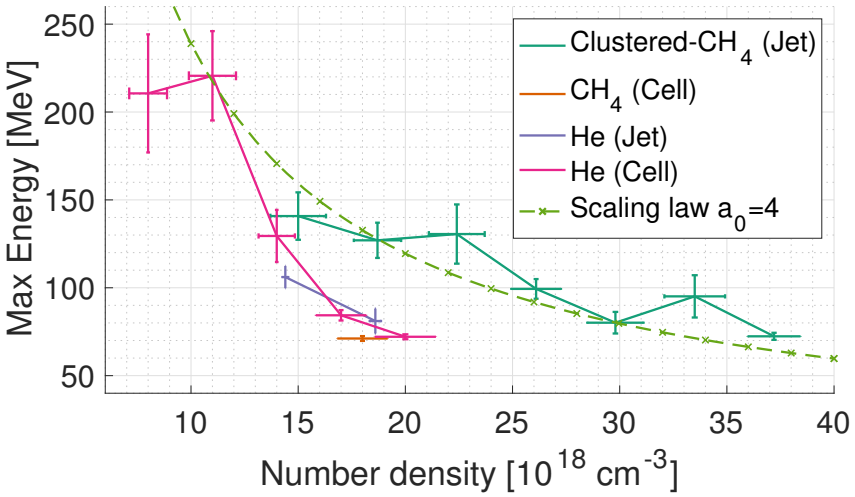


Figure 4.11: The maximum energy of the electron beam spectrum as a function of the number density. Red represents the clustered medium (gas jet) and blue represents the non-clustered medium (gas cell). The scaling law used in this figure is the energy gain equation $W[MeV] = a_0 m_e[MeV]\frac{2n_c}{3n_e}$

beam was less than 0.5 pC as the noise dominates the measurement of maximum energy for these values.

In Figure 4.11, we see that the highest energy electrons are generated by self-injection with helium in a gas cell, where electron beam energies of 221 ± 25 MeV were measured at electron densities of $1.28 \pm 0.09 \times 10^{19}\text{cm}^{-3}$. For cluster injection, we observed maximum beam energies of 141 ± 13 MeV at a density of $1.67 \pm 0.01 \times 10^{19}\text{cm}^{-3}$. For helium in the equivalent gas jet, we obtained a maximum beam energy of 106 ± 6 MeV at a density of $1.46 \pm 0.02 \times 10^{19}\text{cm}^{-3}$. Finally, for methane in a gas cell, we obtained a maximum beam energy of 71 ± 1 MeV at an electron density of $1.94 \pm 0.01 \times 10^{19}\text{cm}^{-3}$.

Electron beams were observed over a greater range of densities for cluster injection $1.67 \times 10^{19}\,\text{cm}^{-3} - 3.95 \times 10^{19}\,\text{cm}^{-3}$, than self-injection in a gas cell $9.5 \times 10^{18}\,\text{cm}^{-3} - 2.74 \times 10^{19}\,\text{cm}^{-3}$. The threshold density at which we being seeing injection was lower for self injection in a gas cell than cluster injection. We now move onto examining the spatial properties of the electron beam, in-particular the beam divergence as measured on the beam profile monitor.

Beam divergence

The divergence of the electron beam was measured on the beam profile diagnostic. First, the contour points representing the full-width half-maximum was extracted. Then, a least square fit was performed using an ellipse to these contour points [208] and the long and short axis of the ellipse was extracted. These quantities are plotted as a function of density in Figure 4.12 for helium and methane in both a gas jet and a gas cell.

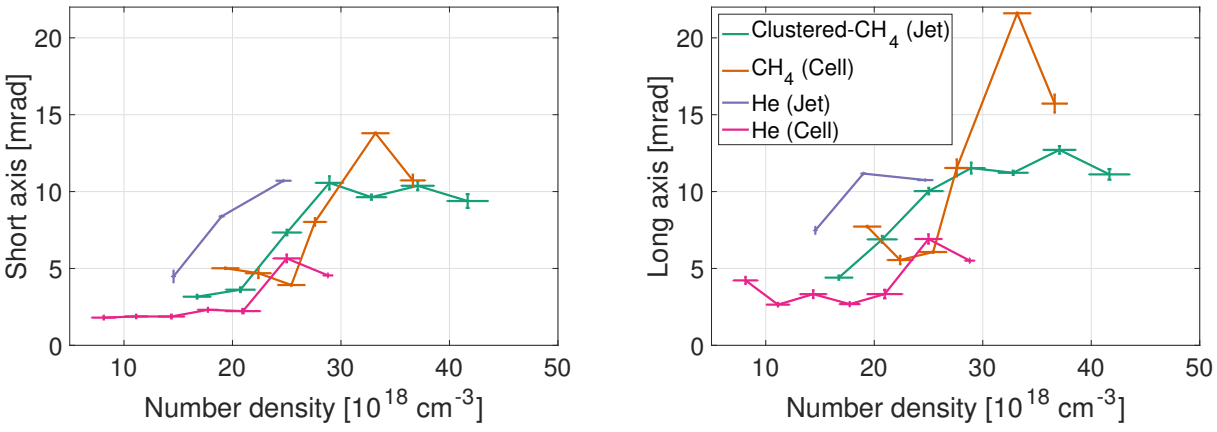


Figure 4.12: Figure showing the long axis and short axis beam divergence observed on the beam profile monitor for various targets.

From Figure 4.12, we can see that the lowest divergence electron beams were generated for helium in a gas cell. For this target, the lowest measured beam divergence value was 1.6 ± 0.1 mrad at an electron density of $8.4 \pm 0.1 \times 10^{18} \mathrm{cm}^{-3}$. Helium in a gas jet had a minimum beam divergence of 2.4 ± 0.1 mrad at an electron density of $2.07 \pm 0.08 \times 10^{19} \mathrm{cm}^{-3}$. The target with the next lowest beam divergence was methane in a gas jet, where electron beams with a divergence of 3.2 ± 0.1 mrad were measured at an electron density of $1.71 \pm 0.10 \times 10^{19} \mathrm{cm}^{-3}$. Finally, the lowest beam divergence attained by methane in a gas cell was 3.9 ± 0.1 mrad at an electron density of $3.3 \pm 0.2 \times 10^{19} \mathrm{cm}^{-3}$.

We also see that the long axis divergence of electron beams are appreciably larger than their short axis, suggesting that all injection mechanism can generate eccentric electron beams. Methane in a gas cell reaches the largest beam divergences of all the targets examined. The fast variation in beam divergence which occurs at the highest density is attributed to a low sample size for the bin. This causes outlier data-points to dominate the mean value for the beam divergence of this density bin.

In the next section, using particle-in-cell codes, we will simulate the interaction of the clustered medium with the laser pulse to understand how wake formation, injection and acceleration of electron beams occur in such a non-uniform medium.

4.4 Simulations: Clustered medium vs un-clustered medium

Motivation

In the previous section, results from a wakefield acceleration experiment in a clustered medium were presented. The plasma density of the target was varied and properties of the electron beam such as beam charge, maximum energy and divergence were extracted. Four different types of interaction were presented; methane in a gas jet, methane in a gas cell, helium in a gas jet and helium in a gas cell. Helium in both gas cells and gas jets are well explored in literature [121, 209]. The only way to inject particles into the accelerator when using helium is by wave-breaking and is called self-injection [210] (SI). We use the helium data set as a control to include the influence of different targets towards the observed electron beam properties. Methane in a gas jet has been reported in literature [204] to cluster and in this simulation section we will address some questions pertaining to wakefield acceleration in such a media.

There are many unknowns from this interaction, for example, what does the wakefield look like for such a medium? How are electron injected into the wakefield? From the results section, we have already seen that the clustered target generates the highest charge electron beams, 20% greater than helium in a gas cell and 24 times greater than methane in a gas cell or helium in a gas jet. The discrepancy between gas cells and gas jets has been reported in literature [121] and is likely to arises from non-uniformities in the density profile which results in lower electron beam charge. The non-uniformities arise from manufacturing defects in gas jets. For the clustered case, however, we see the opposite trend where it is the gas jet which generates beams of greater charge. The fine structure of the density profile was not measured on this experiment, instead we will assume a flat density profile.

This chapter will compare, a high resolution simulation at equivalent average electron densities, for the interaction between the laser pulse with a clustered medium and a medium utilising ionisation injection for electron acceleration. The purpose of this simulation, is to gain insight into the wake formation and the energies predicted by the interaction.

Simulation setup

Particle-in-cell simulation were performed using SMILEI [2] in the 2D-3V geometry. Two simulations were performed; one with a clustered medium and one for ionisation injection using carbon and ion as the injection species. We assume that the inner shell electrons of carbon up-to C^{4+} are ionised for the uniform ionisation injection simulation as they are fully ionised before the peak of the laser pulse. For the clustered medium, there are three particle species; the background electrons, the electrons from the cluster and the ions from the cluster.

For simplicity, we have assumed that the atomic species in the clustered medium are fully ionised. This assumption is validated by the fact that clusters absorb energy significantly more efficiently than an underdense atomic medium. Alongside tunnel ionisation, collisional ionisation [93, 95] will act to liberate all the electrons bound in the atomic energy levels to generate hot plasma in the pre-pulse of the laser. We have also assumed that all the clusters have hydrogen as the ionic species making up the cluster. Additionally, the medium is split into two components; an unclustered portion and a clustered portion. The fraction of atoms in the cluster phase, f_{cl} is assumed to be 0.25 [90, 91] as this is reported in literature for similar gas jet parameters. Hence, the density of the background electrons is the average electron density multiplied by (1-f_{cl}).

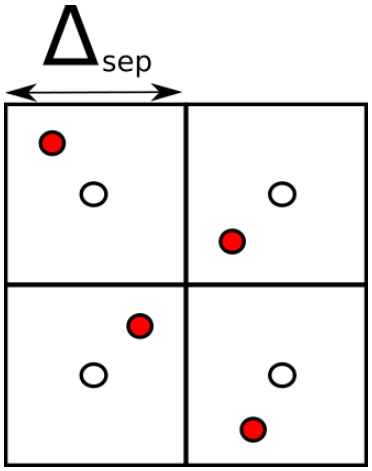


Figure 4.13: Diagram showing how the clusters are randomly spaced. Δ_{sep} is the average separation between clusters. The white circles are the centres of the clusters and the red circles shown how they are randomly placed about this point.

For the background electrons, we have assumed that immobile ions provide the charge neutralising force for the plasma. However, for the clusters, the ion species was assumed to be mobile. This mobility allows the cluster to undergo Coulomb explosions within the moving window of the simulations.

Clusters were modelled as a small ionised Gaussian modulation, randomly spaced across the simulation grid at 10% of the mean cluster spacing, with a peak density of $5n_c$. The separation between each cluster was determined by imposing the condition that in each cluster grid, the average density must be equal to the total average electron density. As this is a 2D simulation, the cluster expands as a cylindrical rod and we need to ensure the average density in a square is matched. Consider,

$$\int \int_{-\Delta_{sep}/2}^{\Delta_{sep}/2} n_{cl,peak} \exp\left[\frac{-((x-x_{0,cl})^2+(y-y_{0,cl})^2)}{\sigma_{cl}^2}\right] \mathrm{d}x\,\mathrm{d}y \approx n_{cl,peak}\pi\sigma_{cl}^2 \tag{4.2}$$

this is a reasonable assumption if $\Delta_{sep} \gg \sigma_{cl}$. Hence, we can relate this to the average cluster density as

$$\Delta_{sep} = \sigma_{cl}\sqrt{\frac{n_{e,cl}\pi}{n_e f_{cl}}}, \tag{4.3}$$

for an electron density of $n_e = 2.77 \times 10^{19}\,\mathrm{cm}^{-3}$ and $f_{cl} = 0.25$, we obtain $\Delta_{sep} = 2\,\mu\mathrm{m}$. The cluster is assumed to be pre-expanded to $5n_c$, where this pre-expansion is attributed to the prepulse heating up the cluster. The reason for choosing $5n_c$ is because as the cluster interacts with the laser pulse its average density will drop and go through the resonance density of a spherical cluster, $3n_c$ [101]. This allows us to capture phenomena which occur at these densities such as the transient beam self-focussing [104]. Finally,

Variable	Value	Variable	Value
dx	4.0 nm	dy	6.4 nm
no. cells x	13824	no. cells y	14336
Window length x	53 µm	Window length y	90 µm
a_0	1.13	Spot size	18 µm
Laser wavelength	800 nm	Pulse duration	45 fs
Total electron density	$2.77 \times 10^{19}\text{cm}^{-3}$	Unclustered fraction	0.75
Peak cluster density	$5n_c$	Cluster size	32 nm

Table 4.5: Input parameters of the simulation, where dx, dy are the sizes of the cells of the simulation in the x, y direction.

we determine the expanded cluster radius r_f by considering a spherical redistribution of mass from a cluster which has an initial radius of r_i and initial density of n_i,

$$r_f = r_i \left(\frac{n_i}{n_f} \right)^{1/3}, \tag{4.4}$$

where n_f is the final cluster density. The size of the cluster is not the primary uncertainty but rather the cluster fraction, also expressed as condensation rate η and dryness degree β. This is the fraction of atoms in the cluster phase and has been shown to not be strongly correlated to properties of the jet [89].

The main parameters of the simulation are shown in Table 4.5. The distribution of the range of sizes of clusters in such a medium takes a log-normal functional form with a width equivalent to the number of clusters. The effect of the range of cluster size is expected to be small as the radius of the cluster scales with $r \propto N_{cl}^{1/3}$. Given that these clusters are expanding rapidly, the variation in number of atoms in a cluster is expected to have a small impact on the simulation.

Simulation results

In Figure 4.14, we can see a snapshot of the electron density on the simulation grid at a given instant in time for (a) clustered plasma and (b) unclustered plasma. The plasma wave structure in a clustered plasma is formed primarily by the background electrons arising from the unclustered part of the medium. The uniform spatial distribution of ions is needed to generate the space charge force necessary to set up the wakefield.

We notice that even though the electrons are momentarily ejected from clusters by the laser pulse, the ions move much more slowly, and so the background electrons which are

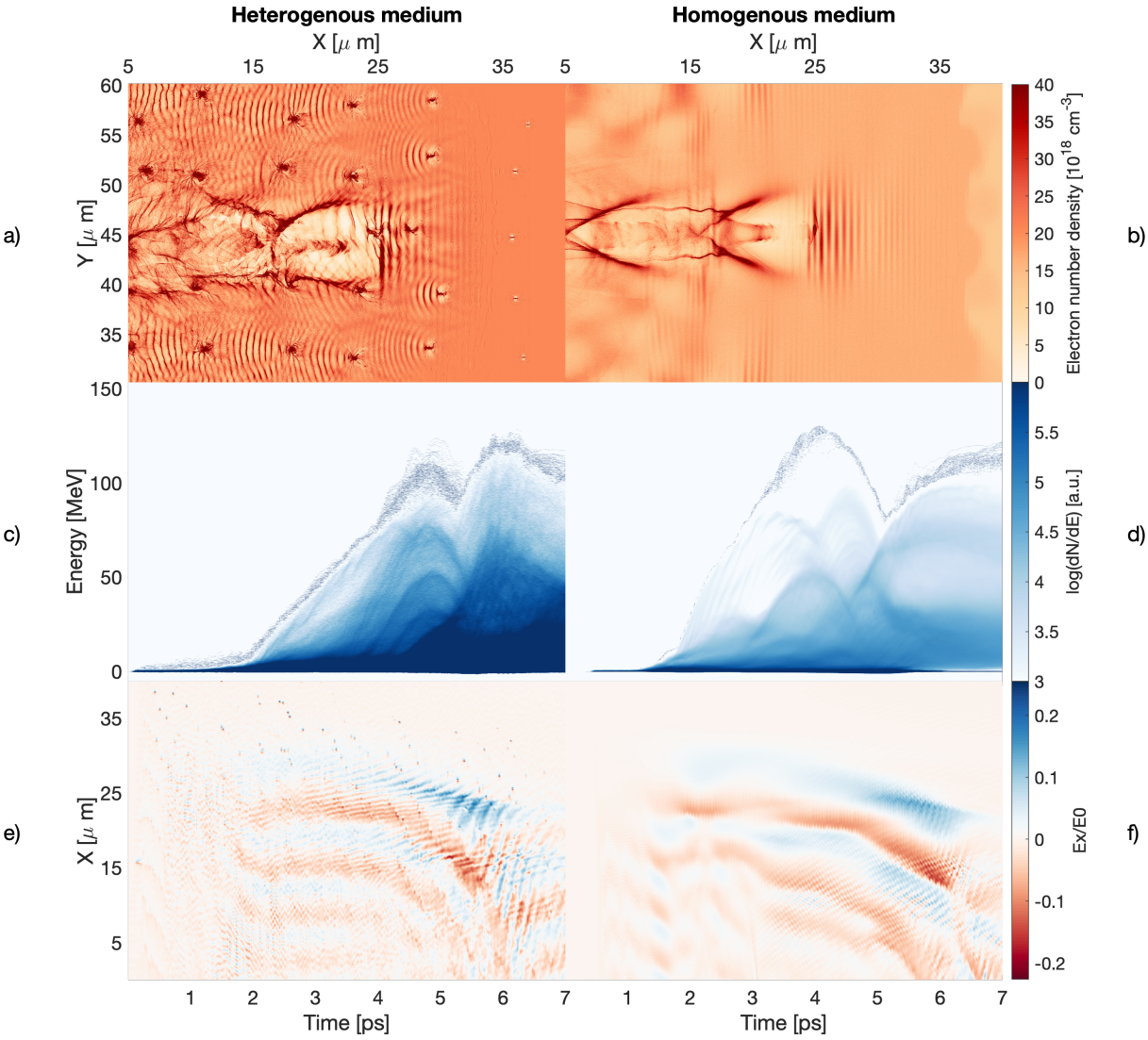


Figure 4.14: Simulation comparing the two scenarios for an average electron density of $2.77 \times 10^{19}\,\mathrm{cm}^{-3}$. The left hand side panels are for the clustered medium and the right hand side panel is for the un-clustered medium. Panels a) and b) show the electron density as a function of space. Panels b) and c) show the evolution of the energy of the particles for different timesteps. Panels e) and f) show the evolution of the amplitude of the wakefield, along the axis of the wakefield for different timesteps.

part of the unclustered plasma are drawn to these cluster cores. As the ion density of the cluster is much greater than the ion density of the uniform background ions, which we recall are assumed to be immobile, the background electrons effectively replace the electrons which were initially present in the cluster. This is evident in Figure 4.14a by the build up of electrons near these cluster cores.

We also observe that there are modulations in the electron density behind the cluster core. This is attributed to the laser pulse being scattered by near the solid electron density

population near these clusters. The superposition between the scattered pulse and the incoming pulse sets up a standing wave structure, in the electron density map in Figure 4.14a, clearly visible behind, but not ahead of the clusters.

In Figure 4.14c and d, we can see the momentum history of the injected particles. Each vertical slice of this image is the distribution of energies of the electrons in the simulation. We observe greater charge in the clustered case than the non-clustered case but not at the observed energies. These simulations do not predict the discrepancy observed in experimental data where the clustered medium generates over an order of magnitude greater charge than the unclustered simulation. One limitation of these simulations is that their 2D nature does not capture the effects of self-focussing accurately and the cluster expansion is limited to 2 dimensions. In these simulations, the cluster expands cylindrically. This would cause clusters to expand slower, and hold on to more charge against the potential of the wakefield.

Finally in Figure 4.14e and f, we can see that the plasma wave, in both scenarios, follow approximately the same behaviour. There are some modulations in the field of the plasma wave, which can also be seen in the density plots, corresponding to filaments of density across the top and bottom of the plasma wave structure. This is attributed to the electric field of the cluster superimposing on the the field of the wake to create a modulated electric field longitudinally.

4.5 Discussion

In the previous sections, we have presented data investigating the properties of a wakefield accelerator in a clustered medium. Methane and helium targets were explored in both a gas jet and a gas cell. Helium is used as the control gas medium to ensure that the observed effects are not due to features of the targetry. Of the four combinations of gas/targets, we have three different types of injection mechanisms. Helium in a gas cell and gas jet injects particles into the wakefield by self-injection, methane in a gas cell will inject particles into the wake by ionisation injection. The inner shell electrons of carbon will delay the injection such that they are born later with a lower longitudinal momentum than the particles which form the bulk of the wake, which allows them to be trapped and injected.

Finally, methane in a gas jet, will form clusters for the present jet parameters. The particles trapped in the spherical nanoplasma that forms when a cluster ionises will facilitate injection into the wake. The cluster acts to delay the ejection of electrons when

it interacts with the laser pulse, much like ionisation injection, except that much more charge is available for injection.

In this section, we begin by presenting the main data-sets for the various electron beam parameters; charge, maximum energy and beam divergence for all 4 target configuration. We comment on the implications of this data and refer to the simulation data where relevant.

Charge

For methane in a gas jet, the highest beam charge we observe is $60.0 \pm 2.5\,\mathrm{pC}$ at a density of $2.3 \pm 0.1 \times 10^{19}\mathrm{cm}^{-3}$. One question which arises from this data set is why the optimum density of total beam charge occurs at a value of $n_e = 2 \times 10^{19}\,\mathrm{cm}^{-3}$. Consider the matched a_0 for this density,

$$a_{0,m} = \left(\frac{w_{0,vac} a_{0,vac} \omega_p}{2c} \right)^{2/3}, \tag{4.5}$$

where $w_{0,vac} = 18\,\mu\mathrm{m}$ and $a_{0,vac} = 0.6$, where we obtain an $a_{0,m} = 3.1$. Hence, we expect to be driving a non-linear wake at this point. Using the expression for the optimal beam loading limit from Lu et al [135],

$$N = 2.5 \times 10^9 \frac{\lambda_\mu}{0.8} \sqrt{\frac{P_{\mathrm{TW}}}{100}}, \tag{4.6}$$

where $\lambda_\mu = 0.8$ and $P_{\mathrm{TW}} = 10$, we obtain $N_{pC,opt} = 126\,\mathrm{pC}$ from 3D non-linear theory. This suggests that we are at $\approx 48\%$ of the highest charge we can accelerate for these parameters. For helium in a gas cell, we obtain a maximum beam charge of $50.0 \pm 2.3\,\mathrm{pC}$, at a density of $1.65 \pm 0.13 \times 10^{19}\mathrm{cm}^{-3}$. The higher charge in the cluster case could be a result of the lowering of the injection threshold and the continuous nature of injection. The accelerator will keep on injecting in the cluster case until the onset of beam loading. We notice that the density at which the highest beam charge is observed for cluster injection is much higher than for self-injection. Varying the density will also increase the average size of clusters. We recall that the Hagena scaling laws [88] predict the relationship between number of atoms in a cluster and the backing pressure as $N_{cl} \propto P^{4.7}$. Pressure is linearly dependant on the average electron number density This gives us a rough estimate for the cluster size as a function of density $r_{cl} \propto n_e^{1.6}$. The wake will begin trapping stationary electrons once the amplitude of the wake is large enough. This scaling for cluster size with densities suggests that for higher densities we will reach the beam-loading threshold more quickly.

We recall from the simulation section in Figure 4.14 on p.116 that we had to assume some fraction of the medium to be unclustered as it was the unclustered part of the medium which supports the space charge force needed to support a wakefield. If we assume the pulse evolution is identical for both scenarios, this might indicate that the unclustered density is similar for the cluster injection and the self-injection case. Under this argument, we would obtain a $f_{cl} = 0.28$, which is not too dissimilar from what we assumed for our simulations or measurements from literature. However, for absolute certainty we would have to measure this quantity on-shot to know conclusive. One way in which this measurement could be performed would be through the use of few-femtosecond shadowgraphy to map out the wakefield modulation [211]. This would be a direct indicator of the local plasma wavelength and combining this measurement with the average electron density of the medium will allow the cluster fraction to be extracted.

We move on to helium in a gas jet and methane in a gas cell where the maximum charge observed is 2.55 pC at densities of $1.93 \pm 0.12 \times 10^{19}\text{cm}^{-3}$ and $1.74 \pm 0.13 \times 10^{19}\text{cm}^{-3}$ respectively. For gas jets, density gradients allow spurious wave-breaking events along the length of the accelerator [121]. These small scale density gradients arise from imperfections in the longitudinal density profile from manufacturing defects in gas jets. This is one possible reason for the significantly lower charge for electron beams generated using self-injection in a gas jet. The advantage that cluster injection brings here is that even if large density transitions cause a loss of beam charge from the accelerator cavity, once the laser pulse has passed the density transition, it can inject charge at a later point in its evolution due to the continuous nature of the injection mechanism and lower injection threshold.

For methane in a gas cell, we would also expect a lower injection threshold when compared to self-injection and so it is rather surprising that we similarly observe extremely low charge in this scenario. We know that the lack of charge is not a facet of the targetry as helium in the very same cell at the identical length generates 20 times more charge. Instead, we recall the discussions about ionisation defocussing [212]. This is where an ionisation front in the medium causes the pulse to experience defocussing effects. The threshold density at which this occurs was calculated earlier to be $5 \times 10^{18}\,\text{cm}^{-3}$. We know that for these highly mismatched parameters where $w_0 = 18\,\mu\text{m}$, and the spot size needed to drive a wakefield strong enough to trap the stationary ions from ionisation injection $a_0 > 1.6$ is much lower than this. Consider the definition of a_0, rearranged to

extract the spot size for $a_{0,II} = 1.6$,

$$w_0 = \sqrt{\frac{7.29 \times 10^{-11} \lambda_\mu^2 P_{TW}}{\pi a_{0,II}}}, \tag{4.7}$$

where λ_μ is the laser wavelength in micrometers, P_{TW} is the peak power of the laser pulse in TW, resulting in an injection spot size of $w_{0,inj} = 7.6\,\mu\text{m}$. Hence, by defocussing the laser pulse, the a_0 can drop below the threshold for injection. This is attributed to the difference in focusing of laser pulses in 2D compared to 3D. Simulations need to be performed in cylindrical geometry or 3D to determine the extent of the defocussing force on the laser pulse. We now move on to addressing the maximum energies obtained by these various targets.

Maximum energy

Using the electron spectrometer, we can extract the maximum energy for the various target configurations. The maximum energy is defined as the energy at which the cumulative charge reaches 3σ of its maximum value. The highest energy electron beams were observed for helium in a gas cell, where maximum energies of $221 \pm 25\,\text{MeV}$ were measured at a density of $1.28 \pm 0.10 \times 10^{19}\text{cm}^{-3}$. The clustered case, comparatively generates much lower energy electron beams, with maximum energies of $141 \pm 13\,\text{MeV}$ at a density of $1.67 \pm 0.13 \times 10^{19}\text{cm}^{-3}$. Cluster injection generates electron beams with 35% lower maximum energies than self-injection in a gas cell.

For helium in a gas jet, where self-injection is again the main method of injection, we measured a maximum electron beam energy of $106 \pm 6\,\text{MeV}$ at a density of $1.46 \pm 0.18 \times 10^{19}\text{cm}^{-3}$. One possible explanation for the energies being much lower than the gas cell, using self-injection, could be due to the scale length of the density modulations along the interaction as suggested earlier.

Propagating the laser pulse through many density modulations could diffract the energy away from pulse, reducing the self-focussed a_0 that is attained at the lower densities. Hence, injection is only possible when we are at a significantly higher density that the critical threshold for self-injection.

Finally, we consider the maximum energy attained for methane in a gas cell, where we achieve $71 \pm 1\,\text{MeV}$ at a density of $1.94 \pm 0.12 \times 10^{19}\text{cm}^{-3}$. In the discussion for beam charge, we have discussed how the ionisation defocussing effect can result in a reduced peak a_0 of the interaction. The consequence of this can be seen in the energies of the elec-

tron beam being much lower than all other target configuration. We only begin observing charge for extremely high densities $1.94 \pm 0.12 \times 10^{19}\text{cm}^{-3}$, which suggests that the peak a_0 of the interaction must only just be exceeding the threshold for injection with ionisation.

We know that the laser pulse evolves towards its matched spot size given by Eq. 4.5. For this density, $a_{0,m} = 2.9$. Instead, the onset of injection would suggest that the $a_0 \approx 1.6$. If we assume the a_0 corresponding to the matched spot size, the expected energy gain should be 91 MeV instead of 71 ± 1 MeV. Hence, we can conclude that the effects of ionisation defocussing act to reduce the peak a_0 of the interaction and this is why we observe much lower energies and charges than for the other targets examined.
Now we move onto the final set of results presented; the beam divergence extracted from the beam profile monitor.

Beam divergence

The lowest divergence electron beams were observed for helium in a gas cell where the divergence measured was 1.6 ± 0.2 mrad at a electron density of $8.4 \pm 1.0 \times 10^{18}\text{cm}^{-3}$. For helium in a gas jet, the lowest measured divergences was 2.4 ± 0.1 mrad at a density of $2.07 \pm 0.08 \times 10^{19}\text{cm}^{-3}$.

The increase in beam divergence between the two sets of targets is attributed to the need for density to be higher to achieve greater self-focussing. The propagation of the laser pulse through a medium with density modulations [121] will cause energy to be diffracted away from the focal spot. Hence, by the time the pulse is focused to its matched spot size, it will not have the energy to drive a non-linear wake and deplete before being able to accelerate particles.

By operating at higher densities, the length over which the pulse reaches its matched spot size is smaller and the $a_{0,m}$ is higher, hence, we can be significantly higher than the threshold for self-injection to allow for diffractive losses. By operating at higher densities, the divergence of the electron beam will also be larger. Consider the following relation for beam divergence,

$$< \theta_{div} >= \frac{< p_y >}{p_z}, \tag{4.8}$$

where $< p_y >$ is the rms transverse momentum of the electron beam and p_z is the longitudinal momentum of the electron beam.
Considering $p_z \approx W_{gain}/c \propto \frac{a_0}{n_e}$, from Thomas et al. [119], we obtain an expression for the tranverse momentum as $< p_y > \propto \frac{a_0}{n_e^{1/8}}$. Hence, we can see that as $< \theta_{div} > \propto n_e^{7/8}$, the divergence of the electron beam increases with density. Therefore, by needing to go to a

higher density for injection we also get larger divergences for the gas jet case.

For methane in a gas jet, we measured a minimum beam divergence of 3.2 ± 0.2 mrad at an electron density of $1.71 \pm 0.09 \times 10^{19}\text{cm}^{-3}$. We see that the arguments of divergence increasing with density do not hold for this situation as helium with a gas jet has a lower beam divergence at a higher density. Instead, we suggest that the injection mechanism is responsible for the increase in the beam divergence. The initial transverse momentum of electron beams in the cluster injection can be larger than the self-injection case as the plasma has a much higher temperature due to the various heating mechanisms in clusters such as collisional, inverse bremsstrahlung, vacuum and resonance heating [93].

Finally, we address the minimum divergence of the electron beam generated from using methane in a gas cell. This large value of beam divergence is again attributed to operating a high density for injection.

4.6 Conclusion

The aim of this section was to understand how a clustered medium can alter the properties of the electron beam generated by wakefield acceleration by making a direct comparison to self-injection. We have examined four targets for wakefield acceleration, methane and helium are examined in a gas jet and gas cell, where methane was known to cluster for the gas jet used in this experiment. The backing pressure of all four targets were varied and the energy spectrum and spatial profile of the generated electron beam was measured using an electron spectrometer and beam profile monitor respectively.

We began by examining the highest charge, across the range of densities where electron beams were observed on the spectrometer. The clustered target generated the highest charge electron beams with 60.0 ± 2.5 pC at a density of $2.30 \pm 0.12 \times 10^{19} \mathrm{cm}^{-3}$. Helium in a gas cell generated electron beams with 50.0 ± 2.3 pC at a density of $1.65 \pm 0.13 \times 10^{19} \mathrm{cm}^{-3}$. The reason for the shifted density at which the highest charge electron beam is observed, is attributed to the fact that it is the unclustered part of the medium, responsible for the generation of the wakefield. This is observed in the simulations of the medium where we observe that the wakefield has a plasma wavelength which corresponds to the number density of the unclustered part of the medium. Methane in a gas cell generated 24 times less charge than methane in a gas jet.

Diminished electron beam charge is attributed to ionisation induced defocussing. This particular experimental configuration is heavily reliant on the self-focussing and pulse compression effects of the plasma as the vacuum a_0 is not large enough to drive a bubble regime wake. Hence, any defocussing effects results in a reduction in the amplitude of the wakefield. This is not observed in the gas jet case with methane for either of the following reasons. The self-focussing component due to the presence of cluster [104] or the full ionisation of the medium due to the enhanced energy absorption in a clustered medium [93]. Helium in a gas jet generated electron beams with a maximum charge of 2.5 ± 0.5 pC at a density of $1.93 \pm 0.12 \times 10^{19} \mathrm{cm}^{-3}$. In this case, the loss of charge is attributed to the non-uniformity of the medium [121]. Density scale lengths in the medium cause injection/ejection of particles from the wake at spurious points, longitudinally along the medium.

Electron beams with the highest energies are generated for helium in a gas cell where a maximum energy of 211 ± 25 MeV was measured at a density of $9.5 \pm 0.9 \times 10^{18} \mathrm{cm}^{-3}$. A clustered medium on the other hand generates electron beams with a maximum energy of 140 ± 13 MeV at a density of $1.67 \pm 0.13 \times 10^{19} \mathrm{cm}^{-3}$.

	Methane-jet	Methane-cell	Helium-cell	Helium-jet
Highest charge [pC]	60.0 ± 2.5	2.5 ± 0.4	50.0 ± 2.3	2.5 ± 0.5
Highest energy [MeV]	141 ± 13	71.1 ± 1	211 ± 25	106 ± 6
Lowest divergence [mrad]	3.2 ± 0.1	3.9 ± 0.3	1.6 ± 0.1	2.4 ± 0.1

Table 4.6: Table showing the highest charge, energy and lowest divergence observed for each of the four targets examined.

Finally, the beam divergence of the electron beam was measured using the beam profile monitor where helium in a gas cell again generates the most collimated electron beam with a divergence of minimum 1.6 ± 0.1 mrad at a density of $8.4 \pm 1.0 \times 10^{18}\text{cm}^{-3}$. Electron beams from a clustered medium have a larger divergence minimum of 3.2 ± 0.1 mrad at $1.71 \pm 0.01 \times 10^{19}\text{cm}^{-3}$. These results are also summarised in Table 4.6.

Particle-in-cell simulations for one particular density show that the nanoplasma that forms when the cluster is inner ionised looses the electrons that were initially present in the medium due to interactions with the laser pulse. However, due to the Debye screening that occurs in the medium, electrons from the background plasma localise at the cluster centres and this results in the availability of charge for injection into the wakefield. We see that on the time-scale of the wakefield, the ions forming the cluster are still available for the injection process.

In this chapter, we have shown how a clustering medium can be used for the wakefield acceleration scheme. By comparing a clustered medium (methane) to a non-clustered medium (helium), we have shown that the presence of nanometer scale collection of molecules, change the dynamics of the injection of particles into the wakefield accelerator. In the next chapter, we will examine how these effects scale for laser systems with higher peak power $P > 100$ TW and higher a_0, the Astra-Gemini TA3 laser facility.

5 Comparison between cluster injection, self-injection and ionisation injection at 200 TW

5.1 Introduction

In the previous section, we have seen that a clustered medium has some clear advantages over a non-clustered medium. Cluster generation occurs naturally in some gas jet configurations and the electron beams generated in such a medium show comparable levels of beam charge to gas cells. Gas jets have been used extensively in the wider field of laser-plasma interaction for a large range of densities and interaction lengths. Gas cells are being adopted in numerous LWFA research facilities as they have significantly more stable longitudinal density profiles [121]. Almost all reported comparison of gas jets and gas cells have reported gas cells as being the superior target of choice, generating stable electrons beams with higher charge and energy [121]. Although it should be noted, that very few gas cells have been operated at a high repetition mode, due to the gas load from steady state gas flow, the current record is 800 Hz by He et. al. [213]. For TW and above LWFA experiments, the highest reported repetition for laser facilities is at the 10 Hz level [214, 215]. There is currently only one published experiment demonstrating high repetition rate laser-plasma experiments at this level [112], which uses a gas jet at its target.

Gas jets have been reported in literature to operate at the kHz level [216] and experiments with free flowing gas jets have been performed at the 1 MHz level [217, 218]. The gas jet nozzle has the advantage that can be easily replaced and it allows for more practical probing arrangements along with experimental configurations with multiple laser beams. High repetition rate laser facilities, which can be used for wakefield acceleration, such as the SYLOS laser at the ELI-ALPS facility [219] will have the capability to explore laser wakefield acceleration at the 100 kHz level, motivating the need to explore targets which can deliver these repetition rate. The gas load delivered by targets poses a significantly problem for vacuum chambers when operating at high repetition rates.

In the previous section, we have seen that the clustered medium is significantly more favourable to a non-clustered medium, methane, in a gas cell, for a 10TW laser facility, where vacuum $a_0 < 1$. This motivates examining the effect of higher power systems, where $a_0 > 1$ on a clustered medium, using the Astra Gemini TA3 facility. The clustered medium is hypothesized to be advantageous, as long as the clusters remain intact during the initial part of the laser pulse. We compare the efficacy of the clustered plasma, to that of a traditional monomer target and also with an ionisation injection case, to see how the properties of the electron beam and the generated x-rays vary.

5.2 Experimental setup

The Astra-Gemini TA3 laser has two beamlines, called North and South. For this experiment, the South beam was used to drive the wakefield and the North beam was used as an optical probe beam to diagnose the plasma conditions on every laser shot. The experimental configuration is shown in Figure 5.1.

The value for a_0 is estimated using the focal spot size on low power pulsed mode before

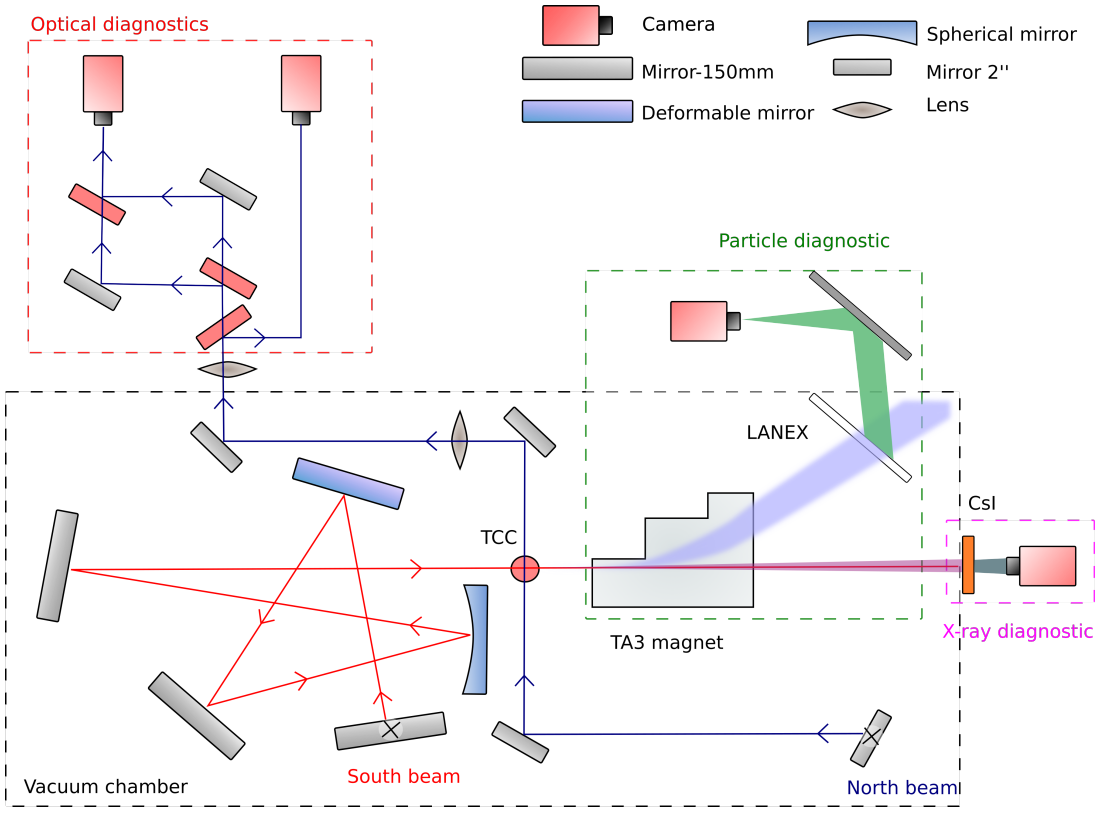


Figure 5.1: Schematic layout of the experiment performed in the TA3 chamber. TCC stands for target chamber centre, this is where the interaction occurs.

Laser parameters	
Laser energy	9.7 ±0.2 J
Pulse duration (τ)	46.7 ± 3.5 fs
Spot size (w_0)	$35 \pm 5 \times 50 \pm 5$µm
Peak intensity [10^{18}W cm^{-2}]	3.8 ± 0.9
Focussing geometry	$f/40$

Table 5.1: Table showing the nominal parameters of the laser during the TA3 2016 experimental run.

the full power data set is obtained. A pulse duration of 46.7 ± 3.5 fs and energy on target of $E = 9.7 \pm 0.2$ J results in a mean a_0 =1.33 ± 0.07 and the fraction of counts in the FWHM =0.25 ± 0.02. The laser parameters, for the results presented in this chapter, are summarised in Table 5.1.

Gas target

The south beam is focused using an $f/40$ spherical mirror onto a 10 mm gas jet with different backing gases. Helium was chosen as one of the gases for the target. The primary way in which electrons can become injected into the plasma wave in helium, is by self-injection from the background plasma. Methane, as was shown in Chapter 4, can cluster due to the adiabatic cooling that the medium experiences as it exits the gas jet orifice. Ionisation injection is also possible in methane as it contains carbon atoms.

Finally, helium is mixed with 1 % nitrogen, to be used as an ionisation injection scheme. This form of injection has a lower injection threshold than self-injection and so will generate electron beams with different properties to the others. The parameters of these targets are highlighted in Table 5.2.

Target parameters	Gas jet
d_{exit}, d^*, L_{opt}	10, 1, 1 mm
Nozzle half angle	20.8 deg
Backing pressure	$10 - 70$ bar
Electron number density	$0.5 - 5 \times 10^{18}$ cm^{-3}
Backing medium	CH_4, He and He +1% N_2
Reduced Hagena parameter -Γ^*	2.5×10^5-1.8×10^6
Mean cluster size	4.5×10^5-6×10^6 No. of atoms

Table 5.2: Table showing the target parameters during the TA3 2016 experimental run.

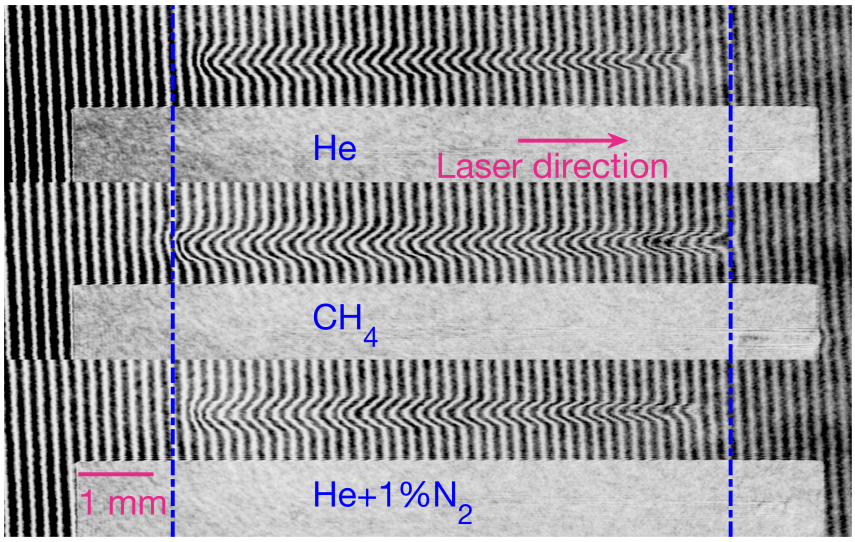


Figure 5.2: Figure showing the interferogram for helium, methane and helium +1% nitrogen at an averaged electron density of $3 \times 10^{24}\,\mathrm{cm}^{-3}$. The dashed blue line shows the beginning and the end of the plasma as observed for CH_4. We see that different gases expand at different rates resulting in different start and end points for the plasma.

Optical diagnostics

The plasma conditions are probed using the other laser beam available at this facility, the north beam. The two beams are timed grossly by using a photodiode with a fast rise time. This typically achieves a timing accuracy on the $\approx 10\,\mathrm{ps}$ time scale. We then use the interferometry diagnostic to fine tune the position of the laser pulse, as observed by the probe beam, in the gas jet. This allows for a timing accuracy of $\approx 100\,\mathrm{fs}$ which is acceptable for our applications.

The delay between the two beams is adjusted such that, the probe arrives after the main pulse exits the nozzle. In Figure 5.2, we can see the 10 mm nozzle with the fringes for methane, helium and helium +1% nitrogen. Both shots were taken at identical target positions and are from similar retrieved densities.

Particle diagnostics

After the interaction the electron beam is swept up using a dipole electron spectrometer magnet. This consists of three magnets held together as a single assembly to provide sufficient deflection to measure the energy spectrum of the electron beam from 100 MeV-2 GeV on a single screen.
The layout of the electron spectrometer is depicted in Figure 5.3 and the relevant dimensions are shown in Table 5.3. The distance to the magnet is defined relative to the

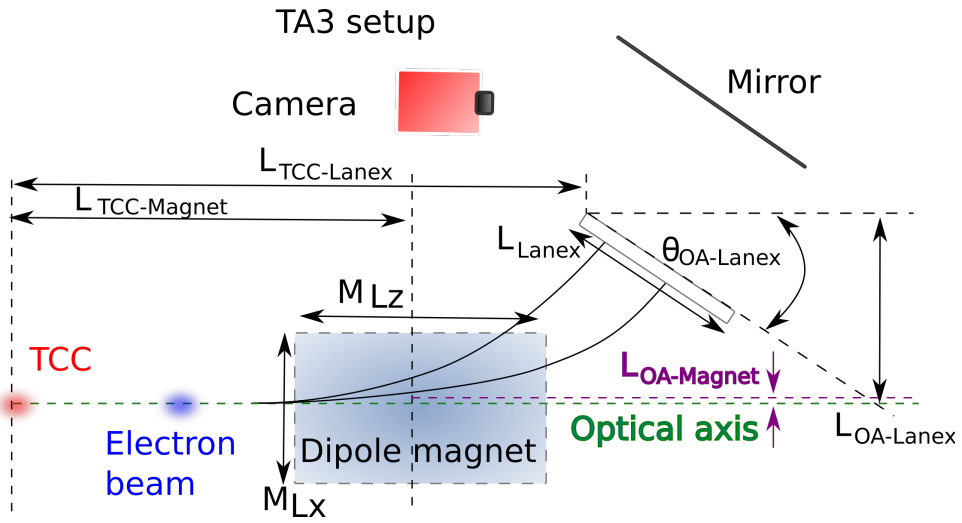


Figure 5.3: Illustration of the electron spectrometer diagnostic as viewed in the dispersion plane.

midpoint of the mapped field. For the TA3 case, it is the midpoint of the final magnet in the triple magnet assembly.

In Figure 5.4, the analysis steps for the TA3 experimental configuration are outlined. Figure 5.4a shows the raw image obtained from the electron spectrometer. In Figure 5.4b, we extract the background, notice that there is a gradient in the dispersion direction which must be accounted for. The background subtracted, cropped and projectively transformed image is shown in Figure 5.4c. Finally, we vertically bin the spectrometer image to obtain the energy spectrum of the electron beam in Figure 5.4d.

Dimension	Value/mm	Description
M_{Lz}, M_{Lx}	500, 150	Length and width of the magnet
$L_{TCC-Magnet}$	753	Distance from TCC to magnet
$L_{OA-Magnet}$	25	Distance from the optical axis to the magnet axis
$L_{TCC-Lanex}$	965	Distance from TCC to the beginning of the LANEX screen
L_{Lanex}	300	Length of the LANEX in the dispersion direction for the electron spectrometer
$\theta_{OA-Lanex}$	350	Angle between the optical axis and the LANEX screens
Peak B-field	1.2 T	Peak magnetic field of the magnet

Table 5.3: Relevant labelled dimensions of the electron spectrometer setup. All distances are in mm, with a measurement error of ±1 mm and angles in degrees. All distances from the magnet are relative to the midpoint of the magnet.

The noise floor is estimated using the subtracted background image. From this energy spectrum, we can infer properties such as the mean energy, maximum energy, which is defined as the energy at which the signal is 3σ from the background level. This is different to how the maximum energy is estimate on the TA2 experiment in Chapter 4,6 and 7 where the 99% of the cumulative integral of the energy spectrum is used. This method for choosing the maximum energy is chosen as it was possible to accurately model the noise due to scattered electrons.

The peak energy/full-width half maximum is extracted using a local peak finding algorithm in MATLAB. Charge is obtained by performing calibration shots using IP and LANEX simultaneously. The IP is taken to a scanner which outputs the charge of the beam directly and this is correlated to the counts obtained using LANEX on the electron spectrometer to extract the charge of the electron beam for every shot.

The x-rays pass through the Kapton window at the end of the chamber towards the indirect x-ray camera. This diagnostic consists of a filter pack and a caesium iodide scintillator.

X-ray diagnostics

The filter pack used on this experiment consisted of 64 elements and was designed by M. Bloom, [183]. This filter pack was imaged using an Andor iKon-L [220] with a caesium iodide scintillator in front of the CCD camera to convert the x-rays into visible light. The output window for the x-ray beam is made of Kapton [221] and was used to extract the x-ray beam from the vacuum chamber.

A thin layer of aluminium with a thickness of 100 µm was placed 10 cm from the window in the vacuum chamber to prevent any forward transmitted laser light, from the interaction, damaging the window. The front surface of the scintillator in the x-ray camera was situated 1.57 ± 0.01 m from TCC.

5.3 Results

We start by showing a small sample of the electron spectrometer and x-ray camera data in Figure 5.5. The backing pressure of the gas jet was varied to change the electron number density of the medium in order to study how the properties of the electron beam generated for each of these different types of targets varies. Five shots at equally spaced intervals of density are chosen to demonstrate the general trend in the properties of the electron

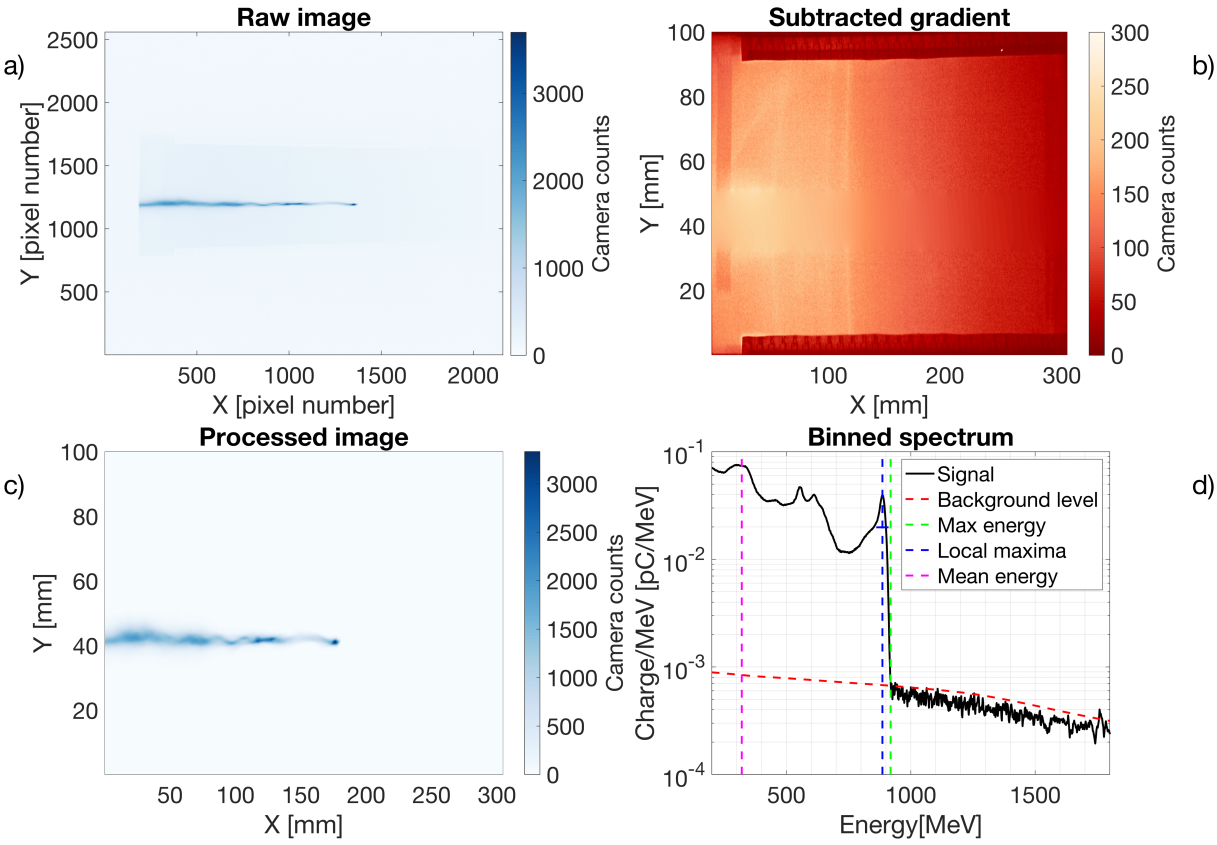


Figure 5.4: Analysis steps in retrieving the energy spectrum of the electron beam for the TA3 electron spectrometer configuration. In a) we have the raw image acquired by the camera. In b) the background is calculated by interpolating over the region where we see signal. In c) the image is warped and cropped to show the signal where oscillations can be seen in the orthogonal direction to dispersion. In d) we integrate the signal along the spatial axis to obtain the energy spectrum with some key features overlaid.

beam with density in Figure 5.5. The lower half of Figure 5.5 shows the corresponding image from the x-ray diagnostic.

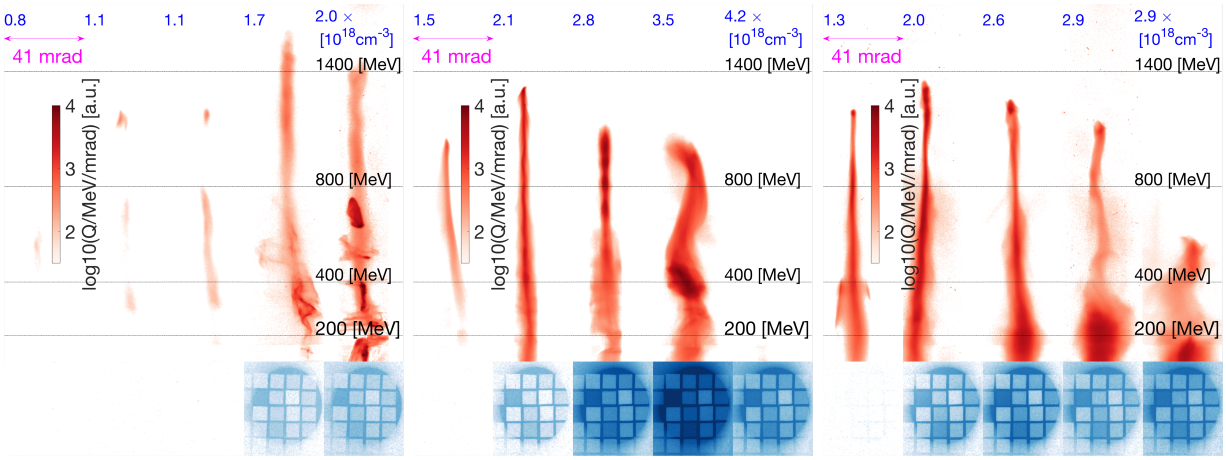
We can see that for the self-injection (SI) case, narrow energy spread electrons beams are present at densities of $1.1 \times 10^{18}\,\mathrm{cm}^{-3}$. At higher densities, the divergence of the beam increases and the electron beam goes to higher energies. The x-ray camera only sees betatron radiation when the beams go to higher energies and have more charge for densities greater that $1.7 \times 10^{18}\,\mathrm{cm}^{-3}$.
Next we address the cluster injection (CI) case in Figure 5.5b, where the charge of the electron beam is already significantly greater than the SI. Electron beams are observed over a much larger range of densities for cluster injection $1.5 \times 10^{18}\,\mathrm{cm}^{-3} - 3.5 \times 10^{18}\,\mathrm{cm}^{-3}$. At the density of $3.5 \times 10^{18}\,\mathrm{cm}^{-3}$, the electron beam has a large beam divergence and the spectrum is exhibiting a large transverse oscillation.

This behaviour is correlated to the flux of the betatron radiation, which can be seen to be maximised for this particular density. Interestingly, we still see a betatron beam of x-rays without a signal on the electron spectrometer for a higher electron density of $4.2 \times 10^{18}\,\mathrm{cm}^{-3}$. This suggests that the radiation is generated during the accelerating phase of the electron beam. Once the particles dephase interactions with the laser pulse or dephasing itself can result in the electron beam either not having enough energy to be visible on the spectrometer.

Finally, in Figure 5.5c, we can see that the ionisation injection (II) scheme with nitrogen as the dopant achieves similar energies and charges in comparison to CI. The energy spectrum of the electron beam is very broad and uniform. The variation in maximum energy from $1.3 \times 10^{18}\,\mathrm{cm}^{-3}$-$2.9 \times 10^{18}\,\mathrm{cm}^{-3}$ is very weak in comparison to the SI case, where the maximum occurs at a similar density to CI.

At higher densities, a dramatic reduction in the maximum energies is accompanied by a large increase in divergence in the orthogonal axes and a large transverse oscillation. We can see that the flux of x-rays generated by these electron beams remains relatively constant except for the lowest density.

We now move on to exploring these trends in more quantitative detail, beginning with the charge of the electron beam extracted from the electron spectrometer.



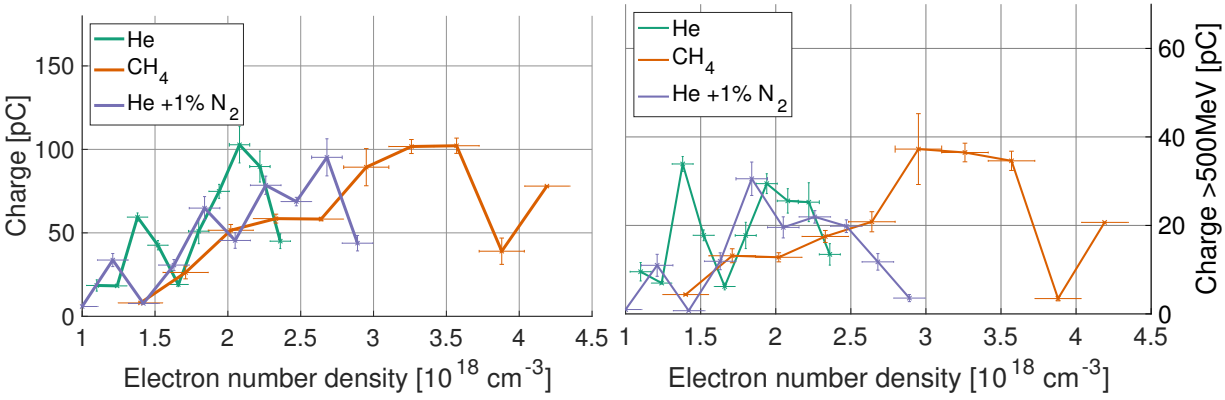
(a) He: Self-injection (b) CH_4: Cluster injection (c) He+1%N_2 : Ionisation injection

Figure 5.5: Raw data from the electron spectrometer and x-ray camera for various densities and gases. The number at the top is the average electron number density measured using interferometry. The divergence is shown relative to the high energy end of the electron spectrometer.

Charge

The charge of the electron beam is proportional to the intensity of the scintillation light from the LANEX on the electron spectrometer and is accumulated over an energy range of 200 MeV-2 GeV in Figure 5.6a. The maximum charge that electrons injection by SI attain is 104 ± 11 pC at a density of $2.1 \pm 0.1 \times 10^{18} \mathrm{cm}^{-3}$. For CI, we obtain a similar maximum charge of 101 ± 4 pC, but at a much higher density of $3.6 \pm 0.2 \times 10^{18} \mathrm{cm}^{-3}$. Finally for II, we also observe a maximum charge of 101 ± 12 pC at a density of $2.7 \pm 0.1 \times 10^{18} \mathrm{cm}^{-3}$.

We recall from the raw data in Figure 5.5, there is a large component of charge at the lower energies. Thus, we also examine the charge from 500 MeV − 2000 MeV in Figure 5.6b. For SI, we see obtain 27 ± 1.4 pC at a density of $1.4 \pm 0.1 \times 10^{18} \mathrm{cm}^{-3}$. For CI, we measure 32 ± 7.4 pC at a density of $3.0 \pm 0.2 \times 10^{18} \mathrm{cm}^{-3}$, 19% greater than the SI case. For II, we measure 25.9 ± 3.1 MeV at a density of $1.8 \pm 0.1 \times 10^{18} \mathrm{cm}^{-3}$.



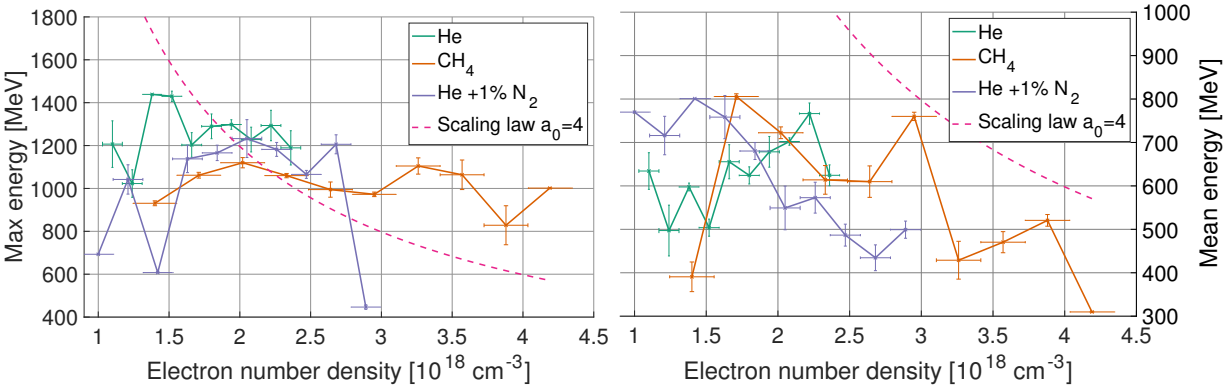
(a) Total charge (b) Charge greater than 500 MeV

Figure 5.6: The variation in charge of the electron beam as a function of electron number density.

Electron beam energy

From the electron spectrometer, we extract the maximum energy of the electron beam by determining the energy at which the signal reaches 3σ above the noise floor in Figure 5.7a. We see that SI beams reach the highest energies out of all the targets examined, where electron beams are measured to have a maximum energy of 1.44 ± 0.05 GeV at a density of $1.4 \pm 0.1 \times 10^{18} \mathrm{cm}^{-3}$.

Electron beams generated using II reach a maximum energy of 1.23 ± 0.09 GeV at a density of $2.0 \pm 0.1 \times 10^{18} \mathrm{cm}^{-3}$. CI generates electron beam with a lower maximum en-



(a) Maximum energy (b) Mean energy

Figure 5.7: The variation in maximum and mean energy of the spectrum of the electron beam as a function of density.

ergy that SI and II at $1.12 \pm 0.02\,\mathrm{GeV}$ at a density of $2.0 \pm 0.2 \times 10^{18}\mathrm{cm}^{-3}$. We also observe that the maximum energy does not follow the usual $1/n_e$ scaling law for the maximum energy of the electron beam [135]. Particularly note-worthy is the maximum energy of the electron beam remains between $0.82 - 1.12\,\mathrm{GeV}$ across a large density range of $1.4 \times 10^{19}\,\mathrm{cm}^{-3} - 4.2 \times 10^{19}\,\mathrm{cm}^{-3}$.

Along with the maximum energy, we also extract the mean energy of the energy spectrum in Figure 5.7b. The highest mean energy of the electron beam is actually observed for CI, where we attain $806 \pm 6\,\mathrm{MeV}$ at a density of $1.7 \pm 0.2 \times 10^{18}\mathrm{cm}^{-3}$. II generates electron beams with similar values for its highest mean energy across all densities of $801 \pm 27\,\mathrm{MeV}$. Finally SI, despite having the highest maximum energy, has a lower mean energy of $767 \pm 24\,\mathrm{MeV}$.

Critical energy of betatron radiation

The critical energy of the betatron radiation is measured by fitting the relative differences in transmission across the various elements that constitute a filter pack to a synchrotron function where the critical energy of the synchrotron function is the free parameter of the fit. The synchrotron function has the following form

$$S(E, E_{crit}) = \frac{\left(\frac{E}{E_c}\right) K_{2/3}\left[\left(\frac{E}{2E_c}\right)^2\right]}{\int \left(\frac{E}{E_c}\right) K_{2/3}\left[\left(\frac{E}{2E_c}\right)^2\right] \mathrm{d}E}, \tag{5.1}$$

where K is a bessel function of the second kind, E is the energy of the radiation and E_c is the critical energy of the spectrum. The methodology is outlined in more detail in the

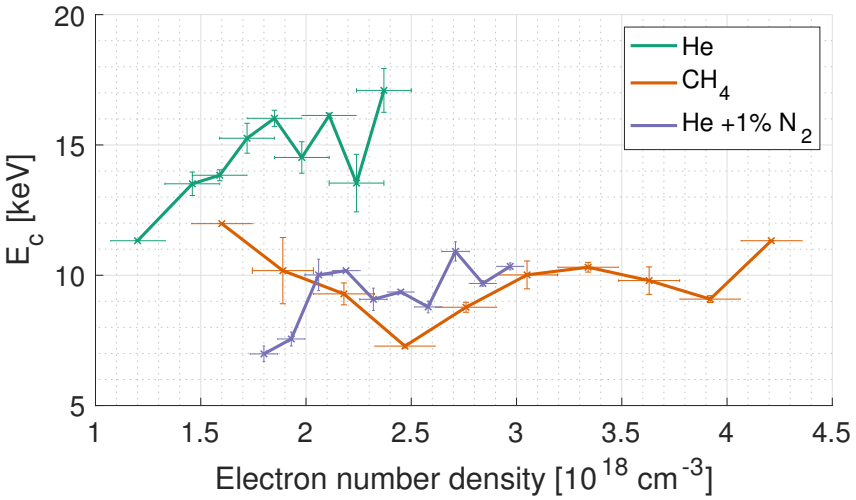


Figure 5.8: The variations of the inferred critical energy as a function of electron number density.

methods section on p.88. In Figure 5.8, we plot the variation in the critical energy of the betatron radiation as a function of electron density. Datasets where a unique value for the critical energy are shown in Figure 5.8.

We see that SI beams have the highest generated critical energy of $17.1 \pm 0.8\,\mathrm{keV}$ at a density of $2.4 \pm 0.1 \times 10^{18}\mathrm{cm}^{-3}$. CI generates betatron radiation with a critical energy of $12 \pm 1.3\,\mathrm{keV}$ at a density of $1.6 \pm 0.1 \times 10^{18}\mathrm{cm}^{-3}$. II generates betatron radiation with a lower critical energy of $11.0 \pm 0.4\,\mathrm{keV}$.

From this data set, we can see that critical energy of the betatron radiation generated from SI is very distinct to II and CI. The critical energy for SI and II is linearly correlated with density. For SI, we obtain a gradient in the critical energy of $3.1\,\mathrm{keV}/10^{18}\mathrm{cm}^3$ and for II we obtain a gradient of $2.1\,\mathrm{keV}/10^{18}\mathrm{cm}^3$. For CI, the relationship is more complicated and cannot be expressed by a single gradient. For densities less that $2.5 \times 10^{18}\,\mathrm{cm}^{-3}$, the critical energy is decreasing with electron density, in contrast to SI or CI. For intermediate densities between $2.5 \times 10^{19}\,\mathrm{cm}^{-3} - 4 \times 10^{19}\,\mathrm{cm}^{-3}$ we see a parabolic dependence in the critical energy.

Photon flux of betatron radiation

The intensity of photons measured on the x-ray scintillator is proportionally to the intensity of the scintillation light. This is then used to estimate the flux of the betatron x-ray beam, as a function of density, for the various targets in Figure 5.9. For SI, we observe a maximum photon flux of $1 \times 10^8 \pm 3 \times 10^7\mathrm{ph/mrad}$ at a density of $2.0 \pm 0.1 \times 10^{18}\mathrm{cm}^{-3}$.

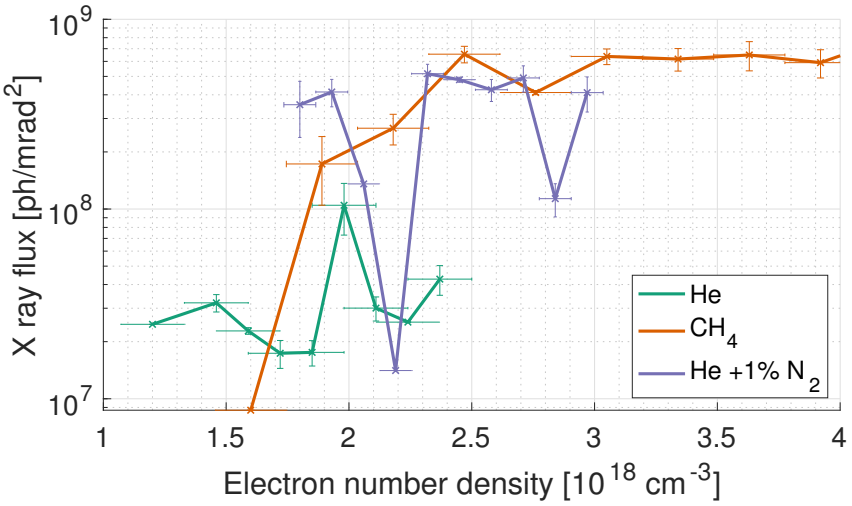


Figure 5.9: The variations of flux observed on the x-ray diagnostic as a function of the electron number density.

We observe a greater flux of x-ray photons for II with a maximum photon flux of $5.2 \times 10^8 \pm 6 \times 10^7$ph/mrad at a density of $2.3 \pm 0.1 \times 10^{18}$cm^{-3}. The brightest x-ray beams are observed for CI where a maximum photon flux of $8.0 \times 10^8 \pm 1.1 \times 10^8$ph/mrad at a density of $4.2 \pm 0.1 \times 10^{18}$cm^{-3}. For II, we note that there is a large drop in the x-ray flux at $2.2 \pm 0.1 \times 10^{18}$cm^{-3} and this is attributed to the sample size in the density bin being too small and hence the mean inside the bin is dominated by an outlier point.

5.4 Discussion

Charge

We begin by examining the relationship between the total integrated beam charge that the spectrometer measures for each medium as a function of density in Figure 5.6. All three targets attain a similar maximum value of total beam charge $Q_{tot} \approx 100\,\mathrm{pC}$ for the total charge in the electron beam in the $200\,\mathrm{MeV} - 2\,\mathrm{GeV}$ spectral range. The reason the electron beams look so different on the electron spectrometer images is because the beam divergence and spectral shape is different between the three cases.

We can examine the beam loading estimate for non-linear wakes [135] to estimate the upper bound on the charge of the electron beam that we expect for these laser powers, using the beam loading limit given by,

$$N_{max} \cong 2.8 \times 10^9 \left(\frac{\lambda_{0,\mu\mathrm{m}}}{0.8}\right)\left(\frac{P_{\mathrm{TW}}}{100}\right)^{1/2} \tag{5.2}$$

The power of the laser pulse across all the data sets is $208 \pm 27\,\mathrm{TW}$. We note that the fraction of laser energy in the focal spot is $\alpha = 0.25 \pm 0.2$ and so we define an effective power that we use with this expression as the energy outside of the focal spot is not guided and hence does not contributed to the formation of the wakefield. Using $P_{eff} = \alpha P$, where $P_{eff} = 52 \pm 6.8\,\mathrm{TW}$, we obtain a beam loading charge of $323 \pm 21\,\mathrm{pC}$.

This equation is derived from an energy balance argument for a spherical bubble in the non-linear regime. This suggests that we are achieving 31% of the total charge which can be accelerated by a laser of this power, driving a blow-out spherical plasma wave. It is possible that some charge is dephased to the point where there energy is below the threshold of the electron spectrometer or we are loosing some energy in the focussing of the laser pulse.

The next observation from Figure 5.6 is that the value of optimum charge occurs at different values of density for each of the three targets. For SI, it occurs at the lowest density of $2.1 \pm 0.1 \times 10^{18}\mathrm{cm}^{-3}$, for II, it occurs at $2.7 \pm 0.1 \times 10^{18}\mathrm{cm}^{-3}$ and for II we obtain $3.6 \pm 0.1 \times 10^{18}\mathrm{cm}^{-3}$. These densities are measured using interferometry $\approx 30\,\mathrm{ps}$ after the laser pulse has interacted with the leading edge of the target. For II case, the delayed occurrence of the charge optimum with density could be due to reduced self-focussing due to ionisation defocussing due to the presence of dopant's. For the CI case, much like in Chapter 4, we suggest that some fraction of the medium is bound up in clusters.

As we measure the free electron density using interferometry, the measurement of density will be different to the density of the unclustered medium. It has been shown that the unclustered medium is responsible for the formation of the plasma wave in Chapter 4.

For SI and CI, we begin observing electron beams at $1.0 \pm 0.1 \times 10^{18}\text{cm}^{-3}$. Consider the density at which the critical power of self-focussing exceeds the laser power, $n_{e,sf}$,

$$n_{e,sf} = \frac{1.75 \times 10^{10} m_e \epsilon_0 \omega^2}{e^2 P \alpha}, \tag{5.3}$$

which gives us an $n_{e,sf} = 6 \times 10^{17}\,\text{cm}^{-3}$. We note that the peak vacuum $a_0 = 1.38$ of the interaction, is not high enough for self-injection to occur $a_0 > 3$. This implies that, in the absence of any energy loss during self-focussing. The spot size of the laser pulse must be go from $w_{0,vac} = 42\,\mu\text{m}$ to $w_{0,foc} = 19\,\mu\text{m}$ to observe injection. Consider the matched spot size equation,

$$k_p w_0 = a_0 \sqrt{2}, \tag{5.4}$$

where $k_p = \frac{\omega_p}{c}$, the plasma wave vector. Using $w_0 = 19\,\mu\text{m}$ and $a_0 = 3$, we obtain a density of $9 \times 10^{17}\,\text{cm}^{-3}$, which agrees well within the error bars of the density at which electron injection begins.

Electron beam energy

We now move on to discussing the maximum energy of the electron beam. The highest values for the maximum energy are attained for helium in a gas jet, where $1.44 \pm 0.05\,\text{GeV}$ electron beams are observed at a density of $1.4 \pm 0.2 \times 10^{18}\text{cm}^{-3}$. Consider the non-linear energy gain equation [135] and the matched $a_{0,m}$,

$$\begin{aligned} W_{gain} &= \frac{2 a_0 m_e c^2 n_c}{n_e}, \\ a_{0,m} &= \left(\frac{w_0 a_0 \omega_p}{2c} \right)^{2/3}, \end{aligned} \tag{5.5}$$

using $w_0 = 42\,\mu\text{m}$ and $a_0 = 1.38$ we obtain $a_{0,m} = 3.49$ and $W_{gain,SI} = 1.44\,\text{GeV}$. Hence, we obtain good agreement with the maximum energy for the self-injection case. For II, using the same argument as for SI, we obtain $a_{0,m} = 3.9$ and $W_{gain,II} = 1.16\,\text{GeV}$, which agrees well with the experiment where we observe $1.23 \pm 0.09\,\text{GeV}$. Finally for CI, we see that the electron density at which the maximum energy of the electron beam is maximised is the same as for II. We observe lower energies than the prediction for the energy gain,

$W_{gain,II}$, compared to the observed $1.12 \pm 0.02\,\mathrm{GeV}$. As the a_0 of the laser pulse is critical in determining the maximum energy of the electron beam, we see that the density at which this parameter can be maximised are when the highest energy electron beams are observed. The lower injection threshold for II does not necessarily prove to be beneficial for attaining the highest energy electron beams. In-fact, one reason for the requirement of density to be higher for the II and CI case could be due to ionisation defocussing [212]. Hence, to overcome this effect, we have to operate at higher densities than SI.

Alongside considering the maximum energy, we also consider the mean energy of the electron beam in Figure 5.7 on p.134. We see that SI has the lowest value for its mean energy of $767 \pm 24\,\mathrm{MeV}$ at a density of $2.2 \pm 0.1 \times 10^{19}\mathrm{cm}^{-3}$. The mean energy of the spectrum being much lower than the maximum energy is an indication of the presence of a large amount of dark current [222] in the accelerator. Dark current is the spurious trapping of charge at the incorrect phase leading to a the low energy tail of the electron beam.

The charge at the lower energies of the spectrum dominates the charge content of the electron beam for SI. We see that II has a higher value for its mean energy of $801 \pm 27\,\mathrm{MeV}$ at a density of $1.4 \pm 0.1 \times 10^{18}\mathrm{cm}^{-3}$. For CI, we also observe similar values for the highest mean energies of $806 \pm 6\,\mathrm{MeV}$ at a density of $1.7 \pm 0.1 \times 10^{18}\mathrm{cm}^{-3}$.

We see for II that the lower the density the less likely charge is spuriously trapped along the length of the accelerator. This results in the relationship where the maximum energy is decreasing as a function of the accelerator length for II and CI. For SI, a high density is required to reach the a_0 needed to achieve its injection threshold $a_0 > 3$. Hence, the same relationship is not observed for SI.

Critical energy of betatron radiation

The critical energy of the generated x-ray radiation was measured using the filter pack method outlined in Chapter 3 on p.86. The radiation generated from SI, CI and II are compared. For SI, we measure a critical energy of the spectrum of $17.1 \pm 0.8\,\mathrm{keV}$ at a density of $2.37 \pm 0.01 \times 10^{18}\mathrm{cm}^{-3}$. Using the scaling law, for the critical energies of betatron radiation in plasma, we can obtain an expression for the oscillation radius of the electron beam [168, p.147]

$$r_\beta = \frac{4E_c c}{3\hbar\gamma^2\omega_p^2} \tag{5.6}$$

using the values for E_c and n_e for SI and the maximum energy for the corresponding density $\gamma_{max} = 2.3 \times 10^3$, we obtain an oscillation radius of $r_\beta = 0.24\,\mu\mathrm{m}$.For CI, the

highest critical energy observed is $12.0 \pm 1.3\,\mathrm{keV}$ at a density of $1.6 \pm 0.1 \times 10^{18}\mathrm{cm}^{-3}$. The corresponding maximum gamma at this point is $\gamma_{max} = 2.1 \times 10^3$ giving an oscillation radius of $r_\beta = 0.25\,\mu\mathrm{m}$. For II, similarly we obtain energies of $12.0 \pm 1.3\,\mathrm{keV}$ at a density of $2.7 \pm 0.1 \times 10^{18}\mathrm{cm}^{-3}$ with a maximum gamma factor of $\gamma_{max} = 2.4 \times 10^3$ giving an oscillation radius of $r_\beta = 0.14\,\mu\mathrm{m}$.

We see that the radiation generated from II has a lower r_β than SI. The lower injection threshold causes the injected electrons to have a low initial transverse momentum and hence small oscillation radius. It is interesting to note that the radiation generated in the CI case has the same oscillation radius for the brightest x-rays observed as for the CI case. The upper bound on the the transverse momentum is determined by the largest trajectory which can inject particles into the wake.

The injection from CI can occur at any point transversely in the wake as clusters stream through the wakefield. Consider the frame in which the plasma wave is stationary, the cluster streams through the wakefield at the seperatrix boundary and electrons can be injected with the largest transverse momentum and hence the electron beams can have a large r_β when compared to II. The low critical energy arises from the reduced gamma factor of the electron beam for CI compared to SI.

Photon flux of betatron radiation

The flux of photons is measured using the portion of the filter pack image on the x-ray camera without any filters in its path. The scintillation light has been calibrated to measure the intensity of x-ray photons incident on the scintillator [168, p.102]. The x-ray beam passes through the optic collecting the forward transmitted radiation. This optic has a hole in the optical axis to allow the x-ray beam to pass through, unfortunately the hole was not large enough to see the full contour of the x-ray beam. We none-the-less estimate the peak flux with the portion of signal that is measured.

For SI, we measure a maximum photon flux of $1 \times 10^8 \pm 3 \times 10^7\mathrm{ph/mrad}$ at a density of $2.0 \pm 0.1 \times 10^{18}\mathrm{cm}^{-3}$. This is much less than for II where we observe $5.2 \times 10^8 \pm 6 \times 10^7\mathrm{ph/mrad}$ at a density of $2.3 \pm 0.1 \times 10^{18}\mathrm{cm}^{-3}$. This increase in flux is attributed to the larger total charge of the electron beam. Our measurements of E_{crit} and r_β suggest that these are not responsible for the increase in x-ray flux. Instead, we suggest that the continuous injection is responsible for the increased emission of radiation in the plasma cavity.

Finally, for CI we measure a maximum photon flux of $8.0 \times 10^8 \pm 1.1 \times 10^8\mathrm{ph/mrad}$ at

a density of $4.2 \pm 0.1 \times 10^{18}\text{cm}^{-3}$. We note that this dramatic increase in photon flux is correlated with the large transverse oscillation which we observe in the electron spectrometer images. This suggest the radiation could be generated from a hosing-style instability which occurs more rapidly at higher densities. The transition from laser-driven to beam driven wakefield acceleration has been suggested as a mechanism for the onset of hosing [223].

The electron hose instability occurs when the electric field of the electron bunch perturbs the plasma density and the centroid of the electron beam begins to oscillate about propagation direction of the electron beam [224]. This can occur when we have depleted the laser pulse sufficiently which occurs at higher densities. A plasma wave driven by the electron beam is more susceptible to hosing instabilities. In order to confirm this hypothesis we will need to perform additional experiments examining the self-emission from the channel to see if laser hosing is indeed observed [225]. A large data-set examining the threshold density for the onset of hosing and how this influences the critical energy will help test this hypothesis.

5.5 Conclusion

In this chapter, we have presented experimental data for laser wakefield acceleration, in a 10 mm gas jet, using a 200 TW laser facility. Three different injection mechanism are analysed using the energy spectrum of the electron beam and the betatron radiation spectrum. We build upon the results from Chapter 4 to examine the differences in the injection and acceleration of electron beams in a clustered medium at a 100 TW laser facility.

The total electron beam charge is comparable between SI, II and CI, where all three methods of injection attain a maximum beam charge of $\approx 100\,\text{pC}$. The density that this charge occurs at is different for all three injection mechanisms, with CI requiring unusually high electron densities of $3.6 \pm 0.2 \times 10^{18}\text{cm}^{-3}$. In Chapter 4, we concluded that the density of the unclustered part of the medium is responsible for the generation of the wakefield. The density that we measure from interferometry is the disassembled, free electron density. This is why the density optimum for CI is observed to be higher for SI and II.

We then examined the maximum electron energies over the range of densities where charge was observed on the spectrometer. Electron beams injected from SI reach the highest energies of 1.44 GeV, whereas for CI and II, energies of 1.12 GeV and 1.23 GeV are measured. For SI, mono-energetic peaks are observed in the spectrum for some densities whereas, for CI and SI the energy spectrum is uniformly distributed.

On this experiment, an x-ray camera was utilised with a filter pack to determine the critical energy of the betatron radiation spectrum generated from the interaction. SI generates the highest critical energy spectrum with energies of $17.1 \pm 0.8\,\mathrm{keV}$. CI and II respectively have critical energies of $12.0 \pm 1.3\,\mathrm{keV}$ and $11.0 \pm 0.4\,\mathrm{keV}$. This diagnostic was also utilised to extract the peak flux of photons for this x-ray source.

CI generates the highest flux betatron beam with $8 \times 10^8 \pm 3 \times 10^7$ph/mrad. For II, the highest flux betatron radiation generated was $5 \times 10^8 \pm 1.1 \times 10^8$ph/mrad and SI has a much lower flux radiation with the highest flux x-ray beam measured was $1 \times 10^8 \pm 3 \times 10^7$ph/mrad. The electron beam for CI exhibits large transverse modulations in its energy spectrum and these modulations coincide with the occurs of high flux betatron radiation.

The next step for this work is to examine these various injection simulations using particle-in-cell simulations to understand how these various beam parameters arise for these targets. The origin of the potential hosing induced enhancement of betatron radiation offers an attractive application for imaging experiments with high flux but low critical energy requirements [63].

One key limitation of this setup was the inability to diagnose the size of the cluster and the cluster density of the target on shot. The experimental setup can be improved from the diagnostic side but also from a consideration of targetry. The ability to control the backing temperature of the medium would give an additional control over the side of the cluster, allowing the cluster size to be varied independently of the unclustered density such that an optimum cluster size for wakefield acceleration can be determined for each unclustered density.

6 Investigation of the density-length parameter space in a mismatched, self-guided, self-injecting laser wakefield accelerator at 10 TW

6.1 Introduction

The final output of a fixed length target does not provide the full dynamic of the interaction. A density-length parameter scan, consists of varying the backing pressure of the target in order to change its electron density and altering the separation between the walls of the cell to vary its length. The ability to vary the length of the interaction in-situ, is one of the key advantages of these types of gas cells, over other fixed length targets like gas jets. In a plasma accelerator, there are various output parameters available for optimisation, such as, total beam charge, maximum energy etc.

Crucially, each of these parameters will most likely not have the same value of density and/or length, for which their optimum value occurs. Density/length parametric scans have not been extensively covered in literature [115, 168, 226]. To date, no such work where the measurement of the electron beam properties, across density and length simultaneously and its impact on the implicit assumptions about the target and the interaction are known. This chapter seeks to show the optimal density-length parameters for spectral and spatial properties of the electron beam. The experimental setup is identical to that shown in Chapter 4.

The aim of this chapter is to understand what the density-length conditions of the target need to be, for a fixed laser pulse, to optimise a particular metric of the electron beam using self-injection (SI). There are various parameters available for optimisation in the electron beam as mentioned previously. Maximum energy, charge, beam divergence, beam eccentricity and transverse momentum are chosen as metrics to assess optimality. Optimal parameters for one metric are not necessarily the same as for others.

This chapter will begin with examining the scaling laws, to understand what we expect for these experimental conditions. We will then cover the various beam properties extracted from the electron spectrometer and the beam profile diagnostic available from this experiment. Finally, simulations will be presented to compare with the experimental data and to understand the underlying pulse evolution effects which lead to the the observed results.

Density-length dependency for self-injection

We begin by characterising the expected density-length parameter space for a laser plasma accelerator is by using the expected guiding, dephasing and depletion lengths in order to maximise the electron energy. To first order, we would expect that these are the dominant effects which determine the length of the accelerator. We begin by imposing the condition that the length of the accelerator L_{acc} must be less than the depletion length for a particular density,

$$L_{acc} < \frac{c\tau n_c}{n_e}, \tag{6.1}$$

where τ is the pulse duration, n_c is the critical density and n_e is the electron density. This sets the upper bound on the length of the interaction. We have used the non-linear depletion length as self-injection requires us to operate the accelerator in the non-linear regime. We then impose that the length of the target should be greater than the dephasing length,

$$L_{acc} \geq \frac{4\sqrt{a_0}}{3k_p}\frac{n_c}{n_e}, \tag{6.2}$$

where k_p is the plasma wavevector and a_0 is the peak normalised vector potential of the laser pulse. We have used the 3D non-linear dephasing length as self-injection requires $a_0 > 3$ [121]. The dephasing length is the length over which the electron beam gains energy and outruns the wakefield.

The reason for it to be greater than the dephasing length is because the pulse will have to undergo self-focussing to reach the matched spot size for that particular density. This occurs over some length known as the evolution length. As the dephasing length is only valid from the point of injection, the length of the target must be at-least of this length to accelerate particles to the highest energies. The prediction of the point of injection is difficult for self-injection as it depends on pulse evolution effects and the uniformity of the medium [120, 121]. We can none-the-less predict the density at which the self-focussing

effects become important using the critical power for self-focussing as

$$n_{e,sf} > \frac{1.75 \times 10^{10} m_e \epsilon_0 \omega^2}{\alpha e^2 P}. \tag{6.3}$$

Where $n_{e,sf}$ is the density at which the the power of the laser pulse exceeds the critical power for self-focussing and P is the power of the laser pulse, α is the fractional energy in the full-width half-maximum of the focal spot. We can also use the semi-empirical model developed by Mangles et al. [120] which defines the density threshold for self-injection,

$$\frac{\alpha P n_{e,SI}}{1.75 \times 10^{10} n_c} - \frac{1}{16}\left[\ln\left(\frac{2n_c}{3n_e}\right) - 1\right]^3 = 0, \tag{6.4}$$

where P is the laser power, α is the fraction of energy inside the full-width-half-maximum of the focal spot and $n_{e,SI}$ represents the threshold of self-injection.

Finally, for efficient excitation of a plasma wave, we know that the pulse must be shorter than the plasma wavelength. We also know that for longer pulse lengths, we will begin to observe the plasma wave breaking up the laser pulse into beamlets which resonantly drive a plasma wave. This is referred to as the self-modulated laser wakefield acceleration (SM-LWFA). We can impose the final condition on the electron number density, so that the length of the pulse is shorter that the plasma wavelength,

$$\begin{aligned} c\tau &< n\lambda_p \\ n_e &< \frac{n^2 \pi^2 \epsilon_0 m_e c^2}{(ec\tau)^2}. \end{aligned} \tag{6.5}$$

where τ is the duration of the laser pulse and n a number of plasma wavelengths and typically $n > 2$. We can represent these limitations graphically in Figure 6.1. The shaded blue region of interest is the resulting inequality from the constraints placed from out discussion earlier. This gives us a guide for what density-length parameters we should expect to see electron beams. For self-injection, the injection threshold is reached when the plasma wave is sufficiently non-linear. The vacuum a_0 for the TA2 setup system is approximately 0.7. This alone would not be enough for SI to occur in this medium. However, by operating at mismatched conditions, self-focussing [110] and compression [227] help increase the a_0 of the laser pulse such that injection can occur. This is why we require the length of the medium, to be greater than simply the dephasing length.

Using all these constraints we can try to identify what the highest energy of the electron beam will be, and the density-length which this occurs at. In Figure 6.1, using the constraints discussed earlier, operating at the point where the dephasing length is equal to the

depletion length at $L_{int} = 3.3\,\text{mm}$ and $n_e = 7.4 \times 10^{18}\,\text{cm}^{-3}$ and using $W_{max} = \frac{2m_e c^2 a_0}{3}\frac{n_c}{n_e}$, we attain a maximum energy of 240 MeV. Although this scenario will only be realised if the length over which it takes the pulse to self-focus is smaller than the length over which the pulse depletes.

Finally, the profile of the laser pulse, its power [112] and even its wavelength can change during its propagation. These pulse evolution effects are not captured by the scaling laws. Hence, by having the ability to vary the density and the interaction length, we can not only fold out the dynamic nature of injection and acceleration of the electron beam but also gain insight into the evolution of the driver pulse.

In this chapter, we present a multi-parameter scan, where density and length, in that order, were varied to understand the range of electron beam properties observed for self-injection. The data set was acquired using the 10 TW laser system Astra Gemini TA2 [146]. Helium was the medium of choice, where in the absence of any dopant's, the only form of particle injection will be self-injection. The level of agreement of this density-length scan dataset with simulations and scaling law estimates will also be examined.

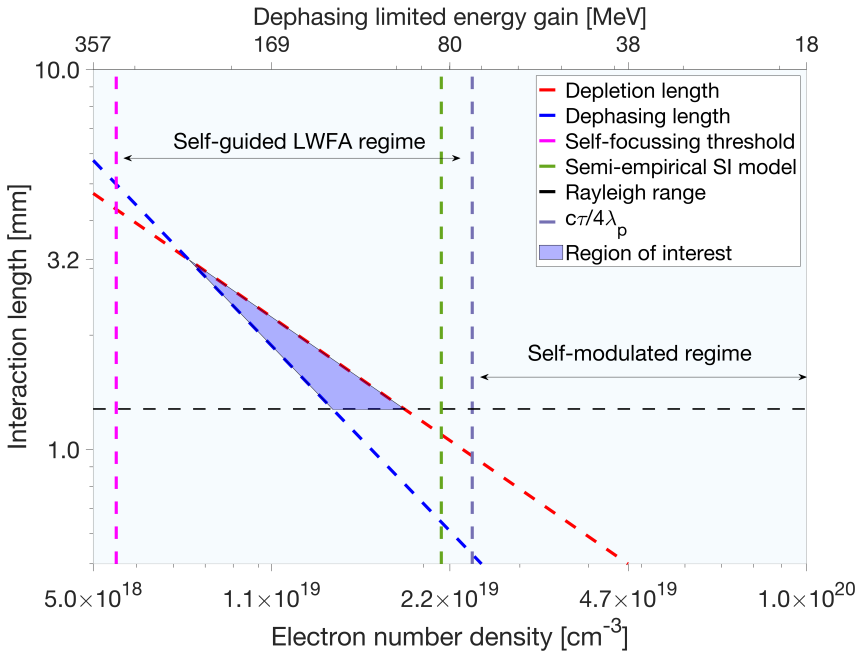


Figure 6.1: Density-length dependency of key laser wakefield acceleration parameters using the dephasing, depletion and guiding limits. The blue region represents the region where we expect the highest energy electron beams to be present. The dephasing limited energy gain is calculated using $W_{max} = \frac{2m_e c^2 a_0}{3}\frac{n_c}{n_e}$. This parameter space assumes a fixed $a_0 = 3$ and pulse duration of 45 fs.

6.2 Experimental setup

The experiment was performed using the same TA2 setup as Figure 4.4 in Chapter 4. The density scan was performed by setting the backing pressure to the highest density. Then as the gas solenoid was pulsed, the pressure in the backing line to the cell decreased, which in turn reduced the electron density of the target.

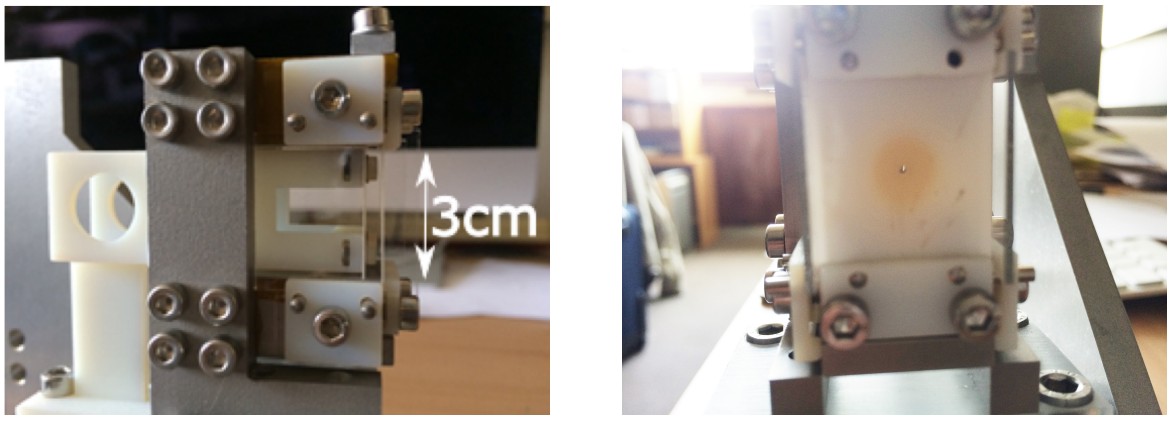
The gas cell used on this experiment was designed to have transverse probing capabilities along with the ability to vary the length of gas available longitudinally as can be seen in Figure 6.2a. A stepper motor is coupled to the rear face plate of the gas cell, which allowed the length of the medium to be varied in-situ. The backing pressure was measured

Interaction parameters	Gas cell
Backing pressure	$90 - 550\,\text{mbar}$
Electron number density	$0.48 - 2.9 \times 10^{19}\,\text{cm}^{-3}$
Length	$2.8 - 5.8\,\text{mm}$
Gas	Helium

Table 6.1: The target parameters during TA2 experiment.

Laser parameters	
Laser energy	597 ±37 mJ
Pulse duration- τ	45 ±2 fs
Spot size- w_0	$18 \pm 2 \times 23 \pm 5$ µm
Peak intensity	$1.0 \pm 0.5 \times 10^{18}\text{W cm}^{-2}$
Focussing geometry	$f/18$

Table 6.2: The parameters of the laser pulse for this dataset.



(a) Side view of the gas cell.

(b) The face plates of the gas cell.

Figure 6.2: Gas cell used on the Astra TA2 2016 campaign. Designed by N. Lopes.

using a pressure transducer near the gas inlet to the cell. A probe line consisting of shadowgraphy and interferometry was used to diagnose the plasma structures in the cell and extract plasma densities. A Mach-Zender interferometer was used to extract the phase shift incurred by a probe beam passing through the plasma. This phase shift was then converted into a measurement of electron density. Abel transformations were performed to retrieve the radial profile of the plasma column from the transverse projection. This was performed using a Matlab software developed by J. Cole [173].
The gas cell backing pressure was varied, which subsequently varied the electron density, for one particular length and this was then repeated for each length. Each pressure scan was repeated twice before the cell length was varied. For the self-injection case, we varied the length from 2.8 mm to 5.8 mm, in mm steps, involving 135 shots taken in total. The stability of the laser pulse is shown in Figure 6.3, where we see the a_0 variation for each run is $\approx 10\%$ which arises from variations in the energy of the laser pulse. As the variation between the average a_0 between datasets is smaller than this variation, we are justified in making comparisons and inferences between the various length data-sets.

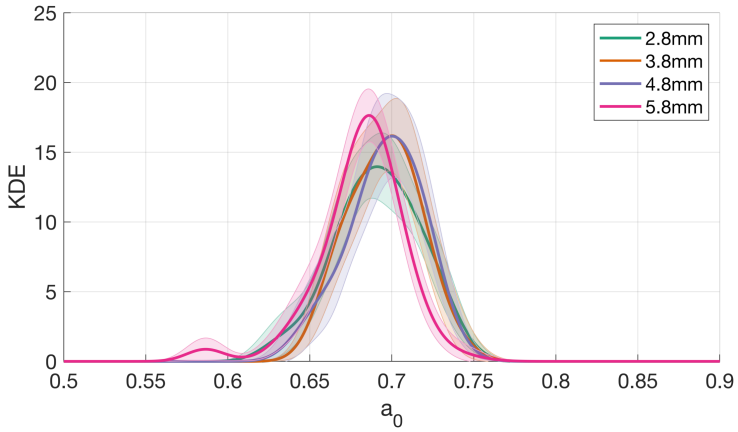


Figure 6.3: The stability of the a_0 of the laser pulse across the various runs. KDE stands for kernel density estimation and highlights the underlying distribution for the a_0. The shaded region represents the uncertainty in the density distribution estimation using bootstrapping.

6.3 Results

We begin by outlining the raw data from the electron spectrometer diagnostic in Figure 6.4. By examining a small subset of the full raw data, we can begin to understand some of the over-arching trends in the dataset. This will then be supplanted by more quantitative analysis of the diagnostics. Five shots were selected, such that they are equally spaced within the electron number density range explored for that particular cell length.

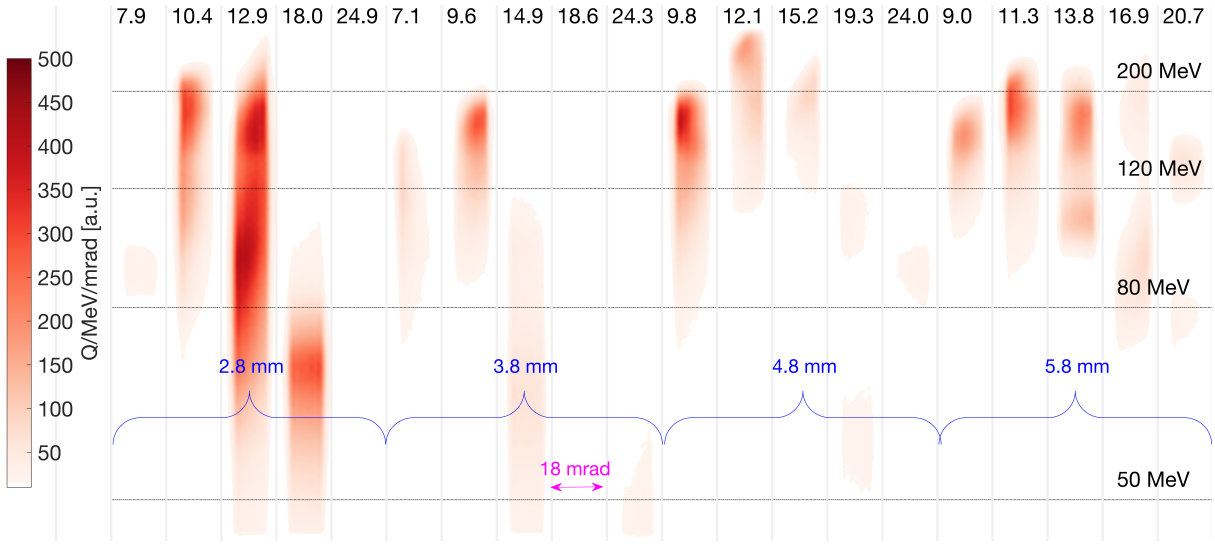


Figure 6.4: Figure showing the raw electron spectrometer data for various lengths and densities. The length (blue, at bottom) is given in mm and the electron density (black, at top) is given in 10^{18}cm^{-3}.



Figure 6.5: The beam profile data for various lengths and densities. The length (red, at side) is given in mm and the electron density (black, at top) is given in $1 \times 10^{18}\,\mathrm{cm}^{-3}$. The red dashed lines represents the laser centeroid and the black dashed grid has a spacing of 2 mrad. The charge is normalised to the highest value across all shots. The logarithm of charge is plotted due to the large dynamic range of charge over which electron beams are present.

The value for the electron density is shown at the top of the figure for each shot and the length of the cell for each set of 5 shots is shown at the bottom of the figure. The dashed line representing the pointing of the electron beam for trajectories on axis. This

can introduce a significant error at the higher energy end of the spectrometer and is corrected by using the information from the beam profile diagnostic as this was present for all shots shown. We include this in the detailed analysis of the electron energies in the subsequent figures in this chapter.

One immediate observation from this small subset of the data is that shorter interaction lengths produce higher charge beams. Data from the beam profile diagnostic, for the corresponding shots shown in Figure 6.4 are shown in Figure 6.5. We observe a similar trend where the shorter cell length generates substantially greater charge than the longer cell. For the highest densities of $\approx 2 \times 10^{19}\,\mathrm{cm}^{-3}$, we observe that electron beams are only present for the shortest cell length. For intermediate densities of $\approx 1 \times 10^{19}\,\mathrm{cm}^{-3}$, electron beams are present even for the longest cell lengths.For the longest cell length, at densities around $\approx 1 \times 10^{19}\,\mathrm{cm}^{-3}$, the pointing of the electron beam can be seen to be large $\approx 3\,\mathrm{mrad}$ from the laser axis. We move onto examining the data in more quantitative detail by extracting various parameters from the electron spectrometer and beam profile diagnostics.

Charge

Firstly, the total beam charge ($E > 45\,\mathrm{MeV}$), as observed on the high energy electron spectrometer is shown in Figure 6.6 across the range of densities and lengths that were explored in the experiment. We see our initial assessment of the correlation between charge and acceleration length was vindicated in that a short cell generates substantially more charge than longer cell lengths.

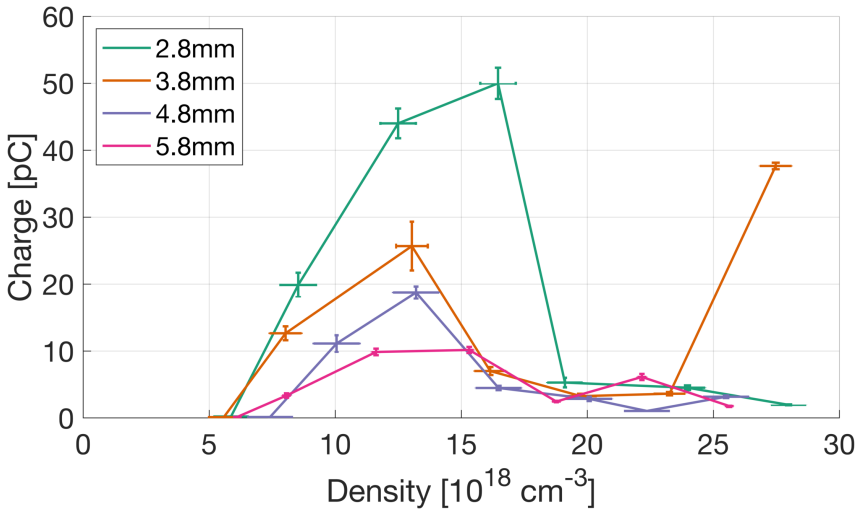


Figure 6.6: The charge observed on the high energy electron spectrometer as a function of density for various cell lengths.

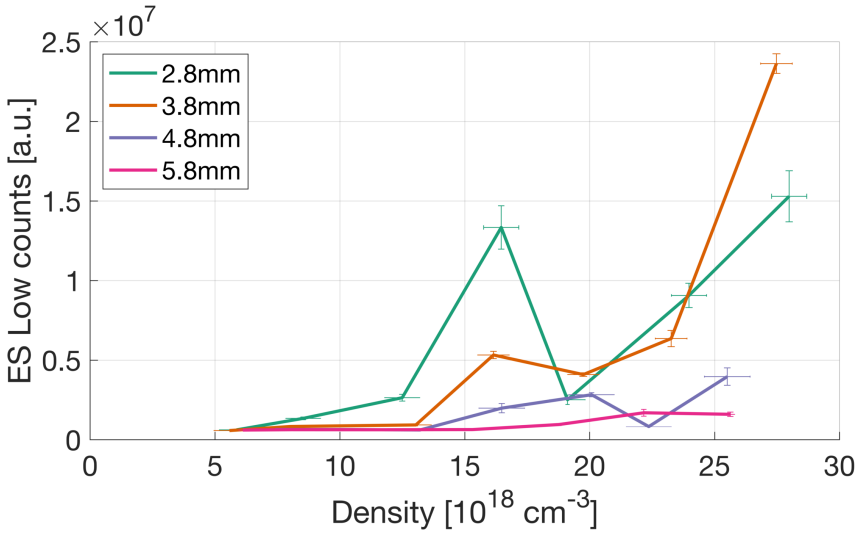


Figure 6.7: The charge observed on the low energy electron spectrometer as a function of density for various cell lengths.

The data binning procedure, discussed in the Methods section in Chapter 3 on p.95. The data is split over 7 equally spaced density intervals, which we refer to as bins. The data in each bin is averaged and the mean charge is plotted against the mean density in each data bin. The errors for both the dependant and independent variable are a combination of the measurement error and the error from the standard deviation in the bin, combined in quadrature.

In Figure 6.6, the highest charge over the density range sampled, for a fixed cell length, decreases as a function of cell length. For each cell length, there is a optimum density which maximises charge. We can see that, excluding the outlier data point for 3.8 mm, this typically occurs between $1.2 - 1.7 \times 10^{19}\,\mathrm{cm}^{-3}$. The range of densities over which electron beams are observed does not vary with length. The highest charge electron beams, across all density and length was measured to be $50.0 \pm 2.3\,\mathrm{pC}$ for the shortest length of 2.8 mm and at a density of $1.7 \pm 0.2 \times 10^{19}\mathrm{cm}^{-3}$. The relationship between charge and density is asymmetric as the charge decreases with higher densities faster than for lower densities. We also observe an anomalously high charge for the 3.8 mm case at the highest density. The physical mechanism which could be responsible for this point will be addressed in the discussion section.

The charge for the high energy electron spectrometer only accumulated electrons with energies greater than 45 MeV. We now move onto examining the charge from the low energy spectrometer in Figure 6.7. This diagnostic observes charge from $10 - 45$ MeV.
In Figure 6.7, we see that when the cell length is at 3.8 mm, the low energy spectrometer

measures the highest charge for a density of $2.7 \pm 0.2 \times 10^{19}\text{cm}^{-3}$. This agrees with the anomalously high charge observed on the high energy electron spectrometer aswell. For electron beams in this spectral range of $10 - 45\,\text{MeV}$, we see that the highest charge electron beams were present at the highest densities for most cell lengths. Additionally, we also observe that for densities $n_e < 1.2 \times 10^{19}\,\text{cm}^{-3}$, only the shortest cell length shows charge above the detector background level.

Maximum energy

Next we consider, the energy of the electron beams, observed on the high energy electron spectrometer in Figure 6.8. The maximum energy is chosen as the metric to assess the energy spectrum of the electron beam. Due to highly variable background noise present on this this experiment, the maximum energy is determined by considering the threshold at which the cumulative charge per unit energy reaches 99 % of its highest value.

Electron beams with charge greater than 1 pC are selected for the shorts shown in Figure 6.8. We can see that the electron beam energy reaches a maximum value of $210 \pm 19\,\text{MeV}$ at a cell length of 4.8 mm and a density of $1.16 \pm 0.08 \times 10^{19}\text{cm}^{-3}$. Hence, we can see that the optimum of charge ($Q > 45\,\text{MeV}$) is different to the optimum of maximum energy. We observe that for a cell length of 4.8 mm, the electron beam energy shows a high degree of variability.

The error bars in Figure 6.8, represent the error on the mean, of the shots selected within a density window. We also observe that the energy of the electron beam for

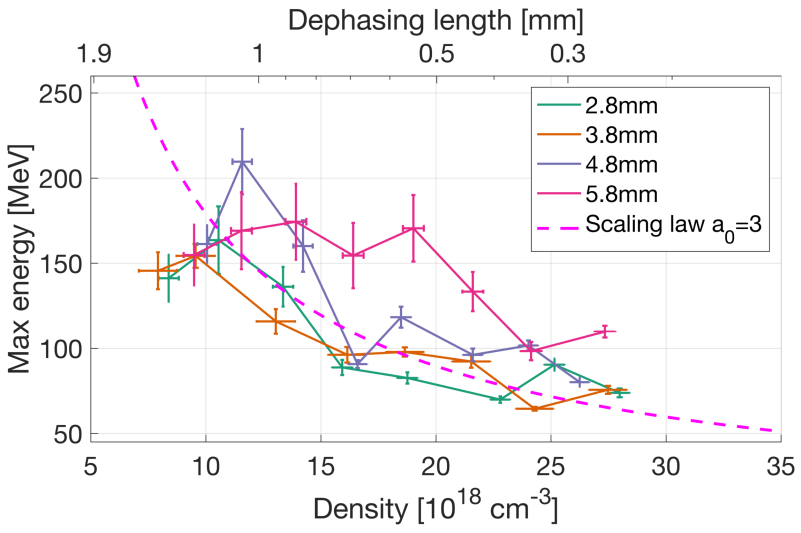


Figure 6.8: The maximum energy observed on the high energy electron spectrometer as a function of density for various cell lengths.

the longest cell length, exceeds the scaling law estimate of maximum energy, for most densities, assuming an $a_0 = 3$. This contrasts with the short cell lengths of 2.8 mm and 3.8 mm, where we observe a reasonable agreement with this energy estimate. The energy of the beam is influenced primarily by the longitudinal fields of the wake, we can also examine the properties of the transverse fields using the divergence and the pointing of the electron beam, measured on the beam profile monitor.

Beam divergence

The beam divergence for different cell length and densities is shown in Figure 6.9.

We can see that increasing the density of the medium has the effect of increasing the beam divergence. This is valid for most densities except for the highest densities where for cell lengths of 2.8, 3.8 and 5.8 mm, the long axis divergence decreases at the highest densities. The largest long axis divergence value for the electron beam is 10.1 ± 0.1 mrad, occurring at a density of $2.2 \pm 0.1 \times 10^{19}\text{cm}^{-3}$ and a cell length of 3.8 mm.

Conversely, the smallest short axis beam divergence is 1.5 ± 0.1 mrad, at a density of $1.37 \pm 0.05 \times 10^{19}\text{cm}^{-3}$ and cell length of 4.8 mm. In Figure 6.9, we see that for a cell length of 3.8 mm, the short axis divergence, increases much more rapidly with density than for other cell lengths. The difference in density, between 3.8 mm and other cell lengths becomes more pronounced, at higher densities.

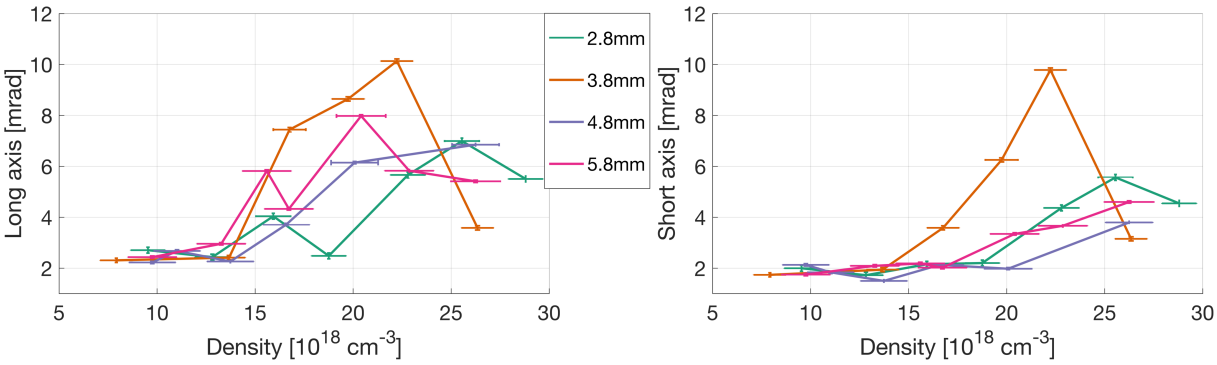


Figure 6.9: The long axis and short axis divergence observed on the beam profile diagnostic as a function of density for various cell lengths.

Eccentricity

We notice that the electron beams are asymmetric for some densities as the long and short axis divergences have different values for some densities. In order to characterise

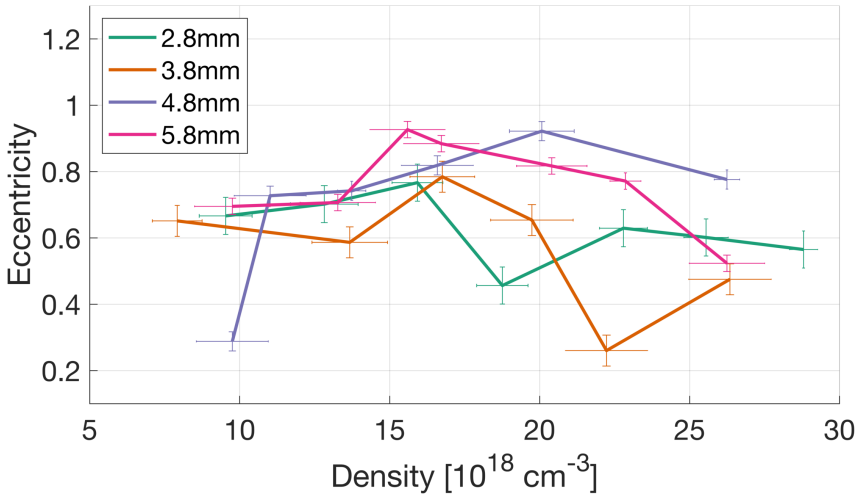


Figure 6.10: The beam eccentricity as a function of density for various cell lengths.

this effect, we examine the linear eccentricity of an ellipse, which is defined as

$$e = \sqrt{1 - \left(\frac{a}{b}\right)^2}. \tag{6.6}$$

where e is the linear eccentricity, b is the short axis of the ellipse and a is the long axis of the ellipse. When $e = 0$, we have perfectly symmetric electron beams. In Figure 6.10, we examine the eccentricity for a range of densities and length. We can see that the largest value for the eccentricity of the beam, i.e. the most elliptical electron beam, has an eccentricity of $e_{max} = 0.93 \pm 0.06$, occurring at a cell length of 5.8 mm and a density of $1.56 \pm 0.13 \times 10^{19}\text{cm}^{-3}$.

The minima in the eccentricity of the electron beam has an eccentricity of $e_{min} = 0.26$, at a cell length of 3.8 mm and a density of $2.22 \pm 0.01 \times 10^{19}\text{cm}^{-3}$. In general, within the error bars, we see that the eccentricity is low for the lowest densities where electron beams are observed. It increases as the density is increased, reaching maximum and then decreasing again.

Transverse momentum

The use of both the beam profile diagnostic and the electron spectrometer, allows one to estimate the transverse component of momentum p_r. We have already seen how the divergence of the electron beam can be related to its components of momenta in the case

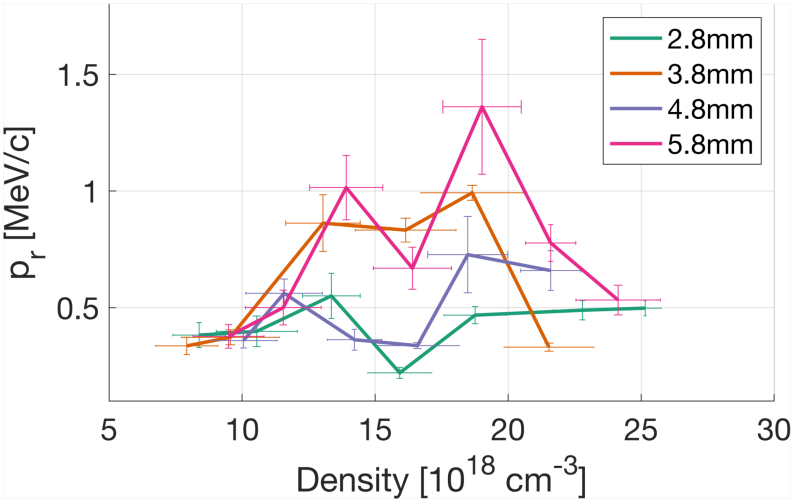


Figure 6.11: The transverse momentum as a function of density for various cell lengths.

of an uncorrelated energy spread,

$$\langle \theta_{div} \rangle = \frac{\langle p_r \rangle}{p_z}, \tag{6.7}$$

where $\langle \theta_{div} \rangle$ is the root mean square (RMS) beam divergence, p_z is the forward momentum of the electron beam and $\langle p_r \rangle$ is the RMS transverse momentum of the electron beam. The beam divergence is obtained using the beam profile diagnostic and the forward momentum is measured using the electron spectrometer. This provides us with an expression for the transverse component of momentum as

$$\langle p_r \rangle = p_z \langle \theta_{div} \rangle \tag{6.8}$$

In Figure 6.11, we plot the transverse component of momentum for a range of different densities and cell lengths. This momentum is for particles within a 30 mrad angle of the optical axis and for energies $E > 45$ MeV. In Figure 6.11, we can see that the highest value of the transverse momentum is $p_{r,max} = 1.36 \pm 0.52$MeV/c, occurring at a cell length of 5.8 mm and a density of $1.9 \pm 0.1 \times 10^{19}$cm^{-3}.

The lowest value of transverse momentum, $p_{r,min} = 0.22 \pm 0.04$MeV/c, at a cell length of 2.8 mm and a density of $1.6 \pm 0.1 \times 10^{19}$cm^{-3}. We also observe the relationship between transverse momentum and density, for a fixed cell length, within the uncertainty for each dataset, falls into two categories; interactions which occur at 2.8, 4.8 mm and 3.8, 5.8 mm. For long cell lengths the transverse component of momentum becomes highly variable. This is more pronounced at the higher densities that the lower densities. This uncertainty is dominated by the error in the measurement of the longitudinal momentum of the electron beam.

In this section, we have seen how the properties of the electron beam can vary across the density and length parameters space. Optimality for some parameters such as charge are different for others such as maximum energy. We have seen how self-injection can generate extremely high charge, high energy and low divergence beams and the wake-evolution is purported to play an important role in the final beam properties. In the next section, simulations of the interaction using particle-in-cell codes are presented to understand the behaviour of the measured beam properties.

6.4 Simulations: 6mm density scan of self injection at TA2

In the previous section, we have presented some experimental measurements on the spectral and spatial properties of electron beams generated using the self-injection mechanism at a 10 TW laser facility. Electron beam energies upto 210 ± 19 MeV were observed on the spectrometer. Electron beam charge upto 50.0 ± 2.3 pC was also observed. We are operating at mismatched conditions and for this particular configuration, the vacuum spot size for this configuration is 18 µm. Consider the matched spot size equation,

$$k_p w_0 = 2\sqrt{a_0}. \tag{6.9}$$

Assuming an $a_0 \approx 3$, and electron densities of $1 \times 10^{19}\,\mathrm{cm}^{-3}$ from the experimental data, where we observe electron beams, the required spot size is $w_{0,m} = 5.8\,\mu\mathrm{m}$. We can see that the vacuum a_0 is quite far from this and that we are reliant on the effects of self-focusing and pulse compression to reach the a_0 needed to drive a non-linear wakefield. The highly dynamic nature of the evolution of the accelerator will now be addressed using the 2D-3V particle-in-cell code FBPIC [3].

This PIC code uses a pseudo-spectral solver, which for the purposes of this chapter is utilised with an infinite stencil order which is akin to using spectral modes as large as the simulation grid can support [228]. This has the advantage of eliminating numerical dispersion which time-domain PIC codes suffer from. Numerical dispersion causes the laser pulse group velocity to depend on the spatial resolution of the simulation.

This PIC code also utilises a cylindrical PIC algorithm with azimuthal Fourier decomposition, sometimes referred to as quasi-3D [229, 230]. These quasi-3D codes capture the non-linear self-focussing effects in plasma, crucial to having an accurate picture of the underlying physics while only requiring a little more computational resources than 2D-3V simulations.

Simulation setup

A parameter scan was performed over the density range over which we observe electron beams and the injection of electrons into the wakefield and the energy they reach at their exit was examined. The density was varied for each simulation from $7 \times 10^{18} - 3 \times 10^{19}\,\mathrm{cm}^{-3}$ in 8 logarithmically spaced intervals.

The simulations assumed a trapezoidal density profile for helium, which was assumed to be fully ionised and the ramp length was 100 µm. A moving window was employed with the velocity of the window set to be the non-linear group velocity of the laser pulse in the plasma $\gamma = 1 - \frac{3n_c}{2n_e}$. In Table 6.3, the parameters of the simulation are shown.

In Figure 6.12, we show an overview of the dynamics of the injected electrons in the wakefield. Each row of the plot represents a simulation performed at increasing density. For breviety, only half of all the densities sampled are shown in this figure. Each column highlights a different aspect of the electron beam.

The first column presents the momentum-history plot for the total energy of the electron beam. In this plot, every vertical slice of the image is the histogram of the energy of the particle at a particular instant in time. This allows us to visualise the evolution of the particle energy to see the electron injection, acceleration and dephasing processes.

The second column is the on-axis longitudinal electric field evolution plot or wake-evolution plot for short. Within each figure, the vertical slice of the image is the z component of the electric field (E_z) in the simulation along the axis of symmetry at $r = 0$. The longitudinal contribution to the electric field is dominated by the wakefield and we can examine how the wakefield evolves along the length of the plasma.

Variable	Value	Variable	Value
dz	20.0 nm	dr	83.3 nm
no. cells z	2699	no. cells r	540
no. θ modes	3	ppc z, r, θ	1,1,12
Window length z	54.0 µm	Window length r	45 µm
a_0	0.6	w_0	18 µm
Laser wavelength	800 nm	τ	45 fs
Electron density	$0.7 - 3 \times 10^{19}\,\mathrm{cm}^{-3}$	No. densities	8

Table 6.3: Input parameters of the simulation. ppc stands for particles per cell, dz is the longitudinal spatial resolution, dr is the radial spatial resolution. The θ modes represent the number of Fourier azimuthal modes that the fields are decomposed into.

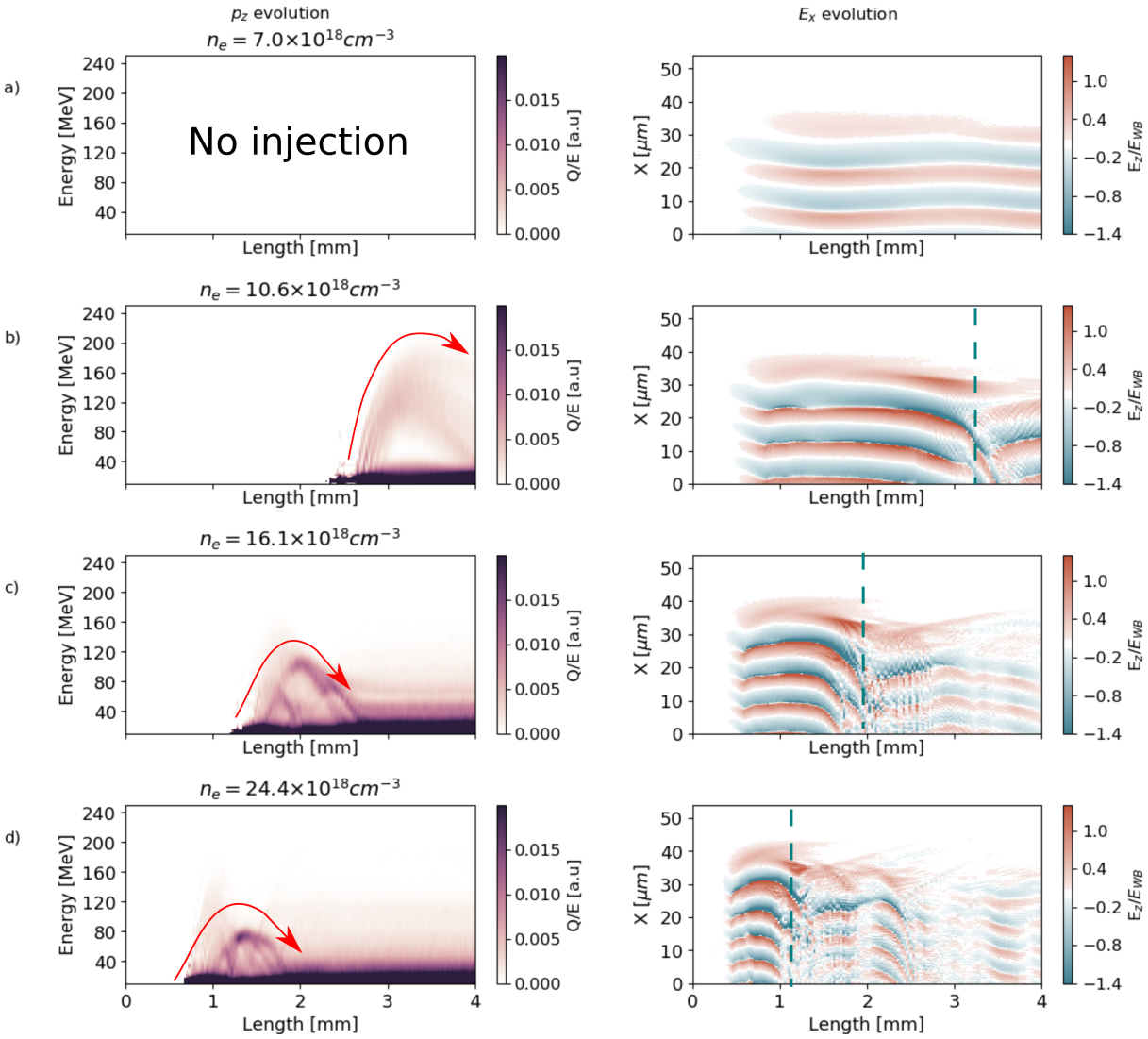


Figure 6.12: Simulation overview showing the momentum-history plot for the longitudinal momentum in the first column and the line-out of the on-axis longitudinal electric field as a function of time in the second column. Every row represents a simulation performed at a different density. The density for each panel is given in the title of the first column. The red arrow on the p_z evolution plot shows the acceleration and dephasing of particles in the accelerator. The dashed green line on the E_x evolution plot shows where the wake amplitude decreases due to depletion.

From this overview-plot we can see that self-injection begins for densities between $7 \times 10^{18}\,\mathrm{cm}^{-3} > n_e > 1.06 \times 10^{19}\,\mathrm{cm}^{-3}$ and particles reach $\approx 190\,\mathrm{MeV}$ in Figure 6.12b. Increasing densities, as could be expected due to dephasing, has the effect of reducing the highest energies that the particles are accelerated to. In the wake-evolution plots in Figure 6.12, we can see that for densities where particle injection is observed, the wake amplitude grows until the wake beaks or until the laser pulse driving the wake is depleted.

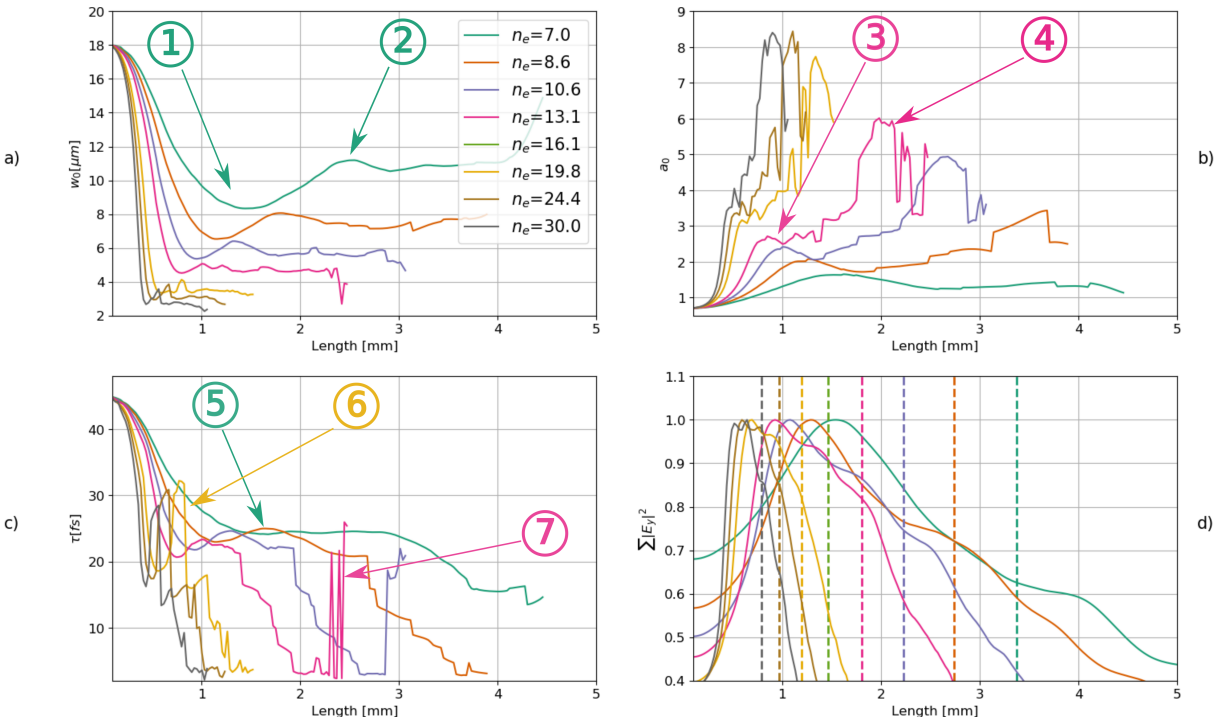


Figure 6.13: Variation of laser pulse parameter over its evolution in the accelerator for a range of different densities. The dashed vertical line in d) represents the depletion length $L_{pd} = c\tau\frac{n_c}{n_e}$. In a) is the evolution of the spot size of the laser pulse. ① shows the effect of self-focussing which reduces the spot size of the pulse to a minimum. ② shows the matched spot size at which the laser pulse evolves to. In b) the peak a_0 of the laser pulse is shown. ③ shows the initial increase in the peak a_0 of the pulse due to transverse and longitudinal compression. ④ shows the secondary increase in a_0 due to the central wavelength of the pulse increasing. In c) the evolution of the pulse duration is shown. ⑤ shows that the initial pulse compression approaches a plateau. ⑥ shows the increase in pulse duration for the higher density simulations as some part of the pulse is trapped in the second bucket of the wake. ⑦ is noise due to a lack of signal for determining the pulse duration. In d) the evolution of the energy of the y component of the electric field is shown.

The highly discontinuous nature of the wake evolution for long interaction lengths is attributed to the laser pulse driving the wakefield depleting and breaking up into many beamlets. The acceleration of particles is terminated for these interaction lengths where the particle energies can be see to remain relatively constant. We now move onto examining properties of the laser pulse as it traverses the medium in Figure 6.13. The pulse duration and spot size are extracted by first performing a Hilbert transform on the laser pulse to extract the pulse envelope. The $\frac{1}{e}$ contour of the electric field is extracted and the longitudinal width is taken to be the pulse duration and the transverse width is the spot size of the laser pulse.

The evolution of the spot size is highlighted in Figure 6.13a, where we can see the effect of self-focussing for interaction lengths $0.2 - 2\,\mathrm{mm}$. The spot size approaches a minima and if the pulse is not depleted by the end of the simulation or diffracted it will guide at its matched spot size. This is referred to as self-guiding and allows the interaction length to be much greater than the Rayleigh range, which for this experimental configuration is $z_r = \frac{\pi w_0^2}{\lambda} = 1.3\,\mathrm{mm}$.

In Figure 6.13c, we can see that the pulse experiences some compression in the plasma, depending on its $\frac{n_e}{n_c}$. Pulse front etching occurs as the front of the laser pulse is being eroded from driving a wakefield. Energy is either diffracted away from the laser spot or red-shifted causing them to fall behind the main driving pulse resulting in a gradual loss of pulse duration. When the laser pulse depletes, the calculation of pulse duration from simulations becomes spurious, as the beam breaks up into many beamlets, as observed by the highly discontinuous nature of the pulse duration and spot size. In Figure 6.13c, we have omitted the plotting of timesteps where the total energy of the pulse drops below 50% of its maximum value.

In Figure 6.13b, we extract the peak a_0 of the laser pulse. The central frequency is calculated by using the Fourier transform of the on-axis lineout of the y component of the electric field E_x and then extracting the frequency at which the amplitude of the transform is maximised. Using this we can calculate the peak a_0 in simulations as,

$$a_0 = \frac{eE}{m_e c \omega_L}. \tag{6.10}$$

We can see that the a_0 of the laser pulse increases even in the presence of pump depletion [112, 134]. Finally in Figure 6.13d we show the energy loss of the y-component of the electric field. We see that the pump depletion varies across the length of the accelerator with depletion occurring earlier for lower densities. We now move onto examining the particle properties of the injected electron beam. Specifically, we will address the charge of the electron beam $E > 45\,\mathrm{MeV}$, the maximum energy and the time-scale for injection to occur.

Charge

In Figure 6.14, the charge $Q(E > 45\,\mathrm{MeV})$ is shown across the various densities sampled. we see that the maximum charge is achieved for cell lengths between $1 - 2\,\mathrm{mm}$ and is $\approx 40\,\mathrm{pC}$, which is close to the measured charge of $\approx 50\,\mathrm{pC}$.

For lower densities, the injected charge decreases, with the peak in the charge of the electron beam occurring at later instances in the simulation. The injected of charge is

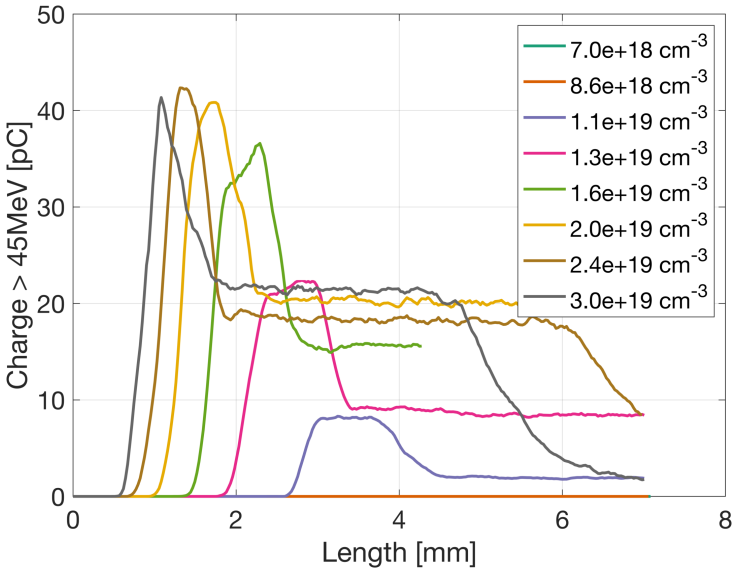
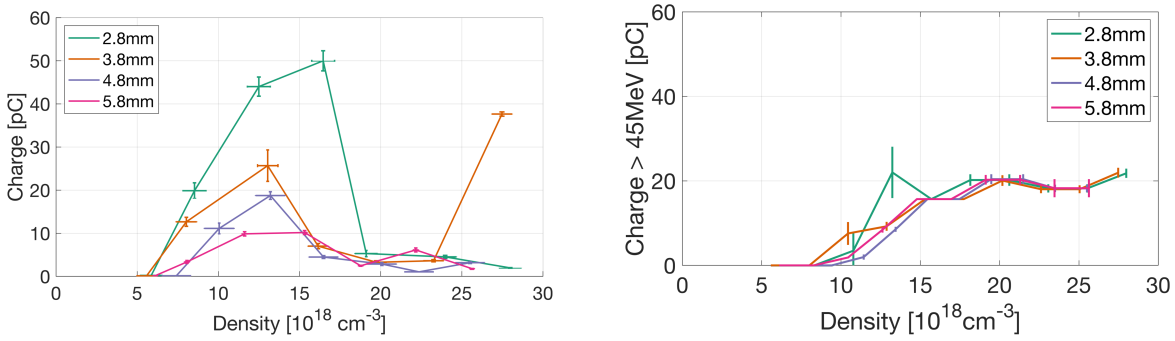


Figure 6.14: The charge of particles with $E > 45\,\mathrm{MeV}$, extracted from simulations as a function of length for a range of densities. For densities where injection occurs we can see that the charge reaches a maximum value and then settles at an intermediate value afterwards. Lower densities begin injecting charge after greater propagation distances in the plasma. Additionally they also inject a lower quantity of charge in the accelerator.

linked to rate of self-focussing, for lower densities, the reduced rate of self-focussing from the vacuum spot size to its guided spot size results in a reduction in the peak trapped charge in simulations. We also see that as a function of length, for charge above the spectrometer energy threshold, we see a reduction in the predicted charge as electrons are being dephasing. For extremely long lengths, where the wakefield amplitude is diminished as the driver is depleted, we see that there is negligible variation in charge with length.



(a) Experiment (b) Simulation

Figure 6.15: The charge of particles with $E > 45\,\mathrm{MeV}$ from the experiment on the left hand side and simulations on the right hand side, as a function of density for different interaction lengths.

We now recast the data from Figure 6.14 to compare to the experimental dataset. This is shown in Figure 6.15. The error-bar in Figure 6.15b is the standard deviation of all values of charge ±0.5mm from the mean value of length.

From Figure 6.15, we can see that except for the shortest cell length where experiments measure much larger peak electron beam charges, for all other cell lengths we observe reasonable agreement for the charge below $n_e \leq 1.5 \times 10^{19}\,\mathrm{cm}^{-3}$. The highest charge is attained for cell length $< 2\,\mathrm{mm}$ with a value of 40 pC which is not far from the highest charge measured in experiments.

The charge from simulation, at the highest densities, does not decrease as the experimental data does. One limitation of these simulations is that as the system departs from being cylindrically symmetric, the number of Fourier modes required to accurately describe the interaction increases. This departure at higher densities represents a limitation of the simulations.

Maximum energy

Figure 6.16 presents the maximum particle energy, defined as the point at which the cumulative integral of the energy spectrum reaches 99% of its maximum value, which is equivalent to the way maximum energy is calculated with the experimental data. We can see that the highest energies are attained for the lowest densities at which charge is observed, reaching a maximum energy of 194 MeV at a density of $1.1 \times 10^{19}\,\mathrm{cm}^{-3}$ and a cell length of 3.5 mm.

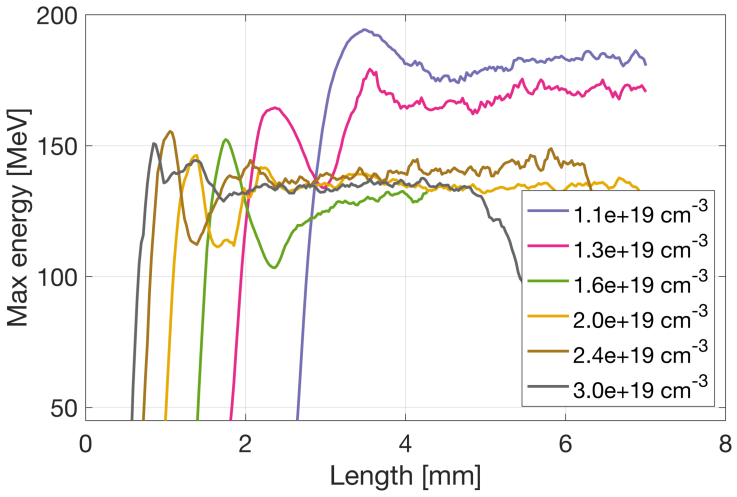
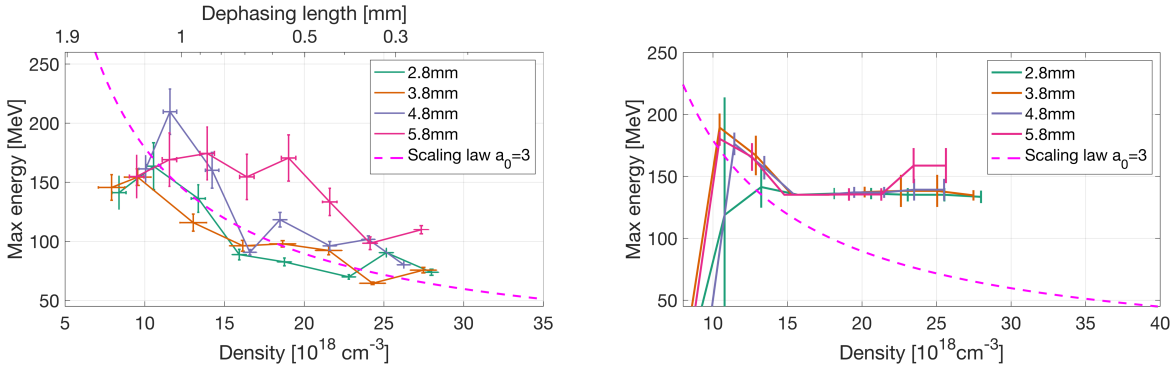


Figure 6.16: The maximum energy extracted from simulations for particles with $E > 45\,\mathrm{MeV}$ as a function of the interaction length for a range of densities.



(a) Experiment (b) Simulation

Figure 6.17: Figure showing the maximum energy of the electron beam from the experimental data on the left hand side and simulations on the right hand side.

The electron beam maximum energy reaches a limiting value after which it does not vary significantly with length, for the same density. We see that for the lowest densities, this limiting value is higher than for the higher densities. We see that the for lengths greater than 3 mm and densities greater than $1.3 \times 10^{19}\,\mathrm{cm}^{-3}$, this threshold energy does not vary with density as would be expected of the $\frac{1}{n_e}$ relationship with density.

Power amplification is attributed to this modification to the energy gain scaling law. In a similar manner to the beam charge section, we re-plot the data from Figure 6.16 to allow for a visual comparison with the experimental data in Figure 6.17. We can see that the simulations, qualitatively confirm the observations of the peak energies of the highest energy electron beams occurring at the lowest densities. The agreement breaks down for the highest densities where simulations predicts higher energies than we observed on experiments.

A more interesting observation from this comparison of experiment and simulation is the increasing maximum energies for densities around $1 \times 10^{19}\,\mathrm{cm}^{-3} = 1.2 \times 10^{19}\,\mathrm{cm}^{-3}$. We can see that as the length is increases from $2.8\,\mathrm{mm} - 5.8\,\mathrm{mm}$, the maximum energy increases. This is attributed to power amplification of the laser pulse in the medium.

Evolution length

We now address the modifications to the familiar matched evolution scenario using the concept of evolution length, L_{evo} developed by Bloom et al. [231]. We define evolution length as the distance at which the injection of particles occurs in the plasma wave. The threshold for this injected is defined as the time at which the cumulative charge as a function of length reaches 1% of its maximum value.

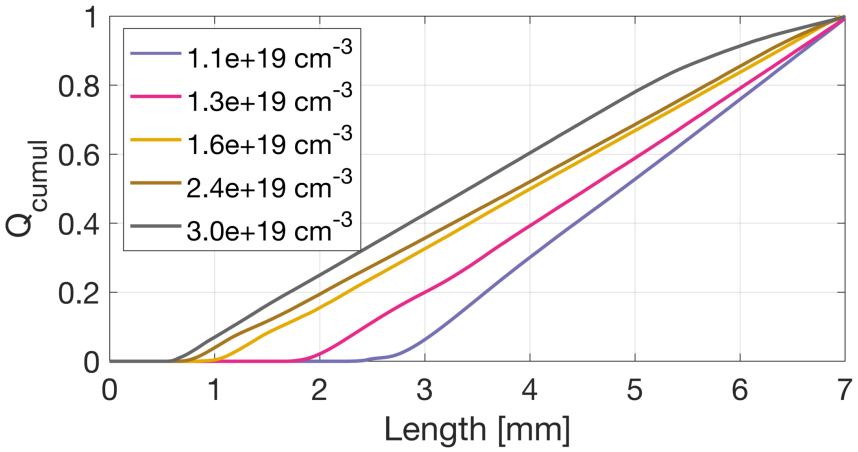


Figure 6.18: The normalised cumulative charge, Q_{cumul}, used to predict the point of injection threshold for various densities.

$$Q_{cumul}(L) = \frac{1}{L}\int_0^L Q_{>45\,\mathrm{MeV}}(L')\mathrm{d}L', \tag{6.11}$$

where L_{evo} is defined as a length at which the $Q_{cumul}(L_{evo}) \equiv 0.01\max(Q_{cumul})$. We plot this quantity in Figure 6.18 to show how it is used for the injection threshold.

Even when the charge as a function of interaction length is not varying monotonically, we can use this definition to uniquely extract the injection point. The other advantage of this definition is that is defines the threshold for injection based on the largest injected event across the entire simulation length. This accounting of the charge across the entire simulation length allows the discrimination of small injection events.

In Bloom et al. [231], the evolution length is defined as,

$$L_{evo} = S\frac{n_c}{n_e}, \tag{6.12}$$

where n_e is the electron density, n_c is the critical density and S is a free parameter which characterises the length scale over which the self-focussing and pulse compression effects occur. S is independent of density and dependant on the laser pulse parameters.

In Figure 6.19, we can see that the evolution length scales quadratically with $\frac{n_c}{n_e}$, rather than linearly. One reason for this is that self-focussing and pulse compression both independantly increase the peak a_0 of the laser pulse. Both these effects scale with $\frac{n_c}{n_e}$ and their combined effect results in a quadratic dependence on the evolution length. Hence, we redefine the evolution length as,

$$L_{evo} = S\left(\frac{n_c}{n_e} + \alpha\right)^2, \tag{6.13}$$

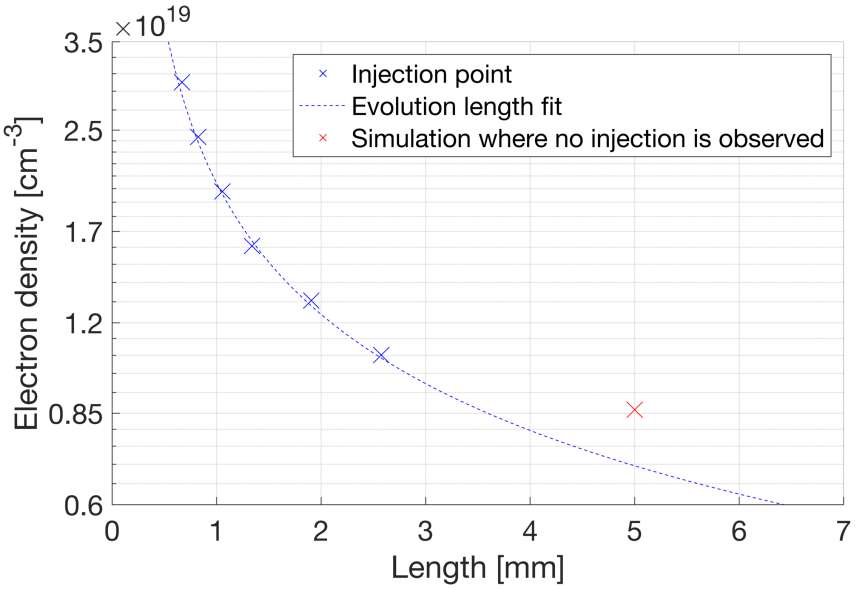


Figure 6.19: The predicted evolution length for self-injection extracted from simulations. The blue marker are simulation points where injection is observed. The blue line is the corresponding fit using the blue markers to Eq. 6.13. The red marker is the lowest density at which injection is not observed and the red line depicts the boundary at which we exclude any injection.

where α is an additional fitting parameter introduced from requiring a quadratic fit. By performing a least square fit, it was found that $S = 55.6 \pm 8.9\,\text{nm}$ and $\alpha = 48.4 \pm 10.5$. The additional fitting parameter along with the requirement that $\frac{n_c}{n_e} > 1$ gives a minimum evolution length for injection of $136 \pm 22\,\mu\text{m}$ for this system by self-injection. The error bars represent the 95% confidence interval in the coefficients of the fit. The red marker represents the simulation at which particle injection is not observed.

In order to understand why the injection threshold occurs at this density, we examine the peak a_0 obtained over the evolution of the laser pulse in Figure 6.20. We also plot the matched a_0, which is the a_0 that the pulse focuses down to in the medium [115, p .60]. We have seen how the a_0 in the simulation varies dramatically depending on the density but takes the same functional form across the density range sampled in simulations from Figure 6.13b. The aim of this figure is to examine the minimum a_0 needed for injection and to see if we can predict the peak and matched a_0 evolution as a function of density.

We can see that for lower electron densities, the highest value of a_0 achieved by self-focussing and pulse compression decreases. Simulations imply that injection occurs when the peak a_0 of the driver pulse is $3 > a_0 > 5$. The following numerical fits were obtained

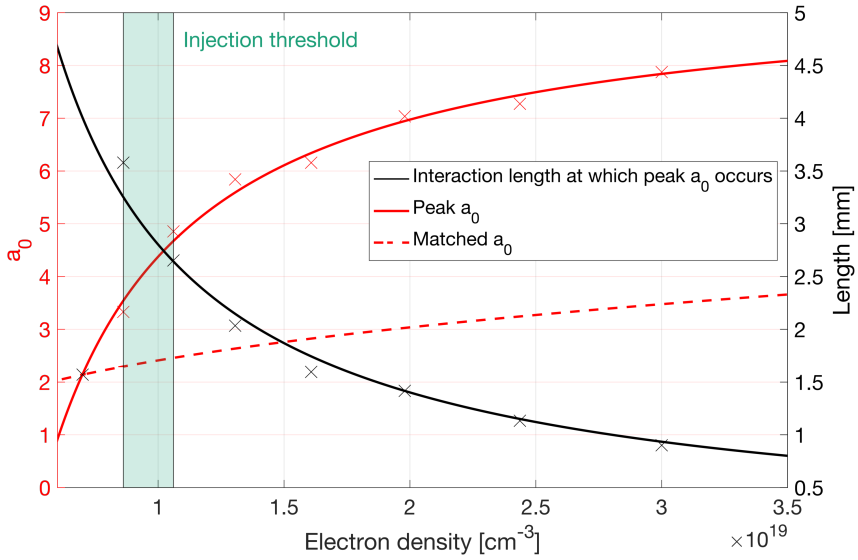


Figure 6.20: On the left hand side the highest value of a_0 obtained in the simulation is shown. The red markers are the data points corresponding to values extracted from simulations. The solid line is the result of the fit from Eq. 6.14. On the right hand side the simulation length at which the peak a_0 occurs is shown. For the matched a_0 (dashed red line), we have used $a_0 = (w_0 a_{0,i} \omega_p/(2c))^{2/3}$ with $w_0 = 18\,\mu\text{m}$ and $a_{0,i} = 0.7$.

from simulations for the peak a_0 - $a_{0,p}$ and the length required to reach the peak a_0-$L_{a0,p}$.

$$a_{0,p} = b_1 - a_1 \frac{n_c}{n_e} \qquad L_{a0,p} = a_2 \frac{n_c}{n_e}, \tag{6.14}$$

where $a_1 = 3.0 \pm 0.4 \times 10^{-2}$, $b_1 = 9.6 \pm 0.6$, $a_2 = 1.6 \pm 0.5 \times 10^{-2}$. As self-focussing and pulse compression rely on $\frac{n_c}{n_e}$, we can see that the peak a_0 and the length scale required to reach it also scale similarly for SI. The difference between the evolution length and the length at which the peak a_0 occurs, for densities where injection is observed is $\approx 30\%$, where injection always occurs before the peak a_0 is reached. This model for a_0 is also only valid for $P > P_c$. We can see that in this model b_1 physically represents the maximum a_0 we can achieve through pulse evolution effects.

6.5 Discussion

This section is divided into the various electron beam parameters shown in section 6.3, where, models and scaling laws for each of these parameters available in literature, are discussed. Most of these models are strictly valid for the matched regime but we will none-the-less discuss how they compare with observations to understand if they can capture the underlying interaction. We will address extensions to existing models which help improve the predictive capabilities of these scaling laws for this evolving regime.

Secondly, we address the particle-in-cell simulations performed for the setup in Section 6.4, within the context of each specific electron beam parameters. These simulations include the highly dynamic evolution of the laser pulse, the generated plasma wave and the injected and accelerated electron beams. The differences and similarities between the simulations, scaling law and experimental data are examined, concluding with assumptions of the interaction which can be improved to attain better agreement between simulations and the experimental data.

Charge

First, we address the charge observed on the high energy electron spectrometer (E> 45 MeV) as a function of density and length in Figure 6.6. We recall that the highest charge observed across the all densities and cell lengths is $Q_{max} = 50.0 \pm 2.3\,\mathrm{pC}$, at a density of $1.65 \pm 0.13 \times 10^{19}\mathrm{cm}^{-3}$ and cell length of 2.8 mm. We can compare this to the beam loading limit examined by Lu et al. [130],

$$N_{max} \approxeq 2.8\left(\frac{\lambda_{0,\mu\mathrm{m}}}{0.8}\right)\left(\frac{P_{\mathrm{TW}}}{100}\right)^{1/2}. \tag{6.15}$$

Using $P = 10\,\mathrm{TW}$, $\lambda_{0,\mu\mathrm{m}} = 0.8$ we obtain a maximum charge of 142 pC. We can see that experimentally we are at 35% of the highest charge which can be accelerated by the system for these conditions.

Next we examine the charge at $n_e = 2.75 \pm 0.15 \times 10^{19}\mathrm{cm}^{-3}$ for a cell length of 3.8 mm, where we see an anomalously large charge. We note from the introduction section of this chapter, the density region of interest where, for this pulse duration of 45 fs, the laser pulse is twice the plasma wavelength, occurs at $n_{e,SM} = 2.5 \times 10^{19}\,\mathrm{cm}^{-3}$. The interaction departs from the ideal regime for a self-guiding LWFA towards and self-modulated LWFA. The energy spectrum of electron beams for self-modulated laser wakefield accelerators are exponential. Due to the energy cut-off of the high energy electron spectrometer, we do not observe charge on this diagnostic until the energy of the beams has exceeded the minimum

threshold of the accelerator of 45 MeV. The energy threshold of the spectrometer explains why the largest charge observed on the low energy electron spectrometer in Figure 6.7, occurs at these identical conditions of $n_e = 2.75 \pm 0.15 \times 10^{19}\text{cm}^{-3}$ and $L = 3.8\,\text{mm}$ as the dephased electrons now contribute to the charge in the $10\,\text{MeV} < E < 45\,\text{MeV}$.

We move on to examining the effect of varying cell length. Ideally, if the operation of varying the length of the cell was uncoupled to the density of the target, by varying the length of the cell we perform a measurement of the electron beam at various points along its path in the plasma. For a fixed length, we pick the density at which the charge was at its highest and plotted them against various cell lengths in Figure 6.21. The highest charge electron beams were observed between $9 \times 10^{18}\,\text{cm}^{-3}$-$1.5 \times 10^{19}\,\text{cm}^{-3}$.

We note that the 3D non-linear dephasing length for electron beams, assuming an $a_0 = 3$, which was the minimum needed for self-injection [121], at these densities were $L_{dp} = 2.4\,\text{mm}$-$1.1\,\text{mm}$. As the interaction length was varied 1 mm at a time, we would not have observed detailed dynamics in the evolution of the charge, on the length scale of its evolution. We can still identify regimes of optimality for charge and see how this changes as a function of length. In Figure 6.21, we can see that the charge is continuously decreasing along the length of the accelerator at an average gradient of $-12.6\,\text{pC}\,\text{mm}^{-1}$.

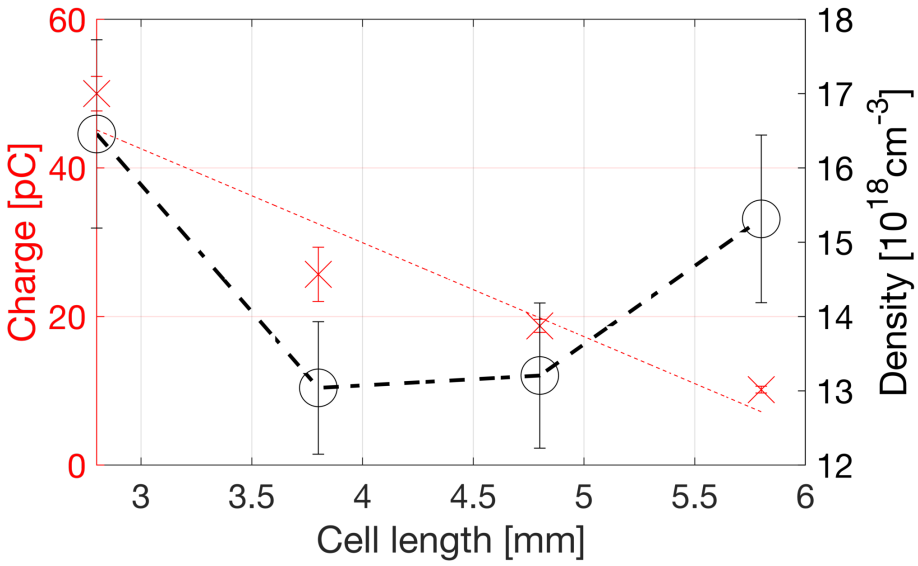


Figure 6.21: The highest charge obtained across all values of density for each cell length is shown by the red x marker on the left hand axis. The dashed red line is a fit the experimental data for charge as a function of length. On the right hand axis, the corresponding density at which this charge occurs is shown by the black circle marker. The black dashed line is a linear trend-line between each point.

The loss of charge observed on the high energy spectrometer ($E > 45\,\mathrm{MeV}$) is attributed to particles dephasing from early injection events. The density on the RHS of Figure 6.21 is the density at which this charge is observed. We can see that between $2.8 - 3.8\,\mathrm{mm}$, the optimum density for charge decreases but then increases for subsequent interactions lengths. One reason for this could be that in order to access the extended interaction length attained by self-guiding, lower densities are more preferable for generating higher charge electron beams, as they extend the depletion/dephasing lengths. However, after 3.8 mm, we are well beyond the depletion length. For densities in the range of $1 \times 10^{19}\,\mathrm{cm}^{-3} - 1.5 \times 10^{19}\,\mathrm{cm}^{-3}$, $L_d = 2.4\,\mathrm{mm} - 1.7\,\mathrm{mm}$.

Another source of beam charge loss could be due to scattering with the remaining plasma in the path of the electron beam. The unionised gas contribution to the scattering of the electron beam is assumed to be minimal as the electron beam has to go through the laser dump and the beam profile screen, both of which will be of significantly higher areal density.

Particle-in-cell simulations were used to make predictions on the beam charge as a function of density for a range of different cell lengths in Figure 6.15. These simulations predict similar beam charge upto 40 pC in Figure 6.14, but this charge occurs at interaction lengths much shorter than those observed from the experimental data. The profile of charge as a function of density from the experimental data shows a large variation with cell length where as the simulations do not reflect this.

One possibility for the mismatch between simulations and experiments could be due to the density profile of the medium varying as a function of interaction length. The shortest cell lengths could cause perturbations if the cell length approaches the diameter of the exit and entrance holes [232]. The entrance hole was initially 100 µm but rapidly expands to $\approx 300\,\mu\mathrm{m}$ over 100 shots. Differences in the entrance and exit hole diameters could cause gradients in density to be present in this target [152]. Further investigation using fluid simulations will be required to assess the significance of these effects on the interaction.

Maximum energy

The maximum energy of the electron beam was presented in section 6.8. We recall that the largest electron beam energy observed was $210 \pm 19\,\mathrm{MeV}$, at a density of $1.16 \pm 0.08 \times 10^{19}\mathrm{cm}^{-3}$. Consider, for a fixed cell length, the highest energy across a range of electron densities. We can plot this as a function of cell length in Figure 6.22. Here we observe that between $3.8 - 4.8\,\mathrm{mm}$, there is a sharp increase in the energy of the electron beam and

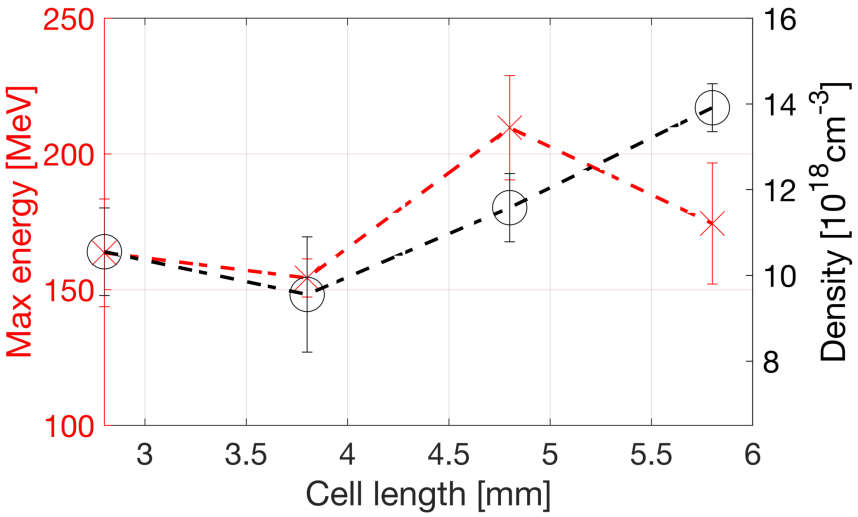


Figure 6.22: Maximum energy as a function of the cell length is shown by the red x marker on the left hand axis. The dashed red line is the maximum energy on the left hand axis. On the right hand axis, the corresponding density at which this maximum energy occurs is depicted by the black circle marker. The dashed black line is a trend-line between these density points.

a small increase in the density at which this occurs. Consider the energy gain equation,

$$\begin{aligned} W_{max} &= m_e c^2 \frac{2a_0 n_c}{3n_e} \\ W_{max} n_e &\propto a_0. \end{aligned} \tag{6.16}$$

Using the relative differences in density and energy gain, we can conclude the the free parameter in the energy gain equation, a_0 must increase along the interaction length. The a_0 of the laser pulse must increase by 56% to explain the difference in the maximum energy between 3.8 mm and 4.8 mm at corresponding densities of $9.6 \times 10^{18}\,\mathrm{cm}^{-3}$ and $1.16 \times 10^{19}\,\mathrm{cm}^{-3}$.

In Section 6.4, we explored this beam parameter using PIC codes. The highest energies observed in simulations was 194 MeV, occurring at a density of $n_e = 1.1 \times 10^{19}\,\mathrm{cm}^{-3}$ and cell length of 3.5 mm. We obtain a reasonable agreement with the experimental data for densities $n_e < 1.5 \times 10^{19}\,\mathrm{cm}^{-3}$. For higher densities, the simulation predicts maximum beam energy higher than the scaling law. This is due to limitations in the simulations arising from the use of a finite number of azimuthal modes.

Divergence

From the beam profile diagnostic, the divergence of the electron beam was extracted in Figure 6.9 for a range of densities and cell lengths. Only shots with charge $Q > 1\,\mathrm{pC}$ were

chosen for analysis. The divergence of the electron beam in the laser polarisation direction was always greater than the orthogonal direction. The largest observed divergence was 10.1 ± 0.1 mrad, at a density of $2.2 \pm 0.1 \times 10^{19}\text{cm}^{-3}$ and cell length of 3.8 mm. The acceptance of the electron spectrometer was 33 mrad, so it is possible that beams could have divergences greater than this. However, for the equivalent charge, the electron beams would be below the noise threshold of the detector. The smallest divergence observed was 1.5 ± 0.1 mrad, for a density of $1.37 \pm 0.05 \times 10^{19}\text{cm}^{-3}$ at a length of 4.8 mm.

We found that there is a stronger dependence on beam divergence with density than cell length in Figure 6.9. The largest beam divergence occurred at a density around $2 \times 10^{19}\,\text{cm}^{-3}$-$2.6 \times 10^{19}\,\text{cm}^{-3}$ and the smallest beam divergences occur at densities around $8 \times 10^{18}\,\text{cm}^{-3}$-$1.3 \times 10^{19}\,\text{cm}^{-3}$ for all cell length. Recall, the non-linear energy gain equation

$$\begin{aligned} W_{gain} &= a_0 m_e c^2 \gamma_p^2, \\ \gamma_p &= \sqrt{\frac{n_c}{n_e}} \end{aligned} \tag{6.17}$$

for $\frac{n_c}{n_e} \gg 1$, $W_{gain} \approx p_z c$. We assume the transverse component of momentum scales as

$$p_r \approx a_0 m_e c, \tag{6.18}$$

due to the laser pulse ponderomotively imparting momentum to the particles. We recall that the beam divergence can be expressed as

$$\begin{aligned} < \theta_{div} > &= \frac{p_r}{p_z} \\ < \theta_{div} > &= \frac{a_0 m_e c}{a_0 m_e c \gamma_p^2} \\ < \theta_{div} > &\propto n_e \end{aligned} \tag{6.19}$$

Consider the short axis divergence, if we plot these values solely against their densities, ignoring the 3.8 mm cell length, we obtain Figure 6.23. In this figure, we have used a power law fit to compare the experimental data with the derived scaling law.

$$\theta = a n_e^b \tag{6.20}$$

where a, b are fitting parameters, n_e is the density in 10^{18}cm^{-3} and θ is the beam divergence in mrad. For the axis orthogonal to the laser polarisation, the small axis, we obtain $a = 0.1 \pm 0.46\,\text{mrad}/10^{18}\text{cm}^3$ and $b = 1.15 \pm 0.6$, where the errors represent the 1σ confidence interval of the fitting parameters. For the axis parallel to the laser polarisation

axis, the long axis, we obtain $a = 0.24 \pm 0.34$ and $b = 0.98 \pm 0.39$. Hence, we can see that we obtain reasonable agreement with the obtained scaling law.

A larger data set needs to be acquired to reduce the uncertainty of the fit of the power law to test deviations from this qualitative scaling for beam divergence with density. It should be noted that we have assumed that the variations in the ramp are negligible when density is varies. It has been shown in literature that the downramp as the electron beam leaves the plasma accelerator is extremely important to minimise the divergence of the electron beam on the exit of the accelerator [233, 234]. An area for future study would be to understand how the ramp contributes to the changes in the divergence of the electron beam.

Finally, we address the anomalous increase in beam divergence for lengths of 3.8 mm at densities between $1.5 \times 10^{19}\,\mathrm{cm}^{-3}$-$2.5 \times 10^{19}\,\mathrm{cm}^{-3}$, the beam divergence is significantly greater in the short axis, and greater in the long axis directions. One possibility is that at these densities, the injected electron beam is interacting with the remaining laser pulse for this length. The increase in beam divergence with density, under this conjecture, assuming that the injection point is fixed, will result in separation between the electron beam and the laser pulse, as it exits the accelerator, with a dependence on n_e. This will arise from the group velocity of the laser pulse being lower for higher densities. We notice that the beam divergence is larger in the polarisation axis than the other orthogonal axis, as such, we will now proceed to examining the eccentricity of the electron beam

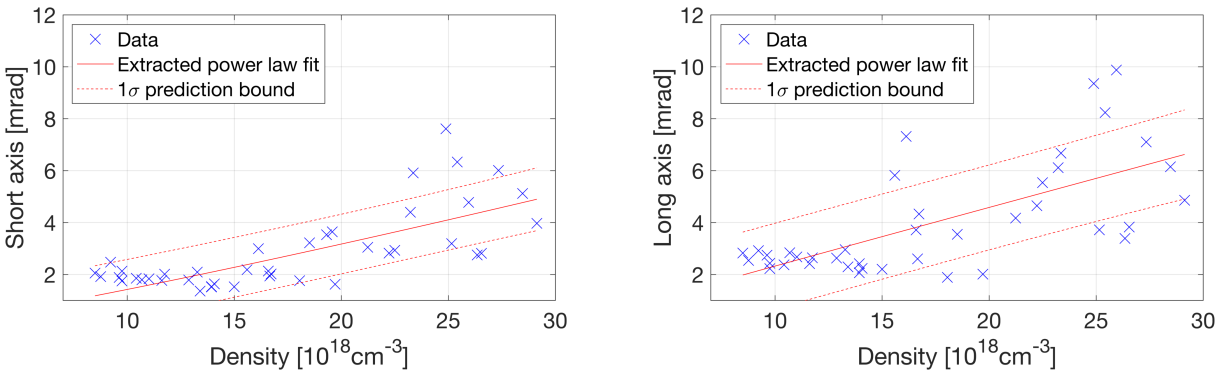


Figure 6.23: The dependence of the beam divergence along the laser polarisation (long axis) and orthogonal to it (short axis) with density. An associated power-law fit is extracted with density of the form $y = an_e^b$. The solid red line represents the power law fit and the dashed red-line represents the 1σ confidence interval for the fit.

Eccentricity

The eccentricity of the electron beam is defined as the ratio of the long axis to its short axis. Hence, when the eccentricity, $e = 0$, the electron beam is spherical. The largest value of eccentricity across density and lengths is $e_{max} = 0.93 \pm 0.01$, occurring at a density of $2.2 \pm 0.1 \times 10^{19}\text{cm}^{-3}$ and a cell length of 3.8 mm. High degrees of eccentricity can arise from an asymmetric injection into the wake, transverse forces on the electron beam which are not radially symmetric or multiple injection events with differing amounts of transverse momenta.

Asymmetric injection events can arise from small scale density modulations in the medium, or imperfections in the spatial profile of the laser pulse [235]. These can result in the formation of an asymmetric wake, which injects particles into the wakefield with different transverse momenta in different directions. The lowest value of eccentricity measured for these sets of parameters is $e_{min} = 0.26 \pm 0.01$ at a density of $2.22 \pm 0.14 \times 10^{19}\text{cm}^{-3}$ and a cell length of 3.8 mm.

Consider the eccentricity at the density of $2 \times 10^{19}\,\text{cm}^{-3}$ and a length of 4.8 mm and 5.8 mm. We can see that the eccentricity of the beam increases. We recall the depletion length $L_{pd} = c\tau \frac{n_c}{n_e}$, for this density gives us a depletion length of $L_d = 1.2$ mm. In-fact, PIC simulations show that the laser pulse must be depleted by this point in the simulation section. So the question arises, of how the eccentricity of the electron beam can decrease, for these densities and cell lengths. One possibility is that we transition to beam driven wakefield acceleration and the electron beam does not interact with the laser pulse strongly [223].

Transverse momentum

We finally address the transverse component of momentum in Figure 6.11. The largest value of transverse momentum inferred is $p_y = 1.36 \pm 0.52\,\text{MeV/c}$ at a density of $1.9 \pm 0.1 \times 10^{19}\text{cm}^{-3}$ and a cell length of 5.8 mm. The transverse momentum appears to fall into two different cell length categories; 2.8 mm, 4.8 mm and 3.8 mm, 5.8 mm. The first category have much lower values of transverse momentum that the latter category. For longer cell lengths, we observe a larger variation in the transverse momentum of the electron beam.

6.6 Conclusion

In this section, we have explored the density and length parameter space where self-guided laser wakefield acceleration occurs and self-injects electron into the plasma wave. We have examined various properties of the electron beam such as charge, maximum energy, beam divergence. Using these we have also other additional inferred beam properties such as beam eccentricity and p_r. The most notable values for these parameters and the density-length which they occur at, are presented in Table 6.4.

Parameter	Value	Density [10^{18}cm^{-3}]	Length [mm]
Highest charge	50.0 ± 2.3 pC	16.5±1.3	2.8
Highest energy	210 ± 19 MeV	11.6±0.8	4.8
Lowest beam divergence	1.5 ± 0.1 mrad	13.7±0.5	4.8
Highest eccentricity	0.93 ± 0.01	15.6±1.3	5.8
Lowest/Highest p_r	0.22±0.03,1.36±0.3 MeV/c	15.9±1.2,19±1.5	2.8,5.8

Table 6.4: The optimal values for various electron beam parameters along with their associated density-length values.

For this particular system, where the vacuum a_0, is significantly less than the a_0 required to drive a non-linear wakefield and attain injection, we have observed that we must be above the threshold density for self-focusing, if we are to observe any wave-breaking. PIC simulations indicate that the peak a_0 of the laser pulse must be between $3 > a_0 > 5$ in order to observe injection for this experimental configuration. This reliance on self-focusing is in-fact what causes the density-length parameter space to become coupled.

The interaction length can be limited by the length of the target or the extended Rayleigh range provided by self-focusing, which depends on the density. We see this in the maximum energy against density for a range of lengths in Figure 6.8 where the maximum energy is also a function of acceleration length despite the target length being larger than the dephasing length. From these scans we deduce that the a_0 of the laser pulse must be amplified as it traverses the medium, allowing the energy of the electron beam to exceed the scaling law estimates.

We also see signatures of the electron beam interacting with the laser pulse as its beam divergence increases dramatically around 3.8 mm and 5.8 mm at a density of 1.5×10^{19} cm^{-3} due to the dramatic increase in the transverse component of momentum. We see that the most circular beams are generated at the longest cell lengths and at a higher density. The faster rate of depletion, can limit the interaction of the electron beam with the laser pulse

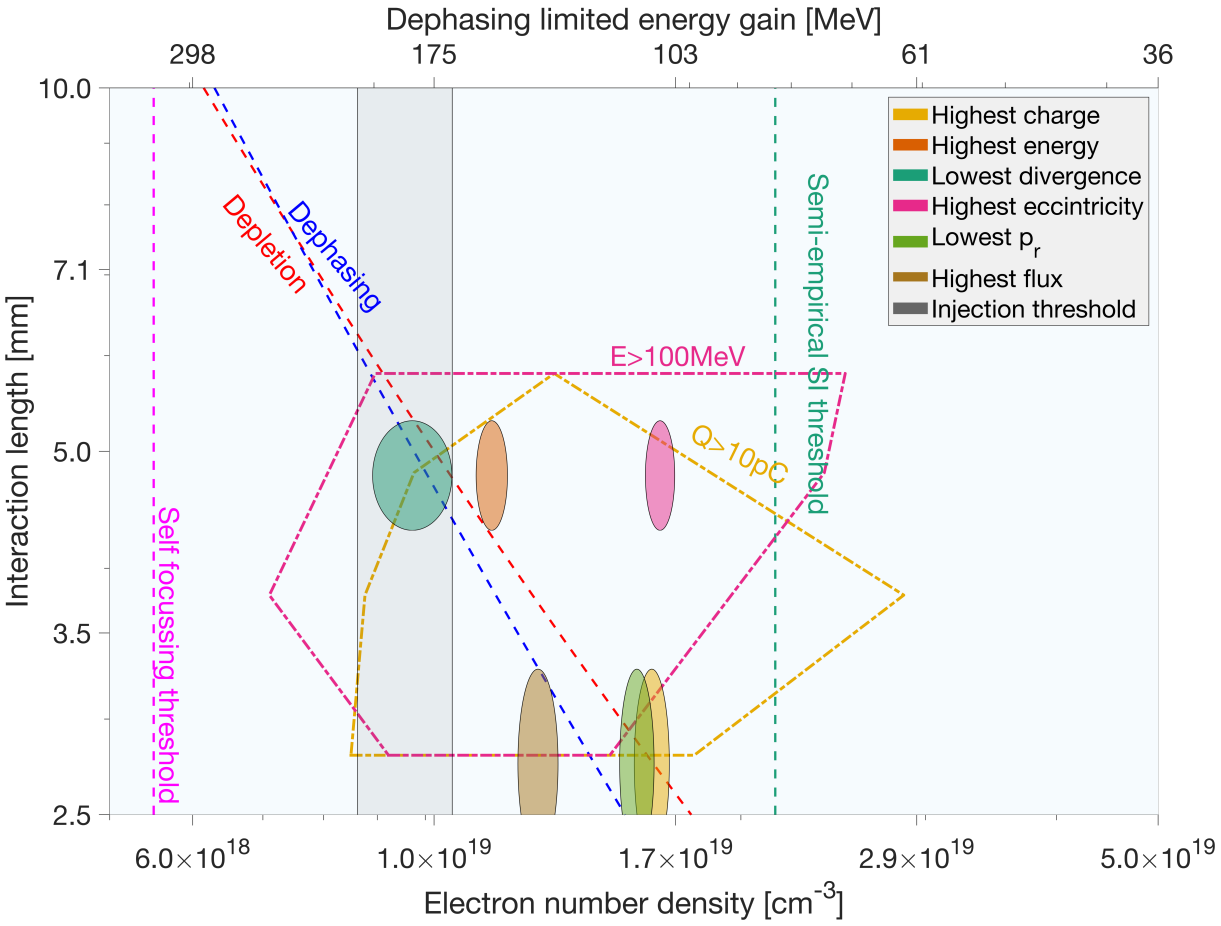


Figure 6.24: Figure showing the parameter space using the constraints with some key results overlaid. The dephasing limited energy gain equation $W_{max} = \frac{2m_e c^2 a_0 n_c}{3n_e}$ is used with an $a_0 = 3$. The injection threshold is determined from PIC simulations.

and thus ensures the forces of the electron beam in the plasma are radially symmetric. We can represent all these results graphically in Figure 6.24, where we compare them to scaling law estimates highlighted in the introduction section of this chapter. We have used the concept of evolution length L_{evo} from Bloom et al. [231]. This is the time it takes the system to inject particles into the wakefield, which we have adapted as,

$$L_{evo} = S\left(\frac{n_c}{n_e} + \alpha\right)^2 \tag{6.21}$$

with $S = 55.6 \pm 6.8\,\mathrm{nm}$ and $\alpha = 48.4 \pm 10.5$ extracted from simulations to correct the dephasing and depletion length estimates in the parameter space plot such that

$$\begin{aligned} L_{dp} &= \frac{4\sqrt{a_0}n_c}{k_p n_e} + L_{evo} \\ L_{pd} &= \frac{n_c}{n_e} c\tau + L_{evo}, \end{aligned} \tag{6.22}$$

where L_{dp} is the non-linear dephasing length and L_{pd} is the non-linear pump depletion length [236]. This was done to make the comparison with the scaling laws valid for mismatched conditions. We can see now that most notable parameters of interest such as highest charge or highest energies all lie close to the extended dephasing or depletion estimate. The eccentricity is the only exception to this.

We have seen how the dynamic nature of the interaction can lead to a range of different parameters for the electron beam using SI in a gas cell. The density and length parameters which optimise various beam parameters are shown in Figure 6.24. For the highest energies, it is better to operate at lower densities and longer interaction lengths. For the highest charge, it is better to operate at higher densities and shorter interaction lengths. In the next chapter, we examine the performance of ionisation injection in a gas cell to understand how these two injection mechanism can lead to differing beam properties.

7 Examining the density-length parameters space for ionisation injection in a self-guided wakefield accelerator at 10TW

7.1 Introduction

In the previous chapter, we explored the density-length parameter space for self-injection (SI), using a gas cell, as a target of LWFA. Helium was used as the target gas to achieve SI in this medium as the only way to inject particles in such a medium, is by forcing the plasma wave to undergo wavebreaking. The density and length of the gas cell was sequentially varied to explore the parameter space for laser wakefield acceleration at the 10 TW laser facility known as Astra-Gemini TA2. Pulse evolution effects were necessary to attain the injection threshold for wavebreaking which is typically $a_0 > 3$ [121], whereas the vacuum a_0 for this laser system for comparison is 0.6.

Density and length are two of the most important parameters to vary and optimal values for both these parameters were investigated. It was noted that the optimality for one parameter, such as charge, was not equivalent for another, like maximum energy. By combining measurements of various properties of the electron beam, it was possible to unfold the evolution dynamics of the electron beam in the plasma wave and the role of laser pulse evolution in the acceleration process.

Self-injection, is a highly dynamic process and relies heavily on self-focussing. As such, the stability of the laser pulse, directly translates into the stability of the electron beam. This motivates examining ionisation injection (II) in this gas cell, for which, helium+5% carbon dioxide was chosen as the medium. We sampled the density-length space to not only find the optimal electron beam properties that we can obtain from such a configuration, but also to understand the dynamics of the injection and acceleration process along the length of the accelerator.

There are no datasets in literature examining the combined density-length parameter space for ionisation injection schemes simultaneously. The nearest examples of prior work are by Hansson et al. [237], where the author presents data showing either variations in length or variations in density but never both parameters. Helium with 1% nitrogen was used as the dopant and the laser power was not too dissimilar to the experiment performed in this chapter. Hansson et al. highlights the generation of narrow energy spread beams from II and performed a comparison to SI.

The other significant parametric scans relevant to ionisation injection in literature is the variation of the dopant concentration by González et al. [238]. This experiment was performed at a 15 TW, with nitrogen as the ionisation injection dopant, where it was observed that increasing the dopant concentration influences the charge, maximum energy and divergence of the electron beam. In this chapter, we keep the dopant concentration fixed, but vary both density and length over a much larger range than in [237]. Where the length was varied from 0.7-3.4 mm in [237], compared to $2.8 - 8.8$ mm in this work.

Hence, building upon the results from the previous chapter, we explore how the addition of dopants modify the evolution of the plasma wave and the injection process. One advantage of ionisation injection is the lowering of the injection threshold, which as stated above for SI is $a_0 \gtrsim 3$ and for II $a_0 \gtrsim 1.6$ [124]. If we assume that the total power is conserved during the self-focussing event, the SI case needs to focus from $w_0 = 18\,\mu$m to $w_0 = 4.2\,\mu$m. The II case on the other hand only needs to attain $w_0 = 7.9\,\mu$m, before injection can begin. As we relax the spot size constraint, II can be operated at electron densities lower than those needed for SI. If we assume that the laser pulse evolves to the matched spot size, we can calculate a density threshold at which this process occurs

$$\begin{aligned} k_p w_0 &= 2\sqrt{a_0}, \\ a_0 &= 0.85\lambda_{\mu m}\sqrt{I_{18,cm2}}, \\ n_{e,m} &= 6.8\times 10^{-4}\frac{1}{w_0^3}, \end{aligned} \tag{7.1}$$

where $\lambda_{\mu m}$ is the laser wavelength in microns and $I_{18,cm}$ is the laser intensity in $10^{18}\mathrm{cm}^{-3}$. Hence, by allowing a larger w_0 of the accelerator, we also reduce the electron density at which we can begin injecting.

Although, here we run into the problem of not having an electron density high enough to allow self-focussing to occur. So the actual density that we begin injecting electron,

will be the density at which the self-focussing occurs

$$n_{e,sf} = 1.75 \times 10^{10} \frac{m_e \epsilon_0 \omega^2}{e^2 \alpha P} \tag{7.2}$$

where $P = 10\,\mathrm{TW}$ is the laser power, $\alpha = 0.5$ is the fractional energy in the FWHM of the focal spot and ω is the laser frequency. For the parameters of this experiment, we obtain $n_{e,sf} = 6.1 \times 10^{18}\,\mathrm{cm}^{-3}$ as a rough guide for the onset of self-focussing. This motivates us to constrain the electron density of our target for densities larger than this to look for the generation of electron beams by ionisation injection.

In previous sections, we have seen how carbon and nitrogen have been used as a dopant for ionisation injection schemes in laser wakefield accelerators. In Figure 7.1, we can see how the ionisation fraction of oxygen and carbon vary for different laser intensities. For an ionisation injection scheme, it has been shown that the minimum a_0 of the driver pulse needed to create a potential deep enough to trap stationary particles is for $a_0 > 1.6$ [124].

This a_0 can be achieved in our case through self-focussing of the laser pulse in the plasma and the ionisation fraction for the relevant atomic levels are shown in Figure 7.1a. Note that carbon is suitable since it provides ionised electrons near the peak of the pulse. As this is the minimum a_0 needed for injection, we also explore the effect of increasing the a_0 on the ionisation probability in Figure 7.1b. We can see that the addition of oxygen provides additional electron available for injection for more non-linear wakes as the inner shell electrons of carbon are ionised earlier, the higher the laser amplitude.

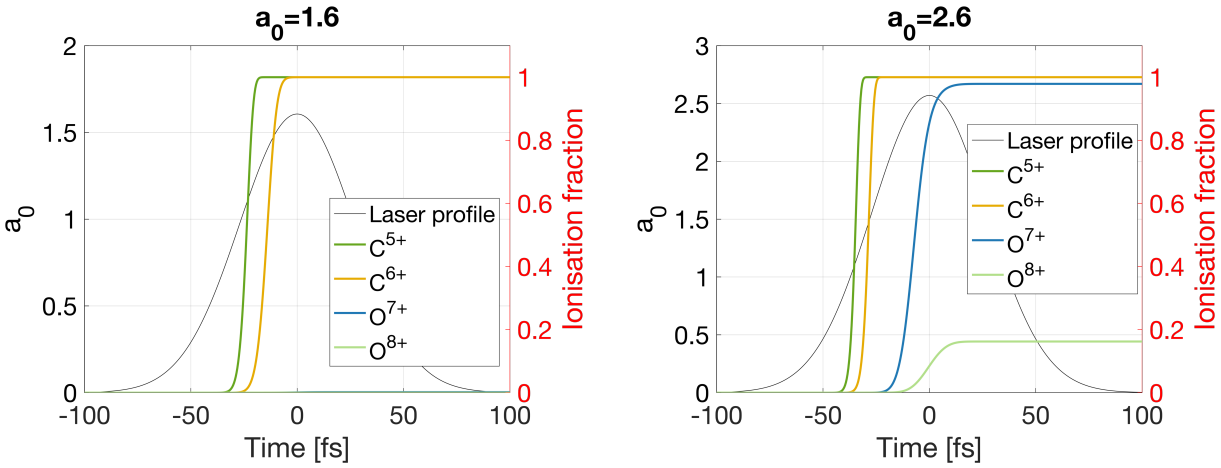


Figure 7.1: The ionisation probability for carbon and oxygen. The left hand axis is the a_0 of the laser pulse and the right hand axis is the fraction of energy levels which are ionised.

7.2 Experimental setup

We have seen how the density-length scan can be used to understand the how the electron beam's injection, dephasing and the interaction with the laser pulse works for a self-injected case. We now explore the effects of ionisation injection using the same experimental conditions. The medium used for ionisation injection was helium + 5% carbon dioxide. The inner shell electrons of carbon and oxygen provide the levels needed for ionisation injection.

The density and length scan was performed in the same way as for the previous section where the density was varied by pulsing the gas and shutting off the backing line. This reduced the backing pressure for the gas cell and each subsequent shot was performed at a lower density. This was performed until the density drops below the threshold for injection at which point the backing pressure was set to a high value and the length was varied. The experimental setup for this section is identical to Chapter 4 and Chapter 6.

For this data-set we varied the cell length from $2.8-8.8\,\mathrm{mm}$ and two density scans were performed for each cell length. The results presented were collated from a total of 342 shots taken over these parameters. We begin by examining the laser conditions for each cell length data set in Figure 7.2, where we can see that the interaction conditions are comparable. There was a slight drop in the energy of the laser causing the a_0 to decrease along the dataset with a 5% drop in a_0 between the shortest length and the largest length. We will account for this in the interpretation of the results.

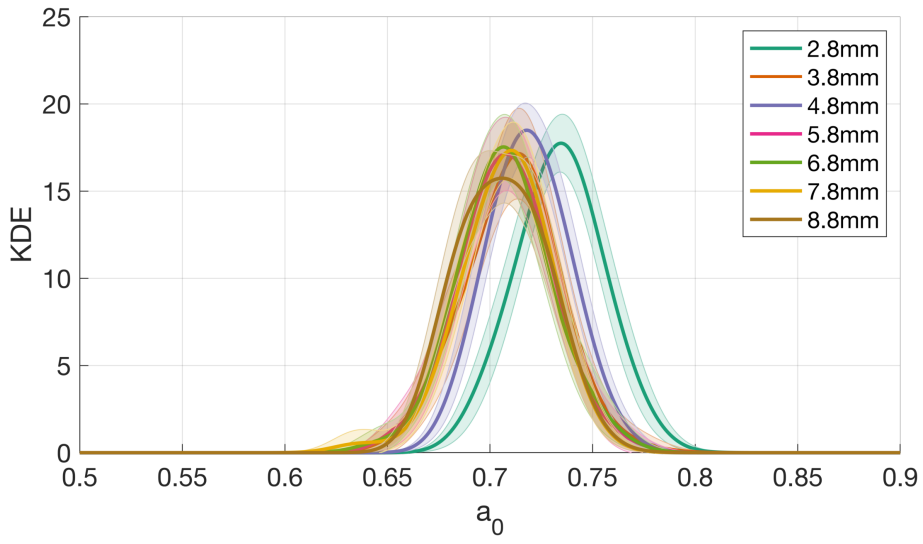


Figure 7.2: Figure showing the stability of the a_0 of the laser pulse across the various runs.

Interaction parameters	Gas cell
Backing pressure	$78 - 531\,\text{mbar}$
Electron number density	$0.4 - 2.8 \times 10^{19}\,\text{cm}^{-3}$
Length	$2.8 - 8.8\,\text{mm}$
Gas	Helium +5% Carbon dioxide

Table 7.1: The target parameters during TA2 experiment.

Laser parameters	
Laser energy	$597 \pm 37\,\text{mJ}$
Pulse duration (τ)	$45 \pm 5\,\text{fs}$
Spot size (w_0)	$(18 \pm 2 \times 23 \pm 5)\mu\text{m}$
Peak intensity	$1.0 \pm 0.5 \times 10^{18}\text{W}\,\text{cm}^{-2}$
Focussing geometry	$f/18$

Table 7.2: The parameters of the laser pulse for this dataset.

The a_0 was calculated using the low power focal spot information acquired before this data run was performed to extract the focal spot size. This was then combined with the on-shot laser energy measured using a transmitted leakage of the laser pulse and a SPIDER measurement of the pulse duration performed by the facility. The range of target parameters is outlined in Table 7.1 and averaged laser parameters are shown in Table 7.2.

7.3 Results

In this section, we present the two main diagnostics on this experiment, which were the electron spectrometer and the beam profile monitor. We begin by surveying some of the data from the electron spectrometer diagnostic in Figure 7.3. For such a large dataset, it is instructive to examine a reduced set to understand the general trends in the dataset.

For this Figure, five shots were chosen, equally spaced in electron density for a range of different cell lengths. Unlike the SI case in the previous section, we see high charge electron beams present for much lower densities in the ionisation injection case than the self-injection case. They are also present over a much larger range of cell lengths with electron beams persisting at interaction lengths of 8.8 mm, with some of these beams also containing mono-energetic features.

We can see that the length of the cell does not reduce the highest energies of the electron beam. The electron beams do not reach as high energies with II as they do with SI. For SI,

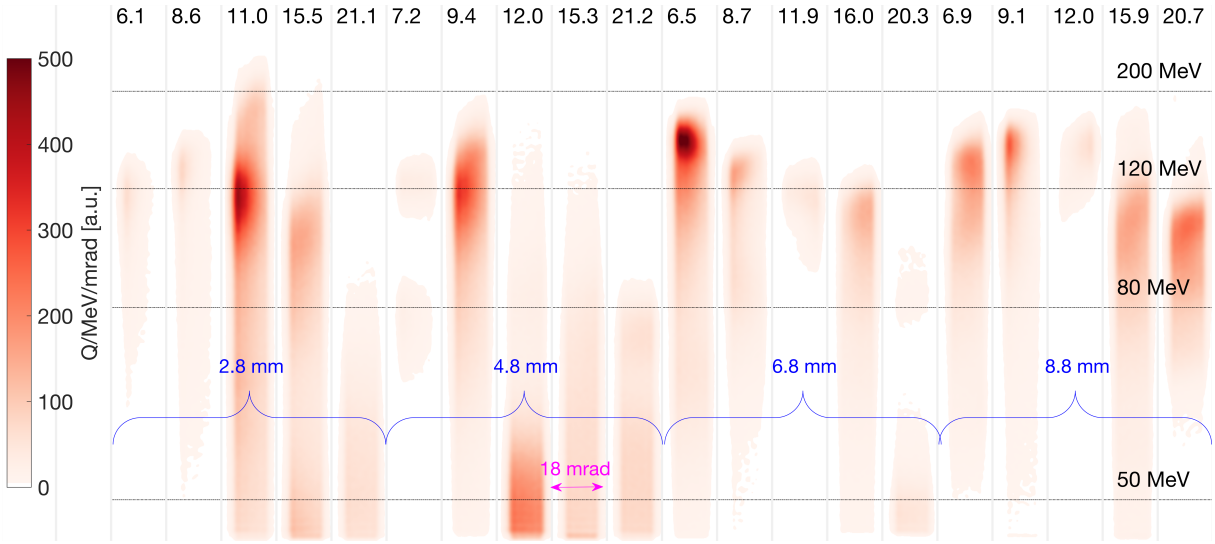


Figure 7.3: Representative subset of the raw electron spectrometer data for various lengths and densities. The length (blue, at bottom) is given in mm and the electron density (black, at top) is given in 10^{18}cm^{-3}. The energy labels are provided for on-axis electron trajectories.

we recall the maximum energy of the electron beams, routinely exceed 200 MeV. Whereas for II, we only see electron beams for the lowest cell length at 2.8 mm exceeded 200 MeV. The transverse extent of the II beams also appear smaller in the direction perpendicular to the dispersion direction. We can examine this in further detail by examining some raw data from the beam profile diagnostic in Figure 7.4.

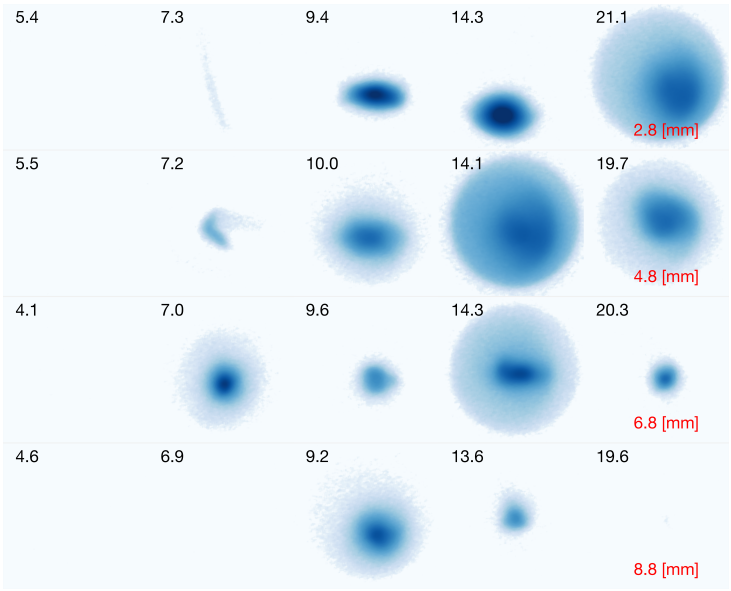


Figure 7.4: Raw beam profile data for various lengths and densities. The length (red, at right) is given in mm and the electron density (black, at top) is given in 10^{18}cm^{-3}. The minor grid (grey) on the figure represents a separation of 2 mrad and the dashed red line represents the centroid of the laser pulse.

We note that electron beams were produced at lower electron densities in the II case ($7 \times 10^{18}\,\mathrm{cm}^{-3}$) than the SI case ($9 \times 10^{18}\,\mathrm{cm}^{-3}$). For the shortest cell lengths at the lowest density, we observed the appearance of highly eccentric beams. The charge of the beams was also much larger for the shortest cell length. We also observed the beam divergence decrease, for densities around $1.3 \times 10^{19}\,\mathrm{cm}^{-3}$ between 6.8 mm and 8.8 mm.

In order to better understand these general trends observed from the reduced dataset, we now extract beam parameters from these diagnostics, using all the available shots, beginning with the total charge observed on the high energy electron spectrometer in Figure 7.5.

Charge

II generates electron beams with a maximum value of charge $Q_{max} = 37.1 \pm 1.6\,\mathrm{pC}$, at an electron density of $1.53 \pm 0.11 \times 10^{19}\mathrm{cm}^{-3}$ and a cell length of 3.8 mm. From the previous section, we have seen that SI generates higher charge electron beams, with the highest charge of $50.0 \pm 2.3\,\mathrm{pC}$ when compared to II.

The highest value of charge across all densities, reduces at a much lower rate for II than SI. This is also seen in the raw data where electron beams were observed for much longer interaction lengths in the II case than the SI case. This is most evident when we examine the maximum charge observed for 5.8 mm case, where we obtain $Q_{max,II} = 33.22\,\mathrm{pC}$. For the corresponding interaction length for SI, we obtain $Q_{max,SI} = 10.2 \pm 0.9\,\mathrm{pC}$. There is also no significant variation in the density at which the optimum charge for a particular cell length occurs.

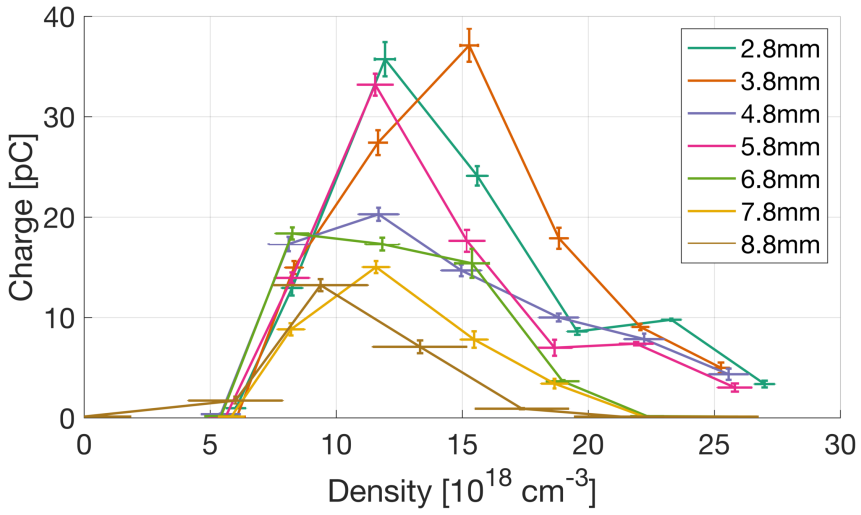


Figure 7.5: The charge observed on the high energy electron spectrometer diagnostic during a density scan for various cell lengths.

For both long and short cell length, we see electron beams over a greater range of densities for II than SI. The range of densities over which charge ($Q(E > 45\,\mathrm{MeV})$) is observed, decreases with density. This occurs asymmetrically, as it is the charge at the higher densities which decreases with cell length more than the charge at lower densities.

Maximum energy

In Figure 7.6, we extract the maximum energy for the electron beam for a range of cell lengths and electron number densities. This is defined as the energy at which the cumulative $\frac{\mathrm{d}Q}{\mathrm{d}E}$ reaches 99% of its maximum value. In this figure, only charge greater than 1 pC is shown.

In Figure 7.6, we can see that there is no significant variation in maximum energy, with cell length, within the error bars of each data point. The maximum energy obtained across the entire data set is $159 \pm 22\,\mathrm{MeV}$, occurring at a density of $7.6 \pm 0.7 \times 10^{18}\mathrm{cm}^{-3}$ and cell length of 4.8 mm. We recall that the maximum energy attains for the SI dataset is $210 \pm 19\,\mathrm{MeV}$, which is 25% lower.

When compared to the Lu scaling law [135], we see that for densities less than $1.7 \times 10^{19}\,\mathrm{cm}^{-3}$, we observe excellent agreement for $a_0 = 2$. However, for higher densities, the scaling law underestimates the energy of the generated electron beam.

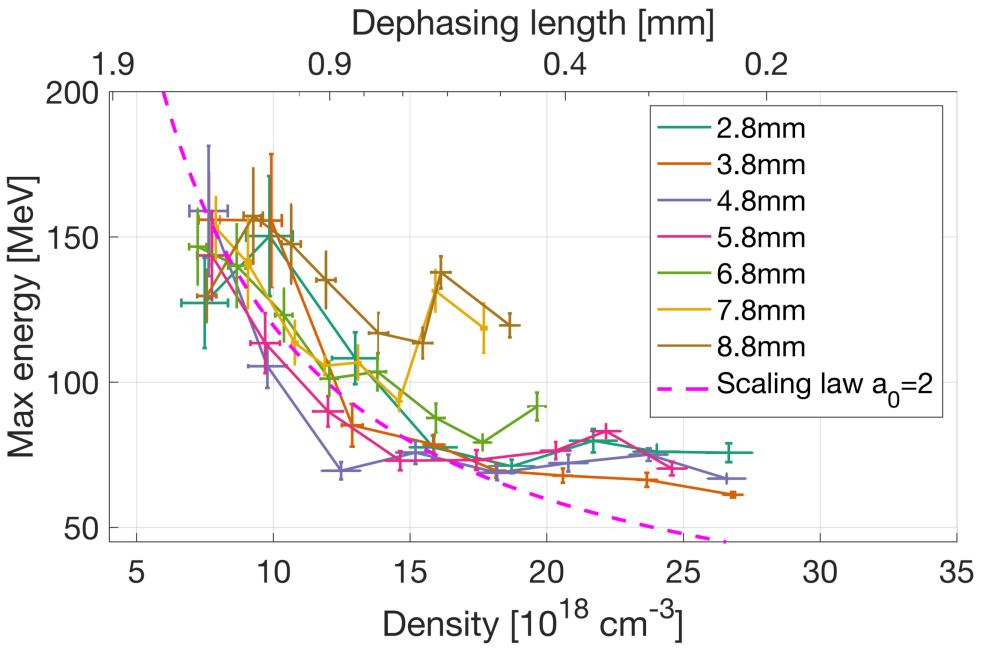


Figure 7.6: The maximum energy observed on the electron spectrometer diagnostic as a function of density for various cell lengths.

For cell lengths around $6.8 - 8.8\,\text{mm}$ at the highest densities, we see that there is an increase in the energy of the electron beam just before the charge on the spectrometer drops below the noise threshold.

Beam divergence

We now move on to the spatial profile of these electron beams to see how they vary with density and length. Firstly, we examine the divergence of the electron beam as observed on the beam profile diagnostic. The divergence is defined by fitting an ellipse to the full-width half-maximum of the contour of the beam profile. The long axis of the ellipse is aligned to the polarisation axis and the short axis is aligned to the axis perpendicular to the polarisation axis.

In Figure 7.7, we observe that the largest value of the divergence is $\theta_{max,II} = 8.1 \pm 0.9\,\text{mrad}$, occurring at a density of $2.3 \pm 0.1 \times 10^{19}\text{cm}^{-3}$ for a cell length of $2.8\,\text{mm}$, in the axis aligned to the laser polarisation. For SI, the largest observed divergence takes a value of $10.1 \pm 0.1\,\text{mrad}$.

The lowest value of divergence for the electron beam using II is $\theta_{min,II} = 1.6 \pm 0.1\,\text{mrad}$, occurring at a density of $1.16 \pm 0.06 \times 10^{19}\text{cm}^{-3}$ and a cell length of $6.8\,\text{mm}$. However, we note that this divergence is attained for all cell lengths, within the uncertainty of the value. For low densities, all cell lengths tend towards a similar value of beam divergence. At higher densities, there is a large disparity in beam divergence between the different cell lengths. The equivalent lowest beam divergence for SI takes a value of $1.5 \pm 0.1\,\text{mrad}$.

For a fixed cell length, we observe that the beam divergence increases and has a unique maxima, before decreasing for higher densities. The correlation of beam divergence with

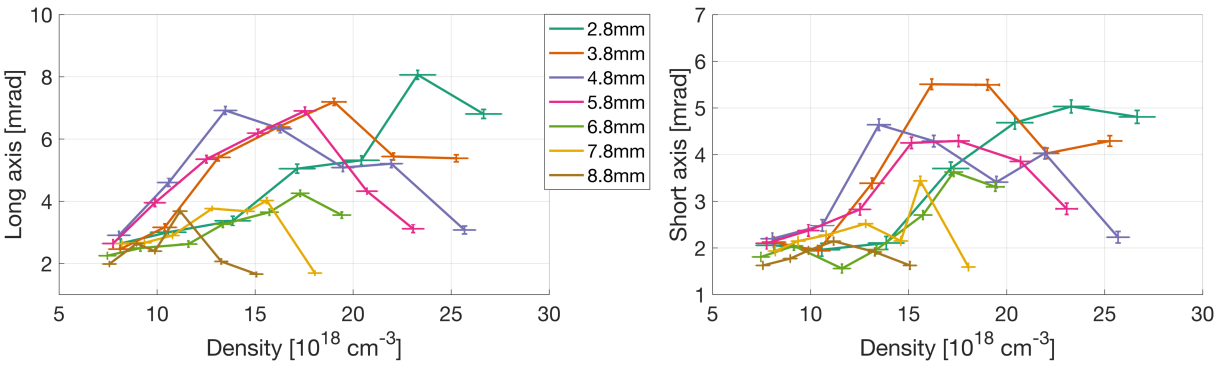


Figure 7.7: The long axis divergence observed on the beam profile diagnostic as a function of density for various cell lengths.

density is much greater than with cell length. Increasing the cell length, has the effect of reducing the range of densities over which electron beams are observed, much like was observed on the electron spectrometer dataset.

Pointing deviation

Next, we examine the angular separation between the centroid of the laser pulse on the beam profile monitor and the centroid of the electron beam, termed pointing deviation. The centroid was chosen by taking the mid-point of the ellipse fit of the half maximum contour of the beam profile. The pointing deviation across a range of electron densities and cell lengths is shown in Figure 7.8. The pointing deviation along the polarisation axis, is labelled Y and shown on the right hand pane. The orthogonal axis is labelled X and shown on the left hand pane of Figure 7.8.

In Figure 7.8, we can see that the largest pointing deviation, for an electron beam injected using II in the X axis is $X_{p,max} = 3.84 \pm 0.3$ mrad, at a density of $8.1 \pm 0.9 \times 10^{18} \mathrm{cm}^{-3}$ and a cell length of 2.8 mm and the largest Y pointing deviation, $Y_{p,max} = 2.65 \pm 0.2$ mrad, at a density of $2.0 \pm 0.1 \times 10^{19} \mathrm{cm}^{-3}$ and a cell length of 2.8 mm. We contrast this with SI where we obtain $X_{p,max} = 4.5 \pm 0.1$ mrad and the largest Y pointing deviation, $Y_{p,max} = 4.4 \pm 0.9$ mrad. Hence, we see that electron beams from II have a lower maximal pointing offset than self-injected electron beams.

Fo the pointing deviation in the X direction, we observe that the it falls linearly with electron density, with a similar gradient for cell lengths of 2.8, 3.8 and 4.8 mm. For even longer cell lengths, the pointing deviation of the electron beam tends towards ≈ 1 mrad. For the pointing in the Y direction, we can see two trends, depending on the density of the interaction. For densities $< 9 \times 10^{18}\,\mathrm{cm}^{-3}$, we see that the pointing offset increases

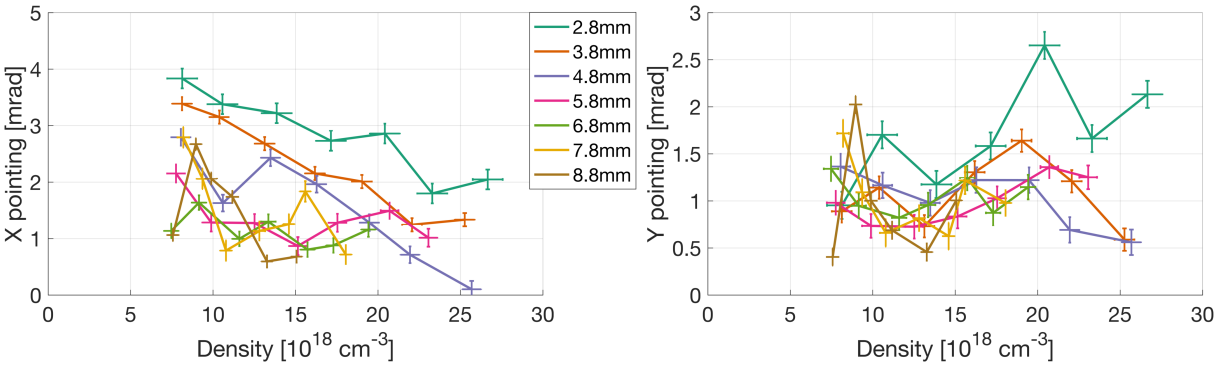


Figure 7.8: Figure showing the pointing of the electron beam along the X and Y axis, as observed on the beam profile diagnostic as a function of density for various cell lengths.

as the length of the interaction increases. Conversely, for densities $> 1 \times 10^{19}\,\mathrm{cm}^{-3}$, we can see that the Y pointing decreases, for increasing cell lengths.

Eccentricity

Next, we examine the eccentricity of the generated electron beam which is defined as

$$e = \sqrt{1 - \left(\frac{a}{b}\right)^2}, \tag{7.3}$$

where a is the short axis of the ellipse and b is the long axis of the ellipse. In Figure 7.9, we plot the eccentricity for II, for a range of densities and cell lengths. We can see in Figure 7.9 that the highest eccentricity electron beam is $e_{max,II} = 0.84 \pm 0.1$, occurring at a density of $1.25 \pm 0.08 \times 10^{19}\mathrm{cm}^{-3}$ and a cell length of 5.8 mm.

This is lower than the most eccentric electron beams observed for SI where $e = 0.93 \pm 0.06$. The lowest value of eccentricity, i.e. the most spherical beam has $e_{min,II} = 0.2 \pm 0.06$. This is slightly lower than the lowest eccentric beams observed for SI, where $e = 0.26 \pm 0.06$.

Generally, we observe that the eccentricity that for low densities the eccentricity of the beam is low. As the density increases, the eccentricity approaches a maxima before decreasing again.

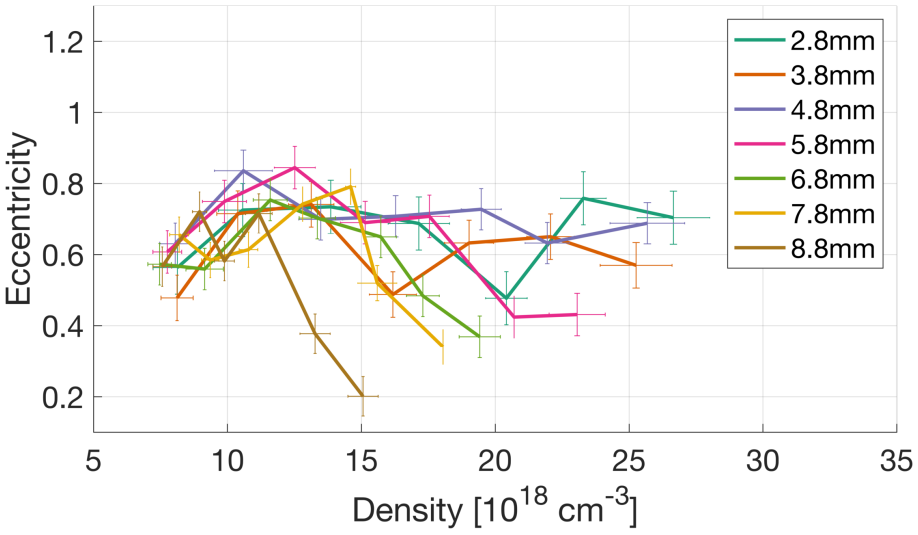


Figure 7.9: Figure showing the eccentricity of the electron beam, as observed on the beam profile diagnostic as a function of density for various cell lengths.

Transverse momentum

Finally, we can extract the transverse component of momentum of the electron beam by combining the divergence from the beam profile diagnostic and the energy from the electron spectrometer as they are related by

$$\langle p_r \rangle = \langle \theta_{div} \rangle p_z. \tag{7.4}$$

Where $\langle p_r \rangle$ is the root mean square (RMS) transverse momentum, and $\langle \theta_{div} \rangle$ is the RMS divergence. We use the long-axis divergence for the value of $\langle \theta_{div} \rangle$ and the maximum energy for p_z to estimate the upper bound on $\langle p_r \rangle$.

From Figure 7.10, we can see that the largest value of transverse momentum for this dataset is $p_{y,max,II} = 0.64 \pm 0.26\,\mathrm{MeV/c}$, occurring at a density of $2.17 \pm 0.13 \times 10^{19}\mathrm{cm}^{-3}$ and a cell length of 2.8 mm. For SI, the largest value of $p_y = 1.36 \pm 0.52\,\mathrm{MeV/c}$, significantly larger than for the II case. The lowest value of transverse momentum obtained is $p_{y,min,II} = 0.19 \pm 0.05\,\mathrm{MeV/c}$, occurring at a density of $1.55 \pm 0.08 \times 10^{19}\mathrm{cm}^{-3}$ and a cell length of 8.8 mm. The lowest value for the transverse momentum obtained for SI is $p_y = 0.22 \pm 0.04\,\mathrm{MeV/c}$.

In Figure 7.10, we notice that for the intermediate density, where there is a plateau in the transverse momentum as a function of density. The transverse momentum does not vary significantly with density for II.

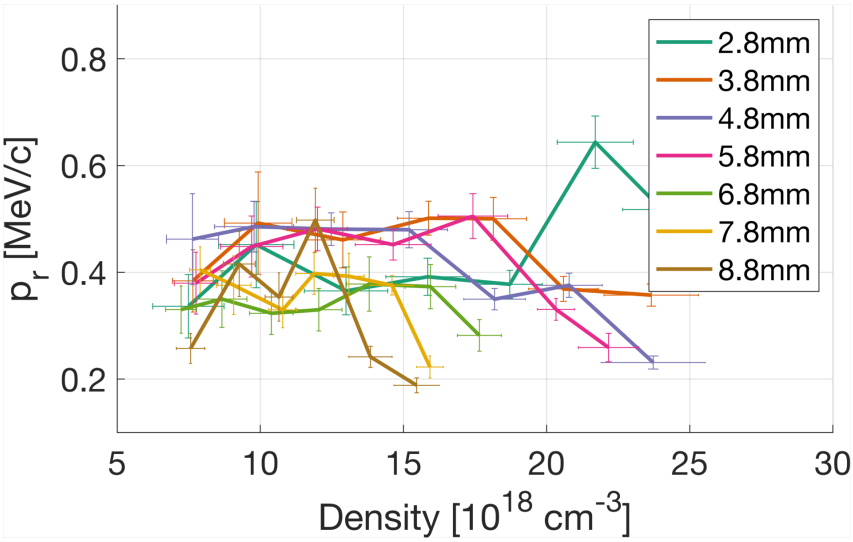


Figure 7.10: The transverse momentum as a function of density for various cell lengths.

7.4 Simulations: 8mm density scan of ionisation injection at TA2

Motivation

In the previous section, results were presented for ionisation injection using helium+5% carbon dioxide in a variable length gas cell. The density and length were sequentially varied and their relationship with the parameters of the electron beam, such as, beam charge, maximum energy, beam divergence and beam pointing were addressed. From these parameters, other significant beam parameters were extracted such as beam eccentricity and maximal transverse momentum.

In this simulation section, we examine the underlying laser-plasma interaction using a cylindrical, pseudo-spectral, particle-in-cell simulation code called FBPIC [3]. The aim of this simulation chapter is to explain the relationship between experimental results and the variation of these parameters with density and length. We will also compare both simulations and experimental results with existing scaling laws for matched conditions. These simulations will allow us to gain an insight into how the laser pulse and the accelerating structure it generates vary as a function of the plasma length.

The highly dynamic nature of the interaction necessitates the use of particle-in-cell codes. These simulations self-consistently capture the relativistic self-focussing, ionisation defocussing, pulse front etching and corresponding a_0 amplification expected to occur in this environment.

Simulation setup

The simulations assume a trapezoidal density profile for helium+5% carbon dioxide by atomic number density. The ramp length was assumed to be 100 µm and was assumed to be the same length for all densities. The variation in length was obtained by extracting the properties of the electron beam at a particular point in the plasma. Helium was treated as being fully ionised, whereas, the last two levels of carbon and oxygen were assumed to be unionised. In Table 7.3, we can see the ionisation levels of the various atomic species. Carbon and oxygen were assumed to be ionised upto C^{4+} and O^{6+} energy levels. A moving window was employed for this simulation using the non-linear group velocity to speed up the computation time, where $\frac{v_{mov}}{c} = 1 - \frac{3}{2}\left(\frac{n_c}{n_e}\right)$ from the Theory chapter on p.61. In Table 7.4 we highlight some of the parameter used in performing this simulation.

Helium	24.6	54.4						
Carbon	11.3	24.4	47.9	64.5	392.1	490.0		
Oxygen	13.6	35.1	54.9	77.4	113.9	138.1	739.3	871.4

Table 7.3: The ionisation energies of the various atomic species used for ionisation injection for He+5 $\%CO_2$ in eV.

Variable	Value	Variable	Value
dz	27 nm	dr	95 nm
no. cells z	2024	no. cells r	473
no. θ modes	3	ppc z, r, θ	1, 1, 12
Window length z	54 µm	Window length r	45 µm
a_0	0.7	w_0	18 µm
Laser wavelength	800 nm	τ	45 fs
Electron density	$0.6 - 3 \times 10^{19}\,\mathrm{cm}^{-3}$	No. densities	8
C ion density	$1 - 5 \times 10^{17}\,\mathrm{cm}^{-3}$	O ion density	$1 - 5 \times 10^{17}\,\mathrm{cm}^{-3}$
C initial charge	4+	O initial charge	6+

Table 7.4: Input parameters of the simulation. ppc stands for particles per cell, dz is the longitudinal spatial resolution, dr is the radial spatial resolution. The θ modes represent the number of azimuthal Fourier modes that the fields are decomposed into.

Simulation results

We begin by examining the evolution of the particle momentum in Figure 7.11. We have only shown a subset of the densities for which simulations were performed for brevity. Consider initially, the left hand side figure, which is the momentum-history plot for accelerated electrons. In this figure, each column is the histogram of the energy distribution of the particles at a particular instant in time. The columns are stacked as a function of interaction length and build up a picture of how particles are being accelerated/decelerated in the simulation.

Each labelled row represents the results from a different simulation where the average densities is successively increased. We can see that particle injection into the wake occurs for densities greater than $7 \times 10^{18}\,\mathrm{cm}^{-3}$. Particle energies up to 220 MeV were observed in simulations for densities of $1.06 \times 10^{19}\,\mathrm{cm}^{-3}$ at lengths of 3.1 mm.
In Panel c) for the momentum-history plot, we see three injection events visible. The first injection event occurs ≈ 1 mm into the interaction and the electron bunch from this even dephases around 2.5 mm. As this electron beam is dephasing, a second injection event occurs. This reaches lower energies but has much more charge in its bunch. The final injection event, similarly begins when the second injection event is dephasing. This

final injection goes to ≈ 200 MeV. The figures on the right hand side, we will term the wake-evolution plot.

In each figure, the column represents the z component of the on-axis electric field, E_z for a particular instant in time. These columns are stacked for multiple points along the

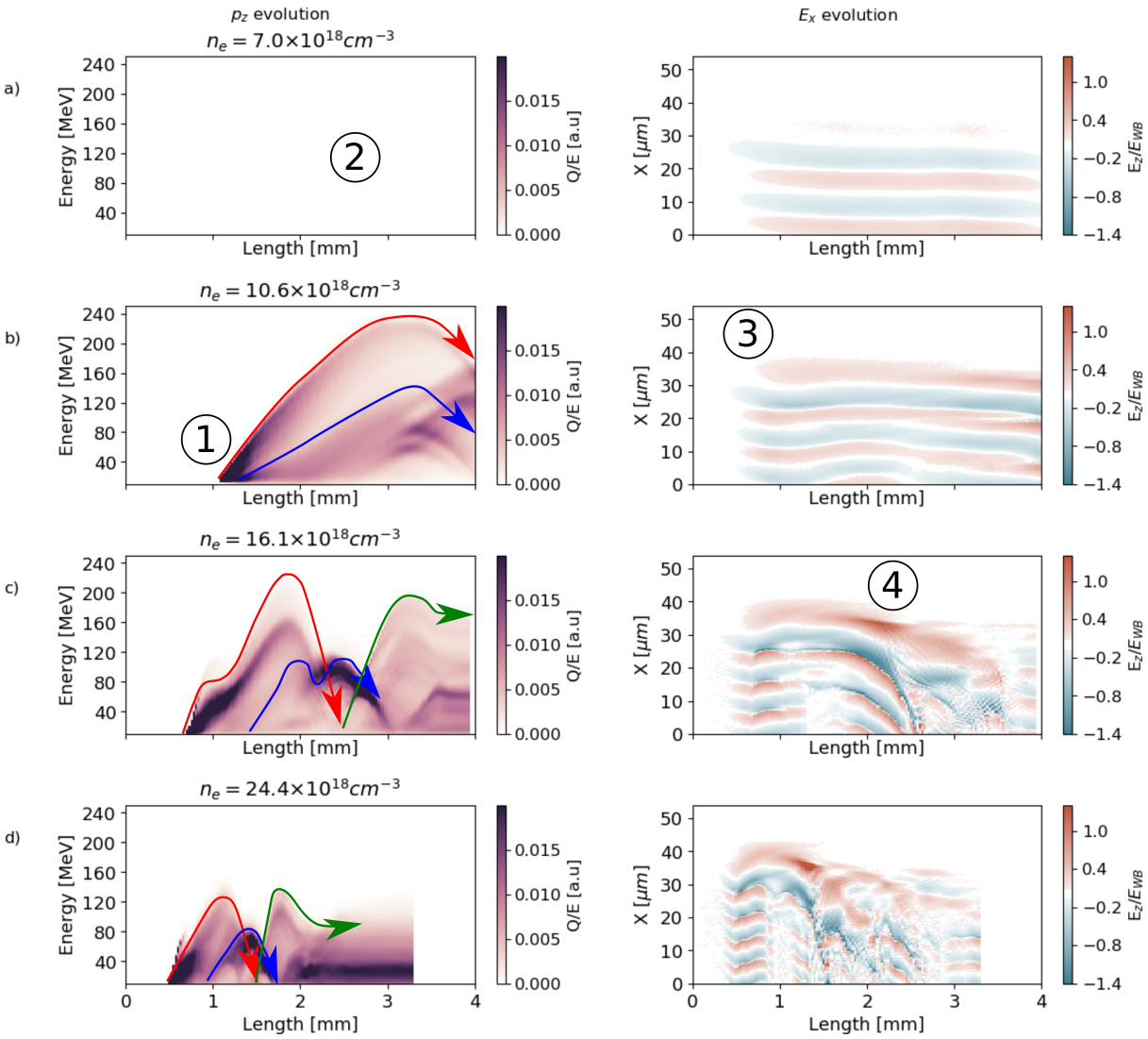


Figure 7.11: On the left hand column, we present the momentum-history plot for the inner shell electrons of carbon and oxygen for 4 different densities. On the right hand column, we present the evolution of the on-axis electric field of the wake. The red, blue and green arrows represent the first, second and third injection event. ① shows the start of injection, ② shows that there is no injection for the lowest density, ③ shows the point at which the wake amplitude becomes a significant fraction of the wave-breaking limit. This coincides with the beginning of particle injection into the accelerator. ④ shows the wake depleting and loosing coherence due to depletion. E_{WB} is the cold wave-breaking electric field which is defined as $E_{WB} = \frac{m_e c \omega_p}{e}$

interaction length horizontally and allow for a visual representation of the evolution of the wake. We can see that increasing the density has the effect of increasing the peak electric field of the wake. For densities greater than $1.61 \times 10^{19}\,\mathrm{cm}^{-3}$, we notice that the wake evolution becomes highly discontinuous and its amplitude is diminished. This is attributed to the laser pulse depletion and occurs more rapidly at higher densities.

In Panel d) we can see that around 1.5 mm, the field of the wake in the first bucket at 30 µm is neutralised. The injected particles are of sufficiently high charge that their fields oppose the field the wake. Around 2.5 mm we also see the wakefield elongates and this correlates with the 3rd injection event. The wakefield becomes highly discontinuous and terminates after 3.5 mm, where we see the energy of the electrons also stop varying.

We examine the evolution of the laser pulse in more detail in Figure 7.12. The spot size and pulse duration seen in Figure 7.12a and c are extracted by first obtaining the Hilbert transform of the laser pulse in the simulation to obtain the pulse envelope. We then extract the $\frac{1}{e}$ contour and from this the pulse duration is defined as the longitudinal extent and the spot size is the transverse extent.

In the previous section, we showed the evolution of the laser spot in the absence of ionisation. For the density of $7 \times 10^{18}\,\mathrm{cm}^{-3}$, we obtain a minima in spot size of $\approx 8.5\,\mu\mathrm{m}$.

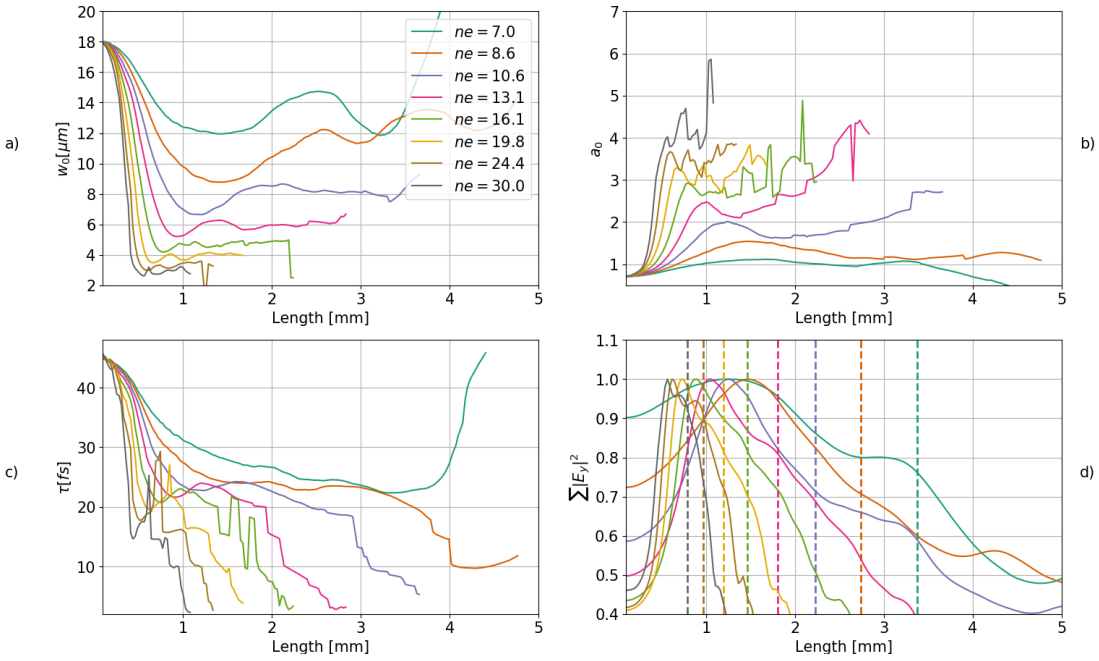


Figure 7.12: Figure showing the evolution of the a) spot size, b) peak a_0 of the interaction, c) pulse duration and d) laser field energy as a function of time. In panel d represents the depletion length estimated using the local pump depletion model [129].

We can see from Figure 7.12a that for II, we do not always reach a unique minima. The local minima which occurs at the corresponding length of $\approx 1.5\,\text{mm}$ has a value of $12\,\mu\text{m}$.

In Figure 7.12c, we extract the peak a_0 of the simulation using the following definition of a_0,

$$a_0 = \frac{eE}{m_e c \omega_L}, \tag{7.5}$$

where ω_L is determined by computing the Fourier transform and extracting the frequency component with the largest amplitude. The injection of particles into the wake scales with the evolution of the a_0 of the driving laser pulse. For higher densities, we can see that the first peak in a_0 increases. This initial increase is due to transverse pulse compression from self-focussing. The subsequent increases are due to a mixture of spot oscillations and longitudinal pulse compression.

We now examine the various electron beam parameters such as, charge, maximum energy and beam eccentricity. The evolution length for a different injection mechanism in comparison to self-injection is also addressed along with differences in the peak a_0 for different types of injection mechanisms.

Charge

In Figure 7.13, we plot the charge of all particles in the simulation with energies greater than 45 MeV as a function of interaction length. The different colours of this plot repre-

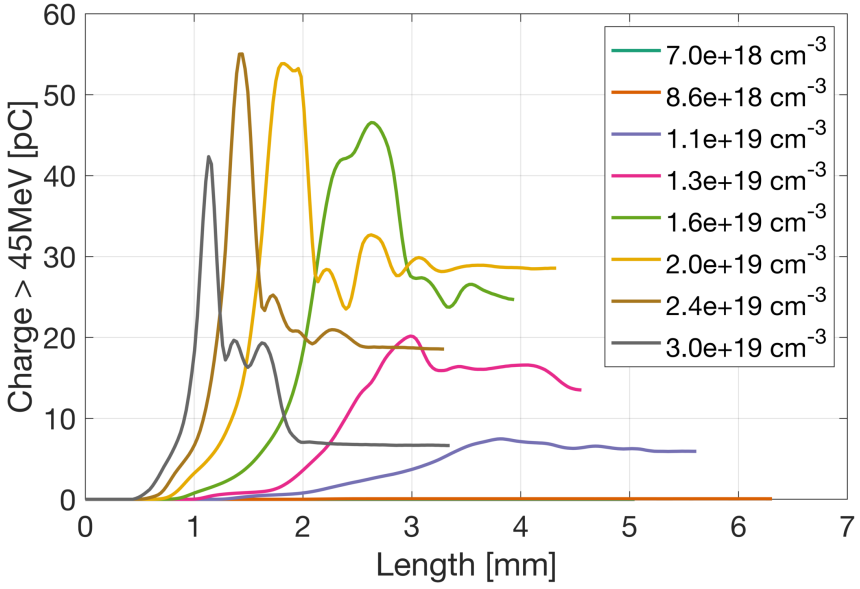


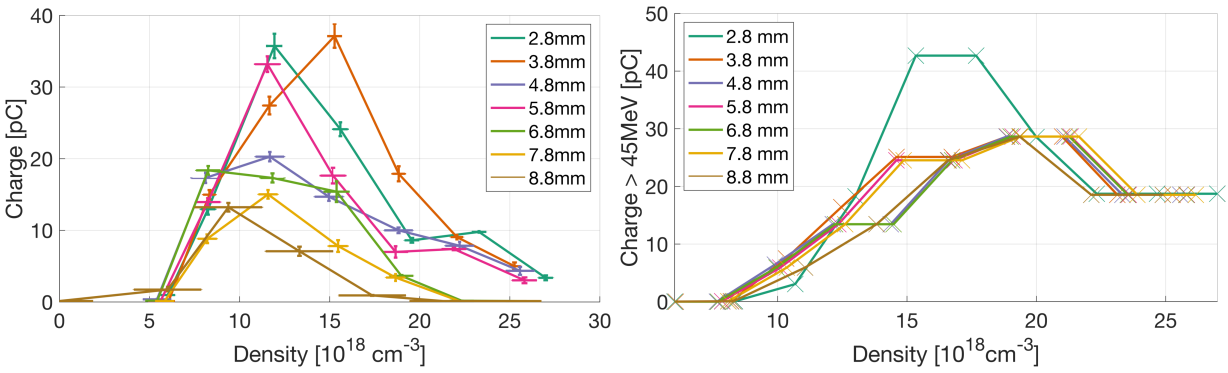
Figure 7.13: Evolution of the charge $Q(E > 45\,\text{MeV})$ from simulations as a function of length for different densities.

sent the different average densities of the simulation. We can see that the highest charge observed in simulations is 57.0 pC occurring at a density of $2.4 \times 10^{19}\,\mathrm{cm}^{-3}$ for a length of 1.4 mm. This is higher that the measured maximum charge on experiment of 37.1 ± 1.6 pC at $1.53 \pm 0.10 \times 10^{19}\mathrm{cm}^{-3}$ and a cell length of 3.8 mm.

The peak charge for each density occurs at an earlier length for higher densities. The value of this charge is maximised for $2.4 \times 10^{19}\,\mathrm{cm}^{-3} - 2 \times 10^{19}\,\mathrm{cm}^{-3}$ and then continues to fall for higher and lower densities. The width of the peak decreases for higher densities, this is due to dephasing as the dephasing length is shorted for higher densities. The plateau of charge is due to the lack of injection events/ termination of the wakefield. We see that this occurs later for lower densities.

We now recast the data from Figure 7.13 in order to make a direct comparison to the experiment data in Figure 7.14. On the left hand side of this figure, we show the data from experiment and on the right hand side we show the charge extracted from simulations.

We can see that simulations predict a density of $2 \times 10^{19}\,\mathrm{cm}^{-3}$ for the optimum density at which the charge is maximised for all densities. While experimental data shows that this is independent of density. Simulations predict that at shorter interaction lengths, it is possible to obtain even higher charges and that the amplitude of this charge is indeed dependant on density. The reason for our prediction of a lower optimum density for charge in experiments is because we could not vary the interaction length to less than 2.8 mm, where this behaviour is most prominent.



(a) Experiment (b) Simulation

Figure 7.14: The charge of particles with $E > 45$ MeV from the experiment on the left hand side and simulations on the right hand side.

Maximum energy

We now move on to examining the maximum energy from simulations. The maximum energy is defined as the energy at which the cumulative integral of the energy distribution of particle energies reach 3σ of its maximum value. This is the same way that maximum energy is extracted from experimental data.

In Figure 7.15, we can see that particles are injected and accelerated up to 220 MeV at a density of $1.1 \times 10^{19}\,\mathrm{cm}^{-3}$ and interaction length of 3.1 mm. The maximum energy for II evolves much more dynamically than SI from Figure 6.16 on p.163.

For SI, we would observe a single peak and the maximum energy would plateau for longer lengths. Here for II, we observe multiple peaks in the maximum energy as a function of accelerator length. Unfortunately, the experimental dataset is not varied in small enough length increments to examine this behaviour.

We recast the information from Figure 7.15 in order to make the comparison between experimental data and simulation easier to interpret by plotting the values of maximum energy at the densities and lengths from the experiment in Figure 7.16.

In Figure 7.16, we can see that the simulation data-sets replicates the functional from of the energy as a function of density. However, simulations predict energies 38% greater than what is observed in experiments. One reason for this discrepancy could be due to

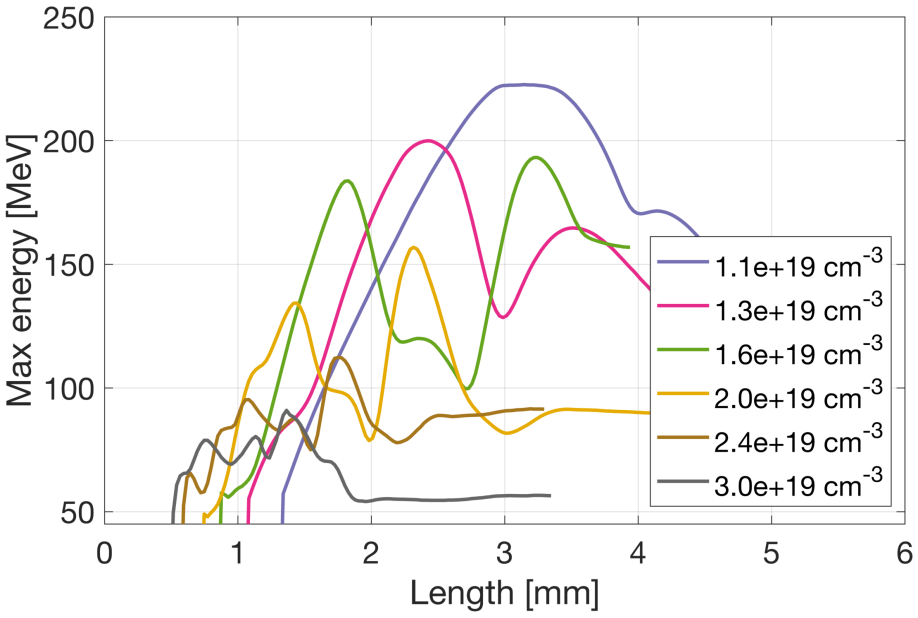
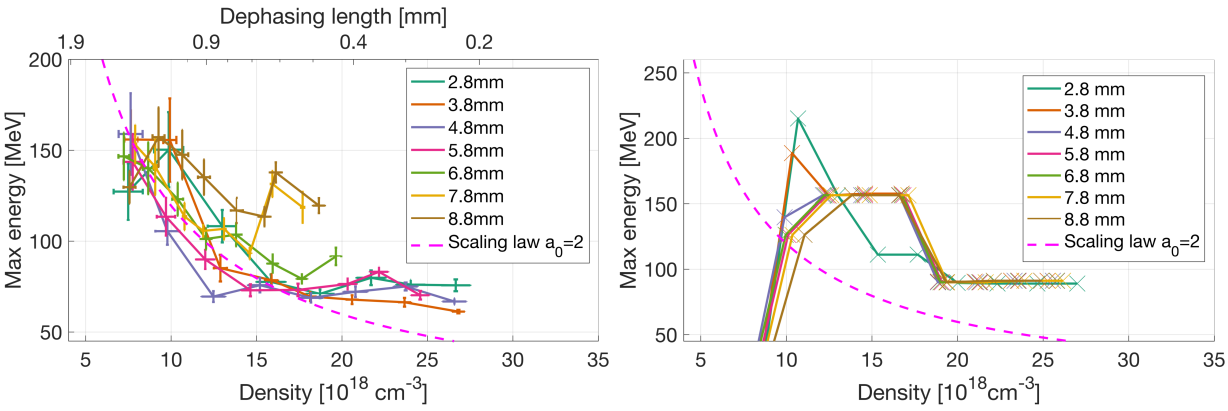


Figure 7.15: Figure showing the maximum energy of the electron beam at various points along the interaction length for a range of different densities



(a) Experiment (b) Simulation

Figure 7.16: The maximum energy of the electron beam from the experimental data on the left hand side and simulations on the right hand side.

the assumption that both atomic species, carbon and oxygen, are ionised upto their outer two levels. The inclusion of more atomic energy levels into the simulation could modify the ionisation defocussing and modify the resultant a_0 achieved in simulation.

Evolution length

In the previous chapter, the concept of the evolution length, L_{evo}, from Bloom et al., has been used to interpret the results for SI in the mismatched regime. We will now consider this concept for ionisation injection. Recall

$$L_{evo} = S\frac{n_c}{n_e}, \tag{7.6}$$

where n_e is the electron density, n_c is the critical density and S is a free parameter which characterises the length scale over which the self-focussing and pulse compression effects occur.

We define the evolution length as the length it takes the accelerator to begin injecting charge into the wakefield. Consider, the cumulative charge $Q_{cumulative}(L)$ as a function of accelerator length in Figure 7.17. This is defined as

$$Q_{cumul}(L) = \frac{1}{L}\int_0^L Q(E > 45\,\mathrm{MeV})\mathrm{dL}', \tag{7.7}$$

The energy threshold in the equation makes the result comparable to high energy electron spectrometer which only observed charge from $E > 45\,\mathrm{MeV}$. Here L_{evo} is defined as a length at which the $Q_{cumul}(L_{evo}) \equiv 0.01\max(Q_{cumul})$. In Figure 7.17, we show how the injection length varies with density for SI and II.

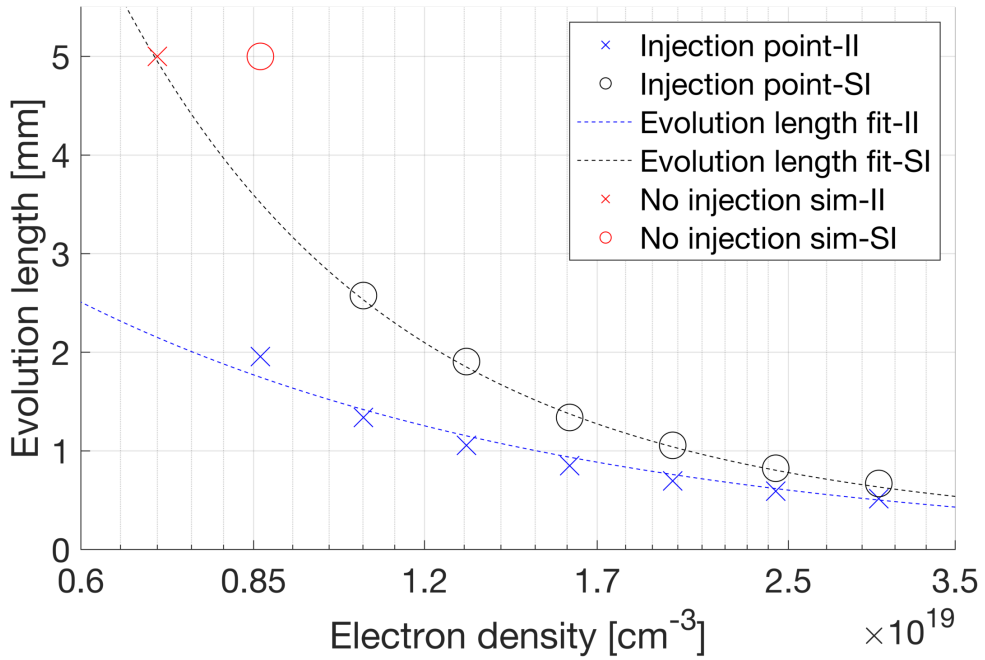


Figure 7.17: The evolution length for the various densities examined in simulations. The blue cross represents the data points from simulation where injection occurs for ionisation injection, the black circle represents the length at which injection occurs for self-injection. The corresponding dashed lines are the evolution length fits with $\frac{n_c}{n_e}$ for II and $\left(\frac{n_c}{n_e}\right)^2$ for SI as the dependant variable. The red markers are simulations where injection is not observed for II (cross) and SI (circle).

We recall from Chapter 6 on p.199, where we discussed the evolution length for SI. It was found that for SI, this length scaled with $\left(\frac{n_c}{n_e}\right)^2$ rather than $\frac{n_c}{n_e}$. For II, we instead observe agreement with the discussion from Bloom et al. [231]. Using this, we obtain an S parameter of $S_{II} = 8.59 \pm 3.7\,\mu\text{m}$. The greater injection length needed for SI is attributed to the higher injection threshold needed for self-injection to occur. We know that both pulse compression and self-focussing depend on $\frac{n_c}{n_e}$ [112]. This suggests that for SI to reach injection, both effects are important. The lower injection threshold might indicate that we do not need to focus the laser pulse as strongly to inject particles into the wake.

With this in mind, we extract the peak a_0 obtained along the entire interaction length for II and SI in Figure 7.18. In this figure, the red marker is the value for the peak a_0 extracted from the ionisation injection simulation for a particular density. The solid red lines represent a numerical fit to the data. For the peak a_0, we can see that there is no dependence with density for II. The fit for SI is shown as the dashed red line. the same

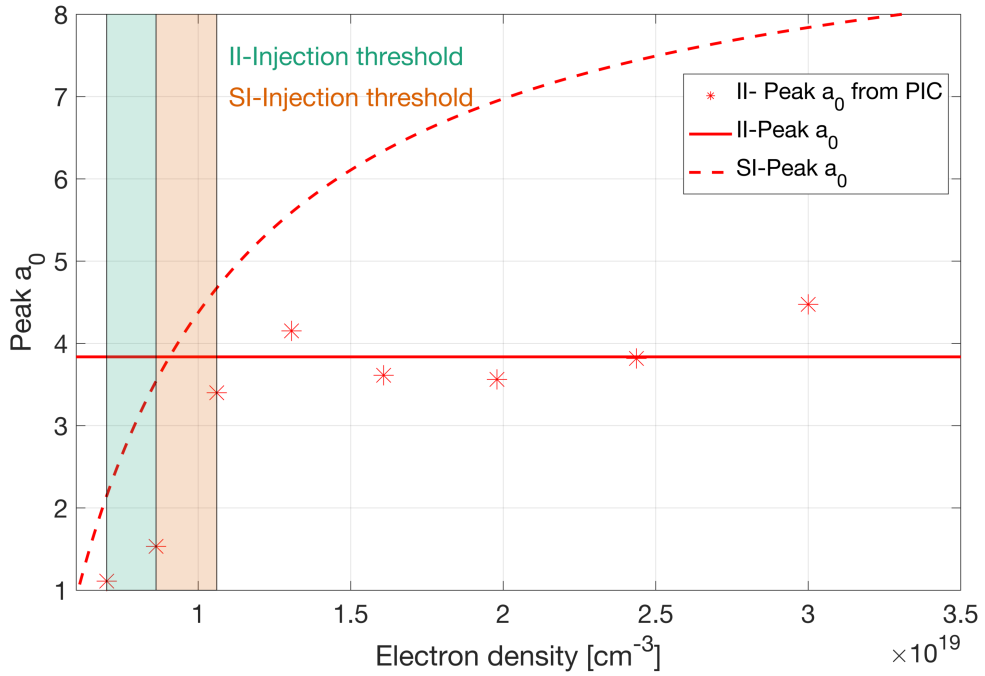


Figure 7.18: The evolution of the peak a_0 of the driving laser pulse along the interaction length for a range of densities for II and SI. The dashed lines represent the SI case and solid lines the II case. The red marker is the data extracted from simulations. We have exclude points below the injection threshold.

analysis for self injection which was presented in Chapter 6 on p.167.

We notice that the value of the peak a_0 does not change with density for the II case for densities greater than the injection density in Figure 7.18. This is in stark contrast to SI, where the peak a_0 scales with $\frac{n_e}{n_c}$. The presence of ionisation defocussing is expected to be responsible for this behaviour. The defocussing effect also scales with $\frac{n_c}{n_e}$[212] and so it is expected to balance the effects of self-focusing at higher densities.

For II, we used the following numerical fits for the length required to reach the peak a_0-$L_{a0,p}$, which we will refer to as the occurrence length. It is described by the following fit,

$$L_{a0,p,II} = a_{II,2}\frac{n_c}{n_e}, \tag{7.8}$$

where $a_{II,2} = 0.019 \pm 0.003$. For SI, we attain a comparable fit coefficient of $a_{SI,2} = 0.016 \pm 0.001$, within their respective errors.

In Figure 7.19, we plot the peak a_0 occurrence length for II and SI. The occurrence length is defined as the length at which the peak a_0 occurs. We can see that II takes longer to reach this value its peak a_0 value when compared to SI. This is even though the peak a_0 is lower.

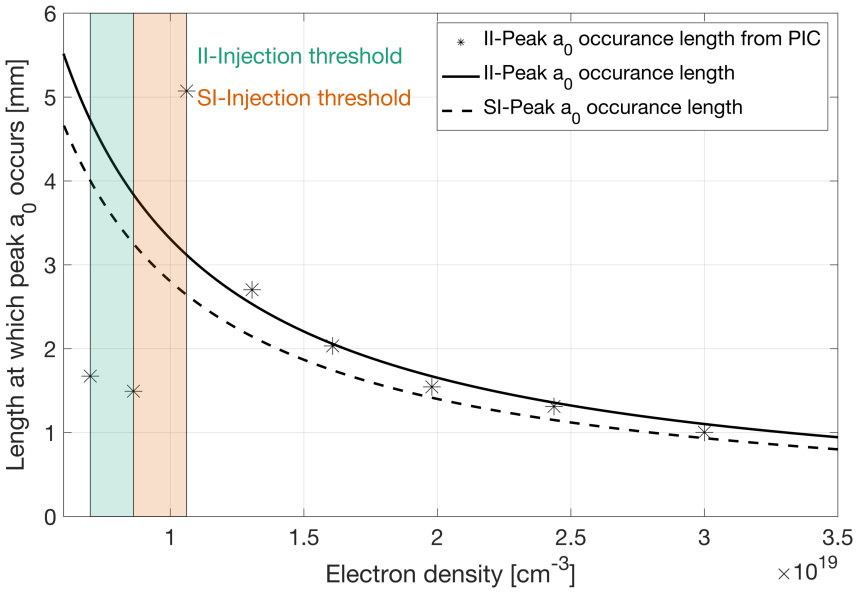


Figure 7.19: The length at which the peak a_0 occurs in the simulations, termed the occurrence length, of the driving laser pulse along the interaction length for a range of densities for II and SI. The dashed lines represent functional fits to the data points from simulations for the SI case and solid lines are functional fits for the II case from Eq. 7.8. We have exclude points below the injection threshold.

The linear fit with $\frac{n_c}{n_e}$ can only describe the data from densities $n_e > 1.1 \times 10^{19}\,\mathrm{cm}^{-3}$. Higher order effects are required to explain the evolution of the peak a_0 near the threshold density for injection. This is again a consequence of the ionisation defocussing effects modifying the evolution of the driver.

7.5 Discussion

In this section, we collate and discuss results from the experimental and simulation chapters. This section is broken up into the various key results shown in the earlier section; charge, maximum energy, divergence, pointing, eccentricity and transverse momentum. Along with attempting to understand how the observations relate to existing scaling laws in literature, we address the similarity with PIC simulations and the differences between the SI and II case.

Charge

Firstly, we address the charge observed on the high energy electron spectrometer $E > 45\,\mathrm{MeV}$ from Figure 7.5 on p185. The electron beams generated using II have a maximum charge of $37.1 \pm 1.6\,\mathrm{pC}$, which is lower than the highest charge obtained using self-injection of $50.0 \pm 2.3\,\mathrm{pC}$. For II this highest charge occurs at a density of $1.5 \pm 0.1 \times 10^{19}\mathrm{cm}^{-3}$, which is higher than for SI, where the highest charge is observed to occur at a density of $1.4 \pm 0.2 \times 10^{19}\mathrm{cm}^{-3}$. It is interesting to note that the highest charge occurs for the shorter cell length for both II and SI.

Another interesting observation is why SI and II do not simultaneously occur in this medium for the shortest cell length. We have sampled the same density region for the shortest cell length and yet the charge of the beam is lower for the II case. One explanation is that SI is suppressed because the trapping threshold is lower for II than SI. For II, once the $a_0 > 1.6$, we begin trapping particles, which occurs until the wake is loaded or the a_0 changes. Hence, this modification to the potential of the wake, suppresses injection into the wakefield. This suppression of SI has been reported in literature [115, 239].

Consider the non-linear beam loading limit derived by Lu et. al. [135]

$$\begin{aligned} N_0 &= \left(\frac{\beta^3}{\alpha}\right)\frac{8/15}{k_0 r_e}\sqrt{\frac{P}{m^2c^5/e}} \\ N_0 &\approx 2.5\times 10^9 \frac{\lambda_{0,\mu\mathrm{m}}}{0.8}\sqrt{\frac{P[\mathrm{TW}]}{100}} \end{aligned} \tag{7.9}$$

where $\alpha = \frac{k_p w_0}{2\sqrt{a_0}}$, $\beta = \frac{k_p R_0}{2\sqrt{a_0}}$, $\alpha = \beta = 1$ for a spherical bubble which results in $N_0 = 127\,\mathrm{pC}$. $N_0 \propto P^{1/2} \propto I^{1/2} \propto a_0$, hence a lower amplitude wakefield will have a lower beam loading limit. While strictly not valid for the mismatched, intermediate a_0 regime, it is still instructive to compare the values obtained to these scaling laws. We see that the density of optimum charge varies much less for II than SI, occurring at an electron density of

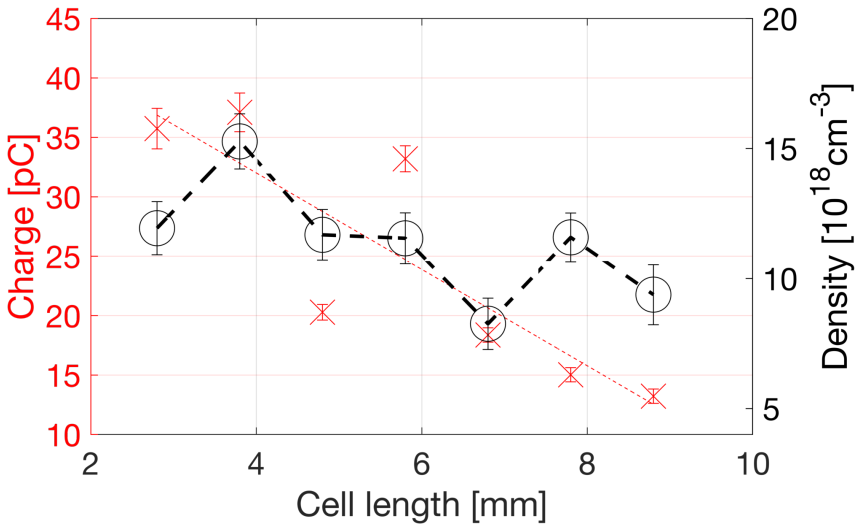


Figure 7.20: The highest value of charge is shown as the red marker on the left hand axis. The corresponding value of density that this value of charge occurs, for a particular cell length is shown as the black circular marker on the right hand side. The black dashed line is a fit is a linear fit between each data point to guide the general trend. The dashed red line is a linear fit to the charge and cell length data points.

$1 \times 10^{19}\,\mathrm{cm}^{-3}$. From Figure 7.5, for each cell length, we extract the highest charge that can be achieved for a particular cell length and the density at which this occurs and plot this a function of cell length in Figure 7.20.

A direct consequence of the lowering of the injection threshold is that electron beams are observed at lower densities. Consider the minimum density at which electron beams appear with charge $Q > 10\,\mathrm{pC}$. For SI, this occurs at densities of $n_e > 7.9 \times 10^{18}\,\mathrm{cm}^{-3}$, whereas for II, $n_e > 6.9 \times 10^{18}\,\mathrm{cm}^{-3}$.

For II and SI, we observe that increasing the cell length, decreases the largest value of charge, for a fixed cell length, over a range of densities. However, the rate at which this maximal value of charge decreases is different for SI than for II. In Figure 7.20, we plot for each cell length, the highest value of beam charge over the range of densities sampled. The density at which this occurs is also plotted on the right hand side of this figure. We can see that the highest beam charge decreases as a function of cell length at a rate of $-4.1\,\mathrm{pC\,mm}^{-1}$ for II. This is a much lower loss of beam charge when compared to SI where we obtained $-12.6\,\mathrm{pC\,mm}^{-1}$. We note that this is a density independent effect as we have chosen the highest charge in a density range.

The lower injection threshold allows injection to occur continuously along the length of the accelerator and at lower intensities. For these densities, we note that the dephasing

length is in the range of 0.8 mm − 1.5 mm. After 5.8 mm, we can see that the charge monotonically decreases. This indicates that the wakefield amplitude has dropped below the threshold needed to inject background electrons. We can calculate the timescale for the wake to become loaded, consider the analysis of trapped charge length from Schroeder et al. [240] ,

$$\begin{aligned} N_t &\approx \pi w_i^2 l_i f_i n_{e,i} \Delta^2, \\ \Delta &= \left(\frac{3\pi r_e a_i}{\alpha^4 \lambda_l}\right)^{1/2} \left(\frac{V_H}{V_Z}\right)^{0.75}. \end{aligned} \tag{7.10}$$

Where α is the fine structure constant, r_e is the classical electron radius, V_H is the ionisation potential of hydrogen, V_Z is the ionisation potential of the relevant atomic species, $n_{e,i}$ is the electron density of the ionisation species, l_i is the interaction length and w_i is the spot size.

Using a spot size of 10 µm, and only examining the charge from the final two levels of carbon and oxygen, we obtain a trapped charge per unit length of $\frac{\mathrm{d}Q_{tr}}{dl} = 133\,\mathrm{pC\,mm^{-1}}$. This results in a trapping length scale of 950 µm. This short length scale over which the beam can become loaded explains why the beam charge can increase by from 20 pC to 33 pC between 4.8 mm and 5.8 mm. In Figure 7.13, we can see the wakefield become fully loaded within this length scale. To see finer details of charge dynamics, we need to vary the interaction length on the 100 µm scale.

We notice that the density at which we obtain optimum charge, varies weakly with cell length. This allows us to treat Figure 7.20 effectively as a length scan. The loss of charge from 3.8 mm to 4.8 mm can then be interpreted as the injected electron beam dephasing. Once the beam begins dephasing, the beam-loading field of the bunch is in the decelerating phase of the wake and this is why we observe a secondary injection event from 4.8 mm to 5.8 mm.

We have already seen that wave-breaking must be suppressed in the medium which suggests the optimal a_0 for II is lower than SI. One consequence of this is that we expect the energy of the electron beam to be lower as the energy gain also scales with a_0. As such, we move on to discussion of the maximum energy gain of the electron beams, when injected through II.

Maximum energy and a_0 along the interaction length

In Figure 7.6, the maximum energy against density and cell length was shown. We see that the highest energy electron beams achieved are 159 ± 22 MeV. This is 25% lower than the highest energy electron beams from the self-injected case, where we obtain 210 ± 19 MeV. In general, for II, the electron beam approximately follows the non-linear scaling law from Lu et al. [135] for densities $n_e < 1.7 \times 10^{19}\,\mathrm{cm}^{-3}$ but underestimates the energy of the electron beam for higher densities. Recall the energy gain equation for the non-linear case,

$$W_{max} = \frac{2a_0 m_e c^2 n_c}{3n_e}, \tag{7.11}$$

where we observe no explicit length dependence, unless the effective a_0 of the interaction varies along the interaction length.

We have already alluded to this in the previous section where we observe for longer cell lengths, the electron beam energy exceeds the scaling law. We can extract the effective $a_{0,eff}$ for the driver, for particles to reach the observed energies, by rearranging Eq.7.11,

$$a_{0,eff} = \frac{3W_{max} n_e}{2m_e c^2 n_c}. \tag{7.12}$$

In Figure 7.21, we can see that increase the length of the accelerator increases the effec-

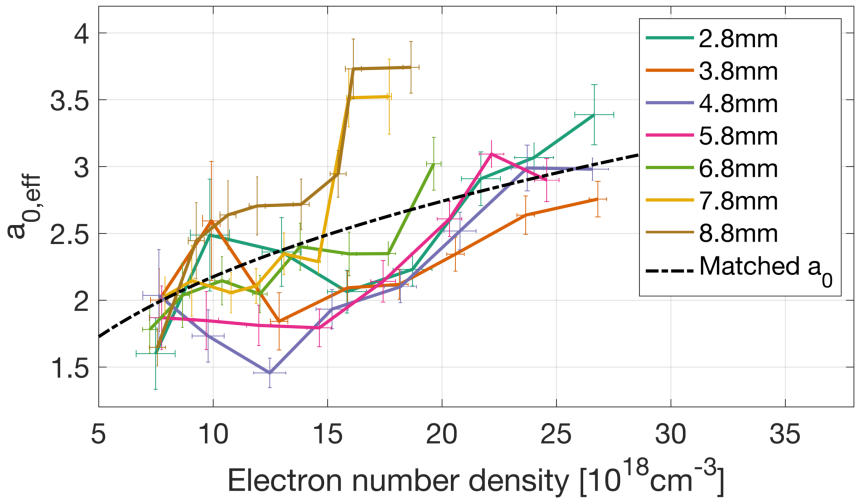


Figure 7.21: The $a_{0,eff}$ from Eq. 7.12 as a function of density for various cell lengths. The black dashed line is the matched $a_{0,m}$ from Eq. 7.13

tive a_0 of the interaction, reaching a maximum value of $a_{0,eff} = 3.7 \pm 0.3$. There are two distinct regions of interest in this figure. First we will address the increase in the a_0 of the laser pulse for cell length < 5.8 mm with density.

The increase in a_0 is due to longitudinal a_0 amplification as the pulse is self-focussed to the matched spot size. The matched a_0 is given as,

$$a_{0,m} = \left(\frac{w_0 a_0 \omega_p}{2c} \right)^{2/3}, \tag{7.13}$$

and represents the a_0 the laser pulse will self-focus to in the absence of energy loss and assuming we are above the critical power for self-focussing. We can see how the matched a_0 agrees well with the value for the $a_{0,\mathit{eff}}$.

Secondly, we address the trend for cell length $< 5.8\,\mathrm{mm}$ with density. This regime represents a much greater increase in a_0 and occurs when we are well past the dephasing length and close to depletion. This increase in a_0 is attributed to power amplification of the laser pulse generated by wavelength red-shifting [112, 134] and is observed in PIC simulations in Figure 7.12b. Close to depletion we can expect the largest amount of red-shifting of the laser pulse and the highest effective $a_{0,\mathit{eff}}$ as $a_0 \propto \sqrt{I\lambda^2}$. This effect will amplify onto the increase in a_0 from the matched spot size to give the largest values for $a_{0,\mathit{eff}}$. We now move on to discussing the variation in beam divergence with density and length for II.

Beam divergence

Now we address the beam divergence data presented for II in Figure 7.7, on p.187. For II, the largest beam divergence value measured was $8.1 \pm 0.4\,\mathrm{mrad}$ at density of $2.3 \pm 0.1 \times 10^{19}\mathrm{cm}^{-3}$ for a cell length of 2.8 mm. Correspondingly, for SI, the largest beam divergence value measured was $10.1 \pm 0.4\,\mathrm{mrad}$ at density of $2.2 \pm 0.1 \times 10^{19}\mathrm{cm}^{-3}$ for a cell length of 3.8 mm.

It in interesting to note that for both injection mechanisms, the largest beam divergence value attained occurred at similar densities and similar cell lengths. While II generates electron beams which have a lower θ_{max} than SI, it still suggests that the origin of divergence growth is intrinsic to the evolution of the plasma wave rather than the injection mechanism.

Beam divergence can increase either due to an increase in transverse momentum and/or a decrease in longitudinal momentum. As the electron beam is accelerated to its dephasing length, its divergence approaches a minimum. However, the laser pulse might also occupy some fraction of the wake and interactions with the laser pulse will increase the transverse momentum [241].

The lowest beam divergence value measured for II was 1.63 ± 0.4 mrad at a density of $7.6 \pm 0.4 \times 10^{18}\text{cm}^{-3}$ and $1.5 \pm 0.1 \times 10^{19}\text{cm}^{-3}$ for a cell length of 8.8 mm. Two densities are given as within the error-bar these values were attain for both values. Similarly for SI, we obtain 1.5 ± 0.1 mrad at density of $1.1 \pm 0.1 \times 10^{19}\text{cm}^{-3}$ for a cell length of 4.8 mm. For II, it is interesting that at such different densities, we see the lowest beam divergences. For the lowest density, we note that using the matched a_0 value the dephasing length and depletion length are $L_{dp} = 2.5$ mm and $L_{pd} = c\tau\frac{n_c}{n_e} = 3.1$ mm respectively. Hence, as the dephasing and depletion length are close to each other, the termination of the plasma wave at the point of dephasing could be one reason for the low beam divergence.

The more curious results is why the divergence of the beam decreases for higher densities. Here, we hypothesis that injection occurs in the second bucket of the wake due to its increased non-linearity from longitudinal a_0 matching and power amplification as the laser pulse is red-shifted. We see that the reduction in divergence at the higher densities occurs more dramatically for longer cell lengths. Another possibility for the reduction in beam divergence is that, as the wakefield amplitude decreases due to laser pulse depletion, the electron beam begins to drive a plasma wave which has a focussing effect on the driving electron beam known as passive plasma lensing [242].

Pointing deviation

The pointing of the electron beam was shown in Figure 7.8 on p.188 to be correlated with density. The Y axis was defined at the axis aligned along the laser polarisation direction, the X axis was the orthogonal transverse axis. For II, we obtain the largest Y axis pointing deviation of 2.7 ± 0.1 mrad at $2.0 \pm 0.8 \times 10^{19}\text{cm}^{-3}$ and cell length of 2.8 mm. For SI, the corresponding values were 3.6 ± 0.1 mrad at $1.7 \pm 0.1 \times 10^{19}\text{cm}^{-3}$ and cell length of 5.8 mm. The largest X axis pointing deviation, for II, was measured to be 3.8 ± 0.3 mrad at $8.1 \pm 0.9 \times 10^{18}\text{cm}^{-3}$ and cell length of 2.8 mm. For SI, we have measured a pointing offset of 4.5 ± 0.1 mrad at $2.3 \pm 0.5 \times 10^{19}\text{cm}^{-3}$ and cell length of 5.8 mm. Hence, we can see that II generates beams which are less offset, relative to the optical axis.

The correlation of electron beam pointing with density and length is a rather odd observation. For the SI dataset, the large pointing variations and smaller size of aggregate shots make it difficult to ascertain any trends. For the II dataset, we see that there is a linear trend in the X offset for cell lengths of 2.8 mm and 3.8 mm. We will constrain our discussion to explain the origin of this relationship. One possibility it that misalignment of the gas cell caused the beam to refract by different amounts, depending on the density of the plasma. Consider the effect of refraction due to a gas cell which is tilted off axis.

The refractive index of plasma is given as

$$\eta = \sqrt{1 - \frac{n_e}{n_c}}, \tag{7.14}$$

using Snell's law, we can examine the angular deflection of the laser pulse entering the plasma as,

$$\begin{aligned} \theta_{vac} &= \eta \theta_{beam} \\ \theta_{vac} &= \theta_{beam} \sqrt{1 - \frac{n_e}{n_c}}. \end{aligned} \tag{7.15}$$

The problem is shown schematically in Figure 7.22.

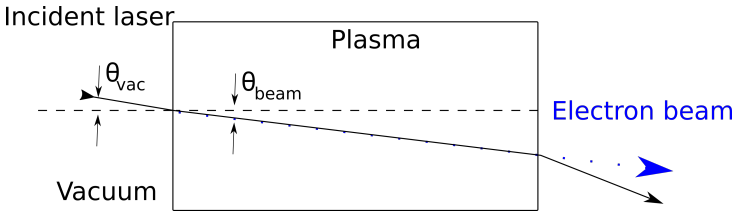


Figure 7.22: The pointing offset generated by refraction in plasma.

We are interested in the gradient of angular shift with electron density, letting $\tilde{n} = \frac{n_e}{n_c}$

$$\begin{aligned} \frac{\mathrm{d}\theta_{beam}}{\mathrm{d}\tilde{n}} &= \frac{\theta_{vac}}{2}\left(1 - \tilde{n}\right)^{-3/2} \\ \frac{\mathrm{d}\theta_{beam}}{\mathrm{d}\tilde{n}} &\approx \frac{\theta_{vac}}{2} \end{aligned} \tag{7.16}$$

Using the experimental data from Figure 7.8 for the X pointing and a cell length of 2.8 mm, we obtain a value of $\frac{\mathrm{d}\theta_{beam}}{\mathrm{d}\tilde{n}} = -176$ mrad, resulting in a $\theta_{vac} = 350$ mrad. However, this is far greater than the acceptance angle of our diagnostic and we can see the transmitted laser pulse on the beam profile diagnostic. We see that refraction from uniform plasma cannot explain the gradient in the pointing deviation of the electron beam with density. Hence, we can rule out the effect of misalignment as a reason for this variation in pointing. The other well reported reason for the steering of electron beams from a wakefield accelerator in plasmas is due to pulse front tilt [235, 243]. The tilt angle of the wake, θ_w, is related to the density of the interaction and the pulse front tilt (PFT) angle $\tan\Phi$ as

$$\begin{aligned} \tan\theta_w &= \frac{-k_p w}{2} \tan\Phi \\ \tan\Phi &= c\left(k_L\beta + \phi_2 \frac{\zeta}{\zeta^2 + \frac{w^2\tau^2}{4}}\right) \end{aligned} \tag{7.17}$$

where k_L is the wavevector of the laser, β is the angular chirp, ϕ_2 is the temporal chirp, ζ is the spatial chirp, w is the spot size and τ is the pulse duration. In this experiment, we do not characterise the PFT angle, but we can estimate if this effect is of the appropriate magnitude to provide the tilts observed. We assume that the spatio-temporal terms are non-evolving and $\tan\theta_w \approx \theta_w$,

$$\begin{aligned} \theta_w &= \tilde{n}\left(\frac{e^2 w^2 n_c}{2 m_e c^2 \epsilon_0}\right)\tan\Phi \\ \frac{\mathrm{d}\theta_w}{\mathrm{d}\tilde{n}} &= \left(\frac{e^2 w^2 n_c}{2 m_e c^2 \epsilon_0}\right)\tan\Phi \end{aligned} \tag{7.18}$$

This give us $\tan\Phi$=0.0176, suggesting that PFT is a possible explanation for the tilting of the electron beams off-axis. When using electron beams generated from such targets, it should be noted that this difference in pointing can become significant for applications such as staged acceleration and must be accounted for by either characterisation of the pointing trend or the spatio-temporal characterisation of the laser pulse.

Eccentricity

We move on to addressing the eccentricity of the electron beams generated using II. We have used the linear definition for the eccentricity of an ellipse, which is defined as the ratio of the minor to the major axes of an ellipse. The largest value of eccentricity achieved for II is $e_{max} = 0.84 \pm 0.06$ at a density of $1.25 \pm 0.08 \times 10^{19}\mathrm{cm}^{-3}$ at a length of 5.8 mm. For SI, we similarly attained a maximum eccentricity of 0.93 ± 0.06 at a density of $1.56 \pm 0.03 \times 10^{19}\mathrm{cm}^{-3}$ at a length of 5.8 mm. The lowest value of eccentricity for II, observed in this dataset is $e_{min} = 0.2 \pm 0.04$ at a density of $1.51 \pm 0.06 \times 10^{19}\mathrm{cm}^{-3}$ and a cell length of 8.8 mm. Furthermore for SI, we attain a larger value of 0.26 ± 0.03 at a density of $2.22 \pm 0.01 \times 10^{19}\mathrm{cm}^{-3}$ and cell length of 3.8 mm.

An increase in the eccentricity of the beam, represents the electron beam preferentially gaining momentum in the axis parallel to the laser polarisation. While for both injection mechanisms it is possible, for certain densities for the gain in transverse momentum to be equal in both axes. For SI, electron beams are observed with the lowest degrees of eccentricity.

In Figure 7.23, we plot the beam eccentricities from both SI and II side-by-side as a function of $\frac{c\tau}{\lambda_p}$. The origin for the generation of elliptical electron beams has been discussed in literature for the self-injection case, where it is suggested that it scales with $\frac{c\tau}{\lambda_p}$ [244]. We define $R_{pl} = \frac{c\tau}{\lambda_p}$ and we are interested in the value of R_{pl} at which the eccentricity is maximised. With the exception of the 4.8 mm case for SI, we see that the

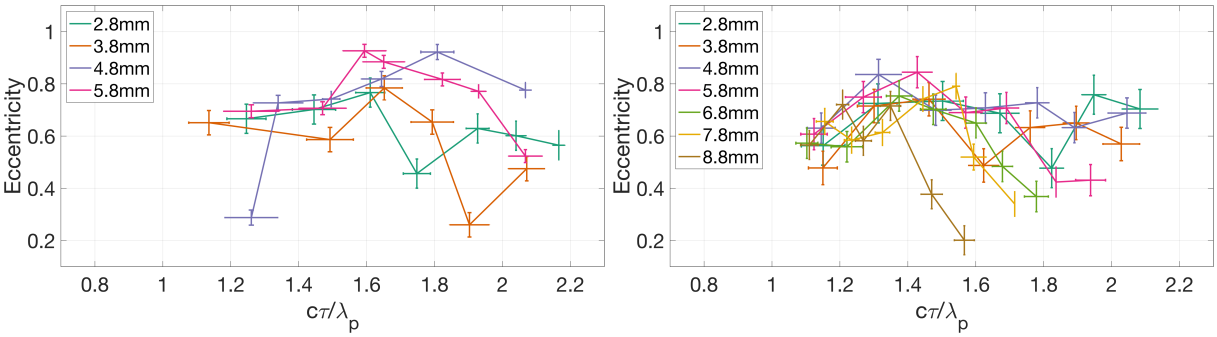


Figure 7.23: Figure showing the beam eccentricity as a function of bunch length normalised to the plasma wavelength, for various cell lengths for self injection (left hand side) and ionisation injection (right hand side)

value for R_{pl} obtained for SI is $= 1.61 \pm 0.16$. In Mangles et al. [244], the most elliptical beams are also observed for $R_{pl,SI} = 1.63$ and so we attain a good agreement for the SI case, despite have different laser conditions.

Now for the II case, we attain $R_{pl} = 1.47 \pm 0.11$. We can see that the a lower value of R_{pl} indicates that, at the equivalent density, in the II case, the electron beam catches up with the laser pulse first and interacts earlier to gain more momentum in one axis, increasing the beam eccentricity. This could be due to the fact that we are driving a more non-linear wake for the SI case, as is necessary to achieve injection primarily, which results in faster pulse compression and relativistic plasma wave lengthening. This causes the value of R_{pl} which maximizes the interaction of the electron beam with the laser pulse to occur at a greater value.

Transverse momentum

Finally, we address the transverse component of momentum, in the axis aligned along the laser polarisation axis. The maximum energy is used for the longitudinal component of momentum, p_z and the transverse momentum is defined as

$$\langle p_y \rangle = \langle \theta_{long} \rangle p_z, \tag{7.19}$$

where $\langle p_y \rangle$ is root mean square (rms) transverse momentum and $\langle \theta_{long} \rangle$ is the rms divergence aligned to the laser polarisation axis. For II, the largest measurement of $p_y = 0.64 \pm 0.05\,\mathrm{MeV/c}$, occurs at a density of $2.17 \pm 0.13 \times 10^{19}\mathrm{cm}^{-3}$ and a cell length of 2.8 mm. We recall from the previous section that for SI, the extracted transverse component of momentum is much larger at $1.36 \pm 0.52\,\mathrm{MeV/c}$, occurring at a density of $1.9 \pm 0.1 \times 10^{19}\mathrm{cm}^{-3}$ and a cell length of 5.8 mm.
The energy that we have used to extract the transverse momentum might not have the

same radius as the half-maximum contour of the beam profile. However, it is still represents an upper bound on the measured value of p_y. For SI, transverse wave-breaking will result in the injected electron bunch having a large transverse momentum. For II, the particles with the largest transverse momentum will be born at the radial extent where the intensity of the pulse is strong enough to ionise the atom. II is thus expected to be generated with a lower transverse momentum than SI.

The lack of dependence on density for the transverse momentum of II can arise due to injection occurring once we have reached the spot size for when the wakefield can begin injecting background electrons $a_0 > 1.6$ and the ionisation injected electrons and this represents the largest momentum that these particles can be born with.

7.6 Conclusion

In this chapter, we have examined the density-length parameter space for a gas cell using ionisation injection at a 10 TW laser facility. This section builds upon the observations of the previous chapter which examined self-injection for identical experimental conditions. In Table 7.5, we present some of these beam parameters and the corresponding densities at which they occur.

Electron beams are present at lower densities for II than SI, with beams observed at $6 \times 10^{18}\,\mathrm{cm}^{-3}$ for II. The highest charge of the electron beam is lower for II at $37.1 \pm 1.6\,\mathrm{pC}$, compared to SI at $50.0 \pm 2.3\,\mathrm{pC}$. PIC simulations predict a maximum beam charge of 55 pC but this occurred at a cell length of 1.5 mm, which is less than the value the targetry was explored for in the experiment. In comparison to the data, the simulations give good agreement with the maximum charge but predict a higher density at which this charge occurs.

II has been shown to generate electron beams with maximum energies of $159 \pm 22\,\mathrm{MeV}$, which is 35% lower than SI. We attribute this to the difference in a_0 of the plasma wave for II and SI. For SI, injection can only occur once $a_0 > 3$, where as for II injection can being at $a_0 > 1.6$. By using the energy gain equation, the maximum energy and the density, we can extract an effective $a_{0,eff}$ for the interaction. For cell lengths less than 6.8 mm $a_{0,eff}$ was observed to follow the matched a_0 form Eq.7.13. For the highest densities and the longest cell length, we observe an effective a_0 higher than this. This is attributed to power amplification effects due to pulse compression in the medium [112]. PIC simulations in cylindrical geometry were used to compare differences in the evolution of a_0 between II and SI. It was observed that the peak a_0 was clamped at ≈ 4 in simulations with II due to ionisation defocussing, whereas for II it scales with $\frac{n_c}{n_e}$.

While the spectral beam parameters are more favourable for SI, electron beams produced using II have low beam divergences of 1.6 mrad and a lower pointing offset when compared to SI, with low divergence electron beams present over a wide range of density-length parameters. The maximum eccentricity of the electron beam is 10% greater for SI than II.

We attributed the correlations between beam pointing and density to the effects of pulse front tilt (PFT)[235] and show that refraction due to misalignment is an order of magnitude weaker than the effects of PFT. The rms transverse momentum of II beams is observed to be relatively uniform as a function of density and length. They are also a

factor of 2 lower than the rms transverse momentum of beams generated by SI. This is ascribed to the injection for SI occurring off axis at larger radial extents, whereas for II, the injection occurs closer to the optical axis.

Parameter	Value	Density [10^{18}cm^{-3}]	Length [mm]
Highest charge	37.1 ± 1.6 pC	15.3±1.1	2.8
Maximum energy	159 ± 22 MeV	7.63±0.7	4.8
Min/max divergence	$1.63 \pm 0.1, 8.1 \pm 0.9$ mrad	11.6 ± 0.1, 23.3 ± 0.9	6.8, 2.8
Highest X,Y offset	$3.8 \pm 0.3, 2.7 \pm 0.2$ mrad	8.1±0.9, 20.4±0.8	2.8, 2.8
Min/max eccentricity	0.20 ± 0.06, 0.84 ± 0.11	15.1±0.6, 12.5±0.8	8.8, 5.8
Min/max p_r	0.19±0.01, 0.64±0.05 MeV/c	15.5±0.8, 21.7±1.3	8.8, 2.8

Table 7.5: The optimal values for various electron beam parameters along with their associated density-length values.

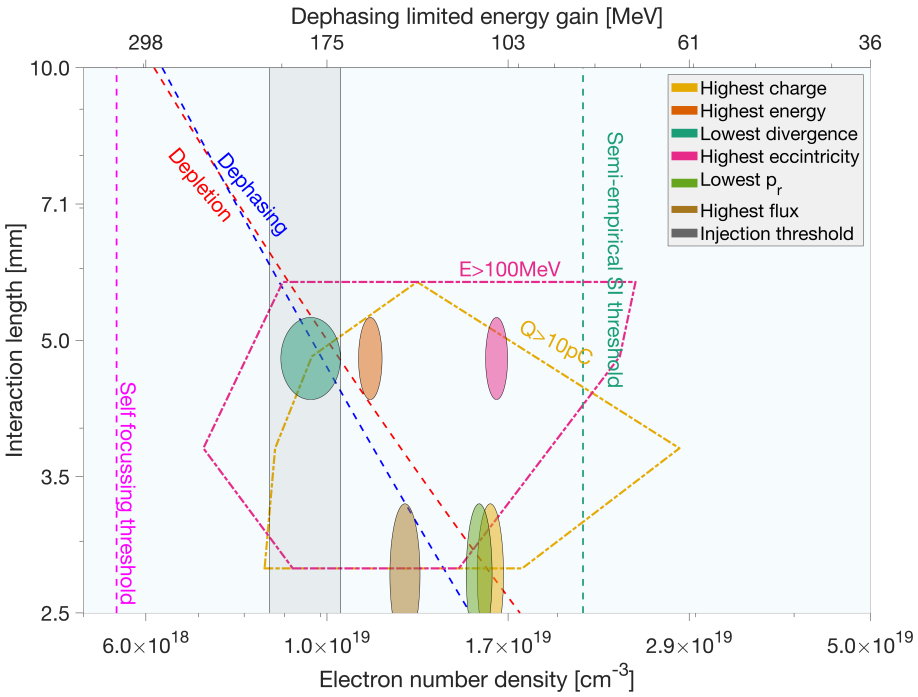
In Figure 7.24, we have plotted all of these values onto the density and length parameter space, where Figure 7.24a is the density-length parameter space plot for SI and 7.24b is the equivalent plot for II. We have used the concept of the evolution length to modify the dephasing and depletion length estimates. It was observed that the evolution length for SI scales as $\left(\frac{n_c}{n_e}\right)^2$ and but for II it scales as $\left(\frac{n_c}{n_e}\right)$.

$$\begin{aligned} L_{evo,SI} &= S_{SI}\left(\frac{n_c}{n_e} + \alpha_{SI}\right)^2, \\ L_{evo,II} &= S_{II}\left(\frac{n_c}{n_e}\right), \end{aligned} \tag{7.20}$$

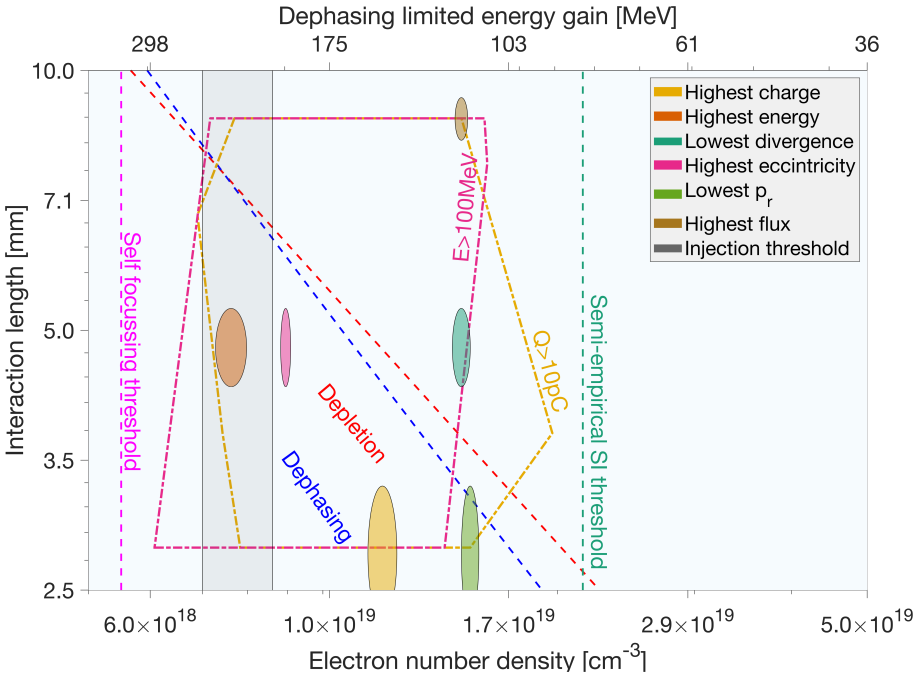
with $S_{SI} = 55.6 \pm 6.8$ nm, $\alpha_{SI} = 48.4 \pm 10.5$ and $S_{II} = 8.59 \pm 3.7$ µm extracted from simulations to correct the dephasing and depletion length estimates in the parameter space plot such that,

$$\begin{aligned} L_{dp,SI/II} &= \frac{4\sqrt{a_0}n_c}{k_p n_e} + L_{evo,SI/II}, \\ L_{pd,SI/II} &= \frac{n_c}{n_e}c\tau + L_{evo,SI/II}. \end{aligned} \tag{7.21}$$

Here L_{dp} is the non-linear dephasing length and L_{pd} is the non-linear pump depletion length [236] for SI and II correspondingly. This was done to make the comparison with the scaling laws valid for mismatched conditions. We can see that the inclusion of the evolution length allows the application of the matched scaling lengths. It is interesting to note that when we use the adjusted values for the depletion and dephasing length, most



(a) Self injection



(b) Ionisation injection

Figure 7.24: Figure showing the parameter space for both SI and II using the constraints with some key results overlaid. The injection threshold is extracted from PIC simulations performed for both scenarios.

of the notable values occur near these lines. The exceptions to this occur for the highest eccentricity for SI and the lowest divergence for II.

One way in which we can use Figure 7.24 is by asking what density and/or length we should operate near to obtain the highest charge electron beams. We can see that the cell length should be 2.8 mm for both injection mechanisms. The density for II should be $1.2 \pm 0.1 \times 10^{19}\text{cm}^{-3}$ whereas for SI we should operate at a higher density of $1.6 \pm 0.1 \times 10^{19}\text{cm}^{-3}$. In order to use the evolution length scaling law for a different laser parameters we have to generate a new evolution length scaling law using PIC simulations. This can be done prior to the commencement of experiments to dramatically reduce the parameter space which we need to search in order to optimise the accelerator.

The other way in which Figure 7.24 can be used for future experiments is by considering multi-parameter optimisations. For some applications, such as a bremsstrahlung source of x-rays using the electron beam, having electron beams with energy > 100 MeV and sufficient charge 10 pC is desired. We can see that there is a larger range of parameters with II where this can be achieved. With more stringent constraints the overlapping regions in the density-length parameter space becomes smaller and we can predict whether an experimental configuration will be able to deliver electron beams with a particular set of characteristics. If not then we have to look for new injection mechanism or a different set of laser parameters.

The results presented thus far have interesting implications both for this particular experimental configuration and for injection mechanisms in general. For experiments performed with these experimental conditions, we have presented data which implies that the highest charge and highest energy electron beams were observed, across both density and length, for SI. The lowest divergence, lowest eccentricity and lowest transverse momentum beams were observed for II. For the particular application sought, these results can be used to predict the performance of attainable wakefield acceleration experiments for 10 TW laser systems.

We see that ionisation defocussing clamps the a_0 of the laser pulse for this particular dopant. This opens up the possibility of tailoring the dopant concentration to modify the evolution of the laser pulse in order to improve the performance of the accelerator, by forcing it to operate in the quasi-linear regime.

8 Conclusion

This over-arching theme of this thesis the exploration of novel targetry and injection mechanisms for laser wakefield accelerators. The first two chapters address the generation of electron beams from wakefield accelerators in a clustered medium. The mechanism is compared to other well examined injection mechanisms to understand the opportunities presented by this new form of targetry. The last two chapters of this thesis address the optimisation of targets across a multi-dimensional input parameter space, namely density and length. We begin by summarising the results from the various chapters and examining the future outlook of this work.

8.1 Summary of results

Chapter 4: Laser wakefield acceleration in a clustered medium

The aim of this chapter was to understand how particle injection and acceleration in a laser wakefield accelerator (LWFA) occur in a clustered medium. Methane and helium were examined as targets in both gas cells and gas jets, where methane in a gas jet is known to cluster. The other targets were utilised as controls to exclude the possibility that this was just ionisation injection/self-injection. The clustered target generates the highest charge electron beam with upto $60 \pm 5\,\mathrm{pC}$ of charge in the beam. Helium in the gas cell generates the highest energy electron beams, with energies upto $211 \pm 4\,\mathrm{MeV}$.

Methane in the gas cell performs poorly in comparison to methane in a gas jet. We attribute this to the ionisation defocussing effects of the medium counteracting the effects of self-focussing. This is not observed in the gas jet either due to self-focussing effects of a clustered medium or the full atomic ionisation due to the additional heating mechanisms that arise in laser-cluster interactions.The gas jet with helium also performed poorly and this is ascribed to imperfections in the nozzle resulting in large scale density variations $\approx 10\%$ in the medium [121].

Simulations were performed using Particle-In-Cell (PIC) codes to understand how a laser wakefield accelerator is established within a clustered medium. The wake formation

was observed to be due to the unclustered portion of the medium. On the time-scale of the plasma wave, the ions of the cluster do not expand significantly. The electrons that are initially bound in the cluster are liberated upon interaction with the laser pulse. The charged cluster draws additional electrons from the background medium to neutralise the generated charge separation. Hence, the cluster will, for the duration of the interaction have sufficient charge to trap into the plasma wave. The results from this section are presently being written up for publication, focussing on the first observation of a clustered medium increasing the charge of an electron beam compared to a non-clustered medium.

Chapter 5: Comparison between cluster injection, self-injection and ionisation injection at 200 TW

We then followed on from the results of the previous chapter to examine a clustered medium for wakefield acceleration with a vacuum $a_0 < 1$ to a higher peak power laser system, the Astra-Gemini TA3 laser facility, where the peak power is 200 TW and the vacuum $a_0 > 1$. Higher peak intensities could result in the cluster ion density at the moment of interaction with the wakefield being lower.

Cluster injection with methane in a gas jet (CI) was compared to self-injection with helium (SI) and ionisation injection with helium+1% nitrogen (II). All three methods of particle injected generated electron beams with ≈ 100 pC. SI generates electron beams with the highest maximum energies of 1.4 ± 0.05 GeV. Distinct monoenergetic bunches were observed for SI at low electron densities. The energy spectrum for CI and II were broad due to the continuous nature of their injection. The divergence of the electron beams with SI was greater than for II and CI. For CI at higher densities, the electron beam exhibited large radial oscillations which were attributed to the hosing instability.

The x-rays generated from betatron oscillations in these interactions were compared. SI generated higher critical energy x-rays than CI and SI, where $E_{c,SI} = 17.1 \pm 0.8$ keV, $E_{c,CI} = 12.0 \pm 1.3$ keV and $E_{c,II} = 11.0 \pm 0.4$ keV. CI and II generate an order of magnitude greater flux than SI, where, the largest flux of radiation in CI was correlated to the electron beams with the largest transverse oscillation. The increase in flux of the betatron radiation is being assembled into a publication highlighting how a clustered target can be used to increase the flux of betatron radiation.

Chapter 6: Investigation of the density-length parameter space in a mismatched, self-guided, self-injecting laser wakefield accelerator at 10 TW

This chapter focused on the density-length parameter space for self-injection using a 10 TW laser, the Astra-Gemini TA2 laser facility. The density of the medium and the interaction length were simultaneously varied to find the optimum beam parameters for the interaction. Density-length optima were found for charge (50.0 ± 2.3 pC), maximum energy (210 ± 19 MeV) and beam divergence (1.5 ± 0.1 mrad). The results of the experiment were compared to PIC simulations where reasonable agreement for beam energies and charge were observed.

The secondary goal of this chapter was to extend the matched evolution scaling laws in order to predict where these optima are likely to occur. The concept of evolution length [231] was utilised to generate a modification to the dephasing and depletion length estimates from Lu et al. [135]. The evolution length was extracted using PIC simulations using FBPIC [3]. This code uses a spectral solver in quasi-3D geometry to more accurately capture the self-focussing in plasma. Contrary to the findings in Bloom et al. [231], the evolution length was found to scale with $\left(\frac{n_c}{n_e}\right)^2$, rather than $\left(\frac{n_c}{n_e}\right)$.
The optimal beam parameters and modified scaling laws were plotted on a 2D map of density and length. Boundary contours were drawn in Figure 6.24, where electron beams with energies > 100 MeV and> 10 pC were also shown in this Figure. This parameter space plot can now be used for the fine tuning of the accelerator towards desired beam properties for this experimental configuration.

Chapter 7: Examining the density-length parameters space for ionisation injection in a self-guided wakefield accelerator at 10TW

In Chapter 3, the density-length parameter space was optimised to find a host of optima for the various properties of the electron beam. In this chapter, we examine the same gas cell but with helium + 5% carbon dioxide, using the ionisation injection (II) mechanism rather than self-injection (SI). The aim of this chapter was to firstly find the optimal parameters for wakefield acceleration for II and asses how it compares to SI.

From the experimental data, we obtain beam charges up to 35.7 ± 1.6 pC and maximum energies up to 159 ± 22 MeV and beam divergences as a low as 1.6 ± 0.1 mrad. PIC simulations were performed using the same PIC code as previously, FBPIC [3]. Good

agreement with the experimentally measured beam charge is observed. The simulations predict higher beam energies of 220 MeV than what is observed in experiments of 159 MeV. The trend in maximum energy with density exhibited good agreement for the experimental data and simulations. In PIC simulations, II actually generates more charge than SI, but this charge occurs at lengths of 1.5 mm and so was inaccessible by our gas cell.

A secondary aim of this chapter was to understand the differences in the interaction which lead to the differences when compared to self-injection. One interesting difference for ionisation injection was that the evolution length scales with $\frac{n_c}{n_e}$, in agreement with Bloom et al. [231] but differently to SI. The second observation is that the peak a_0 does not evolve in the same way as II. The effects of ionisation defocussing modifies the evolution of the pulse resulting in a different matched spot evolution. We will now move on to addressing the future outlook for this work and highlight the direction in which this research could be focused.

8.2 Future outlook

Wakefield acceleration in a clustered medium

The results from chapter show an interesting route to achieving particle injection into plasma wakes across a broad range of intensities. The experiments presented in this thesis showed the performance of a clustered target for one fixed Hagena parameter -Γ^* where

$$\begin{aligned} \Gamma^* &= k_h \left(\frac{0.74d}{\tan(\alpha)^{0.85}} \right) P_0 T_0^{-2.29} \\ < N > &= 33 \left(\frac{\Gamma^*}{1000} \right)^{2.35} \end{aligned} \tag{8.1}$$

This means that as we scan through pressure, we are in-fact changing the average particle size. The way to overcome this coupling for cluster size would be to vary the backing temperature of the fluid, where we see a stronger variation in the Hagena parameter with temperature than pressure. The average cluster size and the cluster mass fraction will need to be measured on-shot for a more accurate description of the interaction. One interesting way to resolve the microphysics of wakefield acceleration in this medium would be through the use of of an ultra short laser pulse ($\approx 2-3$ fs) to directly measure the density modulations of the wake [211]. As this is a measure of the local plasma wavelength [121], this would allow us to infer the mass fraction of clusters as only the unclustered part of the medium is responsible for the formation of the wakefield.

The use of a pre-pulse to shape the medium was also not explored in this thesis but has been by other authors [197]. A clustered medium allows a plasma waveguide to be setup. The efficient absorption of energy into the plasma can be exploited to create a radially symmetric density profile suitable for stabilising the guiding of high intensity laser pulses.

Several questions remain to be addressed for this particular work. What are self-focussing properties of a clustered medium and how do they vary at relativistic intensities for various cluster sizes and mass fractions? Most theoretical work for this topic are only relevant to non-relativistic intensities where fluid descriptions of the process were adopted. What is the depletion length for a clustered medium? How does the energy deposition for the laser pulse scale with cluster size, peak cluster density and mass fraction. A lot of the theoretical models of laser-cluster interaction ignore the background plasma that this cluster is embedded in.

We have seen through PIC simulations that the presence of clusters certainly modifies the injection process. Why does a clustered medium exhibit greater stability for its electron beams than self-injection? [168]. What are the pre pulse constraints to utilise clusters? Can we use an additional low intensity laser pulse to tune the size of clusters by pre-expanding them before they inject particles into the wake? Hence, we see many more avenues of research, through the use of clustered targets, for lowering the requirements of the laser pulse required for efficient wakefield accelerations.

Density length parameter scan: self-injection

Chapter 6 represents an examination into the opportunities for the optimisation of the accelerator by varying the density and length simultaneously. One of the immediate consequences of the multi-parameter scan is the question of how independent density and length really are for a particular gas cell. We observe a small decrease in the electron density as the cell length in increased which was corrected by the measurement of density. This particular cell design was unfavourable for extremely short cell lengths as the density profile is expected to not be very uniform at short cell lengths. However, we see a large injection of charge for the shortest cell lengths.

The modification to the longitudinal density profile at short gas cell lengths has been observed in literature before [232] and is expected to occur when the length of the cell becomes comparable to the cell entrance/exit apertures. This suggests that we might be able to design the target to control this density transition to localise injection at a particular point along the accelerator.

We observed that the evolution length for particle injection scales with $\left(\frac{n_c}{n_e}\right)^2$ in simulations. With a large dataset taken at smaller cell length increments, it will be possible to test this observation. The inclusion of the effect of focal spot quality into the evolution length will help improve the predictive capability of this model. We know that the energy which is outside the full-width half-maximum of the focal spot is not guided by the plasma wave [120] and so the evolution length will depend on this factor.

Density length parameter scan: ionisation-injection

The final chapter (Chapter 7) builds on the results of Chapter 6 to examine the optimisation of the accelerator with density and length, but this time for ionisation injection. Simulations for this interaction predict that the dopants act to defocus the laser pulse and the medium attains a different matched spot size when compared to self-injection. This raises a few interesting questions and implies that there might be a dopant concentration which optimises the generation of the electron beams from II. Firstly, how does this scale with dopant concentration? This needs to be studied experimentally by looking at the transmitted laser mode for different cell lengths and through simulations.

The highest charge in simulations is attained for cell lengths shorter than were possible for this geometry and so redesigning the cell to utilise a conical aperture will allow these smaller cell lengths to be reached. We measured the transverse momentum of the electron beam using the beam profile monitor and the electron spectrometer. A measurement of the emittance across the density length parameter space will be more interesting for applications with stringent beam quality requirements such a pre-injector stages for other accelerators [245, 246]. The comparison between the emittance attainable for SI and II for this mismatched regime still need to be determined. For matched regimes, the emittance produced by II is expected to be large as it depends on the transverse width of the laser pulse [240, 247]. However, motivated by the lower RMS transverse momentum of II compared to SI, the evolution of the accelerator is hypothesised to play a role in attaining narrow energy spread [248] and low emittance beams from ionisation injection.

With the advent of higher-repetition laser facilities [5, 112], these multi-parameter optimisations can be performed much more easily and the properties of the generated electron beam can have an enormous dynamic range. Most conventional accelerators are built towards a particular design energy as there are many beam optics which have limited acceptance criteria. The tunability of a plasma accelerators offers advantages over conventional accelerators in that a wide range of beam properties can be achieved for nominal modifications of the interaction parameters.

9 Appendix

9.1 Symbols and fundamental constants

In this thesis, the symbols for the fundamental constants have been frequently used in equations throughout this thesis and are present in Table 9.1. All equations in this thesis are expression in SI units.

Symbol	Description	Value
c	speed of light in vacuum	$3.00 \times 10^{8}\,\mathrm{m\,s^{-1}}$
e	elementary unit of charge	$1.60 \times 10^{-19}\,\mathrm{C}$
h	Planck's constant	$6.63 \times 10^{-34}\,\mathrm{J\,s}$
m_e	mass of an electron	$9.11 \times 10^{-31}\,\mathrm{kg}$
m_i	mass of an ion	$1.67 \times 10^{-27}\,\mathrm{kg}$
ϵ_0	permittivity of free space	$8.85 \times 10^{-12}\,\mathrm{F\,m^{-1}}$
μ_0	permeability of free space	$4\pi \times 10^{-7}\mathrm{N\,A^{-2}}$

Table 9.1: Symbols and fundamental constants used throughout this work from CODATA [249].

9.2 Maxwell's equations

Maxwell's equation are the foundations of plasma physics. They describe the evolution of electromagnetic fields and are used frequently in derivations throughout this thesis. In their derivative form they are,

$$\begin{aligned} \nabla \cdot \mathbf{E} &= \frac{\rho}{\epsilon_0}, \\ \nabla \cdot \mathbf{B} &= 0, \\ \nabla \times \mathbf{E} &= -\frac{\partial \mathbf{B}}{\partial t}, \\ \nabla \times \mathbf{B} &= \mu_0 \mathbf{J} + \frac{1}{c^2}\frac{\partial \mathbf{E}}{\partial t}. \end{aligned} \tag{9.1}$$

These equations have a degree of freedom which can be reduced by introducing scalar and vector potentials which take the form,

$$\begin{aligned} \mathbf{E} &= -\frac{\partial \mathbf{A}}{\partial t} - \nabla\phi \\ \mathbf{B} &= \nabla \times \mathbf{A} \end{aligned} \tag{9.2}$$

These potentials are then used with a gauge condition to help close the 8 relations from Maxwell's equations for the 6 variables for the electric and magnetic field vectors. The choice of the gauge is determined by its application as they will reduce the length of the calculation. The Coulomb gauge, $\nabla \cdot \mathbf{A} = 0$, makes the potential equal to the electrostatic potential. The Lorentz gauge, $c^2 \nabla \cdot \mathbf{A} + \frac{\partial \phi}{\partial t}$, is useful for wave-related phenomena.

Bibliography

[1] Imperial College London. "Imperial HPC service." (2018). URL `http://doi.org/10.14469/hpc/2232`. (cited on p. 7 and 92.)

[2] Derouillat, J. et al. "Smilei: a collaborative, open-source, multi-purpose particle-in-cell code for plasma simulation." *Computer Physics Communications*, pp. 351–373 (2018). (cited on p. 7, 69, 92, and 113.)

[3] Lehe, R., Kirchen, M., Andriyash, I. A., Godfrey, B. B., and Vay, J.-L. "A spectral, quasi-cylindrical and dispersion-free particle-in-cell algorithm." *Computer Physics Communications*, pp. 66–82 (2016). (cited on p. 7, 92, 157, 191, and 219.)

[4] Streeter, M. et al. "Temporal feedback control of high-intensity laser pulses to optimize ultrafast heating of atomic clusters." *Applied Physics Letters* (2018). (cited on p. 8.)

[5] Dann, S. et al. "Laser wakefield acceleration with active feedback at 5 Hz." *Physical Review Accelerators and Beams*, p. 041303 (2019). (cited on p. 8 and 222.)

[6] Glinec, Y., Faure, J., Guemnie-Tafo, A., Malka, V., Monard, H., Larbre, J., De Waele, V., Marignier, J., and Mostafavi, M. "Absolute calibration for a broad range single shot electron spectrometer." *Review of scientific instruments*, 77(10):103301 (2006). (cited on p. 17 and 77.)

[7] Rutherford, E. "The scattering of α and β particles by matter and the structure of the atom." *Philosophical Magazine*, pp. 379–398 (2012). (cited on p. 22.)

[8] Cockcroft, J. D. and Walton, E. T. S. "Artificial production of fast protons." *Nature* (1932). (cited on p. 22.)

[9] Steere, A. R. "A timeline of major particle accelerators." Ph.D. thesis, Michigan State University (2005). (cited on p. 22 and 23.)

[10] Bryant, P. J. "A brief history and review of accelerators." (1994). URL `https://cds.cern.ch/record/261062/files/p1.pdf`. (cited on p. 22, 23, and 24.)

[11] National museum scotland. "Cockcroft and Walton generator." (2018). URL https://www.nms.ac.uk/explore-our-collections/stories/science-and-technology/cockcroft-walton-generator/. (cited on p. 22.)

[12] Furfari, F. A. T. "A History of the Van de Graaff Generator." *IEEE Industry Applications Magazine*, pp. 10–14 (2005). (cited on p. 23.)

[13] Lawrence, E. O. and Cooksey, D. "On the apparatus for the multiple acceleration of light ions to high speeds." *Physical Review*, pp. 1131–1140 (1936). (cited on p. 23.)

[14] McMillan, E. M. "The synchrotron-a proposed high energy particle accelerator." *Physical Review*, pp. 143–144 (1945). (cited on p. 23.)

[15] Veksler, V. "Concerning some new methods of acceleration of relativistic particles." *Physical Review*, p. 244 (1946). (cited on p. 23.)

[16] Kerst, D. W. "The Acceleration of Electrons by Magnetic Induction." *Physical Review*, (1940) (1941). URL https://journals.aps.org/pr/pdf/10.1103/PhysRev.60.47. (cited on p. 23.)

[17] Courant, E. D. and Snyder, H. S. "Theory of the alternating-gradient synchrotron." *Annals of Physics*, pp. 1–48 (1958). (cited on p. 23.)

[18] Leroy, D., Perin, R., de Rijk, G., and Thomi, W. "Design of a high-field twin aperture superconducting dipole model." *IEEE Transactions on Magnetics*, pp. 1373–1376 (1988). (cited on p. 23.)

[19] Harms, E. et al. "Status of 3.9 GHz superconducting rf cavity technology at Fermilab." In "2007 IEEE Particle Accelerator Conference (PAC)," pp. 2254–2256 (2007). (cited on p. 23.)

[20] CERN. "Rendering of a superconducting RF cavity used at the Large Hadron Collider." (2018). URL http://anim3d.web.cern.ch/content/rf-cavity-radio-frequency-cavity. (cited on p. 23.)

[21] KIT. "Image of a dipole magnet used at the test facility and synchrotron radiation source at kit." (2018). URL https://www.anka.kit.edu/img/dipole-magnet.jpg. (cited on p. 23.)

[22] Bonin, B. "Field emission in rf cavities." Technical report, CEA Centre d'Etudes de Saclay (1996). (cited on p. 23.)

[23] Klein, U. and Turneaure, J. "Field emission in superconducting rf cavities." *IEEE Transactions on Magnetics*, pp. 1330–1333 (1983). (cited on p. 23.)

[24] Higo, T. et al. "Advances in X-band TW accelerator structures operating in the 100 MV/m regime." SLAC National Accelerator Laboratory (2012). (cited on p. 24.)

[25] Evans, L. "The large hadron collider." *New Journal of Physics*, p. 335 (2007). URL http://stacks.iop.org/1367-2630/9/i=9/a=335. (cited on p. 24 and 25.)

[26] Thomson, M. Modern particle physics. Cambridge University Press (2018). (cited on p. 24.)

[27] Ilten, P. "Electroweak and Higgs Measurements Using Tau Final States with the LHCb Detector." Ph.D. thesis, University College Dublin (2013). (cited on p. 25.)

[28] Richter, B. "From the psi to charm: the experiments of 1975 and 1976." *Reviews of Modern Physics*, p. 251 (1977). (cited on p. 25.)

[29] Aad, G. et al. "Observation of a new particle in the search for the Standard Model Higgs boson with the ATLAS detector at the LHC." *Physics Letters B*, pp. 1–29 (2012). (cited on p. 25.)

[30] Mitnick, R. "Birds eye view of the Large Hadron Collider at CERN." (2015). URL https://sciencesprings.wordpress.com/2015/08/02/fermilab-is-an-enduring-source-of-strength-for/cern-lhc-map-31/. (cited on p. 25.)

[31] CERN. "Stanford linear collider image." (2018). URL https://hep-project-dphep-portal.web.cern.ch/content/pep-ii. (cited on p. 25.)

[32] Langacker, P. and Luo, M. "Implications of precision electroweak experiments for m_t, ρ_0, $sin^2\theta_W$, and grand unification." *Physical Review D*, pp. 817–822 (1991). URL https://link.aps.org/doi/10.1103/PhysRevD.44.817. (cited on p. 25.)

[33] Fukuda, Y. et al. "Evidence for oscillation of atmospheric neutrinos." *Physical Review Letters*, pp. 1562–1567 (1998). URL https://link.aps.org/doi/10.1103/PhysRevLett.81.1562. (cited on p. 26.)

[34] Cahn, R. N. "The eighteen arbitrary parameters of the standard model in your everyday life." *Reviews of Modern Physics*, pp. 951–959 (1996). URL https://link.aps.org/doi/10.1103/RevModPhys.68.951. (cited on p. 26.)

[35] Thomson, M. Modern particle physics. Cambridge University Press (2013). (cited on p. 26.)

[36] Kuno, Y. and Okada, Y. "Muon decay and physics beyond the standard model." *Reviews of Modern Physics*, pp. 151–202 (2001). URL https://link.aps.org/doi/10.1103/RevModPhys.73.151. (cited on p. 26.)

[37] C. Liu, J. and Vylet, V. "Radiation protection at synchrotron radiation facilities." *Radiation protection dosimetry*, pp. 345–357 (2001). (cited on p. 26.)

[38] Kornberg, R. D. "The molecular basis of eukaryotic transcription." *Proceedings of the National Academy of Sciences*, pp. 12955–12961 (2007). URL `https://www.pnas.org/content/104/32/12955`. (cited on p. 26.)

[39] Holder, D., Quinn, P., and Wyles, N. "The SRS at Daresbury Laboratory: a eulogy to the world's first dedicated high-energy synchrotron radiation source." (2019). (cited on p. 26.)

[40] Koningsberger, D. C. and Prins, R. e. X-ray absorption: principles, applications, techniques of EXAFS, SEXAFS, and XANES. John Wiley and Sons (1988). URL `https://www.osti.gov/servlets/purl/6748791`. (cited on p. 27.)

[41] Arthur, J. et al. "Lcls conceptual design report." Technical report. URL `http://www-ssrl.slac.stanford.edu/LCLS/CDR/`. (cited on p. 27.)

[42] Stohr, J. "Linac Coherent Light Source II (LCLS-II) Conceptual Design Report." Technical report (2011). URL `https://www.osti.gov/servlets/purl/1029479`. (cited on p. 27.)

[43] Kruer, W. The Physics of Laser plasma interactions. Taylor and Francis, first edition (2003). (cited on p. 27 and 46.)

[44] Veksler, V. I. "Coherent principle of acceleration of charged particles." (1956). (cited on p. 27.)

[45] Fainberg, Y. B. "Acceleration of charged particles in a plasma." *Journal of Geophysical ResearcSov. Phys. Usp.* (1968). URL `http://doi.wiley.com/10.1029/JA091iA09p09973`. (cited on p. 27.)

[46] Tajima, T. and Dawson, J. M. "Laser electron accelerator." *Physical Review Letters*, p. 267 (1979). (cited on p. 27.)

[47] Matveets, Y. A. and Semchishen, V. A. "Subpicosecond pulse generation and amplification in a passively mode-locked cw dye laser." *Soviet Journal of Quantum Electronics* (1979). (cited on p. 28.)

[48] Rosenbluth, M. and Liu, C. "Excitation of plasma waves by two laser beams." *Physical Review Letters*, p. 701 (1972). (cited on p. 28.)

[49] Clayton, C. E., Joshi, C., Darrow, C., Umstadter, D., and Chen, F. F. "Experimental study of the plasma beat wave accelerator." *IEEE Transactions on Nuclear Science*, pp. 3551–3553 (1985). (cited on p. 28.)

[50] Strickland, D. and Mourou, G. "Compression of amplified chirped optical pulses." *Optics communications*, pp. 447–449 (1985). (cited on p. 28 and 70.)

[51] Krall, J., Ting, A., Esarey, E., and Sprangle, P. "Enhanced acceleration in a self-modulated-laser wake-field accelerator." *Physical Review E*, p. 2157 (1993). (cited on p. 28.)

[52] Nakajima, K. "Observation of Ultrahigh Gradient Electron Acceleration by a Self-Modulated Intense Short Laser Pulse." 74 (1995). (Not cited.)

[53] Esarey, E., Hafizi, B., Hubbard, R., and Ting, A. "Trapping and acceleration in self-modulated laser wakefields." *Physical Review Letters*, pp. 5552–5555 (1998). (cited on p. 28.)

[54] Mangles, S. P. D. et al. "Monoenergetic beams of relativistic electrons from intense laser-plasma interactions." *Nature*, pp. 535–538 (2004). (cited on p. 29.)

[55] Faure, J. et al. "A laser–plasma accelerator producing monoenergetic electron beams." *Nature*, p. 541 (2004). (Not cited.)

[56] Geddes, C. G. R. et al. "A laser plasma accelerator producing monoenergetic electron beams." *Nature*, pp. 538–541 (2004). (cited on p. 29.)

[57] Clayton, C. E., Ralph, J. E., Albert, F., et al. "Self-guided laser wakefield acceleration beyond 1 GeV using ionization-induced injection." *Physical Review Letters*, pp. 3–6 (2010). (cited on p. 29.)

[58] Schmid, K. et al. "Density-transition based electron injector for laser driven wakefield accelerators." *Physical Review Special Topics-Accelerators and Beams*, p. 091301 (2010). (Not cited.)

[59] Thaury, C. et al. "Shock assisted ionization injection in laser-plasma accelerators." *Scientific reports*, p. 16310 (2015). (Not cited.)

[60] Faure, J., Rechatin, C., Norlin, A., Lifschitz, A., Glinec, Y., and Malka, V. "Controlled injection and acceleration of electrons in plasma wakefields by colliding laser pulses." *Nature*, p. 737 (2006). (cited on p. 29.)

[61] Leemans, W. P. et al. "Multi-GeV electron beams from capillary-discharge-guided subpetawatt laser pulses in the self-trapping regime." *Physical Review Letters*, p. 245002 (2014). URL `https://link.aps.org/doi/10.1103/PhysRevLett.113.245002`. (cited on p. 29.)

[62] Gonsalves, A. et al. "Petawatt laser guiding and electron beam acceleration to 8 GeV in a laser-heated capillary discharge waveguide." *Physical review letters*, p. 084801 (2019). (cited on p. 29.)

[63] Kneip, S. et al. "Bright spatially coherent synchrotron X-rays from a table-top source." *Nature Physics*, p. 980 (2010). URL `https://doi.org/10.1038/nphys1789http://10.0.4.14/nphys1789`. (cited on p. 29 and 142.)

[64] Wood, J. C. et al. "Ultrafast imaging of laser driven shock waves using betatron x-rays from a laser wakefield accelerator." *Scientific reports*, p. 11010 (2018). (Not cited.)

[65] Cole, J. M., Wood, J. C., Lopes, N. C., et al. "Laser-wakefield accelerators as hard x-ray sources for 3D medical imaging of human bone." *Scientific reports*, 5:13244 (2015). (cited on p. 29.)

[66] Central Laser Facility. "Gemini amplifer area." (2018). URL `https://www.clf.stfc.ac.uk/Pages/The-Astra-Gemini-Facility.aspx`. (cited on p. 29.)

[67] Chen, S. et al. "MeV energy X-rays from inverse compton scattering with laser-wakefield accelerated electrons." *Physical Review Letters*, p. 155003 (2013). URL `https://link.aps.org/doi/10.1103/PhysRevLett.110.155003`. (cited on p. 29.)

[68] Lemos, N. et al. "Bremsstrahlung hard x-ray source driven by an electron beam from a self-modulated laser wakefield accelerator." *Plasma Physics and Controlled Fusion*, p. 054008 (2018). URL `http://stacks.iop.org/0741-3335/60/i=5/a=054008?key=crossref.ea6bd5b4b84659a308307064195fa5b9`. (cited on p. 29.)

[69] Leemans, W. et al. "Observation of terahertz emission from a laser-plasma accelerated electron bunch crossing a plasma-vacuum boundary." *Physical review letters*, p. 074802 (2003). (cited on p. 29.)

[70] Schlenvoigt, H.-P. et al. "A compact synchrotron radiation source driven by a laser-plasma wakefield accelerator." *Nature Physics*, p. 130 (2007). URL `https://doi.org/10.1038/nphys811http://10.0.4.14/nphys811`. (cited on p. 29.)

[71] Fourmaux, S. et al. "Single shot phase contrast imaging using laser-produced Betatron x-ray beams." pp. 2426–2428 (2011). URL `http://arxiv.org/abs/1106.4484{%}0Ahttp://dx.doi.org/10.1364/OL.36.002426`. (cited on p. 29.)

[72] Döpp, A. et al. "Quick x-ray microtomography using a laser-driven betatron source." *Optica*, pp. 199–203 (2018). URL `http://www.osapublishing.org/optica/abstract.cfm?URI=optica-5-2-199`. (cited on p. 29.)

[73] Reed, S. A. et al. "Efficient initiation of photonuclear reactions using quasimonoenergetic electron beams from laser wakefield acceleration." *Journal of Applied Physics*, p. 073103 (2007). URL https://doi.org/10.1063/1.2787159. (cited on p. 29.)

[74] Cole, J. M. et al. "Experimental evidence of radiation reaction in the collision of a high-intensity laser pulse with a laser-wakefield accelerated electron beam." *Physical Review X*, p. 011020 (2018). URL https://link.aps.org/doi/10.1103/PhysRevX.8.011020. (cited on p. 29.)

[75] Poder, K. et al. "Experimental signatures of the quantum nature of radiation reaction in the field of an ultraintense laser." *Physical Review X*, p. 031004 (2018). URL https://link.aps.org/doi/10.1103/PhysRevX.8.031004. (cited on p. 29.)

[76] Caldwell, A. et al. "Path to awake: Evolution of the concept." *Nuclear Instruments and Methods in Physics Research Section A: Accelerators, Spectrometers, Detectors and Associated Equipment*, pp. 3–16 (2016). (cited on p. 30.)

[77] Aicheler, M. et al. "A multi-TeV linear collider based on CLIC technology: CLIC conceptual design report." Technical report, SLAC National Accelerator Lab., Menlo Park, CA (United States) (2014). (cited on p. 30.)

[78] Chen, C. G., Konkola, P. T., Ferrera, J., Heilmann, R. K., and Schattenburg, M. L. "Analyses of vector gaussian beam propagation and the validity of paraxial and spherical approximations." *Journal of the Optical Society of America A*, pp. 404–412 (2002). URL http://josaa.osa.org/abstract.cfm?URI=josaa-19-2-404. (cited on p. 34.)

[79] Standard, I. et al. "Lasers and laser-related equipment-test methods for laser beam widths, divergence angles and beam propagation ratios." *ISO Standard* (2005). (cited on p. 35.)

[80] Wiesemann, K. "A Short Introduction to Plasma Physics." (2014). (cited on p. 35.)

[81] Gibbon, P. Short pulse laser interactions with matter. World Scientific Publishing Company Singapore (2004). (cited on p. 36, 38, 44, and 52.)

[82] Perelomov, A., Popov, V., and Terentev, M. "Ionization of atoms in an alternating electric field: Ii." *Soviet Physics JETP*, pp. 207–217 (1967). (cited on p. 38.)

[83] Keldysh, L. et al. "Ionization in the field of a strong electromagnetic wave." *Soviet Physics JETP*, pp. 1307–1314 (1965). (cited on p. 38.)

[84] Ammosov, M. et al. "Tunnel ionization of complex atoms and of atomic ions in an alternating electric field." *Soviet Physics JETP*, p. 26 (1986). (cited on p. 38 and 60.)

[85] Augst, S., Strickland, D., Meyerhofer, D. D., Chin, S.-L., and Eberly, J. H. "Tunneling ionization of noble gases in a high-intensity laser field." *Physical review letters*, p. 2212 (1989). (cited on p. 39.)

[86] Bruhwiler, D. L., Dimitrov, D. A., Cary, J. R., Esarey, E., Leemans, W., and Giacone, R. E. "Particle-in-cell simulations of tunneling ionization effects in plasma-based accelerators." *Physics of Plasmas*, 10(5):2022–2030 (2003). URL `https://doi.org/10.1063/1.1566027`. (cited on p. 39, 60, and 101.)

[87] Startsev, E. A. and McKinstrie, C. J. "Multiple scale derivation of the relativistic ponderomotive force." *Physical Review E - Statistical Physics, Plasmas, Fluids, and Related Interdisciplinary Topics*, pp. 7527–7535 (1997). (cited on p. 41.)

[88] Hagena, O. and Obert, W. "Cluster formation in expanding supersonic jets: Effect of pressure, temperature, nozzle size, and test gas." *The Journal of Chemical Physics*, pp. 1793–1802 (1972). (cited on p. 43 and 118.)

[89] Boldarev, A., Gasilov, V., Faenov, a. Y., Fukuda, Y., and Yamakawa, K. "Gas-cluster targets for femtosecond laser interaction: Modeling and optimization." *Review of Scientific Instruments* (2006). URL `http://scitation.aip.org/content/aip/journal/rsi/77/8/10.1063/1.2336105`. (cited on p. 44 and 115.)

[90] Dorchies, F., Blasco, F., Caillaud, T., Stevefelt, J., Stenz, C., Boldarev, A., and Gasilov, V. "Spatial distribution of cluster size and density in supersonic jets as targets for intense laser pulses." *Physical Review A*, pp. 1–8 (2003). (cited on p. 44 and 113.)

[91] Gao, X., Wang, X., Shim, B., Arefiev, A. V., Korzekwa, R., and Downer, M. C. "Characterization of cluster/monomer ratio in pulsed supersonic gas jets." *Applied Physics Letters*, 100(6):1–5 (2012). (cited on p. 44 and 113.)

[92] Arefiev, A. V. et al. "Size distribution and mass fraction of microclusters in laser-irradiated plasmas." *High Energy Density Physics* (2010). (cited on p. 44.)

[93] Fennel, T., Meiwes-Broer, K.-H., Tiggesbäumker, J., Reinhard, P.-G., Dinh, P. M., and Suraud, E. "Laser-driven nonlinear cluster dynamics." *Reviews of modern physics*, p. 1793 (2010). (cited on p. 44, 45, 113, 122, and 123.)

[94] Rose-Petruck, C., Schafer, K. J., Wilson, K. R., and Barty, C. P. J. "Ultrafast electron dynamics and inner-shell ionization in laser driven clusters." *Phys. Rev. A*, 55:1182–1190 (1997). URL `https://link.aps.org/doi/10.1103/PhysRevA.55.1182`. (cited on p. 45.)

[95] Lotz, W. "An empirical formula for the electron-impact ionization cross-section." *Zeitschrift für Physik*, pp. 205–211 (1967). (cited on p. 45 and 113.)

[96] Jungreuthmayer, C., Geissler, M., Zanghellini, J., and Brabec, T. "Microscopic analysis of large-cluster explosion in intense laser fields." *Physical review letters*, p. 133401 (2004). (cited on p. 45 and 48.)

[97] Heidenreich, A., Last, I., and Jortner, J. "Extreme ionization of Xe clusters driven by ultraintense laser fields." *The Journal of Chemical Physics*, 127(7):074305 (2007). URL `https://doi.org/10.1063/1.2762217`. (cited on p. 45.)

[98] Silin, V. P. "Nonlinear high-frequency plasma conductivity." *JETP* (1964). (cited on p. 45.)

[99] Skopalova, E. "The interaction of intense few-cycle laser pulses with nanoscale targets." Ph.D. thesis, Imperial College London (2011). (cited on p. 46 and 48.)

[100] Kundu, M. and Bauer, D. "Nonlinear resonance absorption in the laser-cluster interaction." *Physical review letters*, p. 123401 (2006). (cited on p. 46 and 48.)

[101] Ditmire, T., Donnelly, T., Rubenchik, A. M., Falcone, R. W., and Perry, M. D. "Interaction of intense laser pulses with atomic clusters." *Physical Review A*, pp. 3379–3402 (1996). URL `https://link.aps.org/doi/10.1103/PhysRevA.53.3379`. (cited on p. 48 and 114.)

[102] Milchberg, H. M., McNaught, S. J., and Parra, E. "Plasma hydrodynamics of the intense laser-cluster interaction." *Physical Review E* (2001). URL `https://link.aps.org/doi/10.1103/PhysRevE.64.056402`. (cited on p. 48.)

[103] Greschik, F. and Kull, H. "Two-dimensional PIC simulation of atomic clusters in intense laser fields." pp. 137–145 (2004). (cited on p. 48.)

[104] Alexeev, I., Antonsen, T., Kim, K., and Milchberg, H. "Self-focusing of intense laser pulses in a clustered gas." *Physical review letters*, p. 103402 (2003). (cited on p. 49, 99, 114, and 123.)

[105] Symes, D. R. et al. "Blast-wave diagnosis of self-focusing of an intense laser pulse in a cluster medium." *Physics of Plasmas*, p. 063102 (2007). URL `https://doi.org/10.1063/1.2740700`. (cited on p. 50.)

[106] Zharova, N. A., Litvak, A. G., and Mironov, V. A. "Self-focusing of laser radiation in cluster plasma." *Journal of Experimental and Theoretical Physics Letters*, pp. 619–623 (2003). (cited on p. 50.)

[107] Ditmire, T. et al. "High intensity laser absorption by gases of atomic clusters." *Physical review letters* (1997). (cited on p. 50.)

[108] Milchberg, H., Kim, K., Kumarappan, V., Layer, B., and Sheng, H. "Clustered gases as a medium for efficient plasma waveguide generation." *Philosophical Transactions of the Royal Society A: Mathematical, Physical and Engineering Sciences*, pp. 647–661 (2006). (cited on p. 50.)

[109] Durfee, C. G., Lynch, J., and Milchberg, H. M. "Development of a plasma waveguide for high-intensity laser pulses." *Phyical Review E*, pp. 2368–2389 (1995). URL `https://link.aps.org/doi/10.1103/PhysRevE.51.2368`. (cited on p. 50.)

[110] Mori, W. "The physics of the nonlinear optics of plasmas at relativistic intensities for short-pulse lasers." *IEEE Journal of Quantum Electronics*, pp. 1942–1953 (1997). (cited on p. 51 and 145.)

[111] Schreiber, J. et al. "Complete temporal characterization of asymmetric pulse compression in a laser wakefield." *Physical review letters*, p. 235003 (2010). (cited on p. 51.)

[112] Streeter, M. et al. "Observation of laser power amplification in a self-injecting laser wakefield accelerator." *Physical review letters*, p. 254801 (2018). (cited on p. 52, 125, 146, 161, 199, 206, 212, and 222.)

[113] Dawson, J. M. "Nonlinear electron oscillations in a cold plasma." *Physical Review*, p. 383 (1959). (cited on p. 53.)

[114] Katsouleas, T. and Mori, W. "Wave-breaking amplitude of relativistic oscillations in a thermal plasma." *Physical review letters*, p. 90 (1988). (cited on p. 54.)

[115] Poder, K. "Characterisation of self-guided laser wakefield accelerators to multi-GeV energies." Ph.D. thesis, Imperial College London (2016). (cited on p. 56, 78, 79, 143, 166, and 202.)

[116] Esarey, E. and Pilloff, M. "Trapping and acceleration in nonlinear plasma waves." *Physics of Plasmas*, pp. 1432–1436 (1995). (cited on p. 56.)

[117] Corde, S. et al. "Observation of longitudinal and transverse self-injections in laser-plasma accelerators." *Nature Communications*, p. 1501 (2013). (cited on p. 58 and 67.)

[118] Islam, M. et al. "Near-threshold electron injection in the laser–plasma wakefield accelerator leading to femtosecond bunches." *New Journal of Physics*, p. 093033 (2015). (cited on p. 58.)

[119] Thomas, A. G. R. "Scalings for radiation from plasma bubbles." *Physics of Plasmas*, p. 056708 (2010). URL `https://doi.org/10.1063/1.336867`. (cited on p. 58 and 121.)

[120] Mangles, S. P. D. et al. "Self-injection threshold in self-guided laser wakefield accelerators." *Physical Review Special Topics-Accelerators and Beams*, p. 011302 (2012). URL `https://link.aps.org/doi/10.1103/PhysRevSTAB.15.011302`. (cited on p. 58, 144, 145, and 222.)

[121] Kuschel, S. et al. "Controlling the self-injection threshold in laser wakefield accelerators." *Physical review letters*, p. 154801 (2018). (cited on p. 59, 112, 113, 119, 121, 123, 125, 144, 169, 179, 217, and 220.)

[122] Pak, A. et al. "Injection and trapping of tunnel-ionized electrons into laser-produced wakes." *Physical Review Letters*, p. 025003 (2010). URL `https://link.aps.org/doi/10.1103/PhysRevLett.104.025003`. (cited on p. 59.)

[123] Rowlands-Rees, T. et al. "Laser-driven acceleration of electrons in a partially ionized plasma channel." *Physical review letters*, p. 105005 (2008). (cited on p. 59.)

[124] Chen, M., Esarey, E., Schroeder, C. B., Geddes, C. G. R., and Leemans, W. P. "Theory of ionization-induced trapping in laser-plasma accelerators." *Physics of Plasmas* (2012). (cited on p. 59, 60, 180, and 181.)

[125] Esarey, E., Schroeder, C., and Leemans, W. "Physics of laser-driven plasma-based electron accelerators." *Reviews of modern physics*, p. 1229 (2009). (cited on p. 60.)

[126] Kim, J. U., Hafz, N., and Suk, H. "Electron trapping and acceleration across a parabolic plasma density profile." *Phys. Rev. E*, 69:026409 (2004). URL `https://link.aps.org/doi/10.1103/PhysRevE.69.026409`. (cited on p. 61.)

[127] Hansson, M. et al. "Down-ramp injection and independently controlled acceleration of electrons in a tailored laser wakefield accelerator." *Physical Review Special Topics-Accelerators and Beams*, p. 071303 (2015). (cited on p. 61.)

[128] Ekerfelt, H., Hansson, M., Gallardo González, I., Davoine, X., and Lundh, O. "A tunable electron beam source using trapping of electrons in a density down-ramp in laser wakefield acceleration." *Scientific Reports*, 7(1):12229 (2017). URL `https://doi.org/10.1038/s41598-017-12560-8`. (cited on p. 61.)

[129] Decker, C. D., Mori, W. B., Tzeng, K., and Katsouleas, T. "The evolution of ultraintense, shortpulse lasers in underdense plasmas." *Physics of Plasmas*, pp. 2047–2056 (1996). URL https://doi.org/10.1063/1.872001. (cited on p. 61, 64, and 194.)

[130] Lu, W. et al. "A nonlinear theory for multidimensional relativistic plasma wave wakefields." *Physics of Plasmas* (2006). (cited on p. 62 and 168.)

[131] Sprangle, P., Tang, C., and Esarey, E. "Relativistic self-focusing of short-pulse radiation beams in plasmas." *IEEE Transactions on Plasma Science*, pp. 145–153 (1987). (cited on p. 63.)

[132] Thomas, A. et al. "Effect of laser-focusing conditions on propagation and monoenergetic electron production in laser-wakefield accelerators." *Physical review letters*, p. 095004 (2007). (cited on p. 63.)

[133] Geddes, C. G. R. "Plasma channel guided laser wakefield accelerator." Technical report (2005). (cited on p. 64.)

[134] Shadwick, B. A., Schroeder, C. B., and Esarey, E. "Nonlinear laser energy depletion in laser-plasma accelerators." *Physics of Plasmas*, p. 056704 (2009). URL https://doi.org/10.1063/1.3124185. (cited on p. 64, 161, and 206.)

[135] Lu, W. et al. "Generating multi-GeV electron bunches using single stage laser wakefield acceleration in a 3d nonlinear regime." *Physical Review Special Topics-Accelerators and Beams*, p. 61301 (2007). URL https://link.aps.org/doi/10.1103/PhysRevSTAB.10.061301. (cited on p. 65, 98, 118, 134, 137, 138, 186, 202, 205, and 219.)

[136] Wilks, S., Katsouleas, T., Dawson, J. M., Chen, P., and Su, J. J. "Beam loading in plasma waves." *IEEE Transactions on Plasma Science*, pp. 210–217 (1987). (cited on p. 65.)

[137] Tzoufras, M. et al. "Beam loading in the nonlinear regime of plasma-based acceleration." *Physical Review Letters*, p. 145002 (2008). URL https://link.aps.org/doi/10.1103/PhysRevLett.101.145002. (cited on p. 65.)

[138] Jackson, J. D. Classical electrodynamics. John Wiley & Sons (2007). (cited on p. 66 and 85.)

[139] Corde, S., Ta Phuoc, K., Lambert, G., Fitour, R., Malka, V., Rousse, A., Beck, A., and Lefebvre, E. "Femtosecond x rays from laser-plasma accelerators." *Reviews of Modern Physics* (2013). (cited on p. 66.)

[140] Maiman, T. "Stimulated optical radiation in ruby." *Nature*, 187:493–494 (1960). (cited on p. 69.)

[141] McClung, F. J. and Hellwarth, R. W. "Giant optical pulsations from ruby." *Journal of Applied Physics*, pp. 828–829 (1962). URL https://doi.org/10.1063/1.1777174. (cited on p. 69.)

[142] DeMaria, A., Stetser, D., and Heynau, H. "Self mode-locking of lasers with saturable absorbers." *Applied Physics Letters*, pp. 174–176 (1966). (cited on p. 69.)

[143] Al'Tshuler, G., Karasev, V., Kondratiuk, N., Kruglik, G., and Okishev, A. "Generation of ultrashort pulses in a synchronously pumped Ti (3+) laser." *Pisma v Zhurnal Tekhnischeskoi Fiziki*, pp. 779–783 (1987). (cited on p. 69.)

[144] Spence, D. E., Kean, P. N., and Sibbett, W. "60-fsec pulse generation from a self-mode-locked Ti:sapphire laser." *Opt. Lett.* (1991). URL http://ol.osa.org/abstract.cfm?URI=ol-16-1-42. (cited on p. 70.)

[145] Divall, E. J. "Laser performance data analysis tool." (2008). URL https://www.clf.stfc.ac.uk/Pages/ar07-08_s7_laser_performance_data_analysis.pdf. (cited on p. 71.)

[146] Central Laser Facility. "Gemini." (2018). URL https://www.clf.stfc.ac.uk/Pages/The-Astra-Gemini-Facility.aspx. (cited on p. 71, 100, and 146.)

[147] Schmid, K. and Veisz, L. "Supersonic gas jets for laser-plasma experiments." *Review of Scientific Instruments*, p. 053304 (2012). URL https://doi.org/10.1063/1.4719915. (cited on p. 71.)

[148] Rao, B. et al. "High-quality stable electron beams from laser wakefield acceleration in high density plasma." *Physical Review Special Topics-Accelerators and Beams*, p. 011301 (2014). (cited on p. 71.)

[149] Svensson, K. et al. "Supersonic jets of hydrogen and helium for laser wakefield acceleration." *Phys. Rev. Accel. Beams*, p. 051301 (2016). URL https://link.aps.org/doi/10.1103/PhysRevAccelBeams.19.051301. (cited on p. 72.)

[150] Couperus, J. P. et al. "Tomographic characterisation of gas-jet targets for laser wakefield acceleration." *Nuclear Instruments and Methods in Physics Research Section A: Accelerators, Spectrometers, Detectors and Associated Equipment*, pp. 504–509 (2016). (cited on p. 72.)

[151] Osterhoff, J. et al. "Generation of stable, low-divergence electron beams by laser-wakefield acceleration in a steady-state-flow gas cell." *Physical Review Letters*, p. 085002 (2008). URL https://link.aps.org/doi/10.1103/PhysRevLett.101.085002. (cited on p. 72.)

[152] Kononenko, O. et al. "2d hydrodynamic simulations of a variable length gas target for density down-ramp injection of electrons into a laser wakefield accelerator." *Nuclear Instruments and Methods in Physics Research Section A: Accelerators, Spectrometers, Detectors and Associated Equipment*, pp. 125–129 (2016). (cited on p. 72 and 170.)

[153] Mangles, S. P. D. et al. "Controlling the spectrum of x-rays generated in a laser-plasma accelerator by tailoring the laser wavefront." *Applied Physics Letters*, p. 181106 (2009). URL https://doi.org/10.1063/1.3258022. (cited on p. 74.)

[154] Beaurepaire, B. et al. "Effect of the laser wave front in a laser-plasma accelerator." *Physical Review X*, p. 031012 (2015). URL https://link.aps.org/doi/10.1103/PhysRevX.5.031012. (cited on p. 74.)

[155] Nussbaum, P., Voelkel, R., Herzig, H. P., Eisner, M., and Haselbeck, S. "Design, fabrication and testing of microlens arrays for sensors and microsystems." *Pure and applied optics: Journal of the European optical society part A*, p. 617 (1997). (cited on p. 74.)

[156] Platt, B. C. and Shack, R. "History and principles of shack-hartmann wavefront sensing." *Journal of refractive surgery*, pp. S573–S577 (2001). (cited on p. 74.)

[157] Imagine Optic. "HASO wavefront sensor." (2018). URL https://www.imagine-optic.com/product/haso4-nir/. (cited on p. 75.)

[158] Nicolas, L., L., X., E., L., and T., S. "Large deformable mirrors for beam control of high brightness lasers." (2013). URL https://doi.org/10.1117/12.2001841. (cited on p. 75.)

[159] Edmund Optics. "10X Mitutoyo Plan Apo NIR Infinity Corrected Objective." (2018). URL https://www.edmundoptics.co.uk/p/10x-mitutoyo-plan-apo-nir-infinity-corrected-objective/6833/. (cited on p. 75.)

[160] Trebino, R. Frequency-resolved optical gating: the measurement of ultrashort laser pulses. Springer Science & Business Media (2012). (cited on p. 76.)

[161] Krishnakumar, R. "Scintillation screen materials for beam profile measurements of high energy ion beams." Ph.D. thesis, Technische Universität Darmstadt (2016). (cited on p. 76.)

[162] Buck, A., Zeil, K., Popp, A., et al. "Absolute charge calibration of scintillating screens for relativistic electron detection." *Review of Scientific Instruments* (2010). (cited on p. 76.)

[163] Giakoumakis, G. and Miliotis, D. "Light angular distribution of fluorescent screens excited by x-rays." *Physics in Medicine & Biology*, p. 21 (1985). (cited on p. 76.)

[164] Edmund Optics. "Bandpass filter for LANEX." (2018). URL `https://www.edmundoptics.com/p/546nm-cwl-118mm-dia-bandpass-filter/1727`. (cited on p. 77.)

[165] Miyahara, J., Takahashi, K., Amemiya, Y., Kamiya, N., and Satow, Y. "A new type of x-ray area detector utilizing laser stimulated luminescence." *Nuclear Instruments and Methods in Physics Research Section A: Accelerators, Spectrometers, Detectors and Associated Equipment*, pp. 572–578 (1986). (cited on p. 77.)

[166] Tanaka, K. A. et al. "Calibration of imaging plate for high energy electron spectrometer." *Review of scientific instruments*, p. 013507 (2005). (cited on p. 77.)

[167] Fuji Film. "Fluorescent Image Analyzer used to extract the quantum levels from Image plate." (2018). URL `http://www.imb.sinica.edu.tw/core/publicfacilities/pdf/FLA-5000og.pdf`. (cited on p. 77.)

[168] Wood, J. C. "Betatron radiation from laser wakefield accelerators and its applications." Ph.D. thesis, Imperial College London (2017). (cited on p. 77, 84, 85, 90, 98, 99, 106, 139, 140, 143, and 221.)

[169] Alnaimi, R. "The use of BAS-TR imaging plates calibration in determining the resolving power of Fuji BAS-1800II image plate reader." *Journal of Instrumentation*, 13(01):1016 (2018). (cited on p. 78.)

[170] HIRST. "Hall probe." (2018). URL `http://www.hirst-magnetics.com/instruments/gm08_p1.shtml`. (cited on p. 78.)

[171] Scheimpflug, T. "Improved method and apparatus for the systematic alteration or distortion of plane pictures and images by means of lenses and mirrors for photography and for other purposes." *GB patent* (1904). (cited on p. 79.)

[172] Peng, J., Wang, M., Deng, D., Liu, X., Yin, Y., and Peng, X. "Distortion correction for microscopic fringe projection system with scheimpflug telecentric lens." *Applied optics*, 54(34):10055–10062 (2015). (cited on p. 79.)

[173] Cole, J. M. "Diagnosis and application of laser wakefield accelerators." Ph.D. thesis, Imperial College London (2015). (cited on p. 79, 82, 83, and 148.)

[174] Pianthong, K., Zakrzewski, S., Behnia, M., and Milton, B. "Supersonic liquid jets: Their generation and shock wave characteristics." *Shock Waves*, pp. 457–466 (2002). URL `https://doi.org/10.1007/s001930200130`. (cited on p. 80.)

[175] Hutchinson, I. H. "Principles of plasma diagnostics." *Plasma Physics and Controlled Fusion*, p. 2603 (2002). (cited on p. 81.)

[176] Takeda, M., Ina, H., and Kobayashi, S. "Fourier-transform method of fringe-pattern analysis for computer-based topography and interferometry." *Journal of the optical society of America*, pp. 156–160 (1982). (cited on p. 83.)

[177] Krantz, S. G. Explorations in harmonic analysis: with applications to complex function theory and the Heisenberg group. Springer Science & Business Media (2009). (cited on p. 83.)

[178] Goldstein, R. M., Zebker, H. A., and Werner, C. L. "Satellite radar interferometry: Two-dimensional phase unwrapping." *Radio science*, 23(4):713–720 (1988). (cited on p. 84.)

[179] Costantini, M. "A novel phase unwrapping method based on network programming." *IEEE Transactions on geoscience and remote sensing*, pp. 813–821 (1998). (Not cited.)

[180] Volkov, V. V. and Zhu, Y. "Deterministic phase unwrapping in the presence of noise." *Optics letters*, pp. 2156–2158 (2003). (cited on p. 84.)

[181] Cole, J. M. "Interpret phase retrieval." (2018). URL `https://github.com/jasmcole/Interpret`. (cited on p. 84.)

[182] Andor. "iKon M–934 specification." (2018). URL `https://andor.oxinst.com/products/ikon-xl-and-ikon-large-ccd-series/ikon-m-934#product-information-tabs`. (cited on p. 84.)

[183] Bloom, M. S. "Studies on the relativistic electrons and x-rays generated by laser wakefield accelerators." Ph.D. thesis, Imperial College London (2014). (cited on p. 85 and 130.)

[184] Fonseca, R. et al. "Osiris: A three-dimensional, fully relativistic particle in cell code for modeling plasma based accelerators." *Computational Science*, pp. 342–351 (2002). (cited on p. 92.)

[185] Benedetti, C., Sgattoni, A., Turchetti, G., and Londrillo, P. "ALaDyn: A High-Accuracy PIC Code for the Maxwell–Vlasov Equations." *IEEE Transactions on plasma science*, pp. 1790–1798 (2008). (Not cited.)

[186] Arber, T. et al. "Contemporary particle-in-cell approach to laser-plasma modelling." *Plasma Physics and Controlled Fusion*, p. 113001 (2015). (cited on p. 92.)

[187] Chen, Y. "Lecture 6: Density estimation: Histogram and kernel density estimator." (2018). URL `http://faculty.washington.edu/yenchic/18W_425/Lec6_hist_KDE.pdf`. (cited on p. 93.)

[188] Breheny, P. "Nonparametric statistics." (2018). URL `https://web.as.uky.edu/statistics/users/pbreheny/621/F10/notes/10-28.pdf`. (cited on p. 93.)

[189] Falk, M. "Bootstrap optimal bandwidth selection for kernel density estimates." *Journal of statistical planning and inference*, pp. 13–22 (1992). (cited on p. 94.)

[190] Fukuda, Y. et al. "Ultrarelativistic electron generation during the intense, ultrashort laser pulse interaction with clusters." *Physics Letters, Section A: General, Atomic and Solid State Physics*, pp. 130–135 (2007). (cited on p. 97.)

[191] Liseykina, T. and Bauer, D. "Plasma-formation dynamics in intense laser-droplet interaction." *Physical review letters*, p. 145003 (2013). (cited on p. 97.)

[192] Mirzaie, M. et al. "Laser acceleration in argon clusters and gas media." *Plasma Physics and Controlled Fusion*, p. 034014 (2016). (cited on p. 97 and 98.)

[193] Nam, I., Kim, M., Lee, T. H., Lee, S. W., and Suk, H. "Highly-efficient 20 TW Ti: sapphire laser system using optimized diverging beams for laser wakefield acceleration experiments." *Current Applied Physics*, pp. 468–472 (2015). (cited on p. 98.)

[194] Cho, M. H., Pathak, V. B., Kim, H. T., and Nam, C. H. "Controlled electron injection facilitated by nanoparticles for laser wakefield acceleration." *Scientific reports*, p. 16924 (2018). (cited on p. 98.)

[195] Lee, K., Kim, S., and Lee, D. "Aerodynamic focusing of 5–50 nm nanoparticles in air." *Journal of Aerosol Science*, 40(12):1010–1018 (2009). (cited on p. 99.)

[196] Aniculaesei, C. et al. "Proof-of-principle experiment for nanoparticle-assisted laser wakefield acceleration." *arXiv preprint arXiv:1902.00921* (2019). (cited on p. 99.)

[197] Ditmire, T., Smith, R., and Hutchinson, M. "Plasma waveguide formation in predissociated clustering gases." *Optics letters*, pp. 322–324 (1998). (cited on p. 99 and 221.)

[198] Kumarappan, V. et al. "Guiding of intense laser pulses in plasma waveguides produced from efficient, femtosecond end-pumped heating of clustered gases." *Physical review letters* (2005). (cited on p. 99.)

[199] Gao, X., Wang, X., Shim, B., and Downer, M. "Laser-driven acceleration in clustered plasmas." In "AIP Conference Proceedings," volume 1086, pp. 142–146. AIP (2009). (cited on p. 99.)

[200] Hooker, C. J., Blake, S., Chekhlov, O., Clarke, R. J., Collier, J. L., Divall, E. J., Ertel, K., Foster, P. S., Hawkes, S. J., Holligan, P., et al. "Commissioning the Astra Gemini petawatt Ti: sapphire laser system." In "Conference on Lasers and Electro-Optics," p. JThB2. Optical Society of America (2008). (cited on p. 100.)

[201] Iaconis, C. and Walmsley, I. A. "Spectral phase interferometry for direct electric-field reconstruction of ultrashort optical pulses." *Optics letters*, pp. 792–794 (1998). (cited on p. 100.)

[202] Gentec. "Pyroelectric power meter." (2019). URL `https://www.gentec-eo.com/products/qe50lp-s-mb-qed-d0`. (cited on p. 100.)

[203] Wörmer, J., Guzielski, V., Stapelfeldt, J., and Möller, T. "Fluorescence excitation spectroscopy of xenon clusters in the VUV." *Chemical Physics Letters*, pp. 321–326 (1989). (cited on p. 101.)

[204] Smith, R., Ditmire, T., and Tisch, J. "Characterization of a cryogenically cooled high-pressure gas jet for laser/cluster interaction experiments." *Review of scientific instruments*, pp. 3798–3804 (1998). (cited on p. 101 and 112.)

[205] Amplitude. "Sequoia." (2019). URL `https://amplitude-laser.com/wp-content/uploads/2018/11/Sequoia.pdf`. (cited on p. 101.)

[206] MATLAB. "Projective transformation." (2019). URL `https://uk.mathworks.com/help/images/ref/projective2d.html`. (cited on p. 105.)

[207] MATLAB. "Find local maxima." (2019). URL `https://uk.mathworks.com/help/signal/ref/findpeaks.html`. (cited on p. 105.)

[208] Gal, O. "Fit ellipse-File exchange." (2019). URL `https://uk.mathworks.com/matlabcentral/fileexchange/3215-fit_ellipse`. (cited on p. 111.)

[209] Vargas, M. et al. "Improvements to laser wakefield accelerated electron beam stability, divergence, and energy spread using three-dimensional printed two-stage gas cell targets." *Applied Physics Letters*, p. 174103 (2014). (cited on p. 112.)

[210] Modena, A. et al. "Electron acceleration from the breaking of relativistic plasma waves." *Nature*, p. 606 (1995). (cited on p. 112.)

[211] Sävert, A. et al. "Direct observation of the injection dynamics of a laser wakefield accelerator using few-femtosecond shadowgraphy." *Physical review letters*, p. 055002 (2015). (cited on p. 119 and 220.)

[212] Rae, S. "Ionization-induced defocusing of intense laser pulses in high-pressure gases." *Optics communications*, pp. 25–28 (1993). (cited on p. 119, 139, and 200.)

[213] He, Z. et al. "High repetition-rate wakefield electron source generated by few-millijoule, 30 fs laser pulses on a density downramp." *New Journal of Physics*, p. 053016 (2013). (cited on p. 125.)

[214] Ferrario, M. et al. "SPARCLAB present and future." *Nuclear Instruments and Methods in Physics Research Section B: Beam Interactions with Materials and Atoms*, pp. 183–188 (2013). (cited on p. 125.)

[215] Liu, C. et al. "Adaptive-feedback spectral-phase control for interactions with transform-limited ultrashort high-power laser pulses." *Optics letters*, pp. 80–83 (2014). (cited on p. 125.)

[216] Prencipe, I. et al. "Targets for high repetition rate laser facilities: needs, challenges and perspectives." *High Power Laser Science and Engineering*, 5 (2017). (cited on p. 125.)

[217] Lindner, F. et al. "High-order harmonic generation at a repetition rate of 100 khz." *Physical Review A*, p. 013814 (2003). (cited on p. 125.)

[218] Chiang, C.-T., Blättermann, A., Huth, M., Kirschner, J., and Widdra, W. "High-order harmonic generation at 4 mhz as a light source for time-of-flight photoemission spectroscopy." *Applied Physics Letters*, p. 071116 (2012). (cited on p. 125.)

[219] Kühn, S. et al. "The eli-alps facility: the next generation of attosecond sources." *Journal of Physics B: Atomic, Molecular and Optical Physics*, p. 132002 (2017). (cited on p. 125.)

[220] Andor. "iKon–L 936." (2019). URL `https://andor.oxinst.com/products/ikon-xl-and-ikon-large-ccd-series/ikon-l-936`. (cited on p. 130.)

[221] Antimonov, M. et al. "Large-area kapton x-ray windows." In "Advances in X-Ray/EUV Optics and Components X," p. 95880F. International Society for Optics and Photonics (2015). (cited on p. 130.)

[222] Schroeder, C., Esarey, E., Shadwick, B., and Leemans, W. "Trapping, dark current, and wave breaking in nonlinear plasma waves." *Physics of Plasmas*, p. 033103 (2006). (cited on p. 139.)

[223] Dong, C. et al. "High flux femtosecond x-ray emission from the electron-hose instability in laser wakefield accelerators." *Physical Review Accelerators and Beams*, p. 041303 (2018). (cited on p. 141 and 174.)

[224] Whittum, D. H. et al. "Electron-hose instability in the ion-focused regime." *Physical review letters* (1991). (cited on p. 141.)

[225] Mangles, S. et al. "Electron beam pointing instability in a self-injected laser wakefield accelerator." *CLF annual report* (2004). (cited on p. 141.)

[226] Heigoldt, M. et al. "Temporal evolution of longitudinal bunch profile in a laser wakefield accelerator." *Physical Review Special Topics-Accelerators and Beams*, p. 121302 (2015). (cited on p. 143.)

[227] Vieira, J., Fiúza, F., Silva, L., Tzoufras, M., and Mori, W. "Onset of self-steepening of intense laser pulses in plasmas." *New Journal of Physics*, p. 045025 (2010). (cited on p. 145.)

[228] Jalas, S. et al. "Accurate modeling of plasma acceleration with arbitrary order pseudo-spectral particle-in-cell methods." *Physics of Plasmas* (2017). (cited on p. 157.)

[229] Lifschitz, A. et al. "Particle-in-cell modelling of laser–plasma interaction using fourier decomposition." *Journal of Computational Physics*, pp. 1803–1814 (2009). (cited on p. 157.)

[230] Davidson, A. et al. "Implementation of a hybrid particle code with a pic description in r–z and a gridless description in ϕ into osiris." *Journal of Computational Physics*, pp. 1063–1077 (2015). (cited on p. 157.)

[231] Bloom, M. et al. "Bright x-ray radiation from plasma bubbles in an evolving laser wakefield accelerator." *arXiv preprint arXiv:1710.05740* (2017). (cited on p. 164, 165, 176, 199, 219, and 220.)

[232] Audet, T. et al. "Gas cell density characterization for laser wakefield acceleration." *Nuclear Instruments and Methods in Physics Research Section A: Accelerators, Spectrometers, Detectors and Associated Equipment* (2018). (cited on p. 170 and 221.)

[233] Sears, C. M. et al. "Emittance and divergence of laser wakefield accelerated electrons." *Physical Review Special Topics-Accelerators and Beams*, p. 092803 (2010). (cited on p. 173.)

[234] Dornmair, I., Floettmann, K., and Maier, A. "Emittance conservation by tailored focusing profiles in a plasma accelerator." *Physical Review Special Topics-Accelerators and Beams*, p. 041302 (2015). (cited on p. 173.)

[235] Thévenet, M. et al. "Pulse front tilt steering in laser plasma accelerators." *Physical Review Accelerators and Beams*, p. 071301 (2019). (cited on p. 174, 208, and 212.)

[236] Lu, W. et al. "A nonlinear theory for multidimensional relativistic plasma wave wakefields." *Physics of Plasmas*, p. 056709 (2006). (cited on p. 177 and 213.)

[237] Hansson, M. et al. "Localization of ionization-induced trapping in a laser wakefield accelerator using a density down-ramp." *Plasma Physics and Controlled Fusion* (2016). (cited on p. 180.)

[238] González, I. G. et al. "Effects of the dopant concentration in laser wakefield and direct laser acceleration of electrons." *New Journal of Physics*, p. 053011 (2018). (cited on p. 180.)

[239] Desforges, F. et al. "Dynamics of ionization-induced electron injection in the high density regime of laser wakefield acceleration." *Physics of Plasmas*, p. 120703 (2014). (cited on p. 202.)

[240] Schroeder, C. et al. "Thermal emittance from ionization-induced trapping in plasma accelerators." *Physical Review Special Topics-Accelerators and Beams*, p. 101301 (2014). (cited on p. 204 and 222.)

[241] Shaw, J. et al. "Role of direct laser acceleration of electrons in a laser wakefield accelerator with ionization injection." *Physical review letters*, p. 064801 (2017). (cited on p. 206.)

[242] Kuschel, S. et al. "Demonstration of passive plasma lensing of a laser wakefield accelerated electron bunch." *Physical Review Accelerators and Beams*, p. 071301 (2016). (cited on p. 207.)

[243] Popp, A. et al. "All-optical steering of laser-wakefield-accelerated electron beams." *Physical review letters*, p. 215001 (2010). (cited on p. 208.)

[244] Mangles, S. P. et al. "Laser-wakefield acceleration of monoenergetic electron beams in the first plasma-wave period." *Physical review letters*, p. 215001 (2006). (cited on p. 209 and 210.)

[245] Petrillo, V., Serafini, L., and Tomassini, P. "Ultrahigh brightness electron beams by plasma-based injectors for driving all-optical free-electron lasers." *Physical Review Special Topics-Accelerators and Beams*, p. 070703 (2008). (cited on p. 222.)

[246] Walker, P. A. et al. "Horizon 2020 EuPRAXIA design study." In "Journal of Physics: Conference Series," p. 012029. IOP Publishing (2017). (cited on p. 222.)

[247] Barber, S. et al. "Measured emittance dependence on the injection method in laser plasma accelerators." *Physical Review Letters*, p. 104801 (2017). (cited on p. 222.)

[248] Mirzaie, M. et al. "Demonstration of self-truncated ionization injection for GeV electron beams." *Scientific reports*, p. 14659 (2015). (cited on p. 222.)

[249] Mohr, P. J., Taylor, B. N., and Newell, D. B. "CODATA recommended values of the fundamental physical constants: 2010." *Journal of Physical and Chemical Reference Data*, p. 1527 (2012). (cited on p. 224.)